EAST EUROPEAN JOURNAL OF PHYSICS. **2.** 348-358 (2025)
DOI:10.26565/2312-4334-2025-2-44 ISSN 2312-4334

UNSTATIONARY VISCOELASTIC MHD FLOW OF WALTERS-B LIQUID THROUGH A VERTICAL POROUS PLATE WITH CHEMICAL REACTIONS

Karnati Veera Reddy[a]*, G. Ravindranath Reddy[b], K. Jhansi Rani[c], Ayyalappagari Sreenivasulu[d], Gudala Balaji Prakash[e]
[a]*Department of Mathematics, Guru Nanak Institutions Technical Campus, Ranga Reddy (Dt) -501506, Telangana, India*
[b]*MLR Institute of Technology, Dundigal, Hyderabad -500043, Telangana, India*
[c]*Freshman Engineering Department, Lakireddy Bali Reddy College of Engineering, L.B. Reddy Nagar, Mylavaram- 521230, Andhra Pradesh, India*
[d]*Department of Engineering Mathematics, Koneru Lakshmaiah Education Foundation Green fields, Vaddeswaram, Guntur-522302, Andhra Pradesh, India*
[e]*Department of Mathematics, Aditya University, Surampalem-533437 Andhra Pradesh, India*
Corresponding Author e-mail: veerareddymscmed@gmail.com
Received September 30, 2024; revised January 4, 2025; accepted April 16, 2025

This study investigates the transient magnetohydrodynamic (MHD) flow of Walter's-B viscoelastic fluid over a vertical porous plate within a porous medium, incorporating the effects of radiation and chemical processes. The nonlinear governing equations for the flow are solved using a closed-loop method, yielding detailed numerical solutions for velocity, temperature, and concentration profiles. The results indicate that velocity decreases with increasing permeability (K), Schmidt number (Sc), radiation parameter (R), and magnetic field strength (M), while it increases with higher Prandtl number (Pr), permeability (K), and time (t). Temperature decreases with increasing radiation but rises with higher Prandtl number and time. Similarly, concentration decreases with higher permeability and Schmidt number but increases with time. Notably, an increase in the Brownian motion parameter enhances heat and momentum transfer, resulting in thicker velocity and thermal boundary layers. This research has practical applications in various fields, including blood oxygenators, chemical reactors, and polymer processing industries. The study's novelty lies in its comprehensive integration of radiation, chemical processes, and MHD effects in analyzing viscoelastic fluid flows – a topic that remains underexplored in the literature. Future research could focus on optimizing MHD Walter's-B viscoelastic flow systems, particularly by examining the effects of magnetic field strength and viscoelastic parameters on flow behavior.
Keywords: *MHD; Skin friction; Chemical reaction; Radiation and viscoelastic properties*
PACS: 44.20.+b; 47.10.ad; 47.11.Bc; 47.15.Cb; 47.35.Tv; 47.50.-d; 47.55.pb; 47.56.+r; 47.65.-d; 47.70.-n

1. INTRODUCTION

A growing number of mathematicians have recently taken an interest in boundary layer flow due to its applications in studying mass and heat transfer phenomena. This interest is motivated by the wide range of applications in various domains, including blood oxygenators, mixing mechanisms, dissolution processes, milk processing, and polymer processing within manufacturing industries. Non-Newtonian fluids are analyzed using a variety of viscoelastic fluid models, such as the Rivlin-Erickson, Maxwell, Walter's-B, micropolar fluids, and second- and third-grade viscoelastic fluids. The boundary layer problem was initially studied by Sakiadis [1, 2], who assumed a constant velocity for the bounding surface. Applications of the boundary layer deportation problem in absorbent materials include geothermal reservoirs and hydroelectric extraction. Crane [3] provided a solution for Newtonian fluid flow over an elastic sheet stretched proportionally to its distance from the origin. Soundalgekar and Wavre [4] investigated unstable free mass transfer and convection through infinite vertical porous plates in a vacuum. Ramana et al. [5] analyzed unsteady free Casson fluid transmission over a semi-infinite vertical porous plate, considering thermal radiation, Soret and Dufour effects, and MHD numerical solutions. Naga Santoshi et al. [6] *a*nalysis of MHD Slip Flow of Upper-Convected Casson and Maxwell Nanofluids Over a Porous Stretched Sheet: Effects on Heat and Mass Transfer. Hiremath and Patil [7] studied the effects of free displacement in oscillatory flow through a permeable medium with horizontal and vertical boundaries controlling temperature. Subhashini et al. [8] evaluated the effect of diffusion on flow through a vertical porous plate. Veera et al. [9] examined the impact of thermal radiation and viscous dissipation on Cattaneo–Christov heat flux models for electrically conducting Casson-Carreau nanofluid flows. Nandhini et al. [10] analysed Effect of chemical reaction and radiation absorption on MHD Casson fluid over an exponentially stretching sheet with slip conditions: ethanol as solvent. Nield and Bejan [11] provided a comprehensive review of heat transfer in porous media. Sajid and Hayat [12] applied the homotopy analysis method to investigate the effects of radiation on mixed convection flow over an exponentially stretched sheet. Dash et al. [13] examined unsteady free convection magnetohydrodynamic (MHD) flow in porous media of rotating systems, particularly focusing on pulsating heat and mass transfer while ignoring MHD effects. Subsequently. Irshad et al. [14] studied natural convection simulation of Prabhakar-like fractional Maxwell fluid flowing on inclined plane with generalized thermal flux. Anwar Beg et al. [15] found

Cite as: K.V. Reddy, G. Ravindranath Reddy, K.J. Rani, A. Sreenivasulu, G.B. Prakash, East Eur. J. Phys. 2, 348 (2025), https://doi.org/10.26565/2312-4334-2025-2-44

computational solutions for free convection at the interface, incorporating the Dufour and Soret effects. This study investigates the numerical behavior of MHD Casson fluid flow with variable properties over an inclined porous stretching sheet, emphasizing the impact of MHD effects on non-Newtonian Casson fluid flow. The analysis employs the Cattaneo–Christov heat flux model to study heat and mass transport in a Casson nanofluid over an accelerating penetrable plate while also examining the effects of thermal radiation on fluid flow dynamics [16-22]. We investigated the magnetohydrodynamic (MHD) numerical solutions for Casson fluid flow over inclined porous elongated sheets with varying properties. Additionally, the research paper "Radiation and Dufour Effects in Unsteady Magnetohydrodynamic Mixed Convective Flow Over an Accelerating Vertical Wavy Plate with Variable Temperature and Mass Diffusion" has made a significant contribution to this field. Abobasari et al. [23] analyzed the entropy generation in unsteady MHD flow over permeable elastic surfaces in nanofluids. Karnati and GVRR [24] Analyses of the Impact of Melting on MHD Casson Fluid Flow Past a Stretching Sheet in a Porous Medium with Radiation. Benazir et al. [25] examined the instability of MHD Casson fluids in vertical cones and plates, considering the effects of inhomogeneous heat sources and sinks. Reddy et al. [26] investigated the melting effects of MHD Casson fluid flow over a long plate in porous media, incorporating electrical effects. G. V. R. et al. [27] analyzed the Soret-Dufour mechanisms and thermal radiation effects on magnetized SWCNT/MWCNT nanofluid in convective transport and solutal stratification. Reddy et al. [28] studied heat and mass transfer in MHD flow of SWCNT and graphene nanoparticle suspensions in Casson fluid. Karnati et al. [29] analyzed unsteady MHD Walter's-B viscoelastic flow past a vertical porous plate. Yaragani et al. [30] examined heat and mass transfer effects on MHD mixed convective flow over a vertical porous surface in the presence of Ohmic heating and viscous dissipation. Gurrampati [31] investigated thermal radiation effects on MHD Casson and Maxwell nanofluids over a porous stretching surface. Devi and Srinivas [32] studied the two-layered immiscible flow of a viscoelastic liquid in a vertical porous channel, considering the Hall current, thermal radiation, and chemical reactions. This study focuses on the kinetics of unsteady magnetohydrodynamic Walter's-B viscoelastic flow over a vertically porous plate within a porous medium, incorporating the effects of radiation and chemical processes. By employing closed analytical techniques, the dimensionless partial differential equations governing the flow field are solved. Numerical solutions facilitate a comprehensive analysis of the velocity, temperature, and concentration profiles, which are examined both qualitatively and graphically to provide deeper insights into the system's behavior. One of the primary gaps in existing research is the interplay between radiation, chemical processes, and MHD Walter's-B viscoelastic flow in porous media. While viscoelastic fluids and MHD flows have been studied independently, their combined effects, particularly under the influence of radiation and chemical interactions, have received limited attention. This work addresses this gap by providing a detailed analysis of flow dynamics over a vertically porous plate. The study solves the dimensionless partial differential equations driving the system using closed analytical methods, aiming to enhance the understanding of temperature, velocity, and concentration profiles and their influence on flow behavior.

2. PROBLEM STATEMENT AND BASIC EQUATIONS

A fluid exhibiting viscoelastic characteristics, which is incompressible and capable of conducting electricity, is moving within an unstable magnetohydrodynamic environment. The flow of a Casson fluid over an infinitely tall vertical porous plate, which starts abruptly, undergoes changes in temperature and mass diffusion while being influenced by thermal radiation. The plate is surrounded by porous media with the X-axis directed towards the plate and the Y-axis perpendicular.

At outset, the fluid and plate have same concentration, denoted as C_m, and temperature T_m. The plate begins moving in the X-direction at time t is zero, with a constant velocity U_0 . A transverse magnetic induction B_0 - applied upright to the direction of flow. Due to the small magnetic Reynolds number and the characteristics of the transverse magnetic field, the induced magnetic fields are deemed insignificant. The concentration of the fluid decreases exponentially, considering a first-order chemical reaction. Because the system extends infinitely in the other direction, the flow variables depend solely on x and y (34).

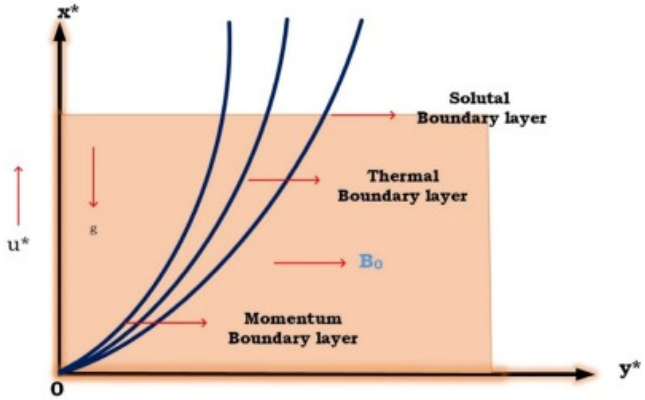

Figure A. Flow geometry of the model

The characteristics of the Casson fluid are:

$$\tau_{ij} = \begin{cases} 2\left(\mu_B^* + \dfrac{p_y}{\sqrt{2\pi}}\right)e_{ij}, & \pi > \pi_c \\ 2\left(\mu_B^* + \dfrac{p_y}{\sqrt{2\pi_c}}\right)e_{ij}, & \pi < \pi_c \end{cases}. \tag{1}$$

Where $\mu_B^*, \pi = e_{ij}e_{ij}$, e_{ij}, π, π_c, p_y be the Non-Newtonian fluid dynamic viscosity, the rate of deformation at the $(i,j)^{th}$ component, The yield stress of the fluid, the critical value of π, and the rate of deformation are considered as separate components.

The governing equations for the boundary layer, taking into account Boussinesq's approximation and the assumptions indicated above, can be expressed as follows (33):
Equation of continuity:

$$\frac{\partial v^*}{\partial y^*} = 0 \Rightarrow v^* = -v_0 \,(\text{constant}). \tag{2}$$

Equation of momentum:

$$\frac{\partial u^*}{\partial t^*} + v^* \frac{\partial u^*}{\partial y^*} = \begin{bmatrix} \nu\left(1+\dfrac{1}{\beta}\right)\dfrac{\partial^2 u^*}{\partial y^{*2}} - \lambda\dfrac{\partial^3 u^*}{\partial y^{*2}\partial t^*} + g\beta_T(T-T_\infty)\cos\alpha \\ +g\beta_C(C-C_\infty)\cos\alpha - \dfrac{\sigma B_0^2 u^*}{\rho} - \dfrac{\nu u^*}{K^*} \end{bmatrix}. \tag{3}$$

Energy formula:

$$\rho C_p\left(\frac{\partial T}{\partial t^*} + v^*\frac{\partial T}{\partial y^*}\right) = k\frac{\partial^2 T}{\partial y^{*2}} - \frac{\partial q_r}{\partial y^*}. \tag{4}$$

Equation of mass transfer continuity:

$$\frac{\partial C}{\partial t^*} + v^*\frac{\partial C}{\partial y^*} = D\frac{\partial^2 C}{\partial y^{*2}} - k_r(C-C_\infty) + \frac{D_T}{T'_\infty}\frac{\partial^2 T}{\partial y^2}, \tag{5}$$

where the coefficient of mass transfer is β_C, the volumetric coefficient of thermal expansion is β_T, the Casson fluid parameter is β, and the gravitational acceleration is represented by g.

This equation ρ describes the relationship between several variables, including fluid density (D), magnetic induction (B_0), radiative heat flow (q_r) in the y-direction, mass diffusion coefficient (D), constant chemical reaction rate (Kr), and porous medium permeability (K^*). The fluid's electrical conductivity is denoted by Sigma. "T" stands for the temperature in dimensions. The specific temperature at constant pressure is shown accordingly as C_p. thermal conductivity of liquids as k, and the viscoelasticity parameter as λ Walter's-B.

The suitable limits to the boundary include

$$\begin{cases} t^* \le 0 \;\; u^* = 0, T = T_\infty, C = C_\infty \quad \forall y^* \\ t^* > 0 \;\; u^* = u_0, v^* = -v_0, T = T_\infty + (T_w - T_\infty)\, e^{At^*} \\ \qquad C = C_\infty + (C_w - C_\infty)\, e^{At^*} \qquad \text{At } y^* = 0 \\ u^* = 0, T \to \infty, C \to \infty, \qquad y^* \to \infty, \end{cases} \tag{6}$$

where, $A = \dfrac{v_0^2}{\nu}, T_w$ and C_w are respectively, the place's concentration and temperature.

The radiative heat flux q_r, by using the Rosseland approximation for radiation, can be written as (Alao et al. [33]):

$$q_r = -\frac{4\sigma}{3k_m}\frac{\partial T^4}{\partial y^*} \tag{7}$$

where k_m and σ stand for a constant absorbance coefficient and the Stefan Boltzmann equation, respectively. It is considered that T^{*4} the temperature contrast in the flow is small adequately that it can be expressed as a function of temperature, by neglecting the higher order terms and expansions in the Taylor series about T_∞^*.

$$T^4 \cong 4T_\infty^3 T \ -3T_\infty^4 \tag{8}$$

Using equations (7) and (8) in (4), we get

$$\frac{\partial T}{\partial t^*}+v^*\frac{\partial T}{\partial y^*}=\frac{k}{\rho C_p}\frac{\partial^2 T}{\partial y^{*2}}+\frac{16\sigma T_\infty^2}{3k_1\rho C_p}\frac{\partial^2 T}{\partial y^{*2}} \tag{9}$$

To obtain a dimensionless equation, the following dimensionless quantities must be included:

$$\begin{cases} u=\dfrac{u^*}{u_0}, y=\dfrac{y^* v_0}{v}, t=\dfrac{t^* v_0^2}{v}, \theta=\dfrac{T-T_\infty}{T_w-T_\infty}, C=\dfrac{C-C_\infty}{C_w-C_\infty}, \\ M=\dfrac{\sigma B_0^2 v}{\rho v_0^2},\ K=\dfrac{v_0^2 K^*}{v^2}, \mathrm{Pr}=\dfrac{\rho Cp}{k}, \Gamma=\dfrac{\lambda v_0^2}{v^2}, Gm=\dfrac{v g\beta^*(C_w-C_\infty)}{u_0 v_0^2}, Gr=\dfrac{v g\beta(T_w-T_\infty)}{u_0 v_0^2}, \\ Kr=\dfrac{krv}{v_0^2}, R=\dfrac{4\sigma T_\infty^3}{k_1 k}, Sc=\dfrac{v}{D} \end{cases} \tag{10}$$

Magnetic term(M), Thermal Grashof(Gr), Mass Grashof(Gm), Permability(K), Radiation term(R), Prandtl(Pr), viscoelastic parameters (Γ), Brownian motion term(Nb), Thermophoresis term(Nt) , Schmidt (Sc), Chemical reaction (Kr). The engineering quantities of interest are Sherwood number (Sh), Skin friction coefficient (C_f) and Nussell number (Nu).

The non-dimensional forms of equations (3), (4), and (9) are obtained by virtue of equation (10).

$$\frac{\partial u}{\partial t}-\frac{\partial u}{\partial y}=\left(1+\frac{1}{\beta}\right)\frac{\partial^2 u}{\partial y^2}-\Gamma\frac{\partial^3 u}{\partial y^2\partial t}+Gr\theta+GmC-(M+\frac{1}{K})u \tag{11}$$

$$\frac{\partial \theta}{\partial t}-\frac{\partial \theta}{\partial y}=\frac{1}{\mathrm{Pr}}\left(1+\frac{4R}{3}\right)\frac{\partial^2 \theta}{\partial y^2} \tag{12}$$

$$\frac{\partial C}{\partial t}-\frac{\partial C}{\partial y}=\frac{1}{Sc}\frac{\partial^2 c}{\partial y^2}-KrC+\frac{Nt}{Nb}\frac{\partial^2 T}{\partial y^2}=0 \tag{13}$$

In non-dimensional form, the appropriate beginning and boundary conditions are:

$$\begin{cases} t\le 0 \ \ u=0,\theta=0,C=0 \quad \forall y \\ t>0 \ \ u=1,\theta=e^t,C=e^t \quad \text{at } y=0 \\ \qquad u=0,u\to 0,C\to 0,y\to\infty \end{cases} \tag{14}$$

Solution of the problem

To simplify the operation of the partial deferential equation given above,
We can use the inequality to express the speed, temperature as follows:

$$u(y,t)=u_0(y)e^{i\omega t} \tag{15}$$

$$\theta(y,t)=\theta_0(y)e^{i\omega t} \tag{16}$$

$$C(y,t)=C_0(y)e^{i\omega t} \tag{17}$$

Definitions and Physical Interpretations

	Definition	Unit	Complex Nature	Physical Interpretation
u(y, t) (Velocity Profile)	Represents the fluid velocity at a given position y and time t.	m/s (meters per second).	Generally a complex quantity due to the exponential term involving i. The real part u represents the physical velocity.	Describes how the velocity of the fluid varies both in the spatial (y) and temporal (t) dimensions.
$u_0(y)$ (Amplitude of Velocity Profile)	Represents the spatially dependent amplitude of the velocity	m/s.	Can be real or complex, depending on the problem context.	Describes the variation of the velocity amplitude as a function of position y, without considering time dependence.
θ(y,t)	Represents the temperature field or another scalar field (such as concentration) as a function of space (y) and time (t).	Depends on the physical quantity; for temperature, it's typically Kelvin (K) or Celsius (°C).	Complex quantity due to the exponential term.	Describes how the field (temperature, concentration, etc.) varies in space and time, with oscillatory behavior introduced by the term.
$\theta_0(y)$	Represents the amplitude of the field as a function of the spatial coordinate y.	Depends on the physical quantity; for temperature, it's typically Kelvin (K) or Celsius (°C).	It can be complex if the system introduces phase shifts spatially.	Defines the spatial variation of the field's amplitude, serving as the base profile modulated by time.
C(y, t) (Concentration or Property of Interest)	Represents the quantity of interest (e.g., chemical concentration, temperature, or similar scalar property) as a function of spatial coordinate y and time t.	Depends on the context (e.g., mol/m³ for concentration).	This is a complex quantity because it involves, which introduces a complex phase.	Describes the variation of the property over space and time. The imaginary part (if considered) can represent oscillatory components such as wave behavior.
C_0 (Amplitude Function)	Represents the spatially dependent amplitude or initial distribution of the property CC at t=0.	Depends on the context (e.g., mol/m³ for concentration).	Real or complex, depending on whether the initial distribution has a phase component.	Provides the baseline or initial profile of the property in the spatial domain y.
$e^{i\omega t}$ (Exponential Oscillatory Term)	Exponential term representing the oscillatory nature of the field with time, where ii is the imaginary unit ($i^2=-1$).	Dimensionless.	Complex quantity, as it includes both real and imaginary parts when expanded: $e^{i\omega t}=\cos(\omega t)+i\sin(\omega t)$.	Describes periodic temporal behavior, with ω as the angular frequency of oscillation.
ω (Angular Frequency)	The angular frequency of the oscillations, representing how quickly the velocity oscillates with time.	rad/s (radians per second).	Real.	Determines the rate of oscillation in the flow. A higher ω implies more rapid oscillations.
y (Spatial Coordinate)	The spatial coordinate perpendicular to the flow direction, where the velocity is evaluated.	meters.	Real.	Describes the position within the flow field where the velocity is measured.
t (Time)	Represents the temporal evolution of the system.	sec.	Real.	Tracks the progression of oscillations or flow changes over time.

We get the following by replacing Eqns (15), (16), and (17) in Eqns (11), (12), and (13).

$$\left(1+\frac{1}{\beta}-i\omega\Gamma\right)u_0''+u_0'-k_3u_0+\left[Gr\theta_0+GmC_0\right]\cos\alpha=0 \tag{18}$$

$$k_1\theta_0''+\theta_0'-i\omega\theta_0=0 \tag{19}$$

$$C_0'' + ScC_0' - (Kr + i\omega)C_0 + \frac{Nt}{Nb}\theta_0'' = 0 \tag{20}$$

In this case, the primes signify the differential about Y - axis.
The equivalent conditions are expressed as:

$$\begin{cases} t \le 0, u_0 = 0, \theta_0 = 0, C_0 = 0 & \forall\, y \\ t > 0,\ u_0 = e^{-i\omega t} & \theta_0 = e^{(1-i\omega)t},\ C_0 = e^{(1-i\omega)t} \quad \text{at} \quad y = 0 \\ t > 0,\ u_0 \to 0, & \theta_0 \to 0, \quad \phi_0 \to 0 \quad \text{as} \quad y \to \infty \end{cases} \tag{21}$$

Equations (18) to (20) contain the parameters leading to the boundary (21) and are given by:

$$u_0(y) = \left(\left(1 - (A_1 + A_2)e^t\right)e^{-i\omega t}\right)e^{-m_5 y} + \left(A_1 e^{-m_3 y} + A_2 e^{-m_1 y}\right)e^{(1-i\omega)t} \tag{22}$$

$$\theta_0(y) = e^{(1-i\omega)t - m_3 y} \tag{23}$$

$$C_0(y) = e^{(1-i\omega)t - m_1 y} \tag{24}$$

Given the aforementioned solutions, the boundary layer's Velocity, Temperature, and Concentration distributions become

$$u(y,t) = \left[\left(1 - (A_1 + A_2)e^t\right)e^{-m_5 y} + \left(A_1 e^{-m_3 y} + A_2 e^{-m_1 y}\right)e^t\right] \tag{25}$$

$$\theta(y,t) = e^{(t - m_3 y)} \tag{26}$$

$$C(y,t) = e^{(t - m_1 y)} \tag{27}$$

Mass flux, local surface heat transfer, and local wall shear stress are three critical physical parameters, and accurately computing them has become increasingly important. Local wall shear stress, commonly referred to as skin friction, can be determined from the velocity field within the boundary layer.
which is currently known as by

$$C_f = \left(\frac{\partial u}{\partial y}\right)_{y=0} = \left[\left((A_1 + A_2)e^t - 1\right)m_5 - (m_3 A_1 + m_1 A_2)e^t\right]$$

Following this, we have a look at the non-dimensional expression of the heat transfer rate from the temperature field:

$$Nu = -\left(\frac{\partial \theta}{\partial y}\right)_{y=0} = m_3 e^t$$

Now, we will analyse the rate at which heat is transferred from the temperature field. This rate is expressed in a non-dimensional, as seen below:

$$Sh = -\left(\frac{\partial C}{\partial y}\right)_{y=0} = m_1 e^t$$

RESULTS AND DISCUSSION

This work investigates the interplay of electrical and chemical interactions in studying the MHD Walter's-B viscoelastic instability in vertical voids within porous media. The solutions are analysed based on parameters such as concentration, velocity, and temperature, while other parameters are held constant. The results are presented in Figures 1 to 15, illustrating the effects of various parameters on wall velocity, temperature, and concentration distributions. We considered flow over an infinite vertical plate of finite length. Consequently, the problem is solved within a finite boundary. In the graphical analysis, the y-axis ranges from 0 to 4, and as y approaches 5, the concentration, temperature, and velocity values asymptotically approach zero. This validates the consideration of finite length for the analysis. The study utilizes the following default parameter values: Gm=3.0, Gr=3, K=0, R=2, Pr=0, t=0, Sc=0, ω=1, and M=5. Additionally, we incorporated inclination, radiation, time and temperature parameters into the analysis.

The results, summarized in the figures, provide a comprehensive understanding of how various factors influence the temperature, velocity, and concentration distributions in MHD Walter's-B viscoelastic flow. A detailed analysis is as follows from figures. Figures 1 and 2: These figures show the effects of media and concentration distributions under the influence of external factors. Both curves decrease with increasing antibody concentration, highlighting the significant role of antibodies in mediating the flow.

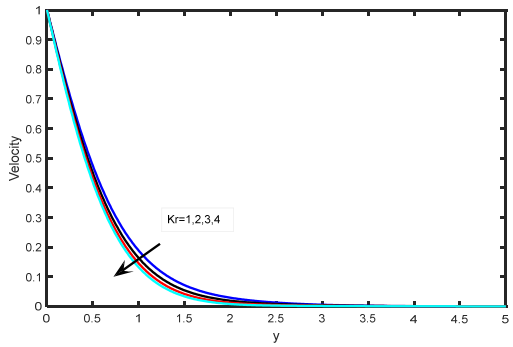

Figure 1. Speed outline for numerous Kr values

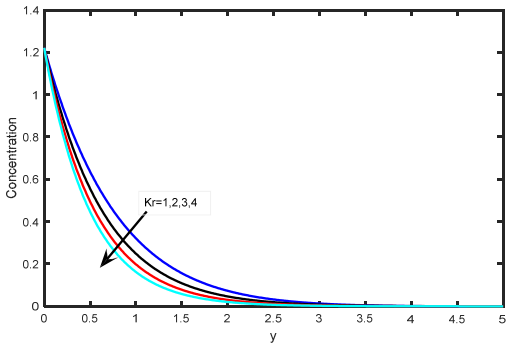

Figure 2. Contour of concentration for varying Kr values

Figure 3: This figure illustrates the impact of the Schmidt number (Sc) on the concentration distribution. Figure 4: It demonstrates how the Schmidt number affects buoyancy-driven flow. As the Schmidt number increases, the concentration buoyancy decreases, leading to reduced velocity and concentration profiles. Figures 5 and 6: These figures depict the temperature profiles under different electric field strengths. Thermal energy coupling increases, causing a reduction in temperature and velocity near the thermal boundary layer.

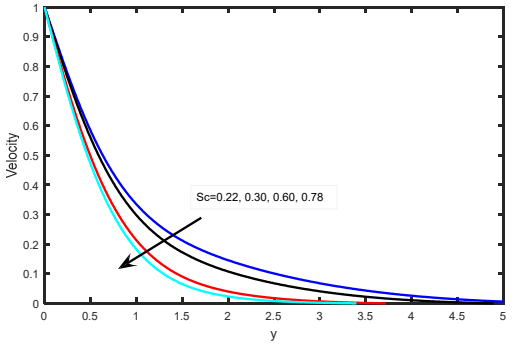

Figure 3. Profiles of Velocity for various Sc values

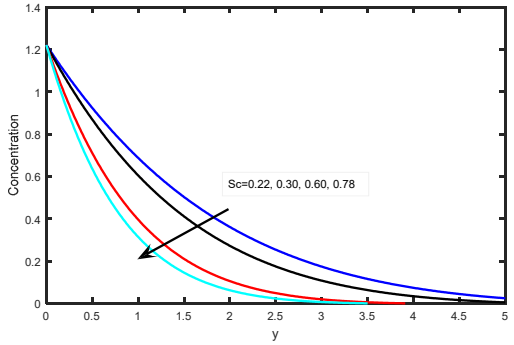

Figure 4. Profiles of concentration for various Schmidt numbers (Sc)

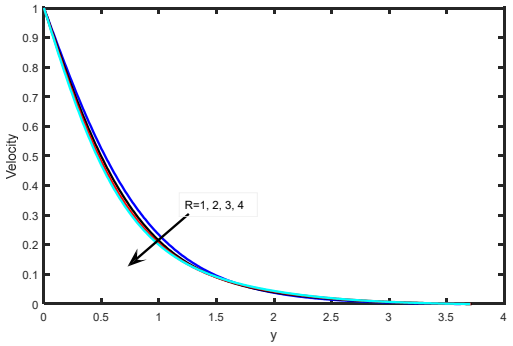

Figure 5. Velocity profiles with various R values

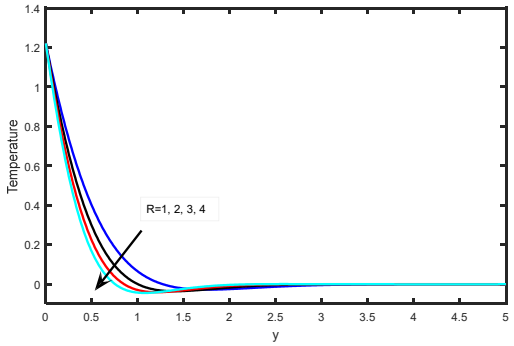

Figure 6. Temperature form with varying R values

Figures 7 and 8: These figures reveal the influence of the Prandtl number (Pr) on temperature and velocity distributions, respectively. Higher Pr values lead to a reduction in flow velocity and thermal diffusion rates.

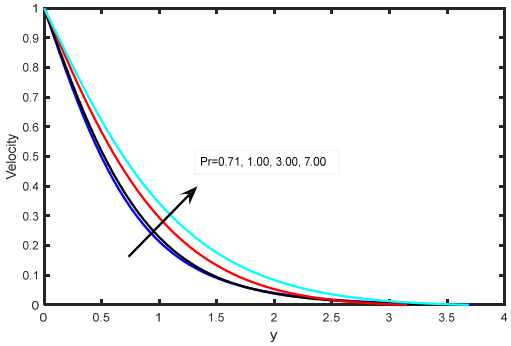

Figure 7. Speed profiles for various Pr values

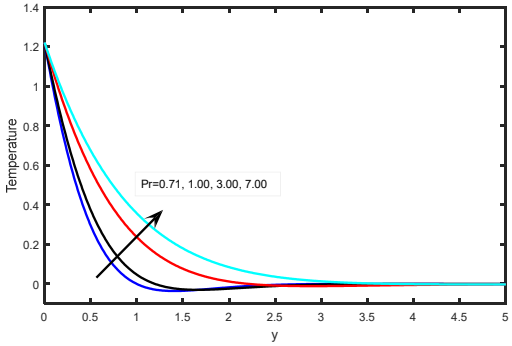

Figure 8. Temperature profiles for various Pr values

Figure 9: This figure highlights the effect of increasing viscoelastic parameters (Γ) on velocity distribution, resulting in a flatter velocity profile. Figure 10: This figure examines the effect of permeability (K) on flow. Increased permeability enhances the velocity of the boundary layer while reducing the resistance within the porous medium.

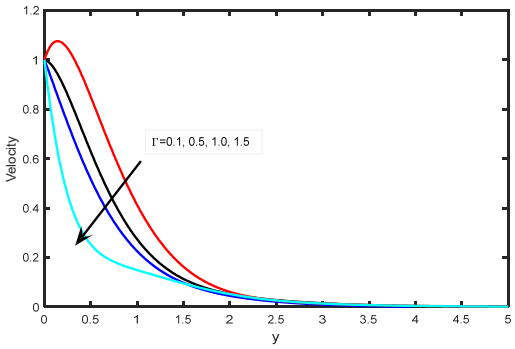

Figure 9. Velocity profiles with varying Γ values

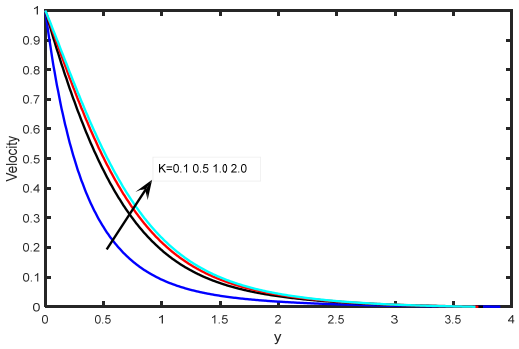

Figure 10. Velocity profiles with varying K

Figure 11: It shows the impact of the magnetic field strength (M) on velocity. A stronger magnetic field reduces velocity due to increased electromagnetic damping. Figures 12, 13, and 14: These figures illustrate the influence of time (t) on concentration, velocity, and temperature profiles, respectively. All three profiles increase over time, reflecting the system's evolving behaviour.

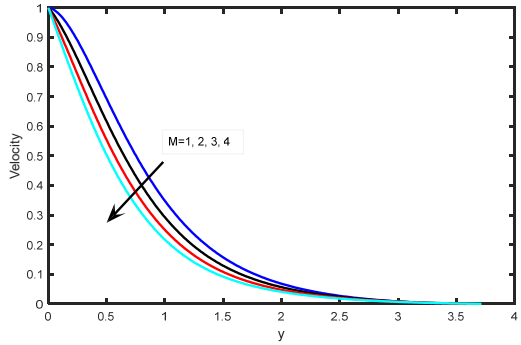

Figure 11. Velocity profiles for various M values

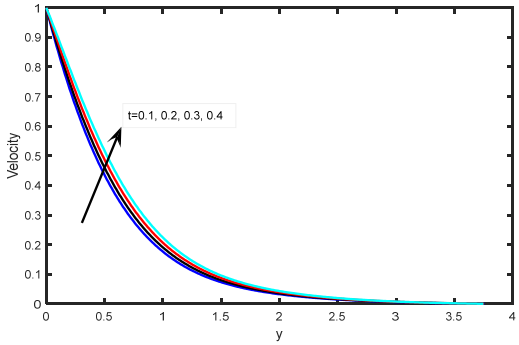

Figure 12. Velocity profiles for various time (t) values

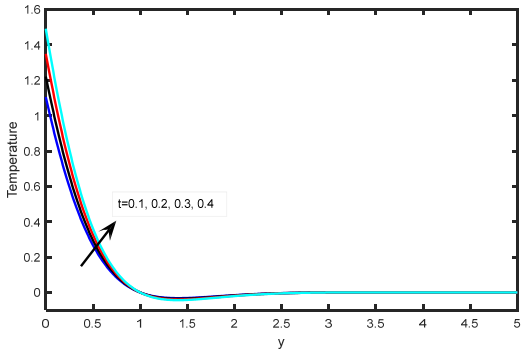

Figure 13. Temperature profiles over various time intervals (t)

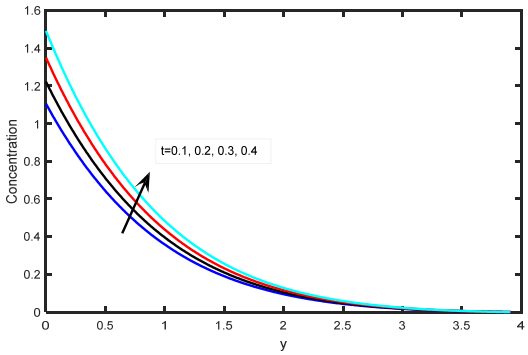

Figure 14. Profiles of concentration for various time values (t)

CONCLUSIONS

This study provides a comprehensive numerical simulation of viscoelastic magneto hydrodynamic (MHD) flow along a vertical plate, using the Walter's-B model to analyze the influence of electrical and chemical interactions. The results are interpreted from a physical perspective, offering insights with potential engineering applications. Key findings include:

➢ **Velocity Dynamics:**

- **Decrease in Velocity:** The velocity of the fluid decreases with increasing values of the chemical reaction parameter (Kr), Schmidt number (Sc), radiation parameter (R), and magnetic field parameter (M). This implies that higher chemical reaction rates, stronger magnetic fields, or greater diffusivity of the solute reduce fluid motion. Engineering systems can exploit these effects to regulate flow speed in applications such as chemical reactors and cooling systems.
- **Increase in Velocity:** Velocity increases with higher values of the Prandtl number (Pr), permeability parameter (K), and time (t). These results highlight the potential to enhance flow velocity by modifying thermal properties or adjusting permeability in porous materials, which is critical in optimizing filtration systems and thermal insulation designs.

➢ **Temperature Behavior:**

- **Decrease in Temperature:** The temperature decreases as the radiation parameter (R) rises, suggesting that stronger radiative heat transfer dissipates thermal energy effectively. This is beneficial in applications like radiative cooling technologies.
- **Increase in Temperature:** An increase in the Prandtl number (Pr) and time (t) leads to a rise in temperature. This highlights the importance of thermal diffusivity and time-dependent heat transfer in systems requiring precise thermal regulation.

➢ **Concentration Variations:**

- **Decrease in Concentration:** Concentration levels decrease with higher values of the chemical reaction parameter (Kr) and Schmidt number (Sc). These findings can be leveraged to control solute transport in processes such as pollutant dispersion or chemical separation.
- **Increase in Concentration:** Concentration increases with time (t), emphasizing the role of prolonged processes in enhancing solute distribution, relevant for long-duration mixing or diffusion-controlled reactions.
- **Impact of Brownian Motion:** An increase in the Brownian motion parameter enhances both temperature and velocity profiles, improving heat and momentum transfer. This effect also thickens the velocity and thermal boundary layers, which is advantageous for applications requiring enhanced energy dissipation or thermal buffering.

Engineering Applications: These findings have significant implications for optimizing industrial systems involving MHD viscoelastic flows, such as:

- **Heat and Mass Transfer Systems:** Understanding the interplay between parameters like Pr, Sc, and R allows for better design of heat exchangers and chemical reactors.
- **Magnetically Controlled Flows:** The effect of the magnetic field parameter (M) on velocity provides a pathway to tailor flow profiles in electromagnetic pumps and magnetic drug delivery systems.
- **Filtration and Separation Technologies:** Insights into the concentration dynamics under varying Sc and Kr values can improve the efficiency of separation processes in chemical engineering.
- **Thermal Insulation and Cooling:** Leveraging radiative heat transfer (R) effects can enhance the performance of cooling and insulation systems.

Future Directions: Future studies could delve into the relationship between antibody concentration and other fluid dynamics parameters, especially in the context of heat and mass transfer rates. Additionally, exploring the effects of varying magnetic field intensities and viscoelastic parameters on complex flow patterns may provide deeper insights into optimizing MHD Walter's-B viscoelastic flow systems for practical engineering applications.

Nomenclature

g	Acceleration due to gravity (unit: m·s^{-2})
Kr	Dimensional chemical reaction component
C	Fluid concentration (unit: kg·m^{-3})
T	Fluid temperature (unit: K)
D	Mass diffusivity (unit: m^2·s^{-1})
Cp	Specific heat at constant pressure (unit: J·kg^{-1}K^{-1})
u^*	Velocity component along x^* (unit: m·s^{-1})
Greek symbols	
ρ	Density at a distance from the plate (unit: kg·m^{-3})
θ	Dimensionless fluid temperature
φ	Dimensionless species concentration
ρ	fluid density (unit: kg· m^{-3})
ν	kinematic viscosity (unit: m^2·s^{-1})
k	Thermal conductivity (unit: W·m^{-1}·K^{-1})
βC	Expansion of concentration coefficient (unit: K^{-1})
βT	Thermal expansion coefficient (unit: K^{-1})

ORCID

Karnati Veera Reddy, https://orcid.org/0000-0003-1073-7551; **G. Ravindranath Reddy,** https://orcid.org/0000-0002-3568-8576
K. Jhansi Rani, https://orcid.org/0000-0002-2400-6576; **Ayyalappagari Sreenivasulu,** https://orcid.org/0000-0003-3992-6436
Gudala Balaji Prakash, https://orcid.org/0000-0003-1892-4634

REFERENCES

[1] B.C. Sakiadis, "Boundary layer behavior on continuous solid surfaces: I. boundary layer equations for two dimensional and axisymmetric flow," AICHE, **7**, 26-28 (1961). https://doi.org/10.1002/aic.690070108
[2] B.C. Sakiadis, "Boundary layer behavior on continuous solid surfaces: II. Boundary layer on a continuous flat surface," AICHE, **7**, 221-225 (1961). https://doi.org/10.1002/aic.690070211
[3] L.J. Crane, "Flow past a stretching plate," ZAMP, **21**, 645-655 (1970). https://doi.org/10.1007/BF01587695

[4] V.M. Soundalgekar, and P.D. Wavre, "Unsteady free convection flow past an infinite vertical plate with constant suction and mass transfer," Int. J. Heat Mass Transf. **20**, 1363-1373 (1977). https://doi.org/10.1016/0017-9310(77)90033-3
[5] K.V. Reddy, G.V.R. Reddy, A. Sandhya, and Y.H. Krishna, "Numerical solution of MHD, Soret, Dufour, and thermal radiation contributions on unsteady free convection motion of Casson liquid past a semi-infinite vertical porous plate," Heat Transfer, **51**(3), 2837-2858 (2022). https://doi.org/10.1002/htj.22452
[6] V. Seethamahalakshmi, R. Leelavathi, T.S. Rao, P.N. Santoshi, G.V.R. Reddy, and A.S. Oke, "MHD slip flow of upper-convected Casson and Maxwell nanofluid over a porous stretched sheet: impacts of heat and mass transfer," CFD Letters, **16**(3), 96-111 (2024). https://doi.org/10.37934/cfdl.16.3.96111
[7] P.S. Hiremath, and P.M. Patil, "Free convection effects on oscillatory flow of couple stress field through a porous medium," Acta Mech. **98**, 143-158 (1993). https://doi.org/10.1007/BF01174299
[8] A. Subhashini, N.R. Bhaskara, C.V.R. Kumari, "Mass transfer effects on the flow past a vertical porous plate," J. Energy Heat Mass Transf. **993**(15), 221-226 (1993).
[9] K.V. Reddy, V.R. Reddy, G., and A.J. Chamkha, "Effects of Viscous Dissipation and Thermal Radiation on an Electrically Conducting Casson-Carreau Nanofluids Flow with Cattaneo-Christov Heat Flux Model," Journal of Nanofluids, **11**(2), 214-226 (2022). https://doi.org/10.1166/jon.2022.1836
[10] C.A. Nandhini, S. Jothimani, and A.J. Chamkha, "Effect of chemical reaction and radiation absorption on MHD Casson fluid over an exponentially stretching sheet with slip conditions: ethanol as solvent," European Physical Journal Plus, 138(1), (2023). https://doi.org/10.1140/epjp/s13360-023-03660-8
[11] D.A. Nield, and A. Bejan, *Convection in Porous Media*, 2nd ed. (Springer-Verlag, Berlin 1998). https://doi.org/10.1007/978-1-4757-3033-3
[12] M. Sajid, and T. Hayat, "Influence of thermal radiation on the boundary layer flow due to an exponentially stretching sheet," Int. Comm. Heat Mass Transf. **35**, 347-356 (2008). https://doi.org/10.1016/j.icheatmasstransfer.2007.08.006
[13] G.C. Dash, P.K. Rath, and A.K. Patra, "Unsteady free convective MHD flow through porous media in a rotating system with fluctuating temperature and concentration," Modell. Controll. B, **78**(3), 1-16 (2009).
[14] I. Khan, R. Ali, M.A. Shakir, A.S. Al-Johani, A.A. Pasha, and K. Irshad, "Natural convection simulation of Prabhakar-like fractional Maxwell fluid flowing on inclined plane with generalized thermal flux,"" Case Studies in Thermal Engineering, **35**, 102042 (2022). https://doi.org/10.1016/j.csite.2022.102042
[15] O.A. Be'g O, A.Y. Bakier, and V.R. Prasad, "Numerical study of free convection magnetohydrodynamic heat and mass transfer from a stretching surface to a saturated porous medium with Soret and Dufour effects," Comput. Mater. Sci. **46**, 57-65 (2009). https://doi.org/10.1016/j.commatsci.2009.02.004
[16] K.V. Reddy, G.V.R. Reddy, A. Akgül, R. Jarrar, H. Shanak, and J. Asad, "Numerical solution of MHD Casson fluid flow with variable properties across an inclined porous stretching sheet," AIMS Mathematics, **7**(12), 20524-20542 (2022). https://doi.org/10.3934/math.20221124
[17] K.V. Reddy, G.V.R. Reddy, and Y.H. Krishna, "Effects of Cattaneo–Christov heat flux analysis on heat and mass transport of Casson nano liquid past an accelerating penetrable plate with thermal radiation and Soret–Dufour mechanism," Heat Transfer, **50**(4), 3458-3479 (2021). https://doi.org/10.1002/htj.22036
[18] M.M. Rashidi, E. Momoniat, and B. Rostami, "Analytic approximate solution for MHD boundary layer viscoelastic fluid flow over continuously moving stretching surface by HAM with two auxiliary parameters," J. Appl. Math. (2012). https://doi.org/10.1155/2012/780415
[19] R. Sivaraj, and B.R. Kumar, "Unsteady MHD dusty viscoelastic fluid Couette flow in an irregular channel with varying mass diffusion," Int. J. Heat Mass Transf. **55**, 3076-3089 (2012). https://doi.org/10.1016/j.ijheatmasstransfer.2012.01.049
[20] T. Poornima, and B.N. Reddy, "Radiation effects on MHD free convective boundary layer flow of nanofluids over a nonlinear stretching sheet," Adv. Appl. Sci. Res. Pelagia Res. **4**(201), 190-202 (2013).
[21] S.R. Mishra, G.C. Dash, and M. Acharya, "Free convective flow of viscoelastic fluid in a vertical channel with DuFour effect," World Appl. Sci. J. **28**(9), 1275-1280 (2013).
[22] J. Prakash, B.R. Kumar, and R. Sivaraj, "Radiation and Dufour effects on unsteady MHD mixed convective flow in an accelerated vertical wavy plate with varying temperature and mass diffusion," Walailak J. Sci. Technol. **11**, 939-954 (2013). https://www.thaiscience.info/Journals/Article/WJST/10958529.pdf
[23] M.H. Abolbashari, N. Freidoonimehr, F. Nazari, and M.M. Rashidi, "Entropy analysis for an unsteady MHD flow past a stretching permeable surface in nanofluid," Powder Technol. **267**, 256-267 (2014). https://doi.org/10.1016/j.powtec.2014.07.028
[24] K.V. Reddy, and G.V.R. Reddy. "Outlining the impact of melting on mhd casson fluid flow past a stretching sheet in a porous medium with radiation," Biointerface Research in Applied Chemistry, **13**, 1-14 (2022). https://doi.org/10.33263/BRIAC131.042
[25] A.J. Benazir, R. Sivraj, and O.D. Makind, "Unsteady MHD Casson fluid flow over a vertical cone and flat plate with non-uniform heat source/sink," Int. J. Eng. Res. Africa, **21**, 69-83(2015). https://doi.org/10.4028/www.scientific.net/JERA.21.69
[26] K.V. Reddy, and G.V.R. Reddy, "Outlining the Impact of Melting on MHD Casson Fluid Flow Past a Stretching Sheet in a Porous Medium with Radiation," Biointerface Research in Applied Chemistry, **13**, 1-14 (2022). https://doi.org/10.33263/BRIAC131.042
[27] B.O. Falodun, O. Ramakrishna, A.S. Ismail, T.M. Oladipupo, O.T. Idiat, A.I. Oyeyemi, and G.V.R. Reddy, "Soret-Dufour mechanisms and thermal radiation effects on magnetized SWCNT/MWCNT nanofluid in a convective transport and solutal stratification analysis," Ain Shams Engineering Journal, **15**(10), 102853 (2024). https://doi.org/10.1016/j.asej.2024.102853
[28] A.S. Oke, B.A. Juma, and G.V.R. Reddy, "Heat and mass transfer in MHD flow of SWCNT and graphene nanoparticles suspension in Casson fluid," ZAMM-Journal of Applied Mathematics and Mechanics/Zeitschrift für Angewandte Mathematik und Mechanik, **104**(12), e202300106 (2024). https://doi.org/10.1002/zamm.202300106
[29] V.R. Karnati, S. Akuri, O. Ramakrishna, M. Gayatri, S.R. Tagallamudi, and V.R.R. Gurrampati, "Unsteady MHD Walter's B Viscoelastic Flow Past a Vertical Porous Plate," CFD Letters, **16**(12), 85-96 (2024). https://doi.org/10.37934/cfdl.16.12.8596
[30] H.K. Yaragani, A. Anumolu, B. Pathuri, and G.V.R. Reddy, "Heat and Mass Transfer Effects on MHD Mixed Convective Flow of a Vertical Porous Surface in the Presence of Ohmic Heating and Viscous Dissipation," CFD Letters, **16**(12), 72-84 (2024). https://doi.org/10.37934/cfdl.16.12.7284

[31] T.S. Rao, M.M. Babu, R.R. Bojja, and V.R.R. Gurrampati, "Thermal radiation effects on mhd casson and maxwell nanofluids over a porous stretching surface," Passer Journal of Basic and Applied Sciences, **6**(1), 171-178 (2024). https://doi.org/10.24271/psr.2024.416203.1389

[32] M.P. Devi, and S. Srinivas, "Two layered immiscible flow of viscoelastic liquid in a vertical porous channel with Hall current, thermal radiation and chemical reaction," International Communications in Heat and Mass Transfer, **142**, 106612 (2023). https://doi.org/10.1016/j.icheatmasstransfer.2023.106612

[33] F.I. Alao, A.I. Fagbade, and B.O. Falodun, "Effects of thermal radiation, Soret and Dufour on an unsteady heat and mass transfer flow of a chemically reacting fluid past a semi-infinite vertical plate with viscous dissipation," Journal of the Nigerian Mathematical Society, **35**, 142–158 (2016). https://doi.org/10.1016/j.jnnms.2016.01.002

[34] Y.D. Reddy, B.S. Goud, and M.A. Kumar, "Radiation and heat absorption effects on an unsteady MHD boundary layer flow along an accelerated infinite vertical plate with ramped plate temperature in the existence of slip condition," Partial Differential Equations in Applied Mathematics, **4**, 100166 (2021). https://doi.org/10.1016/j.padiff.2021.100166

Appendix

$$u(y,t) = u_0(y)e^{i\omega t}$$

$$\theta(y,t) = \theta_0(y)e^{i\omega t}$$

$$C(y,t) = C_0(y)e^{i\omega t}$$

$$C_0(y) = A_1 e^{-m_1 y} + A_2 e^{-m_2 y}$$

$$\theta_0(y) = A_3 e^{-m_1 y}$$

$$u_0(y) = A_6 e^{-m_3 y} + A_4 e^{-m_1 y} + A_5 e^{-m_2 y}$$

$$k_1 = \frac{1}{p_r}\left(1+\frac{4R}{3}\right),\ k_2 = -m_1^2\left(\frac{Nt}{Nb}\right)e^{(1-i\omega)t},$$

$$k_3 = i\omega + M + \frac{1}{k},\ k_4 = \Gamma i\omega$$

$$m_1 = \frac{1+\sqrt{1+4i\omega k_1}}{2}$$

$$m_2 = \frac{Sc+\sqrt{Sc^2+4\left(K_r+i\omega\right)}}{2}, M_3 = \frac{1+\sqrt{1+4k_3k_4}}{K_4}$$

$$A_1 = \frac{k_2}{m_1^2 - Scm_1 - \left(K_r+i\omega\right)}; A_2 = A_3 - A_1; \quad A_3 = e^{(1-i\omega)t};$$

$$A_4 = \frac{-GrA_3 - GmA_1}{k_4m_1^2 - m_1 - k_3};\ A_5 = \frac{-GmA_2}{k_4m_2^2 - m_2 - k_3}; A_6 = e^{-i\omega\Gamma} - A_4 - A_5$$

НЕСТАЦІОНАРНИЙ В'ЯЗКОПРУЖНИЙ МГД ПОТІК WALTERS-B РІДИНИ ЧЕРЕЗ ВЕРТИКАЛЬНУ ПОРИСТУ ПЛАСТИНУ З ХІМІЧНИМИ РЕАКЦІЯМИ

Карнаті Віра Редді[a], Г. Равіндранат Редді[b], К. Джхансі Рані[c], Айялаппагарі Шрінівасулу[d], Гудала Баладжі Пракаш[e]

[a]Кафедра математики, Технічний кампус Інституту Гуру Нанака, Ранга Редді (Dt) -501506, Телангана, Індія

[b]Технологічний інститут MLR, Дандігал, Хайдерабад -500043, Телангана, Індія

[c]Кафедра інженерії для першокурсників, Інженерний коледж Лакіредді Балі Редді, Л.Б. Редді Нагар, Мілаварам - 521230, Андхра-Прадеш, Індія

[d]Кафедра інженерної математики, Освітній фонд Конеру Лакшмаї, Грін-Філдс, Ваддесварам, Гунтур - 522302, Андхра-Прадеш, Індія

[e]Кафедра математики, Університет Адітья, Сурампалем - 533437, Андхра-Прадеш, Індія

У роботі досліджується перехідний магнітогідродинамічний (МГД) потік в'язкопружної рідини Walter's-B над вертикальною пористою пластиною в пористому середовищі, що включає вплив радіації та хімічних процесів. Нелінійні керуючі рівняння для потоку розв'язуються за допомогою методу замкнутого циклу, що дає детальні чисельні рішення для профілів швидкості, температури та концентрації. Результати показують, що швидкість зменшується зі збільшенням проникності (K), числа Шмідта (Sc), параметра випромінювання (R) і напруженості магнітного поля (M), тоді як вона збільшується зі збільшенням числа Прандтля (Pr), проникності (K) і часу (t). Температура знижується зі збільшенням радіації, але підвищується зі збільшенням числа Прандтля та часу. Подібним чином концентрація зменшується з підвищенням проникності та числа Шмідта, але збільшується з часом. Примітно, що збільшення параметра броунівського руху посилює передачу тепла та імпульсу, що призводить до більш товстих швидкісних і теплових прикордонних шарів. Це дослідження має практичне застосування в різних галузях, включаючи оксигенатори крові, хімічні реактори та промисловість переробки полімерів. Новизна дослідження полягає в комплексній інтеграції випромінювання, хімічних процесів і ефектів МГД в аналізі потоків в'язкопружної рідини – теми, яка залишається недостатньо вивченою в літературі. Майбутні дослідження можуть бути зосереджені на оптимізації МГД-в'язкопружних систем Walter's-B потоку, зокрема шляхом вивчення впливу напруженості магнітного поля та в'язкопружних параметрів на поведінку потоку.

Ключові слова: *МГД; поверхневе тертя; хімічна реакція; радіаційні та в'язкопружні властивості*

East European Journal of Physics. **2.** 359-368 (2025)
DOI:10.26565/2312-4334-2025-2-45 ISSN 2312-4334

UNSTEADY FLUID MOTION BETWEEN INFINITELY STRETCHED PARALLEL HORIZONTAL PLATES WITH THE ABSENCE OF VISCOUS DISSIPATION: AN ANALYTICAL APPROXIMATION

J. Srinivas[a], N. Pothanna[a]*, A. Raju[b], M. Anil Kumar[c]
[a]*Department of Mathematics, VNR Vignana Jyothi Institute of Engineering and Technology, Hyderabad-500090, Telangana State, India*
[b]*Department of Applied Sciences, Symbiosis Institute of Technology, Symbiosis International University, Pune-412115, India*
[c]*Department of Mathematics, Anurag University, Venkatapur, Hyderabad-500088, Telangana State, India*
**Corresponding Author e-mail: pothareddy81@gmail.com*
Received March 3, 2025; revised April 15, 2025; accepted April 28, 2025

Unsteady fluid motion between two infinitely stretched parallel horizontal plates with the absence of viscous dissipation is explored in this present study. Plates are maintained at different constant temperatures and separated with the distance of $2h$ units. The flow is produced by a constant oscillating pressure gradient between the plates and parallel to the boundaries of the plates. The solution of the concerned flow equations with suitable boundary limitations have been obtained using most elegant analytical approximation method: A Perturbation technique. The impact of various flow field material parameters has been studied for velocity and temperature fields and deliberated with the help of Graphical interpretations. The obtained results are validated and compared with the results existing in the literature. The obtained results are identified to be exceptional agreement with literature results. The present study will be hopefully helpful to the various industrial applications especially in the nuclear industry for the emergency cooling of nuclear reactors. The researchers and scientists can utilize the methodology of the present work in their interest of study.
Keywords: *Thermo-viscous fluid; Thermo strain conductivity coefficient; Thermal-mechanical stress viscosity; Prandtl number*
PACS: 02.30.Hq, 02.30.Jr, 02.60.Cb, 02.60.Lj

Nomenclature

$\alpha_1 = -p$	Fluid pressure
$\alpha_3 = 2\mu$	Newtonian coefficient of viscosity
$\alpha_5 = 4\mu_c$	Cross viscosity coefficient
α_6	Thermal-mechanical stress constant viscosity
α_8	Thermal stress viscosity coefficient
$-\beta_1 = k$	Thermo conductivity coefficient
β_3	Thermo strain conductivity coefficient
C_1	Non dimensional pressure gradient
C_2	Non dimensional temperature gradient
A_1	Non dimensional classical viscosity
A_6	Non dimensional thermal mechanical stress viscosity
B_3	Non dimensional thermo strain conductivity cofficient
p_r	Prandtl number
Greek Symbols	
η	Ordinate
σ	Period of oscillations
ρ	Density
γ	Energy

1. INTRODUCTION

Over a century ago, there was a great deal of research done on the non-Newtonian properties of fluids. However, the substantial research efforts to extend these analyses into the non-linearity principality have only been conducted in the recent six to seven decades, especially during the Second World War. Koh and Eringen [1] have done preliminary research on the construction of non-linear concept embodying the interplay and association between viscous and thermal impacts. Kelly [2] investigated some incompressible visco-metric flows of thermo viscous fluids. Jithender Reddy *et al.* [3] analyzed nano fluid flow through a stretched sheet with the impact of heat generation. Pothanna and P. Aparna *et al.* [4] investigated unsteady viscous flow with thermal effects in a permeable region over a stretched fluctuating plate. Pothanna *et al*. [5] used numerical and analytical approach on around an oscillating sphere for unsteady fluid flow. Pothanna *et al.* [6] study thermo viscous fluid flow in porous region confined between impervious horizontal plates using four step recursive method of algorithm. Pavan Kumar Reddy et *al.* [7] examined steady flow under sloping magnetic field with suction in a couple stress nature of a fluid via. Rectangular region. Pothanna *et al.* [8] explored steady thermo viscous flow in between infinitely stretched porous parallel horizontal plates. The flow of somewhat thermo viscous fluid in a permeable surface limited in two permeability parallel horizontal stretched plates was explored by

Cite as: J. Srinivas, N. Pothanna, A. Raju, M. Anil Kumar, East Eur. J. Phys. 2, 359 (2025), https://doi.org/10.26565/2312-4334-2025-2-45

Pothanna *et al.* [9]. The impact of thermo strain coefficient of conductivity on a moderately thermos viscous fluid in a permeable surface bounded with permeability stretched parallel plates was investigated by Pothanna *et al.* [10]. P. N. Rao and Pattabhi [11] evaluated the problem of stable flow of an order two thermos viscous fluid over extended plate. The uniform flow of a fluid that is viscous via a permeable sphere soaked with micropolar fluid was explored by Aparna *et al.* [12]. Examined by Aparna *et al.* [13] flow produced in a micro-polar fluid by the gradual, steady rotation of a holey sphere. The fluid that is viscous passing a permeable cylinder was studied by Aparna *et al.* [14]. In Aparna *et al.* [15] study, the fluctuations of a perishing sphere was examined for an incompressible coupled stress fluid were. Padmaja *et al.* [16] examined the numerical computations of multi parameter problem with singular perturbations with exponential spline technique. The numerical exploration of associated nonlinear equations for the problem of thermal viscous fluid movement in a cylindrical configuration was investigated by Pothanna *et al.* [17]. The exact and numerical studies of thermo viscous fluid flow between stretched horizontal plates that are parallel were examined by Pothanna *et al.* [18]. Srinivas Joshi *et al.* [19] investigated the linear behavior of a fluid with thermos viscous nature in a permeable surface that was confined between two immovable passable horizontal stretched parallel plates. Pothanna *et al.* [20] in the paper entitled unsteady forced oscillations of a fluid bounded by rigid bottom studied analytical solutions of governing flows. Srinivas *et al.* [21] examined slow steady motion of a thermo-viscous fluid between two parallel plates with constant pressure and temperature gradients. Srinivas *et al.* [22] studied flow of a thermo-viscous fluid in a radially non-symmetric constricted tube. Srinivas *et al.* [23] investigated peristaltic transport of a thermo-viscous fluid. Meghdadi *et al.* [24] observed mixing enhancement in micro channels using thermo-viscous expansion by oscillating temperature wave.

The incompressible flow of thermos viscous fluids in porous region satisfies the standard conservation equations.
Continuity Equation: $v_{i,i} = 0$

Momentum Equation: $\rho\left[\frac{\partial v_i}{\partial t} + v_k v_{i,k}\right] = \rho f_i + t_{ji,j} - \frac{\mu}{k^*} v_i$,

and the equation of energy: $\rho c \dot{\theta} = t_{ij} d_{ij} - q_{i,i} + \rho\gamma - \frac{\mu}{k^*} v_i v_i$,

where
$f_i = i^{th}$ Component external force/unit mass, $c =$ Heat constant, $\gamma =$ Energy source/unit mass, $q_i = i^{th}$ Component-Heat flux bivector = $\in_{ijk} h_{jk} / 2$.

The fundamental standard equations of thermo viscous second order fluids as given by Koh and Eringen for stress tensor and heat flux bivector are

$$t = \alpha_1 I + \alpha_3 d + \alpha_5 d^2 + \alpha_6 b^2 + \alpha_8 (db - bd)$$

and

$$h = \beta_1 b + \beta_3 (bd + db)$$

where the coefficients $\alpha_i'^s$ and $\beta_i'^s$ are polynomials in terms of $tr\, d, tr\, d^2, tr\, b^2$. The explicit expressions for the constitutive coefficients $\alpha_i'^s$ and $\beta_i'^s$ for the theory of second order can be obtained as

$\alpha_1 = \alpha_{1000} + \alpha_{1010} tr\, d + \alpha_{1020} tr\, d^2 + \alpha_{1002}\, tr\, b^2$,
$\alpha_3 = \alpha_{3010} + \alpha_{3020} tr\, d$
$\alpha_5 = \alpha_{5020}$, $\alpha_6 = \alpha_{6002}$, $\alpha_8 = \alpha_{8011}$,
$\beta_1 = \beta_{1001} + \beta_{1011} tr\, d$, and $\beta_3 = \beta_{1011}$
the secondary coefficients α_{isrt} and β_{isrt} are the functions involving ρ and θ.

In this work, the effects of different material characteristics on the thermos-viscous unsteady flow fields of a fluid through horizontal plates are attempted to be studied. The current study was very much helpful to the scientist and researchers to solve their engineering and research study problems. In industrial and technical systems, impermeable plates that are parallel are quite useful. Some of the application mentioned here are the human circulatory system, as well as a number of engineering instruments, including chromatography columns, chemical reactors, heat and mass exchangers, and other processing machinery. The last several decades have seen a huge increase in interest in the investigation of the flow features of these formations due to the vast range of applications.

Considering the expanding significance and use of non-Newtonian type flows in a chemical technology, industry, and geophysical fluid dynamics, this present work attempts to explore analytical approximation approach to thermo viscous flow of a fluid in between impermeable horizontal stretched plates bound in a porous medium. This current work has not yet been discussed in the literature.

2. PROBLEM STATEMENT AND ANALYSIS

An unsteady flow of thermo viscous fluid in order two can be characterized by constitute basic equations between horizontal stretched plates parallel to each other. The flow is produced by the pressure gradient oscillating with the

direction parallel to the plates. The Cartesian coordinate system $O(X,Y,Z)$ with the origin centered between two plates, the $X-axis$ in the direction of flow and the $Y-axis$ perpendicular to the plates is considered. The two plates are separated by a distance $2h\ units$ and are kept at two different temperatures. The plates are denoted by $y=h$ and $y=-h$. The lower and upper plates are maintained with the constant temperatures θ_0 and θ_1 respectively.

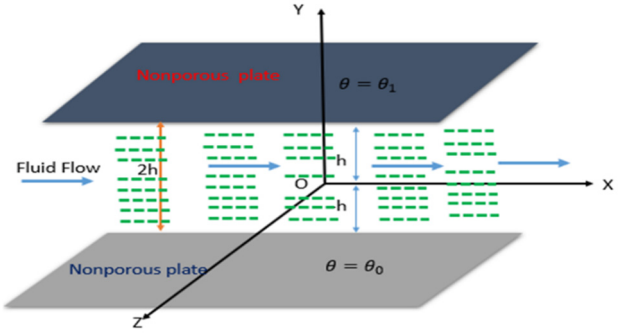

Figure 1. Schematic Representation of Flow

Let us assume the unsteady flow characterized by the velocity $[u(y,t),0,0]$ and temperature $\theta[y,t]$. The continuity equation is satisfied by this assumed velocity selection. Without internal energy sources and external forces, the equation of motion reduces to

$$\frac{\partial u}{\partial t} = -\frac{\partial p}{\partial x} + \mu\frac{\partial^2 u}{\partial y^2} - \alpha_6\frac{\partial \theta}{\partial x}\frac{\partial^2 \theta}{\partial y^2}, \tag{1}$$

and the energy equation reduces to

$$\rho c\left(\frac{\partial \theta}{\partial t} + u\frac{\partial \theta}{\partial x}\right) = \mu\left(\frac{\partial u}{\partial y}\right)^2 - \alpha_6\frac{\partial \theta}{\partial x}\frac{\partial u}{\partial y}\frac{\partial \theta}{\partial y} + k\frac{\partial^2 \theta}{\partial y^2} + \beta_3\frac{\partial \theta}{\partial x}\frac{\partial^2 u}{\partial y^2}, \tag{2}$$

composed with the boundary limitations

$$u[-h,t]=0,\ \theta[-h,t]=\theta_0, \tag{3}$$

$$u[h,t]=0,\ \theta[h,t]=\theta_1. \tag{4}$$

Employing the following dimensionless quantities,

$$y = h\eta\ ,\ u = (\mu/\rho h)\,U,\ T=\frac{\theta-\theta_0}{\theta_1-\theta_0}\ ,\ \frac{\partial\theta}{\partial x}=\frac{\theta_1-\theta_0}{h}C_2\ ,\ -\frac{\partial p}{\partial x}=\frac{\mu^2}{\rho h^3}C_1. \tag{5}$$

The equations (1) and (2) can be reduced to

$$\frac{\partial U}{\partial t} = C_1 + \frac{\partial^2 U}{\partial \eta^2} - A_6C_2\frac{\partial^2 T}{\partial \eta^2}, \tag{6}$$

and

$$\frac{\partial T}{\partial t} + UC_2 = A_1\left[\left(\frac{\partial U}{\partial Y}\right)^2 - A_6C_2\frac{\partial U}{\partial \eta}\frac{\partial T}{\partial \eta}\right] + \frac{1}{p_r}\frac{\partial^2 T}{\partial \eta^2} + B_3C_2\frac{\partial^2 U}{\partial \eta^2}, \tag{7}$$

with $p_r=\frac{c\mu}{k}$ (Prandtle number), $B_3=\frac{\beta_3}{\rho h^2 c}$, $A_1=\frac{\mu^2}{\rho h^2 c(\theta_1-\theta_0)}$,

$$A_6=\frac{\alpha_6(\theta_1-\theta_0)^2}{\mu^2},\ C_2=\text{constant temperature gradient} \tag{8}$$

and C_1 is the dimensionless pressure gradient oscillatory of period $\frac{2\pi}{\sigma}$ (say) i.e.

$$C_1 = p_0\cos(\sigma t) = Re(p_0e^{i\sigma t})\ \text{say} \tag{9}$$

The dissipation absence in the fluid flow, the momentum and energy equations reduce to

$$\frac{\partial U}{\partial t} = C_1 + \frac{\partial^2 U}{\partial \eta^2} - A_6C_2\frac{\partial^2 T}{\partial \eta^2} \tag{10}$$

and

$$\frac{\partial T}{\partial t} + UC_2 = \frac{1}{p_r}\frac{\partial^2 T}{\partial \eta^2} + B_3C_2\frac{\partial^2 U}{\partial \eta^2}. \tag{11}$$

3. METHODOLOGY AND SOLUTION

Let us consider the velocity and temperature of the flow in the form

$$U(\eta,t) = Re\,[g(\eta)e^{i\sigma t}], T(\eta,t) = Re[f(\eta)e^{i\sigma t}], \tag{12}$$

with the boundary limitations:

$$\mathrm{g}(1) = 0, \mathrm{g}(-1) = 0$$
$$\mathrm{f}(1) = \mathrm{T}_1, \mathrm{f}(-1) = \mathrm{T}_0 \tag{13}$$

Only the real parts of the functions in the above-mentioned equations need to be taken into account. Using eqn. (12) in eqns. (10) and (11) we get

$$\mathrm{i}\sigma\mathrm{g}(\eta) = \mathrm{p}_0 + \mathrm{g}''(\eta) - \mathrm{A}_6 C_2 \mathrm{f}''(\eta), \tag{14}$$

$$\mathrm{i}\sigma\mathrm{f}(\eta) + \mathrm{C}_2\mathrm{g}(\eta) = \frac{1}{\mathrm{p_r}}\mathrm{f}''(\eta) + \mathrm{B}_3\mathrm{C}_2\mathrm{g}''(\eta). \tag{15}$$

Using A_6 as the perturbation parameter, the perturbation method solves the aforementioned eqns. (14) and (15).

Let $g(\eta)$ and $\mathrm{f}(\eta)$ can be taken as

$$\mathrm{g}(\eta)=\mathrm{g}^{(0)}(\eta)+\mathrm{A}_6\mathrm{g}^{(1)}(\eta)+\mathrm{A}_6^2\mathrm{g}^{(2)}(\eta)+\ldots \tag{16}$$

$$\mathrm{f}(\eta)=\mathrm{f}^{(0)}(\eta)+\mathrm{A}_6\mathrm{f}^{(1)}(\eta)+A_6^2 f^{(2)}(\eta)+\ldots \tag{17}$$

The following are the consecutive approximations obtained by gathering terms of same powers of A_6 and using eqns. (16) and (17) in eqns. (14) and (15).

The Zeroth order calculation

The equations of this estimation are becomes

$$\mathrm{i}\sigma\mathrm{g}^{(0)}(\eta) = \mathrm{p}_0 + \mathrm{g}^{(0)''}(\eta), \tag{18}$$

$$\mathrm{i}\sigma\mathrm{f}^{(0)}(\eta) + C_2\mathrm{g}^{(0)}(\eta) = \frac{1}{\mathrm{p_r}}\,\mathrm{f}^{(0)''}(\eta) + \mathrm{B}_3\mathrm{C}_2\mathrm{g}^{(0)''}(\eta), \tag{19}$$

with boundary limitations

$$\mathrm{g}^{(0)}(\text{-}1) = 0,\ \mathrm{g}^{(0)}(1) = 0,$$
$$\mathrm{f}^{(0)}(\text{-}1) = T_0,\ \mathrm{f}^{(0)}(1) = T_1. \tag{20}$$

This gives

$$\mathrm{g}^{(0)}(\eta) = \frac{\mathrm{p}_0}{\mathrm{i}\sigma}\left(1 - \frac{\cosh\sqrt{\mathrm{i}\sigma}\,\eta}{\cosh\sqrt{\mathrm{i}\sigma}}\right), \tag{21}$$

$$\mathrm{f}^{(0)}(\eta) = \frac{1}{\sinh 2\sqrt{\mathrm{i}\sigma\mathrm{p_r}}}\left[\mathrm{T}_0\sinh\sqrt{\mathrm{i}\sigma\mathrm{p_r}}\,(1-\eta) + \mathrm{T}_1\sinh\sqrt{\mathrm{i}\sigma\mathrm{p_r}}\,(1+\eta)\right]$$
$$+\frac{\mathrm{p}_0\mathrm{p_r}(1-\mathrm{i}\sigma\mathrm{B}_3)}{\sigma^2(1-\mathrm{p_r})\cosh\sqrt{\mathrm{i}\sigma}}\left[\cosh\sqrt{\mathrm{i}\sigma}\,\eta - \frac{\cosh\sqrt{\mathrm{i}\sigma}}{\cosh\sqrt{\mathrm{i}\sigma\mathrm{p_r}}}\cosh\sqrt{\mathrm{i}\sigma\mathrm{p_r}}\,\eta\right] + \frac{\mathrm{p}_0\mathrm{p_r}\mathrm{c}_2}{\sigma^2}\left[1 - \frac{\cosh\sqrt{\mathrm{i}\sigma\mathrm{p_r}}\,\eta}{\cosh\sqrt{\mathrm{i}\sigma\mathrm{p_r}}}\right] \tag{22}$$

First order calculation (i.e. terms containing A_6)

The equations are

$$\mathrm{i}\sigma\mathrm{g}^{(1)}(\eta) = \mathrm{g}^{(1)''}(\eta) - \mathrm{C}_2\mathrm{f}^{(0)''}(\eta), \tag{23}$$

$$\mathrm{i}\sigma\mathrm{f}^{(1)}(\eta) + \mathrm{C}_2\mathrm{g}^{(1)}(\eta) = \frac{1}{\mathrm{p_r}}\,\mathrm{f}^{(1)''}(\eta) + \mathrm{B}_3\mathrm{C}_2\mathrm{g}^{(1)''}(\eta), \tag{24}$$

with boundary limitations:

$$\mathrm{g}^{(1)}(\text{-}1) = 0,\ \mathrm{g}^{(1)}(1) = 0$$
$$\mathrm{f}^{(1)}(\text{-}1) = 0,\ \mathrm{f}^{(1)}(1) = 0, \tag{25}$$

the above equations solutions yield

$$\mathrm{g}^{(1)}(\eta) = \frac{\mathrm{p}_0\mathrm{C}_2\mathrm{i}}{\sigma^2}\left[\mathrm{p_r}\mathrm{B}_3\sigma - \mathrm{C}_2(\mathrm{i}+\sigma\mathrm{B}_3) + \mathrm{i}\mathrm{C}_2\mathrm{p_r}^2\right]\left[1 - \frac{\cosh\sqrt{\mathrm{i}\sigma}\,\eta}{\cosh\sqrt{\mathrm{i}\sigma}}\right]$$
$$+\frac{\mathrm{p}_0\mathrm{p_r}\mathrm{C}_2(1-\mathrm{i}\sigma\mathrm{B}_3)}{2\mathrm{i}\sigma\sqrt{\mathrm{i}\sigma}\cosh\sqrt{\mathrm{i}\sigma}}\left[\mathrm{C}_2 + \frac{1}{\mathrm{i}\sigma(1-\mathrm{p_r})}\right]\left[\frac{\sinh\sqrt{\mathrm{i}\sigma}}{\cosh\sqrt{\mathrm{i}\sigma}}\cosh\sqrt{\mathrm{i}\sigma}\,\eta - \eta\sinh\sqrt{\mathrm{i}\sigma}\,\eta\right]$$
$$+\frac{4\mathrm{p}_0\mathrm{C}_2^2\mathrm{p_r}^2\sinh\sqrt{\mathrm{i}\sigma\mathrm{p_r}}}{\sigma^2(\mathrm{p_r}-1)}\left[1 + \frac{1-\mathrm{i}\sigma\mathrm{B}_3}{1-\mathrm{p_r}}\right]\left[\frac{\cosh\sqrt{\mathrm{i}\sigma\mathrm{p_r}}}{\cosh\sqrt{\mathrm{i}\sigma}}\cosh\sqrt{\mathrm{i}\sigma}\,\eta - \cosh\sqrt{\mathrm{i}\sigma\mathrm{p_r}}\,\eta\right]$$
$$+\frac{\mathrm{T}_0\mathrm{p_r}\mathrm{C}_2}{(\mathrm{p_r}-1)\sinh\sqrt{\mathrm{i}\sigma\mathrm{p_r}}}\left[\sinh\sqrt{\mathrm{i}\sigma\mathrm{p_r}}\,(1-\eta) - \frac{\sinh 2\sqrt{\mathrm{i}\sigma\mathrm{p_r}}}{\sinh 2\sqrt{\mathrm{i}\sigma}}\sinh\sqrt{\mathrm{i}\sigma}\,(1-\eta)\right]$$

$$+\frac{T_1 p_r C_2}{(p_r-1)\sinh\sqrt{i\sigma p_r}}\left[\sinh\sqrt{i\sigma p_r}\,(1+\eta)-\frac{\sinh 2\sqrt{i\sigma p_r}}{\sinh 2\sqrt{i\sigma}}\,\sinh\sqrt{i\sigma}\,(1+\eta)\right] \tag{26}$$

$$f^{(1)}(\eta)=\frac{p_0 p_r c_2^2}{i\sigma^3}\left[C_2(1-i\sigma b_3)-C_2 p_r+i\sigma b_3\right]\left[\frac{\cosh\sqrt{i\sigma p_r}\,\eta}{\cosh\sqrt{i\sigma p_r}}-1\right]$$

$$+\frac{p_0 p_r^2 C_2^2\,(1-i\sigma b_3)}{\sigma^3(1-p_r)\cosh\sqrt{i\sigma}}\begin{bmatrix} i\langle c_2-p_r C_2+i\sigma b_3(1-C_2)\rangle \\ -\frac{i}{2\sigma(1-p_r)}\frac{\sinh\sqrt{i\sigma}}{\cosh\sqrt{i\sigma}}(1-i\sigma b_3)\big(i-\sigma C_2(1-p_r)\big) \\ -\frac{2ip_r C_2\sinh 2\sqrt{i\sigma p_r}}{(1-p_r)^2}-\frac{iB_3(1+i\sigma)}{2\sigma(1-p_r)}\end{bmatrix}$$

$$*\left[\cosh\sqrt{i\sigma}\,\eta-\frac{\cosh\sqrt{i\sigma}}{\cosh\sqrt{i\sigma p_r}}\cosh\sqrt{i\sigma p_r}\,\eta\right]$$

$$+\frac{2p_0 p_r^3 C_2^3\,(1-i\sigma b_3)(2-p_r-i\sigma b_3)}{\sigma^2\sqrt{i\sigma p_r}\,(1-p_r)^2}\,\sinh\sqrt{i\sigma p_r}\begin{bmatrix}\eta\sinh\sqrt{i\sigma p_r}\,\eta \\ -\frac{\sinh\sqrt{i\sigma p_r}}{\cosh\sqrt{i\sigma p_r}}\,\cosh\sqrt{i\sigma p_r}\,\eta\end{bmatrix}$$

$$-\frac{p_0 p_r^2 C_2^2\,(i-\sigma C_2(1-p_r))(1-i\sigma b_3)^2}{2\sigma^3\sqrt{i\sigma}\,(1-p_r)^2\cosh\sqrt{i\sigma}}\left[\eta\sinh\sqrt{i\sigma}\,\eta-\frac{\sinh\sqrt{i\sigma}}{\cosh\sqrt{i\sigma p_r}}\,\cosh\sqrt{i\sigma p_r}\,\eta\right]$$

$$+\frac{p_0 p_r^2 C_2^2\,(i-\sigma c_2(1-p_r))(1-i\sigma b_3)^2}{i\sigma^4\,(1-p_r)^3\cosh\sqrt{i\sigma}}\left[\cosh\sqrt{i\sigma}\,\eta-\frac{\cosh\sqrt{i\sigma}}{\cosh\sqrt{i\sigma p_r}}\,\cosh\sqrt{i\sigma p_r}\,\eta\right]. \tag{27}$$

Up to the first order estimations, the expressions $g(\eta)$ and $f(\eta)$ in A_6 are as follows:

$$g(\eta)=g^{(0)}(\eta)+A_6\,g^{(1)}(\eta), \tag{28}$$

$$f(\eta)=f^{(0)}(\eta)+A_6\,f^{(1)}(\eta). \tag{29}$$

The solution of velocity and temperature as assumed above is restricted to the first order approximation only. It is common and useful to limit an analysis to first-order perturbation theory in many areas of applied mathematics, fluid dynamics, and physics, particularly when working with complicated or nonlinear systems for which an accurate solution is either impossible or very difficult. In fluid flow, first-order may provide adequate information for design or prediction about how velocity reacts to changes in temperature or pressure. Higher-order corrections may only slightly increase accuracy and greatly increase mathematical effort if the first-order answer matches the experimental data.

The velocity and temperature distribution are thus obtained as

$$U(\eta,t)=Re\,[g(\eta)\,e^{i\sigma t}]\ \text{and}\ T(\eta,t)=\ Re\,[f(\eta)\,e^{i\sigma t}]. \tag{30}$$

4. VALIDATION AND COMPARISON OF RESULTS

The Perturbation method of results for the associated equations of governing motion have been determined in terms of the temperature and velocity fields in this paper. The method have been assumed and calculated up to the first order approximations. The governed modelling equations of momentum and energy are highly non-linear, complex and coupled. The higher order approximation computations becomes difficult and tedious with manual calculations. The numerical computations have been obtained for velocity and temperature with the impact of various material parameters by generating the code of algorithm using *MATLAB* software. The obtained results have been compared with the results of Pothanna *et al.* [4]**.** The excellent agreement was achieved when compared with the present study results of perturbation technique. The results comparison shows the validity and the reliability of current study in the numerical computations.

Table 1. Validation and Comparison of results of velocity and temperature.

Y	Velocity Results of Pothanna et al. [4] for $S=0$, $a_6=0.001$, c=1, $\sigma=1$, ρ=1, μ=1		Present Results for $t=\frac{\pi}{2}$, $a_6=0.001$, c=1, $\sigma=1$, ρ=1, μ=1		Temperature Results of Pothanna *et al*. [4] for $S=0$, $a_6=0.001$ c=1, $\sigma=1$, ρ=1, μ=1		Present Results for $t=\frac{\pi}{2}$, $a_6=0.001$ c=1, $\sigma=1$, ρ=1, μ=1	
	$p_r=0.7$, $B_3=1$	$p_r=1.5$, $B_3=3$	$p_r=0.7$, $B_3=1$	$p_r=1.5$, $B_3=3$	$p_r=0.7$, $B_3=1$	$p_r=1.5$, $B_3=3$	$p_r=0.7$, $B_3=1$	$p_r=1.5$, $B_3=3$
0.0	0.1599	0.2174	0.1599	0.2174	0.0895	-1.6680	0.0895	-1.6680
0.1	0.1580	0.2149	0.1580	0.2149	0.0894	-1.6481	0.0894	-1.6481
0.2	0.1521	0.2076	0.1521	0.2076	0.0890	-1.5886	0.0890	-1.5886
0.3	0.1424	0.1954	0.1424	0.1954	0.0879	-1.4907	0.0879	-1.4907
0.4	0.1292	0.1786	0.1292	0.1786	0.0858	-1.3563	0.0858	-1.3563
0.5	0.1127	0.1574	0.1127	0.1574	0.0819	-1.1881	0.0819	-1.1881
0.6	0.0932	0.1322	0.0932	0.1322	0.0755	-0.9898	0.0755	-0.9898
0.7	0.0713	0.1034	0.0713	0.1034	0.0653	-0.7658	0.0653	-0.7658
0.8	0.0475	0.0716	0.0475	0.0716	0.0504	-0.5216	0.0504	-0.5216

0.9	0.0224	0.0372	0.0224	0.0372	0.0291	-0.2638	0.0291	-0.2638
1.0	0.0033	0.0011	0.0033	0.0011	0.0000	-0.0000	0.0000	-0.0000

5. DISCUSSION ON RESULTS

The impact of different material coefficients such as thermal conductivity coefficient (B_3), prandtl number (p_r), thermal stress coefficient (A_6) and time parameter (t) on velocity and temperatures of the flow field have been discussed and illustrated graphically for fixed parameters taking c=1, $\sigma = 1$, ρ=1 and μ=1.

The effect of time parameter (t) on the velocity field is shown graphically in Fig. (2). It is observed that the velocity variations drifted towards right side of the region from the middle of the channel by increasing the value of 't' from t=0 to $\frac{\pi}{2}$. The fluid velocity increases along the flow direction up to the centre then decreases to attain the velocity of the upper plate. The velocity variations moving towards left of the flow region by increasing the value of 't' from $t = \pi$ to $\frac{3\pi}{2}$ from the centre of the flow region. In this case, the fluid velocity decreases along the flow direction up to the centre then decreases and attain its upper plate velocity. It is depicted that, the flow is oscillating with the period 'π' and also the symmetry of these velocity profile variations is observed with the difference of π period. Transient effects are introduced by the time parameter, which means that the flow and heat fields change over time instead of staying constant. In the flow development of channels or pipes, the velocity profile changes from flat (uniform) to parabolic (developed) over time. For oscillating or pulsatile flows, the velocity may vary periodically with time.

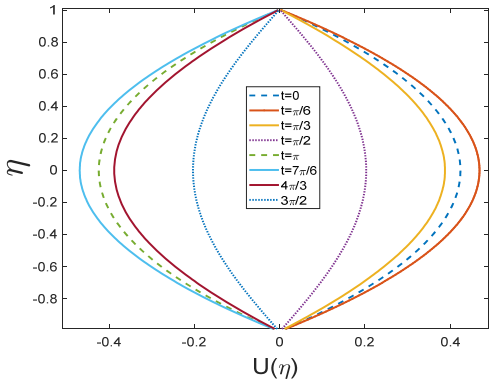

Figure 2. Velocity variations for various values of $'t'$ with fixed a_6 B_3 and p_r

The influence of thermal conductivity coefficient (B_3) for both steady and unsteady flow on the velocity is depicted in Fig. 3(a) and 3(b). Fluid flows are significantly impacted by thermal conductivity, especially when heat transfer is involved. The ability of a material to conduct heat is measured by its thermal conductivity (k). It plays a crucial role in fluids in determining how well heat is transferred through the medium. It is observed that, the fluid velocity increases and moves towards right as the value of B_3 incresing from 1 to 4. The reverse effect has been observed for the steady flow and is depicted in Fig. 3(b). Steep temperature gradients can arise and heat transport is slower in materials with low thermal conductivity, such as oils and gases. Heat spreads faster in materials with strong thermal conductivity (like liquids), which results in more consistent temperature distributions. This may be treated as the natural occurrence of any fluid that will be observed in a flow region. Along the flow direction, the fluid velocity increases up to the middle channel then decreases and attains its upper plate velocity.

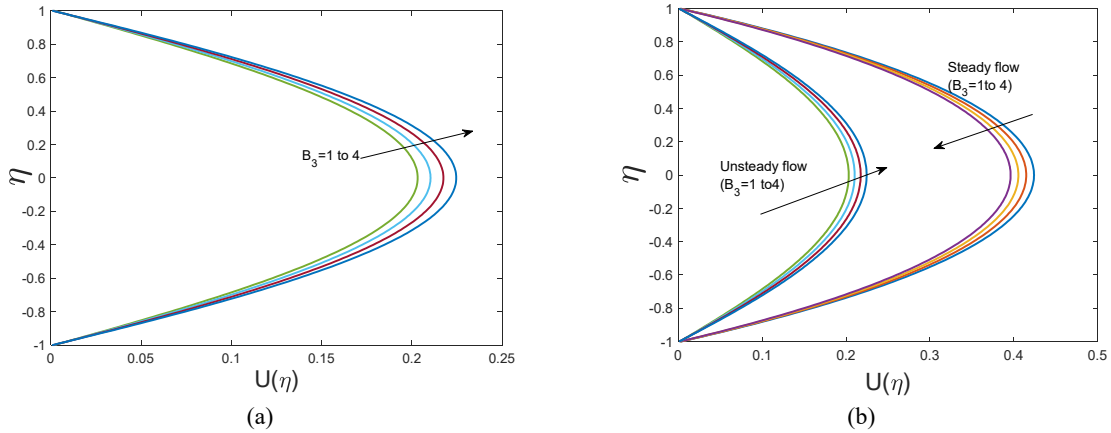

Figure 3. Velocity variations for B_3 (a) Unsteady flow (b) Steady and Unsteady flow

The impact of prandtle (p_r) number for small values on velocity field have illustrated graphically in Fig. 4(a) and 4(b) for steady and unsteady flow respectively.

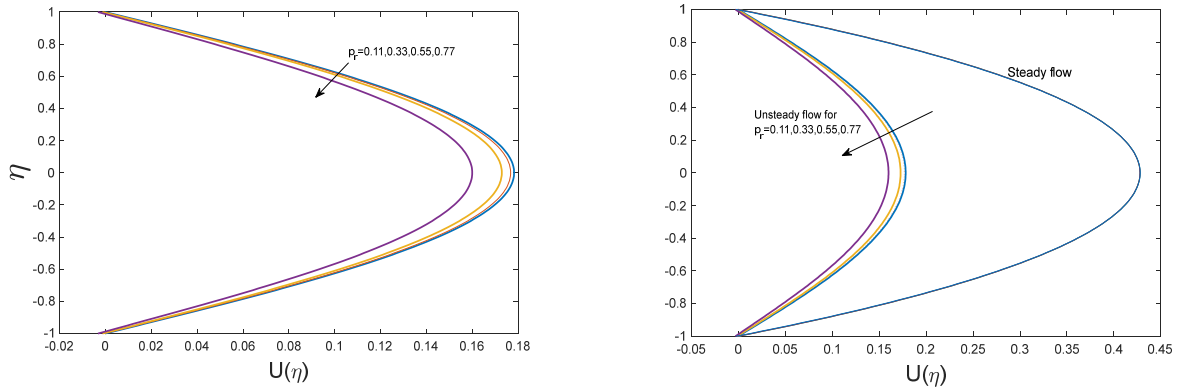

a b

Figure 4. Velocity variations for p_r with $B_3 = 1$ (a) Unsteady flow (b) Steady and Unsteady flow

The effect of p_r for some large values have been shown in Fig. 5(a) and 5(b) for various values of thermal conductivity coefficient (B_3). The velocity variations decreases by increasing the p_r and for the steady flow, the increasing rate is very slow and all the profile variations are coincides which is observed in Fig. 4(a) and 4(b). The velocity variations increases with the increase of p_r and shown in Fig. 5(a) and 5(b). It is also observed from these figures that, the fluid velocity increases with the values of B_3 increases. For large values of p_r , the increasing rate of fluid velocity is more predominant when compare to small p_r values. The p_r doesn't directly affect the velocity profile in purely viscous flows, but it does in thermo-viscous coupling cases where temperature gradients change viscosity or drive buoyancy (natural convection). For the high values of p_r , the flow near the wall is strongly influenced by temperature changes and this affects the velocity profile locally. For low p_r , the more uniform temperature and smoother velocity changes occurs.

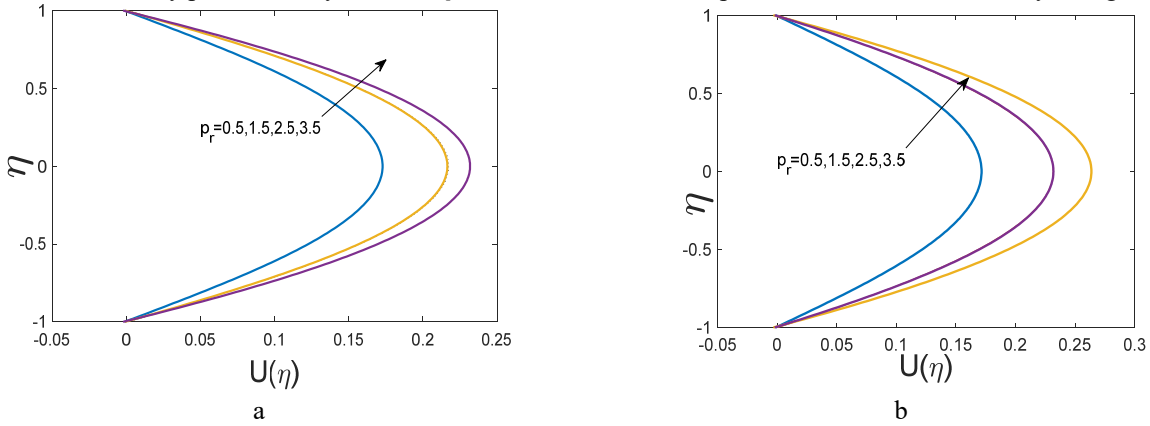

a b

Figure 5. Velocity variations for p_r with (a) $B_3 = 3$, (b) $B_3 = 5$

The impact of thermal conductivity coefficient (B_3) and thermal stress coefficient (A_6) on the flow temperature is depicted in Fig. 6(a) and 6(b).

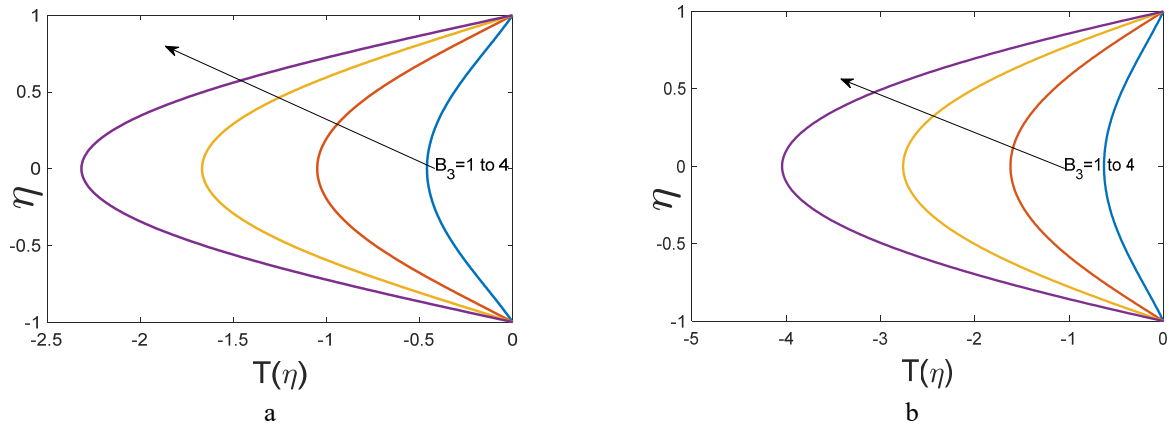

a b

Figure 6. Temperature variations for B_3 with (a) $a_6 = 0.001$ (b) $a_6 = 0.005$

It is observed that, the fluid temperature decreases and moves towards left with increasing the value of B_3 from 1 to 4. The value of A_6 increases, then the temperature of the fluid decreases with the faster rate as it is observed from the Fig.6 (a) and 6(b). Along the flow direction, the fluid temperature decreases up to the middle channel then increases and attains its hotter plate temperature. This is due to the non-homogeneous and anisotropic nature of the fluid considered. The influence of thermal conductivity will differ depending on the location due to its anisotropic nature. The corresponding figures clearly show the same thing. This is particularly noticeable when the thermal conductivity coefficient takes very large values. Therefore, it may be concluded that the anisotropy will rise in situations for large values of thermal conductivity.

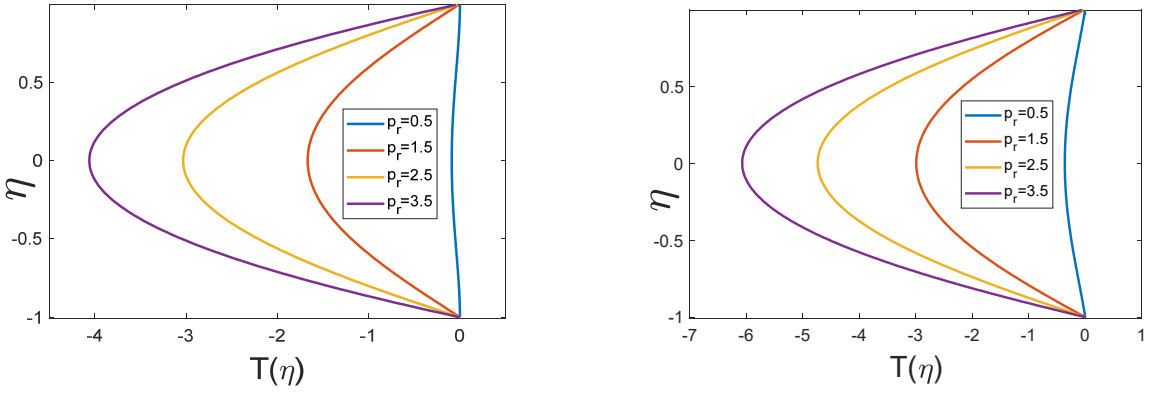

Figure 7. Temperature variations for p_r with (a) $B_3 = 3$ (b) $B_3 = 5$

The influence of Prandtl (p_r) number on temperature field for large values have been illustrated in Fig. 7(a) and 7(b) for various thermal conductivity (B_3) values. The temperature variations decreases with the increase of p_r and shown in Fig. 7(a) and 7(b). For low value p_r fluids, the temperature gradients are spread over a large area which smoother temperature field. For high p_r fluids, the steep thermal gradients are near the surfaces and the thin thermal boundary layer becomes more localized heating.

It is also observed from these figures that the fluid temperature decreases at the faster rate with the values of B_3 increases. This is because the viscosity and specific heat have a direct correlation with the Prandtl number. The fluid domain under consideration in this work has a constant specific heat. Therefore, the skewness in the mirroring will be caused by the viscosity.

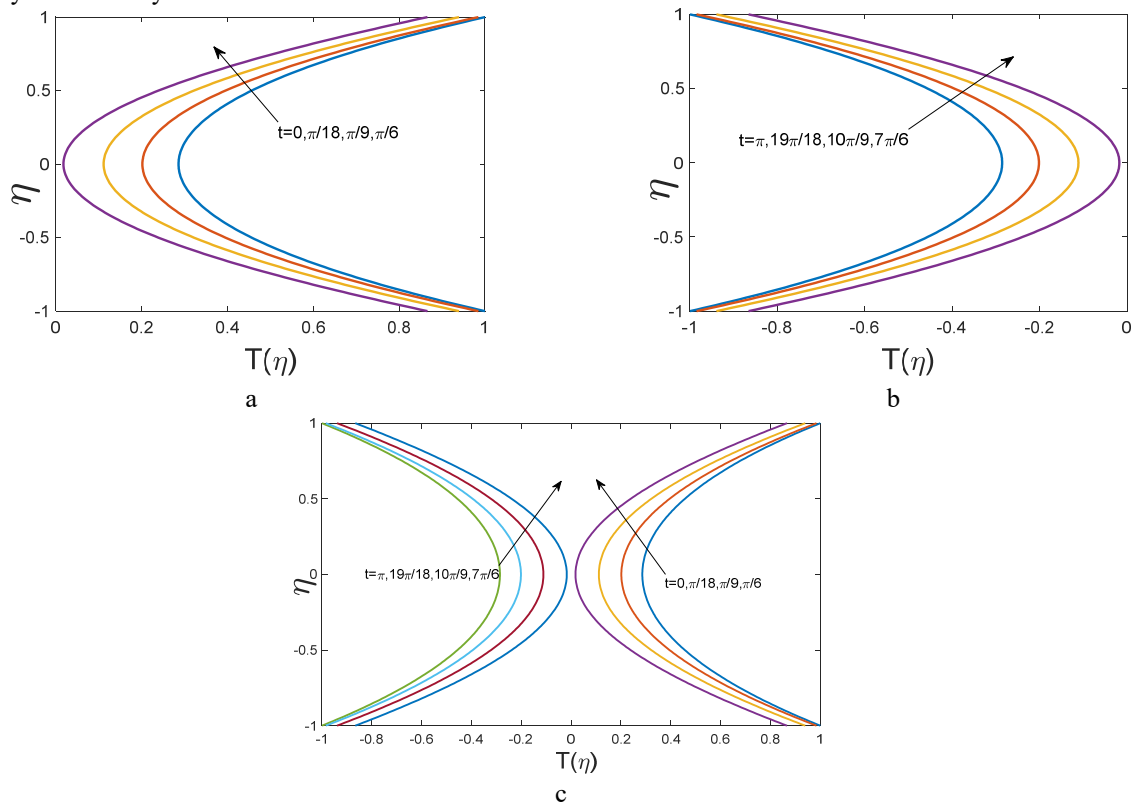

Figure 8. Temperature variations (a), (b) and (c) for different values of $'t'$ with fixed a_6 B_3 and p_r

The impact of time parameter (t) on the temperature field is shown graphically in Fig. (8a), (8b) and (8c). It is observed that the temperature variations increase and drifted towards center from right of the flow surface with the increasing values of time parameter (t) from 0 to $\frac{\pi}{6}$. The fluid velocity increases along the flow direction up to the centre then decreases and attains its upper plate velocity. The velocity profiles drifted towards middle of the with the increasing values of time parameter (t) from π to $\frac{7\pi}{6}$ from left side of the flow region. In this case, the fluid velocity decreases along the flow direction up to the centre then decreases and attain its upper plate velocity. The hyperbolic type profiles are realized for the temperature variations of the fluid. Heat sources, conduction, or convection cause temperature variations over time in transient heating. The temperature can fluctuate if exposed to time-varying heat input, the velocity increases, and the heated region spreads over time in the thermal boundary layer growth.

6. CONCLUSIONS

In this present work an unsteady fluid motion between two infinitely stretched parallel horizontal plates with the absence of viscous dissipation is examined. The following are the conclusions observed from the above graphical illustrations.

- The velocity profile variations are symmetrically oscillating with the difference of period π. Fluid particles in symmetric oscillatory motion move forward during the first half of the cycle and backward for the second half of the same distance. Long-term fluid movement is eliminated as a result, but momentum and energy can still be transferred.
- The fluid velocity increases and shifted towards right from the origin as the value of B_3 increases.
- The velocity variations decrease by increasing small values of p_r. The rate of increase is very slow and the velocity profiles coincides when fluid is steady. For low p_r, the more uniform temperature and smoother velocity changes occurs.
- For large values of p_r, the velocity variations increase with the faster rate. For high values of p_r, the flow near the wall is strongly influenced by temperature changes and this affects the velocity profile locally.
- The fluid temperature decreases as the value B_3 and A_6 increases. The real-world uses of industry, Low-thermal-conductivity fluids, such as oils or gases, need bigger surfaces or longer residence times in heat exchangers, while high-thermal-conductivity fluids, such as water or liquids, increase heat transfer efficiency. The influence of thermal conductivity will differ depending on the location due to its anisotropic nature.
- The hyperbolic type profiles are realized for the temperature variations as the value of $'t'$ increases.

ORCID

Nalimela Pothanna, https://orcid.org/0000-0003-3983-3125

REFERENCES

[1] S.L. Koh, and A.C. Eringen, "On the foundations of non-linear thermo-viscoelasticity," International Journal of Engineering Science, **1**(2), 199-229 (1963). https://doi.org/10.1016/0020-7225(63)90034-X.
[2] P.D. Kelly, "Some viscometric flows of incompressible thermoviscous fluids," International Journal of Engineering Science **2**(5), 519-533 (1965). https://doi.org/10.1016/0020-7225(65)90007-8
[3] G.J. Reddy, P. Mangathai, and N. Pothanna, "Analysis of heat generation impact on nanofluid flow over a stretching sheet," Partial Differential Equations in Applied Mathematics, **11**, 100852 (2024). https://doi.org/10.1016/j.padiff.2024.100852.
[4] N. Pothanna, and P. Aparna, "Unsteady Thermo-Viscous Flow in a Porous Slab over an Oscillating Flat Plate," Journal of Porous Medium, **22**(5), 531–543 (2019). https://doi.org/10.1615/JPorMedia.2019028871
[5] N. Pothanna, "Investigation on unsteady fluid flow around an oscillating sphere-A numerical and analytical approach," Hybrid Advances, **6**, 100257 (2024). https://doi.org/10.1016/j.hybadv.2024.100257
[6] N. Pothanna, P. Aparna, M.P. Reddy, *et al*., "Thermo-viscous fluid flow in porous slab bounded between two impermeable parallel plates in relative motion: Four stage algorithm approach," Applications of Mathematics, 1-21 (2024).
[7] P.K. Reddy, P. Aparna, and N. Pothanna, M. Garvandha, and V.R.M. Josyula, "Steady flow of couple stress fluid through a rectangular channel under transverse magnetic field with suction," Partial Differential Equations in Applied Mathematics, **11**, 100852 (2024). https://doi.org/10.1016/j.padiff.2024.100956
[8] N. Pothanna, S. Joshi, A. Podila, P. Podila, and R. Pemmaraju, "Steady Flow of Thermo-Viscous Fluid between Infinitely Stretched Porous Parallel Plates-A Perturbation Technique," CFD Letters, **17**(1), 78–89 (2025). https://doi.org/10.37934/cfdl.17.1.7889
[9] N. Pothanna, P.N. Rao, and N.Ch.P. Ramacharyulu, "Flow of slightly thermo-viscous fluid in a porous slab bounded between two permeable parallel plates," Int. J. Adv. Appl. Math. and Mech, **2**(3), 1-9 (2015). https://doi.org/10.7726/jac.2015.1003
[10] N. Pothanna, N.Ch.P. Ramacharyulu, and P.N. Rao, "Effect of strain thermal conductivity on slightly thermo-viscous fluid in a porous slab bounded between two parallel plates," Journal of Advanced Computing, **4**(1), 37-58 (2015). https://doi.org/10.7726/jac.2015.1003
[11] P.N. Rao, and N.Ch.P. Ramacharyulu, "Steady flow of a second-order thermo-viscous fluid over an infinite plate," Proceedings of the Indian Academy of Sciences-Mathematical Sciences, Springer India, **8**, 157-161 (1979). https://doi.org/10.1007/BF02871612
[12] Aparna, Podila, Podila Padmaja, N. Pothanna, and J.V.R. Murthy, "Uniform Flow of Viscous Fluid Past a Porous Sphere Saturated with Micro Polar Fluid," Biointerface Research in Applied Chemistry, **13**, 1-12 (2022). https://doi.org/10.33263/BRIAC131.069
[13] P. Aparna, N. Pothanna, J.V.R. Murthy, and K. Sreelatha, "Flow generated by slow steady rotation of a permeable sphere in a micro-polar fluid," Alexandria Engineering Journal, **56**(4), 679-685 (2017). https://doi.org/10.1016/j.aej.2017.01.018

[14] P. Aparna, N. Pothanna, and J.V.R. Murthy, "Viscous Fluid Flow past a Permeable Cylinder," in: *Numerical Heat Transfer and Fluid Flow: Select Proceedings of NHTFF, 2018*, (Springer Singapore, 2019). pp. 285-293. https://doi.org/10.1007/978-981-13-1903-7_33
[15] P. Aparna, N. Pothanna, and J.V.R. Murthy, "Rotary Oscillations of a Permeable Sphere in an Incompressible Couple Stress Fluid," in: *Advances in Fluid Dynamics: Selected Proceedings of ICAFD 2018*, (Springer Singapore, 2020). pp. 135-146. https://doi.org/10.1007/978-981-15-4308-1_10
[16] P. Padmaja, P. Aparna, R.S.R. Gorla, and N. Pothanna, "Numerical solution of singularly perturbed two parameter problems using exponential splines," International Journal of Applied Mechanics and Engineering, **26**(2), 160-172 (2021). https://doi.org/10.2478/ijame-2021-0025
[17] N. Pothanna, P. Aparna, and R.S.R. Gorla, "A numerical study of coupled non-linear equations of thermo-viscous fluid flow in cylindrical geometry," International Journal of Applied Mechanics and Engineering, **22**(4), 965-979 (2017). https://doi.org/10.1515/ijame-2017-0062
[18] N. Pothanna, P. Aparna, G. Sireesha, and P. Padmaja, "Analytical and Numerical Study of Steady Flow of Thermo-Viscous Fluid Between Two Horizontal Parallel Plates in Relative Motion," Communications in Mathematics and Applications, **13**(5), 1427 (2022). https://doi.org/10.26713/cma.v13i5.2254
[19] J. Srinivas, N. Pothanna, P.N. Rao, and N.Ch.P. Ramacharyulu, "Linearization of thermo-viscous fluid in a porous slab bounded between two fixed permeable horizontal parallel plates in the absence of thermo-mechanical interaction coefficient," International Journal of Modern Trends in Engineering and Research, **1**(5), 412-424 (2014).
[20] N. Pothanna, P. Aparna, and J.Srinivas, "Unsteady Forced Oscillations of a fluid bounded by rigid bottom," International Journal of Control Theory and Applications, **9**(19), 9049-9054 (2016).
[21] J. Srinivas, N. Pothanna, P.N. Rao, and N.Ch.P. Ramacharyulu, "Slow steady motion of a thermo-viscous fluid between two parallel plates with constant pressure and temperature gradients," International Journal of Research in Engineering and Technology, **2**(11), 294-299 (2013).
[22] S. Srinivas, and R. Muthuraj, "Flow of a thermo-viscous fluid in a radially non-symmetric constricted tube", Journal of Ultra Scientist of Physical sciences, **17**, 437-442 (2005).
[23] S. Srinivas, Ch.V. Srinivas, and N.Ch.P. Ramacharyulu, "Peristaltic transport of a thermo-viscous fluid," Acta Ciencia Indica, **47**, 1157-1167 (1995).
[24] A.H. Meghdadi, I.R. Nasehi, and E. Shirani, "Mixing enhancement in microchannels using thermo-viscous expansion by oscillating temperature wave", Chemical Engineering and Processing - Process Intensification, **126**, 123-131 (2018). https://doi.org/10.1016/j.cep.2018.02.020

НЕСТАЦІОНАРНИЙ РУХ РІДИНИ МІЖ НЕСКІНЧЕННО РОЗТЯГНУТИМИ ПАРАЛЕЛЬНИМИ ГОРИЗОНТАЛЬНИМИ ПЛАСТИНКАМИ ЗА ВІДСУТНОСТІ В'ЯЗКОЇ ДИСИПАЦІЇ: АНАЛІТИЧНЕ НАБЛИЖЕННЯ

Дж. Срінівас[a], Н. Потанна[a], А. Раджу[b], М. Аніл Кумар[c]
[a]Кафедра математики, Інженерно-технологічний інститут ім. ВНР Віньяна Джйоті, Хайдерабад-500090, штат Телангана, Індія
[b]Кафедра прикладних наук, Технологічний інститут Симбіозу, Міжнародний університет Симбіозу, Пуне-412115, Індія
[c]Кафедра математики, Університет Анураг, Венкатапур, Хайдерабад-500088, штат Телангана, Індія

У цьому дослідженні вивчається нестаціонарний рух рідини між двома нескінченно розтягнутими паралельними горизонтальними пластинами за відсутності в'язкої дисипації. Пластини підтримуються при різних постійних температурах і знаходяться на відстані 2 год одна від одної. Потік створюється постійним коливальним градієнтом тиску між пластинами та паралельно до меж пластин. Розв'язок відповідних рівнянь потоку з відповідними граничними обмеженнями був отриманий з використанням найелегантнішого методу аналітичної апроксимації: методу збурень. Вплив різних параметрів матеріалу поля потоку був досліджений для полів швидкості та температури та обговорений за допомогою графічних інтерпретацій. Отримані результати перевірені та порівняні з результатами, що існують у літературі. Отримані результати визначені як такі, що винятково узгоджуються з результатами літератури. Сподіваємося, що це дослідження буде корисним для різних промислових застосувань, особливо в ядерній промисловості для аварійного охолодження ядерних реакторів. Дослідники та науковці можуть використовувати методологію цієї роботи в інтересах своїх досліджень.

Ключові слова: *термов'язка рідина; коефіцієнт термодеформаційної провідності; термомеханічна в'язкість під напруженням; число Прандтля*

East European Journal of Physics. 2. 369-382 (2025)
DOI:10.26565/2312-4334-2025-2-46 ISSN 2312-4334

EXACT ANALYSIS OF DIFFUSION-THERMO EFFECT ON MHD NATURAL CONVECTIVE FLOW PAST AN OSCILLATING VERTICAL PLATE WITH CHEMICAL REACTION AND THERMAL RADIATION IN POROUS MEDIUM

Dibya Jyoti Saikia[a]*, Nazibuddin Ahmed[b], Richa Deb Dowerah[c], Ardhendu Kumar Nandi[a], Rajdeep Bordoloi[d], Harun Al Rashid[e]

[a]*Department of Mathematics, Basugaon College, Basugaon, BTR, Chirang,783372, India*
[b]*Department of Mathematics Cotton University, Guwahati, 781001, India*
[c]*Department of Mathematics, Gauhati University, Guwahati, Assam, 781014, India*
[d]*Department of Mathematics, Sibsagar University, Sibsagar, Assam, 785640, India*
[e]*Department of Mathematics, Bilasipara College, Bilasipara, 783348, India*
**Corresponding Author e-mail: dssaikia18@gmail.com*
Received September 21, 2024; revised January, 3, 2025; in final form March 1, 2025; accepted May 21, 2025

The primary goal of this investigation is to explore the impact of diffusion-thermo on the flow characteristics of MHD natural convection via a permeable medium past an infinitely oscillating upright plate, while accounting for chemical reaction and thermal radiation effects. The Laplace transformation approach is employed to solve the governing equations for species continuity equation, energy and momentum. The simulation findings show that thermal radiation increases the primary fluid velocity while decreasing the secondary fluid velocity. Furthermore, increasing the Dufour number (Du) results in higher temperature fields as well as an increase in both primary and secondary fluid velocities. Also, the diffusion-thermo effect contributes to improve the temperature field. The equation for skin friction is obtained and graphically shown. Three-dimensional surface plots are used to demonstrate the Nusselt and Sherwood numbers. In addition, graphical representations are used to portray the effect of non-dimensional factors on concentration, temperature, and velocity patterns.
Keywords: *Free convection; Porous medium; Diffusion-thermo; Chemical reaction; Thermal radiation*
PACS: 44.25.f, 44.30.v, 44.40 a, 47.65.d

1. INTRODUCTION

A "porous medium" is a system composed of solid entities with interconnected or related voids. Flow via permeable media is crucial in numerous applications, including crude oil recovery, large-scale chemical reactions which involves adsorbents, filters and catalysts, geophysical phenomena and mineral extraction. Important uses for flow via permeable medium were fully studied in comprehensive research by Alazmi and Vafai [1]. Geophysics, oil recovery techniques, metal processing, die filling, agricultural and industrial water distribution are among the applications. Alazmi and Vafai's research gives important insights into the broad and practical ramifications of porous media flow in a variety of industries and scientific areas. In the presence of a porous inner spinning cylinder, Lahonian et al. [2] investigated the mixed convection of several nanofluids. Haritha et al. [3] discussed the mass and heat transport of magnetohydrodynamics Jeffrey nanofluid flow via a permeable medium, through an inclined plate when Soret effects, radiation and chemical reaction are taken into account. Jauhri and Mishra [4] investigated MHD nanofluid flow across a stretching sheet numerically and in the existence of porous media and including the second-order velocity slip effect. The investigation of mass and heat transport upon unsteady magnetohydrodynamic flow across an endless vertically oscillating permeable plate was conducted by Krishna et al. [5].

Because of its numerous uses in scientific and technical domains, there has been a surge in interest in investigating heat and mass transport processes involving free convection through porous surfaces in recent years. Natural convection, driven simply by density differences caused by temperature gradients and without any external factors, has received a lot of attention. For example, Matta et al. [6] investigated the influence of viscous dissipation upon MHD natural convection flow via a semi-infinite vertically movable permeable sheet in presence of heat sink and chemical reaction. Meanwhile, Hamad [7] investigated the unsteady MHD natural convective flow via a vertically endless permeable plate in the presence of radiation absorption effects. In a distinct line of research, in the presence of hall and ion-slip currents, Singh et al. [8] examined how a rotating fluid's MHD free convective flow is affected by time-varying wall temperature and concentration. In addition, recent studies by other researchers, such as Nabway et al. [9], Saha et al. [10], and Saikia et al. [11], have focused on the use of free convection in their respective studies.

The energy flux generated inside a chemical structure due to composition gradients is known as the Dufour effect. When a notable concentration gradient leads to a heat flux, it presents an inverse phenomenon to thermal diffusion and this effect is often termed as Dufour effect. In their research, Goud et al. [12] examined the impacts of Soret, Dufour and chemical reaction on MHD heat transfer of a Casson fluid over an exponentially permeable stretching surface with slip effects. Additionally, Sekhar et al. [13] investigated the influence of radiative heat sources on fluid flow in the presence

Cite as: D.J. Saikia, N. Ahmed, R.D. Dowerah, A.K. Nandi, R. Bordoloi, H. Al Rashid, East Eur. J. Phys. 2, 369 (2025), https://doi.org/10.26565/2312-4334-2025-2-46

of Soret and Dufour effects for MHD Casson nanofluid over a stretching surface. Meanwhile, Deepika et al. [14] explored the Soret and Dufour effects on MHD mixed convection flow of a Casson hybrid nanofluid over a permeable stretching sheet. Moreover, Choudhary et al. [15] studied the thermal diffusion and diffusion thermo effects in a three-dimensional MHD flow via a semi-infinite vertical plate in the presence of constant heat flux.

Radiation is the electromagnetic transport of heat. Currently, many researchers are using radiation to examine the issues connected with MHD natural convective heat and mass movement in a variety of industrial operations such as archaeology, astronomy, space exploration, energy generation, aeronautics, and radioactive fluxes. In one work, Reddy and Goud [16] looked at how thermal radiation affected the flow of MHD nanofluid across an endless vertical flat plate. Bejwada and Nadeppanavar [17] investigated the influence of thermal radiation on magnetohydrodynamic heat transfer in a micropolar fluid flow over a vertical moving porous plate. Meanwhile, Algehyne et al. [18] investigated the combined effects of thermal radiation and suction/injection on magnetohydrodynamic hybrid nanofluid flow past a convectively heated stretching surface. Furthermore, Koli and Salunkhe [19] have investigated the effects of magnetic fields and thermal radiation on the flow of MHD nanofluids over a stretched sheet.

Chemical reactions, as opposed to physical or nuclear processes, involve the rearrangement of a substance's ionic structure. Chemical reactions are classified as heterogeneous or homogeneous based on whether they occur at an interface or in a single-phase volume. Vijay and Sharma [20] investigated the effect of chemical reaction and thermal radiation on entropy generation analysis in MHD hybrid nanofluid flow. Similarly, Iranian et al. [21] studied the effect of heat generation on Magnetohydrodynamic Powell-Eyring fluid flow along a vertical surface using a chemical reaction. Meanwhile, Omar et al. [22] studied the impacts of thermal radiation and chemical reaction on unsteady magnetohydrodynamics Casson fluid flow in the existence of a porous material. Moreover, additional researchers, including Reddy et al. [23], Appidi et al. [24], have also undertaken their research involving chemical reactions.

In this paper, the impact of the Dufour number, chemical reaction, and heat radiation on the unsteady free convective Newtonian flow through a porous medium employing an indefinitely oscillating vertical plate is investigated. For the flow model, an exact solution for velocity, temperature and concentration profiles is achieved. The novelty of the current investigation is that, in addition to thermal radiation, both diffusion-thermo and a first-order homogeneous chemical reaction are taken into consideration. This research is highly relevant in technical applications, including solar energy collection systems, catalytic reactors, material processing, nuclear waste storage facilities, and petroleum product and gas recovery.

2. MATHEMATICAL FORMULATION AND GEOMETRICAL SETUP FOR THE FLOW PROBLEM

To establish a rectangular Cartesian coordinate system, the x'-axis is aligned vertically upward along the plate's length, while the y'-axis is aligned across the plate's breadth. The z'-axis is perpendicular to the plate. Figure 1 provides a visual representation of the geometric arrangement, illustrating the effects of Dufour number upon the flow characteristics of MHD free convection through a porous medium past an oscillating vertical plate. This analysis incorporates factors such as chemical reaction and thermal radiation. Initially, the fluid and the plate are assumed to maintain a consistent temperature and concentration both on the fluid's surface and within its interior. As time progresses beyond $t' > 0$, the plate experiences rotational motion within its own plane, with a certain velocity $U_o e^{i\Lambda\omega t'}$. Additionally, the plate's temperature and concentration may vary, either increasing or decreasing to values denoted as $T' = T'_{\infty} + (T'_w - T'_{\infty})\Lambda t'$ and $C' = C'_{\infty} + (C'_w - C'_{\infty})\Lambda t'$ respectively. Since the flow possesses an extremely low Reynolds number, the influence of magnetic fields and viscous dissipation is considered insignificant. In this particular flow scenario, the fluid is characterized as "gray," indicating its ability to absorb and emit radiation without scattering light. A uniform transverse magnetic field B_o is applied in the z' direction, perpendicular to the plate. The unsteady flow, subject to the conventional Boussinesq approximation, is governed by a set of equations that are subsequently analyzed.

Momentum equation:

$$\frac{\partial u'}{\partial t'} = \nu \frac{\partial^2 u'}{\partial z'^2} + g\beta'(T' - T'_{\infty}) + g\overline{\beta}(C' - C'_{\infty}) - \left(\frac{\sigma B^2{}_o}{\rho} + \frac{\nu}{K'}\right) u', \tag{1}$$

$$\frac{\partial v'}{\partial t'} = \nu \frac{\partial^2 v'}{\partial z'^2} - \left(\frac{\sigma B^2{}_o}{\rho} + \frac{\nu}{K'}\right) v'. \tag{2}$$

Energy equation:

$$\frac{\partial T'}{\partial t'} = \frac{\kappa}{\rho C_p}\frac{\partial^2 T'}{\partial z'^2} - \frac{1}{\rho C_p}\frac{\partial q'_r}{\partial z'} + \frac{D_M K_T}{C_p C_S}\frac{\partial^2 C'}{\partial z'^2}. \tag{3}$$

Species continuity equation:

$$\frac{\partial C'}{\partial t'} = D_M \frac{\partial^2 C'}{\partial z'^2} + \overline{k}(C' - C'_{\infty}). \tag{4}$$

The velocity, temperature, and concentration fields are subject to the following relevant initial and boundary conditions:

$$\left.\begin{array}{l} u'=0,\ v'=0,\ T'=T'_{\infty},\ C'=C'_{\infty},\ t'\le 0,\ \forall z' \\ u'=U_o\, e^{i\Lambda\omega t'},\ v'=0,\ T'=T'_{\infty}+(T'_w-T'_{\infty})\Lambda t',\ C'=C'_{\infty}+(C'_w-C'_{\infty})\Lambda t',\ for\ t'>0,\ z'=0 \\ u'\to 0,\ v'\to 0,\ T'\to T'_{\infty},\ C'\to C'_{\infty}\quad for\ \ t'>0,\ as\ z'\to\infty \end{array}\right\}. \tag{5}$$

Equations (1) and (2) can be coupled using the complex integer q = u + iv, yielding:

$$\frac{\partial q'}{\partial t'}=\frac{\partial u'}{\partial t'}+i\,\frac{\partial v'}{\partial t'},$$

$$or \tag{6}$$

$$\frac{\partial q'}{\partial t'}=\nu\frac{\partial^2 q'}{\partial z'^2}+g\,\beta'(T'-T'_{\infty})+g\,\overline{\beta}(C'-C'_{\infty})+\left(\frac{\sigma B^2{}_o}{\rho}+\frac{\nu}{K'}\right)q'.$$

In an optically thin, grey gas scenario, the expression for the rate of local radiation absorption is as follows:

$$\frac{\partial q'_r}{\partial z'}=-4a'\sigma'(T'^4_{\infty}-T'^4). \tag{7}$$

The absolute value of $|T'-T'_{\infty}|$ tends to zero as the temperature differential between the boundary layer and the region furthest from the plate becomes minimal. The following result is obtained by expanding the term T'^4 in a Taylor series with respect to the free stream temperature T'_{∞}:

$$T'^4\cong 4T'^3_{\infty}T'-3T'^4_{\infty}. \tag{8}$$

By using equations (7) and (8) concurrently, the term $\frac{\partial q'_r}{\partial z'}$ in equation (3) can be eliminated, resulting in the transformation of equation (3) into:

$$\frac{\partial T'}{\partial t'}=\frac{\kappa}{\rho C_p}\frac{\partial^2 T'}{\partial z'^2}-\frac{16\,a'\sigma'T'^3_{\infty}}{\rho\,C_p}(T'-T'_{\infty})+\frac{D_M K_T}{C_p C_S}\frac{\partial^2 C'}{\partial z'^2}. \tag{9}$$

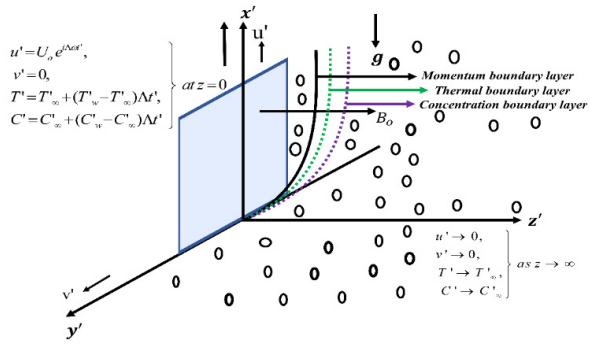

Figure 1. Geometrical configuration of the flow problem

Introducing the non-dimensional parameters:

$$\left.\begin{array}{l} z=\dfrac{U_o z'}{\nu},\ q=\dfrac{q'}{U_o},\ T=\dfrac{T'-T'_{\infty}}{T'_w-T'_{\infty}},\ C=\dfrac{C'-C'_{\infty}}{C'_w-C'_{\infty}}, \\ Sc=\dfrac{\nu}{D_M},\ \Pr=\dfrac{\rho\nu C_p}{\kappa},\ K'=\dfrac{U^2{}_o K}{\nu^2},\ \Lambda=\dfrac{U^2{}_o}{\nu},\ Du=\dfrac{D_M D_T(C'_w-C'_{\infty})}{\nu C_p C_s(T'_w-T'_{\infty})} \\ Gr=\dfrac{\nu g\,\beta'(T'_w-T'_{\infty})}{U^3{}_o},\ k=\dfrac{\overline{k}\nu}{U^2{}_o},\ Gm=\dfrac{\nu g\,\overline{\beta}\,(C'_w-C'_{\infty})}{U^3{}_o}, \\ t'=\dfrac{U^2{}_o t}{\nu},\ M=\dfrac{\sigma B^2{}_o\nu}{\rho U^2{}_o},\ R=\dfrac{16\,a'\sigma'T'^3_{\infty}\nu^2}{\kappa U^2{}_o} \end{array}\right\}. \tag{10}$$

Equations (6), (4), and (9) undergo a transformation when the non-dimensional parameters indicated in equation (10) are applied, yielding:

$$\frac{\partial q}{\partial t}=\frac{\partial^2 q}{\partial z^2}+Gr\,T+Gm\ C-\xi\,q. \tag{11}$$

Where, $\xi = M + (1/k)$.

$$\frac{\partial C}{\partial t} = \frac{1}{Sc}\frac{\partial^2 C}{\partial z^2} - k\,C. \tag{12}$$

$$\frac{\partial T}{\partial t} = \frac{1}{\Pr}\frac{\partial^2 T}{\partial z^2} - \frac{R}{\Pr}T + Du\frac{\partial^2 C}{\partial z^2}. \tag{13}$$

Equations (11), (12), and (13) exhibit dimensionless formulations of the momentum, concentration, and energy equations, respectively. Furthermore, we derive analogous dimensionless initial and boundary conditions which are shown below:

$$\left.\begin{array}{l} q = 0,\ T = 0,\ C = 0,\ t \le 0,\ \forall z \\ q = e^{i\omega t},\ T = t,\ C = t,\ t > 0,\ at\ z = 0 \\ q \to 0,\ T \to 0,\ C \to 0,\ t > 0,\ as\ z \to \infty \end{array}\right\}. \tag{14}$$

3. SOLUTION OF THE FLOW PROBLEM

Using the Laplace transformation method, the system of interconnected partial differential equations provided by equations (11)-(13) was successfully solved. Furthermore, the study took into account the insertion of the boundary conditions shown in equation (14). The Laplace transformation of equations (11), (12), and (13) yielded the following results:

The application of the Laplace transformation to equation (12) yields:

$$\frac{d^2\overline{C}}{dz^2} - Sc\,(s+k)\,\overline{T} = 0. \tag{15}$$

With the implementation of the Laplace transformation, the corresponding boundary conditions were modified to,

$$\begin{array}{l} \overline{C} = \dfrac{1}{s^2}\ at\ z = 0 \\ \overline{C} \to 0, as\ z \to \infty \end{array} \tag{16}$$

The fluid concentration solution is then obtained in the format shown below by applying the inverse Laplace transformation to equation (15) and taking into account the boundary condition supplied in equation (16).

$$\phi = f_1 = f(Sc, k,\ z,\ t). \tag{17}$$

Again, upon performing the Laplace transformation on equation (13), we obtain-

$$\frac{d^2\overline{T}}{dz^2} - (s\,\Pr + R)\,\overline{T} = -\frac{Du\,Sc\,\Pr}{s^2}(k+s)e^{-\sqrt{Sc}\sqrt{k+s}\,z}, \tag{18}$$

With the implementation of the Laplace transformation, the corresponding boundary conditions were modified to,

$$\begin{array}{l} \overline{T} = \dfrac{1}{s^2}\ at\ z = 0 \\ \overline{T} \to 0, as\ z \to \infty \end{array} \tag{19}$$

The fluid temperature solution is then obtained in the format shown below by applying the inverse Laplace transformation to equation (18) and taking into account the boundary condition supplied in equation (19).

$$\theta = (1 - B_1 A_2) f_2 + B_1 A_2 f_3 - D_1\psi_1 + D_2\psi_2 + D_1\psi_3 - D_2\psi_4 \tag{20}$$

Where,

$$\psi_1 = \psi(\beta,\ R\beta,\ z,\ t),\ \psi_2 = \psi(\beta,\ R\beta - B_2,\ z,\ t),$$
$$\psi_3 = \psi(Sc,\ k,\ z,\ t),\ \psi_4 = \psi(Sc,\ k - B_2,\ z,\ t),$$
$$f_2 = f(\beta,\ R\beta,\ z,\ t),\ f_3 = f(Sc,\ k,\ z,\ t),\ \beta = \frac{1}{\Pr},\ B_1 = -\frac{Du\,Sc\,\Pr\,k}{Sc - \Pr},$$
$$B_2 = \frac{Sc\ k - R}{Sc - \Pr},\ B_3 = -\frac{Du\,Sc\,\Pr}{Sc - \Pr},\ A_1 = -\frac{1}{B^2{}_2},\ A_2 = \frac{1}{B_2},\ A_3 = \frac{1}{B^2{}_2}$$

Upon performing the Laplace transformation on equation (11), we obtain:

$$\frac{d^2\,\bar{q}}{dz^2}-(s+\xi)\bar{q}=-Gr\bar{T}-Gm\bar{C}, \tag{21}$$

The boundary conditions undergo modifications as a result of executing the Laplace transformation, taking the following form:

$$\begin{aligned}&\bar{q}=\frac{1}{s-i\omega}\ at\ z=0\\&\bar{q}\to 0, as\ z\to\infty.\end{aligned} \tag{22}$$

Finally, the solution for fluid velocity is produced in the following format by adding the boundary condition indicated in equation (22) and applying the inverse Laplace transformation of equation (21).

$$q=q_1-q_2-q_3-q_4-q_5-q_6-q_7+q_8+q_9+q_{10}+q_{11}+q_{12}+q_{13}\,. \tag{23}$$

Where,

$q_1=e^{i\omega t}\,h(\delta+i\omega,\,z,\,t)=h_1,$

$q_2=G_1K_1\,h_2+G_1K_2\,F_1+G_1K_3\,h_3,$

$q_3=G_3L_1\,h_2+G_3L_2\,F_1+G_3L_3\,h_4+G_3L_4\,h_3,$

$q_4=G_4L_2\,h_2+G_4N_1\,h_4+G_4N_2\,h_3,$

$q_5=G_5P_1\,h_2+G_5P_2\,F_1+G_5P_3\,h_4+G_5P_4\,h_5,$

$q_6=G_7P_2\,h_2+G_7Q_1\,h_4+G_7Q_2\,h_5,$

$q_7=G_8I_1\,h_2+G_8I_2\,F_1+G_8I_3\,h_5,$

$q_8=G_1K_1\,\psi_1+G_1K_2\,f_2+G_1K_3\,\psi_5,$

$q_9=G_3L_1\,\psi_1+G_3L_2\,f_2+G_3L_3\,\psi_2+G_3L_4\,\psi_5,$

$q_{10}=G_4L_2\,\psi_1+G_4N_1\,\psi_2+G_4N_2\,\psi_5,$

$q_{11}=G_5P_1\,\psi_3+G_5P_2\,f_3+G_5P_3\,\psi_4+G_5P_4\,\psi_6,$

$q_{12}=G_7P_2\,\psi_2+G_7Q_1\,\psi_4+G_7Q_2\,\psi_6,$

$q_{13}=G_8I_1\,\psi_3+G_8I_2\,f_3+G_8I_3\,\psi_6,$

$G_1=-\frac{Gr}{\beta-1},\ G_2=\frac{R\beta^2-\xi}{\beta-1},\ G_3=\frac{GrB_1}{\beta-1},$

$G_4=\frac{GrB_3}{\beta-1},\ G_5=-\frac{GrB_1}{Sc-1},\ G_6=\frac{Sc\,k-\xi}{Sc-1},$

$G_7=-\frac{Gr\,B_3}{Sc-1},\ G_8=-\frac{Gm}{Sc-1},$

$K_1=-\frac{1}{G^2{}_2},\ K_2=\frac{1}{G_2},\ K_3=\frac{1}{G^2{}_2},$

$L_1=-\left(\frac{B_2+G_2}{B^2{}_2\,G^2{}_2}\right),\ L_2=\frac{1}{B_2G_2},\ L_3=-\frac{1}{B^2{}_2\left(B_2-G_2\right)},\ L_4=\frac{1}{G^2{}_2\left(B_2-G_2\right)},$

$N_1=\frac{1}{B_2\left(B_2-G_2\right)},\ N_2=-\frac{1}{G_2\left(B_2-G_2\right)},$

$P_1=-\left(\frac{B_2+G_6}{B^2{}_2\,G^2{}_6}\right),\ P_2=\frac{1}{B_2G_6},\ P_3=-\frac{1}{B^2{}_2\left(B_2-G_6\right)},\ P_4=\frac{1}{G^2{}_6\left(B_2-G_6\right)},$

$Q_1=\frac{1}{B_2\left(B_2-G_6\right)},\ Q_2=-\frac{1}{G_6\left(B_2-G_6\right)},$

$I_1=-\frac{1}{G^2{}_6},\ I_2=\frac{1}{G_6},\ I_3=\frac{1}{G^2{}_6}.$

$h_1=e^{i\omega t}\,h(\xi+i\omega,\,z,\,t),\qquad h_2=h(\xi,\,z,\,t),$

$h_3=e^{-G_2t}h(\xi-G_2,\,z,\,t),\qquad h_4=e^{-B_2t}h(\xi-B_2,\,z,\,t),$

$h_5=e^{-G_6t}h(\xi-G_6,\,z,\,t),\qquad \psi_5=e^{-G_2t}\psi(\beta,\,R\beta-G_2,\,z,\,t),$

$\psi_6=e^{-G_6t}\,\psi(Sc,\,k-G_6,\,z,\,t),\quad F_1=F(\xi,\,z,\,t).$

3.1. Solution for skin friction

The following procedure, in accordance with Newton's law of viscosity, can be used to estimate the viscous drag per unit area at the plate.

$$\tau' = -\mu \frac{\partial q'}{\partial z'}\Big]_{z=0} = -\mu U_o \frac{\partial q}{\partial z}\frac{\partial z}{\partial z'} = -\mu U_o \frac{\partial q}{\partial z}\frac{\partial}{\partial z'}\left(\frac{U_o z'}{\nu}\right) = -\frac{\mu U_o^{\,2}}{\nu}\frac{\partial q}{\partial z}$$

The skin friction coefficient at the plate is defined as

$$\tau = \frac{\tau'}{\frac{\mu U_o^{\,2}}{\nu}} = -\frac{\partial q}{\partial z}\Big]_{z=0}$$

$$= -\frac{\partial q_1}{\partial z}\Big]_{z=0} + \frac{\partial q_2}{\partial z}\Big]_{z=0} + \frac{\partial q_3}{\partial z}\Big]_{z=0} + \frac{\partial q_4}{\partial z}\Big]_{z=0} + \frac{\partial q_5}{\partial z}\Big]_{z=0} + \frac{\partial q_6}{\partial z}\Big]_{z=0} + \frac{\partial q_7}{\partial z}\Big]_{z=0}$$
$$- \frac{\partial q_8}{\partial z}\Big]_{z=0} - \frac{\partial q_9}{\partial z}\Big]_{z=0} - \frac{\partial q_{10}}{\partial z}\Big]_{z=0} - \frac{\partial q_{11}}{\partial z}\Big]_{z=0} - \frac{\partial q_{12}}{\partial z}\Big]_{z=0} - \frac{\partial q_{13}}{\partial z}\Big]_{z=0},$$

i.e

$$\begin{aligned}
&\tau = -\hbar_1 + (D_1K_1 + G_3L_1 + G_4L_2 + G_5P_1)\,\hbar_2 + (D_1K_3 + G_3L_4 + G_4N_2)\,\hbar_3 + \\
&(G_3L_3 + G_4N_1 + G_5P_3 + G_7Q_1)\,\hbar_4 + (G_5P_4 + G_7Q_2 + G_8I_3)\,\hbar_5 + \\
&(D_1K_2 + G_3L_2 + G_5P_2 + G_8I_2)\,\Gamma_1 - (G_1K_1 + G_1L_1 + G_4L_2)\,\Omega_1 - \\
&(G_3L_3 + G_4N_1)\Omega_2 - (G_5P_1 + G_7P_2 + G_8I_1)\,\Omega_3 - \\
&(G_5P_3 + G_7Q_1)\Omega_4 - (G_1K_3 + G_3L_4 + G_4N_2)\,\Omega_5 - \\
&(G_5P_4 + G_7Q_2 + G_8I_3)\,\Omega_6 - (G_1K_2 + G_3L_2)\,\varphi_2 - \\
&(G_5P_2 + G_8I_2)\,\varphi_2.
\end{aligned} \tag{24}$$

Where,

$$\hbar_1 = \frac{\partial h_1}{\partial z}\Big]_{z=0} = e^{i\omega t}\,\hbar(\xi + i\omega, t), \qquad \hbar_2 = \frac{\partial h_2}{\partial z}\Big]_{z=0} = \hbar(\xi, t),$$

$$\hbar_3 = \frac{\partial h_3}{\partial z}\Big]_{z=0} = e^{-G_2 t}\,\hbar(\xi - G_2, t), \qquad \hbar_4 = \frac{\partial h_4}{\partial z}\Big]_{z=0} = e^{-B_2 t}\,\hbar(\xi - B_2, t),$$

$$\hbar_5 = \frac{\partial h_5}{\partial z}\Big]_{z=0} = e^{-G_6 t}\,\hbar(\xi - G_6, t), \qquad \Omega_1 = \frac{\partial \psi_1}{\partial z}\Big]_{z=0} = \Omega(\beta, R\beta, t),$$

$$\Omega_2 = \frac{\partial \psi_2}{\partial z}\Big]_{z=0} = e^{-B_2 t}\,\Omega(\beta, R\beta - B_2, t), \qquad \Omega_3 = \frac{\partial \psi_3}{\partial z}\Big]_{z=0} = \Omega(Sc, k, t),$$

$$\Omega_4 = \frac{\partial \psi_4}{\partial z}\Big]_{z=0} = e^{-B_2 t}\,\Omega(Sc, k - B_2, t), \qquad \Omega_5 = \frac{\partial \psi_2}{\partial z}\Big]_{z=0} = e^{-G_2 t}\,\Omega(\beta, R\beta - G_2, t),$$

$$\Omega_6 = \frac{\partial \psi_6}{\partial z}\Big]_{z=0} = e^{-G_6 t}\,\Omega(Sc, k - G_6, t), \qquad \varphi_2 = \frac{\partial f_2}{\partial z}\Big]_{z=0} = \varphi(\beta, R\beta, t),$$

$$\varphi_3 = \frac{\partial f_3}{\partial z}\Big]_{z=0} = \varphi(Sc, k, t), \qquad \Gamma_1 = \frac{\partial F_1}{\partial z}\Big]_{z=0} = \Gamma(\xi, t).$$

3.2. Sherwood number

The Sherwood number, which pertains to the rate of mass transfer at the plate, is computed using Fick's diffusion law. The following approach can be employed to find the mass flux M_w from the plate at z'=0:

$$M_w = -D_M \frac{\partial C'}{\partial z'}\Big]_{z'=0} = -\frac{D_M U_o \left(C'_w - C'_\infty\right)}{\nu}\frac{\partial \phi}{\partial z}\Big]_{z=0},$$

Thus, the coefficient of rate of mass transfer at the plate is,

$$Sh = \frac{M_w}{D_M U_o \left(C'_w - C'_\infty\right)} = -\frac{\partial \phi}{\partial z}\Big]_{z=0}, \quad Sh = -\frac{\partial \phi}{\partial z}\Big]_{z=0} = -\frac{\partial f_1}{\partial z}\Big]_{z=0} = \varphi_1 = \varphi(Sc, k, t).$$

3.3. Solution for Nusselt number

Estimating and comprehending the rate of heat transfer at the plate is crucial in estimating the Nusselt number. This includes computing the ratio of convective to conductive heat transfer in the fluid across the boundary. Fourier's law of conduction is utilized to calculate the heat flux Q' from the plate at z'=0 to the fluid.

$$Q' = -\kappa \frac{\partial T'}{\partial z'}\Big]_{z'=0} = -\frac{\kappa U_o \left(T'_w - T'_\infty\right)}{\nu} \frac{\partial T}{\partial z}\Big]_{z=0}.$$

The coefficient of rate of heat transfer at the plate is,

$$Nu = \frac{\nu Q'}{\kappa U_o \left(T'_w - T'_\infty\right)} = -\frac{\partial \theta}{\partial z}\Big]_{z=0} = (1 - B_1 A_1)\varphi_2 + B_1 A_1 \varphi_3 - D_1 \Omega_1 + D_2 \Omega_2 + D_1 \Omega_3 - D_2 \Omega_4.$$

4. RESULTS AND DISCUSSION

A comprehensive investigation is performed to quantitatively determine primary fluid velocity (u), secondary fluid velocity (v), temperature (θ), concentration (ϕ), rate of heat transfer (Nu), and mass transfer (Sh) to enhance the comprehension of the fluid flow phenomena. In this research endeavor, Prandtl number (Pr) and Schmidt number (Sc) are deliberately chosen to be 0.71 and 0.22, respectively, to match the properties of dry air and hydrogen at a standard pressure of 1 atmosphere. To preserve uniformity and enable comparison analysis, the variables t and R are continually assigned a fixed value of 1.2 and 1 throughout the inquiry.

Figures 2-3 demonstrate how the Schmidt number (Sc) and chemical reaction parameter (k) affect fluid concentration. Figure 2 depicts a drop in fluid concentration as the Schmidt number increases. This discovery is consistent with scientific principles, as a higher Schmidt number correlates to reduced molecule diffusivity, which accelerates concentration decline in the boundary layer.

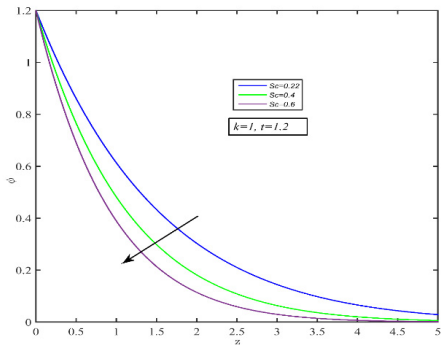

Figure 2. Concentration pattern versus distinct Sc

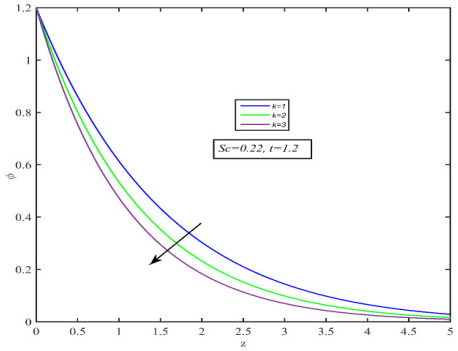

Figure 3. Concentration pattern versus distinct k

Figure 3 depicts the effect of chemical reactions on concentration patterns, exhibiting a decreasing fluid concentration as the chemical reaction parameter (k) climbs. This is due to the physical phenomena in which a rise in k causes a denser fluid, resulting in a declined concentration pattern.

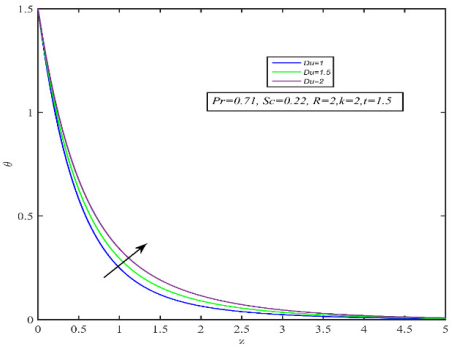

Figure 4. Temperature pattern versus distinct Du

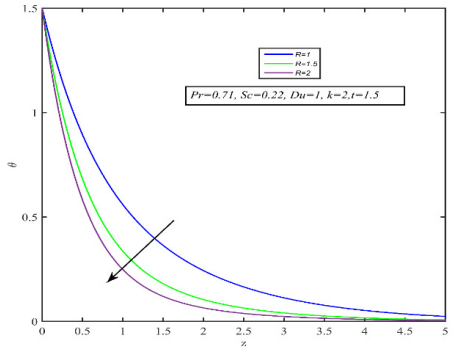

Figure 5. Temperature pattern versus distinct R

Figures 4-6 depict the temperature patterns as the Dufour number (Du), radiation parameter (R) and dimensionless time (t) are varied while the other parameters remain constant. As apparent in Figure 4, raising Du causes a boost in temperature (θ). This is due to the increased heat flux caused by the concentration gradient, which results in increased thermal stimulation in the fluid. Figure 5 shows the effect of the radiation parameter (R) on the temperature profile, indicating a considerable fall in fluid temperature as the radiation parameter increases. This discovery is related to

radiation's inhibitory effect on energy transfer to the fluid, resulting in lower temperatures. Figure 6 depicts the progressive rise in fluid temperature as dimensionless time (t) advances. Figures 7–8 showcase how the magnetic parameter (M) affects the primary velocity profile (u) and secondary velocity profile (v).

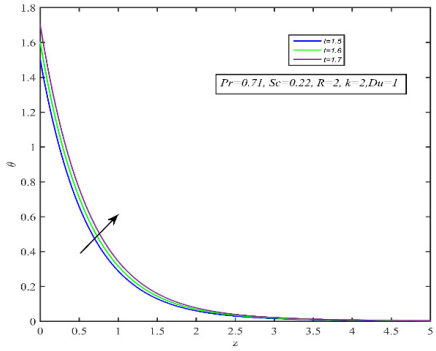

Figure 6. Temperature pattern versus distinct t

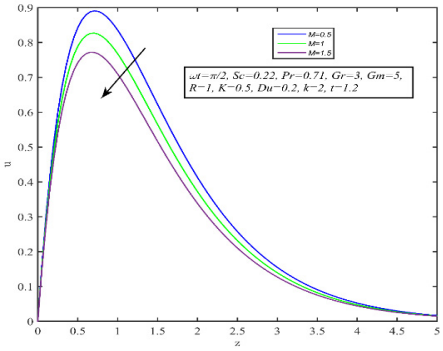

Figure 7. Primary velocity pattern (u) versus distinct M

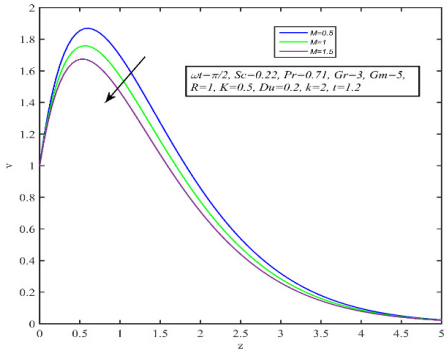

Figure 8. Secondary velocity pattern (v) versus distinct M

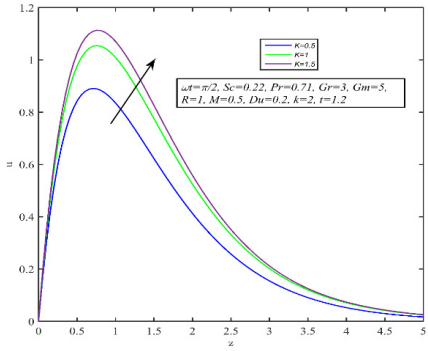

Figure 9. Primary velocity pattern (u) versus distinct K

A rise in the magnetic parameter (M) is accompanied by a decline in the velocity components u and v in both visualizations. The interaction of the magnetic field and the magnetic parameter (M) produces the Lorentz force, a magnetic body force that obstructs the velocity field. As a result, the fluid's mobility is restricted and slowed. Figures 9 and 10 show how the fluid velocity components u and v change as the permeability parameter (K) changes.

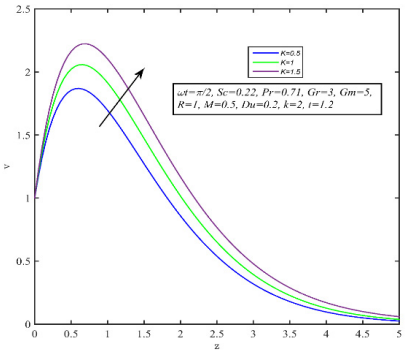

Figure 10. Secondary velocity pattern (v) versus distinct K

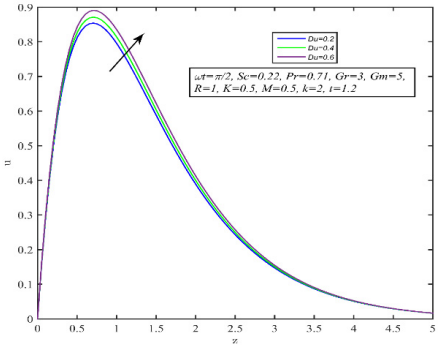

Figure 11. Primary velocity pattern (u) versus distinct Du

These graphs show that an increase in the permeability parameter (K) corresponds to an increase in the velocity components u and v. Significantly, as the permeability parameter (K) upsurges, the resistance of the flow medium reduces, resulting in quicker fluid motion in accordance with physics principles.

The relation between the velocity components u and v and the Dufour number (Du) is demonstrated in Figure 11-12. Both velocity components hike as the Dufour number (Du) grows. This discovery suggests that the fluid's velocity is accelerated as a result of the combined action of the diffusion-thermo effect and thermal buoyancy force. Physically, these factors contribute to the rise in velocity of the fluid observed in the data.

Figures 13-16 demonstrate the impact of thermal Grashof number (Gr) and solutal Grashof number (Gm) on primary and secondary velocity patterns. These graphs, spanning from 13 to 16, indicate that enhancing the thermal and solutal Grashof numbers coincides with a considerable rise in the velocity components u and v. The elevated values of Gr and Gm indicate a strengthened presence of thermal and solutal buoyancy forces near the plate, resulting in a notable acceleration of fluid motion. These empirical findings support the notion that changes in Gr and Gm have a direct effect on the fluid dynamics in the experimental setup.

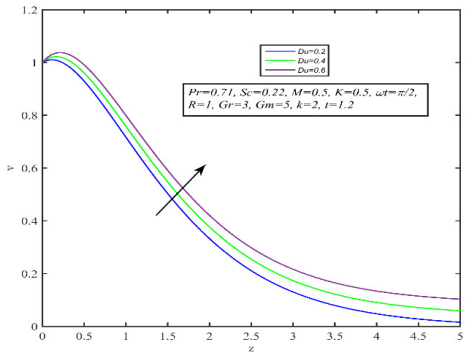

Figure 12. Secondary velocity pattern (v) versus distinct Du

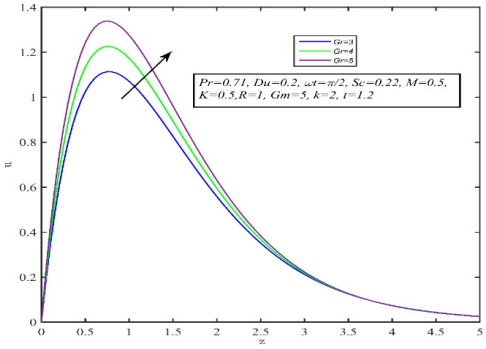

Figure 13. Primary velocity pattern (u) versus distinct Gr

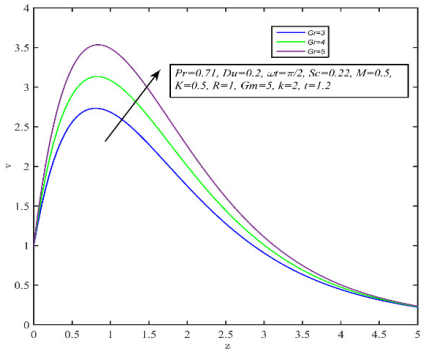

Figure 14. Secondary velocity pattern (v) versus distinct Gr

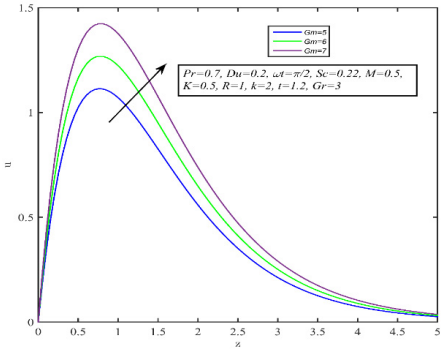

Figure 15. Primary velocity pattern (u) versus distinct Gm

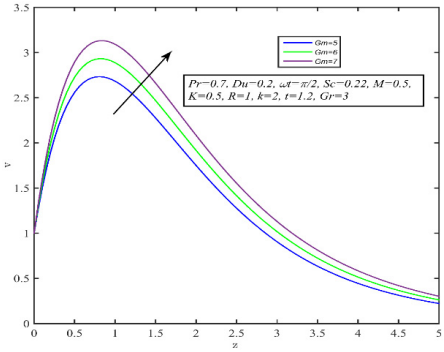

Figure 16. Secondary velocity pattern (v) versus distinct Gm

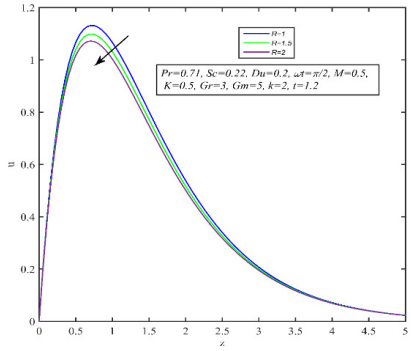

Figure 17. Primary velocity pattern (u) versus distinct R

Figures 17–18 demonstrate the influence of radiation parameter R on the velocity components u and v. Specifically, an increment in the parameter R corresponds to a decrease in the primary velocity component u, whereas it leads to a hike in the secondary velocity component v. Analysis of Figure 19 reveals that an elevation in the oscillation frequency (ωt) is associated with a reduction in the primary fluid velocity u. In contrast, Figure 20 depicts contrasting results, indicating an augmentation in the secondary fluid velocity under the same conditions. These experimental findings provide valuable insights into the impact of radiation parameter R and oscillation frequency (ωt) upon the current flow problem, contributing to a comprehensive understanding of the observed phenomena.

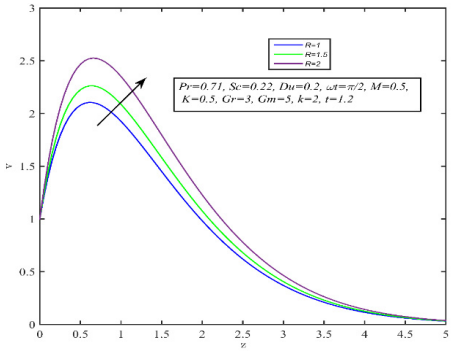

Figure 18. Secondary velocity pattern (v) versus distinct R

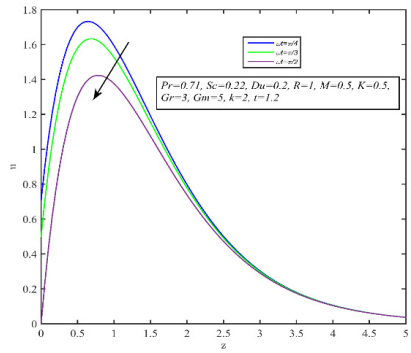

Figure 19. Primary velocity pattern (u) versus distinct ωt

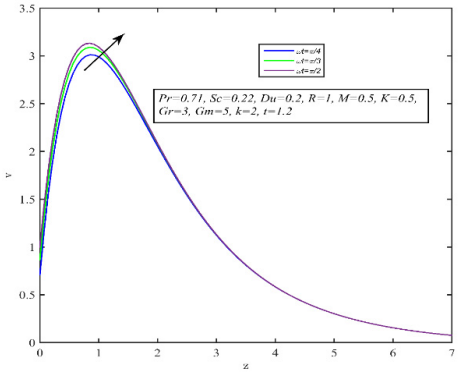

Figure 20. Secondary velocity pattern (v) versus distinct ωt

The Figures 21–24 depict the relationship between skin friction (τ) and the non-dimensional parameters Du, Gr, Gm, and R. Figures 21–23 show that elevating the Dufour number (Du), solutal Grashof number (Gr), and thermal Grashof number (Gm) enhances skin friction. Figure 24, on the other hand, shows that as the radiation parameter (R) grows, skin friction diminishes. These findings demonstrate that these non-dimensional parameters have a major impact on the skin friction phenomena, providing useful insights into the fluid flow behaviour in the investigated system.

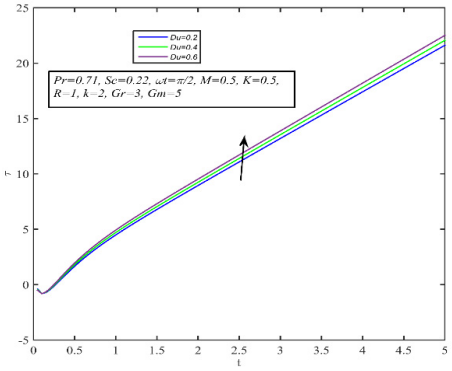

Figure 21. Skin friction (τ) vs distinct Du

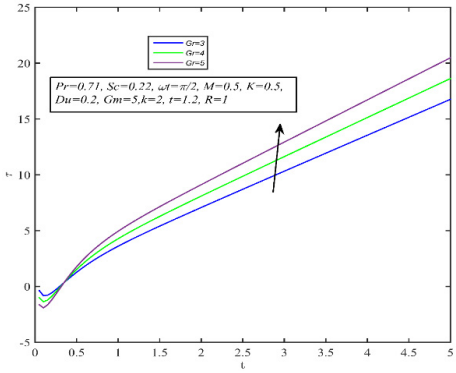

Figure 22. Skin friction (τ) vs distinct Gr

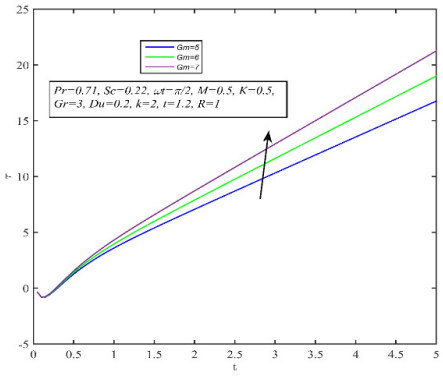

Figure 23. Skin friction (τ) vs distinct Gm

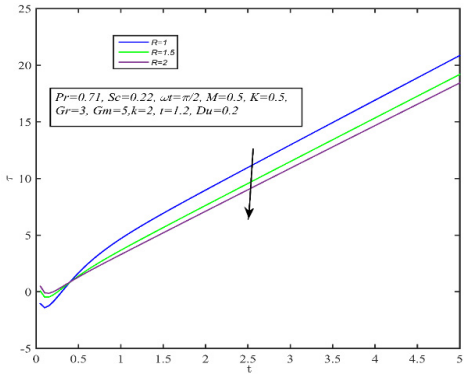

Figure 24. Skin friction (τ) vs distinct R

Surface charts are an effective visualization method for depicting the relationship between a dependent variable and two independent variables in 3D-format, allowing for a more comprehensive understanding of the data rather than individual data points. Figures 25–29 show surface plots of the Nusselt number (Nu) and Sherwood number (Sh) for various flow parameters. The Nusselt and Sherwood numbers are plotted along the z-axis, while the non-dimensional parameters Du, Pr, R, Sc, and k are plotted along the y-axis.

Figure 25 reveals that boosting the Dufour number (Du) and non-dimensional time (t) diminishes the heat transfer rate (Nu). Figure 26, on the other hand, exhibits the effect of the Prandtl number (Pr) on the Nusselt number. The heat transmission rate (Nu) declines as the Prandtl number and duration (t) rise.

Figure 27 illustrates that the rate of heat transfer (Nu) improves as the radiation parameter R and non-dimensional time (t) increase. Furthermore, both surface plots in Figures 28-29 show a significant corelation between the Sherwood number, the Schmidt number (Sc), and the chemical reaction parameter (k). As the Schmidt number and the chemical reaction parameter grow, so does the Sherwood number, which represents the mass transfer rate.

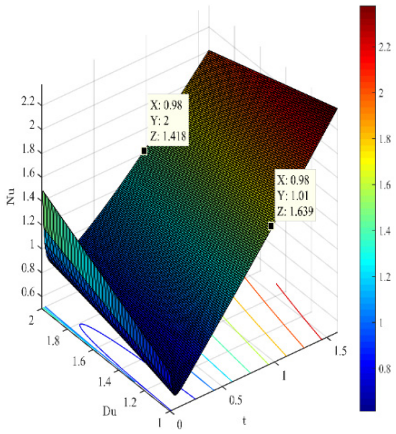

Figure 25. Nu versus Du and t

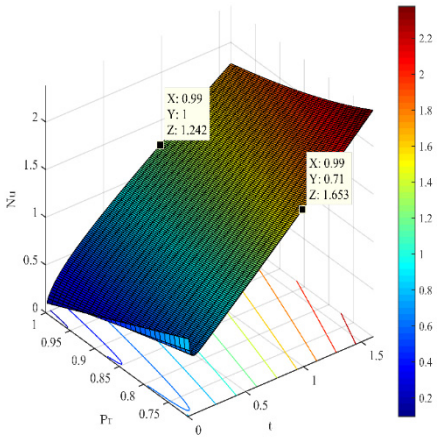

Figure 26. Nu versus Pr and t

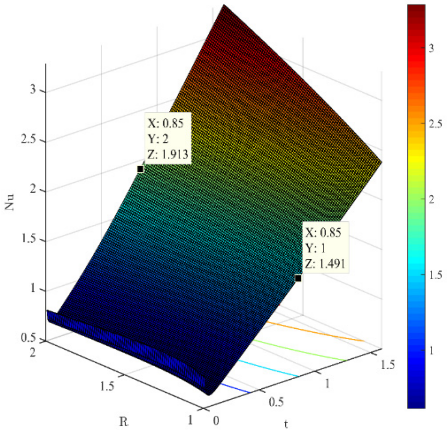

Figure 27. Nu versus R and t

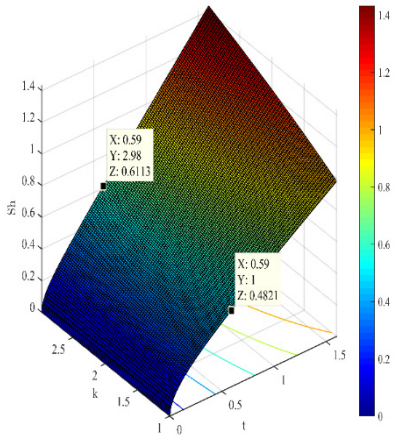

Figure 28. Sh versus Sc and t

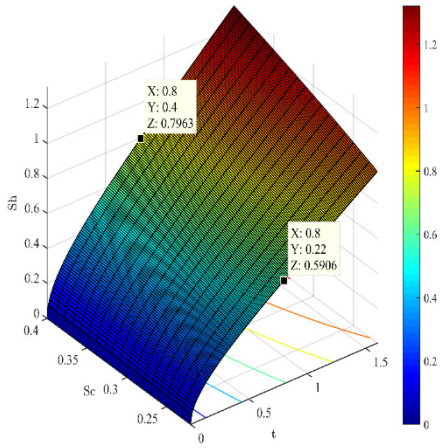

Figure 29. Sh versus k and t

5. CONCLUSIONS

This study examines the impact of diffusion-thermo on the flow characteristics of MHD free convection through a porous medium past an infinitely oscillating vertical plate, taking into account thermal radiation and chemical reaction. The investigation considers a viscous, incompressible fluid with optical properties as an optically thin grey gas, exhibiting both absorbs and emits radiation. The study yields the following key findings:

- With the increase of Dufour number, the momentum boundary layer becomes thicker significantly. As a result, it accelerates the flow.
- Higher mass diffusivity hikes the concentration field and a faster chemical reaction consumes chemical substances present in the fluid rapidly and as a result fluid concentration decline.
- The primary fluid velocity declines with rising radiation parameter R, while the secondary velocity profile shows the opposite trend, with an overall augmentation.

- An elevated radiation parameter R leads to a diminish in temperature patterns, while fluid temperature rises with higher Dufour number (Du) values. A hike in the Dufour number indicates a comprehensive rise in concentration gradient over temperature gradient. Hence increment of concentration gradient hikes the fluid temperature.
- Increased contributions of the Dufour number (Du), solutal Grashof number (Gr) and thermal Grashof number (Gm) result in increased skin friction. However, the radiation parameter R has a contrary effect, causing a decline in skin friction.
- The rates of heat transfer (Nu) decrease due to the effects of Dufour number (Du) and Prandtl number (Pr). Conversely, rates of heat transfer (Nu) accelerate when radiation parameter R hikes.
- The rate of mass transfer (Sh) increases with higher values of the chemical reaction parameter (k) and Schmidt number (Sc), respectively.

Nomenclature

Du	Dufour number	Gr	thermal Grashof number
D_M	molecular diffusivity	T'	fluid temperature
k	chemical reaction parameter	Gm	solutal Grashof number
$\vec{J}$	current density vector	v'	secondary fluid velocity in y' direction
C'_∞	concentration in the free stream	U_o	characteristic plate velocity
C_p	specific heat at constant pressure	u'	primary fluid velocity in x' direction
C'_w	concentration at the wall		**Greek Symbols**
T'_w	temperature at the wall	ν	kinematic viscosity
C_s	concentration susceptibility	σ	Stefan-Boltzman constant
T'_∞	temperature at the free stream	β'	coefficient of volumetric expansion
M	magnetic parameter	$\bar{\beta}$	coefficient of solutal expansion
q'_r	radiating heat flux	κ	thermal conductivity
C'	species concentration	ρ	fluid density
K'	permeability of porous medium		**Subscript**
Sc	Schmidt number	w	wall conditions
a'	absorption co-efficient of the medium	∞	free stream conditions

Appendix

$$h(\xi,z,t)=\frac{1}{2}\left[e^{\sqrt{\xi}z}\,erfc\left(\frac{z}{2\sqrt{t}}+\sqrt{\xi t}\right)+e^{-\sqrt{\xi}z}\,erfc\left(\frac{z}{2\sqrt{t}}-\sqrt{\xi t}\right)\right]$$

$$\psi(\beta,R\beta,z,t)=\frac{1}{2}\left[e^{\beta\sqrt{R}z}\,erfc\left(\frac{z}{2}\sqrt{\frac{\beta}{t}}+\sqrt{R\beta t}\right)+e^{-\beta\sqrt{R}z}\,erfc\left(\frac{z}{2}\sqrt{\frac{\beta}{t}}-\sqrt{R\beta t}\right)\right]$$

$$f(\beta,R\beta,z,t)=\left(\frac{t}{2}+\frac{z}{4}\sqrt{\frac{1}{R}}\right)e^{\beta\sqrt{R}z}\,erfc\left(\frac{z}{2}\sqrt{\frac{\beta}{t}}+\sqrt{R\beta t}\right)+\left(\frac{t}{2}+\frac{z}{4}\sqrt{\frac{1}{R}}\right)e^{-\beta\sqrt{R}z}\,erfc\left(\frac{z}{2}\sqrt{\frac{\beta}{t}}-\sqrt{R\beta t}\right)$$

$$F(\xi,z,t)=\frac{1}{2}\left[\left(t+\frac{1}{2}\sqrt{\frac{z}{\xi}}\right)e^{\sqrt{\xi}z}\,erfc\left(\frac{z}{2\sqrt{t}}+\sqrt{\xi t}\right)+\left(t-\frac{1}{2}\sqrt{\frac{z}{\xi}}\right)e^{-\sqrt{\xi}z}\,erfc\left(\frac{z}{2\sqrt{t}}-\sqrt{\xi t}\right)\right]$$

$$\hbar(\xi,t)=-\left[\frac{1}{\sqrt{\pi t}}e^{-\xi t}+\sqrt{\xi}\,erf\left(\sqrt{\xi t}\right)\right]$$

$$\hbar(\xi+i\omega,t)=-\left[\frac{1}{\sqrt{\pi t}}e^{-(\xi+i\omega)t}+\sqrt{(\xi+i\omega)t}\,erf\left(\sqrt{(\xi+i\omega)t}\right)\right]$$

$$\Omega(\beta,R\beta,t)=-\left[\sqrt{\frac{\beta}{\pi t}}\,e^{-\alpha t}+\beta\sqrt{R}\,erf\left(\sqrt{R\beta t}\right)\right]$$

$$\varphi(\beta,R\beta,t)=-\left[\sqrt{\frac{1}{4R}}\,erf\left(\sqrt{R\beta t}\right)+t\,\beta\sqrt{R}\,erf\left(\sqrt{R\beta t}\right)+\sqrt{\frac{t\beta}{\pi}}e^{-R\beta t}\right]$$

$$\Gamma(\xi,t)=-\left[\left(\frac{1}{2\sqrt{\xi}}+\sqrt{\xi}\,t\right)erf(\sqrt{\xi t})-\sqrt{\frac{t}{\pi}}\,e^{-\xi t}\right]$$

Conflict of Interest

The authors have no conflict of interest.

ORCID

Dibya Jyoti Saikia, https://orcid.org/0000-0001-6067-5390; **Nazibuddin Ahmed,** https://orcid.org/0000-0002-0924-4402
Richa Deb Dowerah, https://orcid.org/0009-0008-1220-8526; **Ardhendu Kumar Nandi,** https://orcid.org/0000-0002-4091-7994
Rajdeep Bordoloi, https://orcid.org/0000-0001-8508-8328

REFERENCES

[1] B. Alazmi, and K. Vafai, "Analysis of variable porosity, thermal dispersion, and local thermal nonequilibrium on free surface flows through porous media," J. Heat Transfer, **126**(3), 389-399 (2004). https://doi.org/10.1115/1.1723470
[2] M. Lahonian, S. Aminian, and M.S. Rahimi, "Study of MHD Mixed Convection of Different Nanofluids Due to the Inner Rotating Cylinder Saturated with Porous Media," Journal of The Institution of Engineers (India): Series C, **104**(1), 169-181 (2023). https://doi.org/10.1007/s40032-022-00903-y
[3] A. Haritha, B. Vishali, and C. Venkata Lakshmi, "Heat and mass transfer of MHD Jeffrey nanofluid flow through a porous media past an inclined plate with chemical reaction, radiation, and Soret effects," Heat Transfer, **52**(2), 1178-1197 (2023). https://doi.org/10.1002/htj.22735
[4] S. Jauhri, and U. Mishra, "Numerical investigation of MHD nanofluid considering second-order velocity slip effect over a stretching sheet in porous mediam," Journal of Integrated Science and Technology, **11**(2), 478-478 (2023). https://pubs.thesciencein.org/journal/index.php/jist/article/view/478
[5] M.V. Krishna, M.G. Reddy, and A.J. Chamkha, "Heat and mass transfer on unsteady MHD flow through an infinite oscillating vertical porous surface," Journal of Porous Media, **24**(1), 81-100 (2021). https://doi.org/10.1615/JPorMedia.2020025021
[6] S. Matta, G.R. Malga, B.S. Goud, L. Appidi, and P.P. Kumar, "Effects of viscous dissipation on MHD free convection flow past a semi-infinite moving vertical porous plate with heat sink and chemical reaction," Materials Today: Proceedings, **92**(Part 2), 1629-1636 (2023). https://doi.org/10.1016/j.matpr.2023.06.108
[7] N.H. Hamad, "Unsteady MHD natural convection flow past an infinite vertical porous plate with radiation absorption effects," Heat Transfer, **52**(2), 1345-1364 (2023). https://doi.org/10.1002/htj.22743
[8] J.K. Singh, G.S. Seth, and P. Rohidas, "Impacts of time varying wall temperature and concentration on MHD free convective flow of a rotating fluid due to moving free-stream with hall and ion-slip currents," International Journal of Thermofluid Science and Technology, **6**(3), 19060301 (2019). https://doi.org/10.36963/IJTST.19060301
[9] H.A. Nabwey, A.M. Rashad, P.B.A. Reddy, S. Jakeer, M.A. Mansour, and T. Salah, "Radiative effects on unsteady MHD natural convection flow in an inclined wavy porous cavity using hybrid nanofluid containing a square obstacle," Alexandria Engineering Journal, **65**, 921-937 (2023). https://doi.org/10.1016/j.aej.2022.10.004
[10] T. Saha, T. Islam, S. Yeasmin, and N. Parveen, "Thermal influence of heated fin on MHD natural convection flow of nanofluids inside a wavy square cavity," International Journal of Thermofluids, **18**, 100338 (2023). https://doi.org/10.1016/j.ijft.2023.100338
[11] D.J. Saikia, N. Ahmed, and R. Bordoloi, "Natural Convective MHD Mass Transfer Flow Past an Infinite Vertical Porous Plate Embedded in a Porous Medium with Thermal Diffusion and Chemical Reaction," Special Topics & Reviews in Porous Media: An International Journal, **14**(2), 63-75 (2023). https://doi.org/10.1615/SpecialTopicsRevPorousMedia.2023045885
[12] B.S. Goud, Reddy, Y.D. Reddy, and K.K. Asogwa, "Chemical reaction, Soret and Dufour impacts on magnetohydrodynamic heat transfer Casson fluid over an exponentially permeable stretching surface with slip effects," International Journal of Modern Physics B, **37**(13), 2350124 (2023). https://doi.org/10.1142/S0217979223501242
[13] P.R. Sekhar, S. Sreedhar, S.M. Ibrahim, and P.V. Kumar, "Radiative Heat Source Fluid Flow of MHD Casson Nanofluid over A Non-Linear Inclined Surface with Soret and Dufour Effects," CFD Letters, **15**(7), 42-60 (2023). https://doi.org/10.37934/cfdl.15.7.4260
[14] A.R. Deepika, K. Govardhan, A. Rana, and M. Reza, "Soret and Dufour effects on MHD mixed convection flow of Casson hybrid nanofluid over a permeable stretching sheet," International Journal of Ambient Energy, **44**(1), 2115-2127 (2023). https://doi.org/10.1080/01430750.2023.2224337
[15] K. Choudhuri, N. Ahmed, and P.J. Parashar, "Soret and Dufour Effects in A Three-Dimensional Mhd Flow Past a Semi-Infinite Uniformly Moving Vertical Plate with Constant Heat Flux: Soret and Dufour effects in a three-dimensional MHD flow," Latin American Applied Research-An international journal, **53**(3), 263-270 (2023). https://doi.org/10.52292/j.laar.2023.1000
[16] Y.D. Reddy, and B.S. Goud, "Comprehensive analysis of thermal radiation impact on an unsteady MHD nanofluid flow across an infinite vertical flat plate with ramped temperature with heat consumption," Results in Engineering, **17**, 100796 (2023). https://doi.org/10.1016/j.rineng.2022.100796
[17] S.G. Bejawada, and M.M. Nandeppanavar, "Effect of thermal radiation on magnetohydrodynamics heat transfer micropolar fluid flow over a vertical moving porous plate," Experimental and Computational Multiphase Flow, **5**(2), 149-158 (2023). https://doi.org/10.1007/s42757-021-0131-5
[18] E.A. Algehyne, S.A. Lone, Z. Raizah, S.M. Eldin, A. Saeed, and A.M. Galal, "Analysis of the electrically conducting magnetohydrodynamic hybrid nanofluid flow past a convectively heated stretching surface with suction/injection and non-linear thermal radiation," Frontiers in Materials, **10**, 1132124 (2023). https://doi.org/10.3389/fmats.2023.1132124
[19] C.M. Koli, and S.N. Salunkhe, "Thermal Radiation and Magnetic Fields Effects on Nanofluids flowing through Stretch Sheet," Journal of Computational Applied Mechanics, **54**(1), 111-126 (2023). https://doi.org/10.22059/jcamech.2023.353492.791
[20] N. Vijay, and K. Sharma, "Entropy generation analysis in MHD hybrid nanofluid flow: Effect of thermal radiation and chemical reaction," Numerical Heat Transfer, Part B: Fundamentals, **84**(1), 66-82 (2023). https://doi.org/10.1080/10407790.2023.2186989
[21] D. Iranian, and S. Karthik, "Heat generation effects on Magnetohydrodynamic Powell-Eyring fluid flow along a vertical surface with a Chemical reaction," Forces in Mechanics, **12**, 100212 (2023). https://doi.org/10.1016/j.finmec.2023.100212
[22] N.F.M. Omar, H.I. Osman, A.Q. Mohamad, R. Jusoh, and Z. Ismail, "Analytical Solution of Unsteady MHD Casson Fluid with Thermal Radiation and Chemical Reaction in Porous Medium," Journal of Advanced Research in Applied Sciences and Engineering Technology, **29**(2), 185-194 (2023). https://doi.org/10.37934/araset.29.2.185194

[23] B.P. Reddy, M.H. Simba, and A. Hugo, "Effects of Thermodiffusion and Chemical Reaction on Magnetohydrodynamic-Radiated Unsteady Flow Past an Exponentially Accelerated Inclined Permeable Plate Embedded in a Porous Medium," International Journal of Chemical Engineering, **2023**, 9342174 (2023). https://doi.org/10.1155/2023/9342174

[24] L. Appidi, P.P. Kumar, S. Matta, and B.S. Malga, "Effects of chemical reaction and thermal radiation on MHD free convective flow of micro polar fluid past an infinite moving vertical porous plate with viscous dissipation," Heat Transfer, **52**(3), 2922-2939 (2023). https://doi.org/10.1002/htj.22811

ТОЧНИЙ АНАЛІЗ ДИФУЗІЙНО-ТЕРМОЕФЕКТУ НА МГД ПРИРОДНИЙ КОНВЕКТИВНИЙ ПОТОК ПОВЗ КОЛИВАЛЬНУ ВЕРТИКАЛЬНУ ПЛАСТИНИ З ХІМІЧНОЮ РЕАКЦІЄЮ ТА ТЕПЛОВИМ ВИПРОМІНЮВАННЯМ У ПОРИСТОМУ СЕРЕДОВИЩІ

Діб'я Джіоті Сайкія[a], Назібуддін Ахмед[b], Річа Деб Доверах[c], Ардхенду Кумар Нанді[a], Раджділ Бордолой[d], Харун Аль Рашид[e]

[a]Департамент математики, Басугаон коледж, Басугаон, BTR, Чіранг, 783372, India
[b]Департамент математики Університет Коттон, Гувахаті, 781001, Індія
[c]Департамент математики, Університет Гаухаті, Гувахаті, Ассам, 781014, Індія
[d]Департамент математики, Сібсагарський університет, Сібсагар, Ассам, 785640, Індія
[e]Департамент математики, Біласіпара коледж, Біласіпара, 783348, Індія

Основна мета цього дослідження полягає в дослідженні впливу дифузії-термо на характеристики потоку МГД природної конвекції через проникне середовище повз безкінечно осцилюючу вертикальну пластину, враховуючи хімічну реакцію та ефекти теплового випромінювання. Підхід перетворення Лапласа використовується для вирішення керівних рівнянь для рівняння безперервності видів, енергії та імпульсу. Результати моделювання показують, що теплове випромінювання збільшує первинну швидкість рідини, одночасно зменшуючи вторинну швидкість рідини. Крім того, збільшення числа Дюфура (Du) призводить до більш високих температурних полів, а також до збільшення первинної та вторинної швидкостей рідини. Також дифузійно-термальний ефект сприяє поліпшенню температурного поля. Отримано рівняння шкірного тертя, яке показано графічно. Для демонстрації чисел Нуссельта та Шервуда використовуються тривимірні графіки поверхні. Крім того, графічні зображення використовуються для зображення впливу безрозмірних факторів на концентрацію, температуру та моделі швидкості.

Ключові слова: *вільна конвекція; пористе середовище; дифузійно-термальний; хімічна реакція; теплове випромінювання*

East European Journal of Physics. **2.** 383-397 (2025)
DOI:10.26565/2312-4334-2025-2-47 ISSN 2312-4334

IMPACT OF JOULE HEATING AND HYDRO-MAGNETIC EFFECTS ON MIXED CONVECTION IN POROUS CAVITY USING LATTICE BOLTZMANN METHOD

C. Venkata Lakshmi[a], Anuradha Aravapalli[a], K. Venkatadri[b]*, O. Anwar Bég[c], V. Ramachandra Prasad[d]

[a]*Department of Applied Mathematics, Sri Padmavati Mahila Visvavidyalayam, Tirupati, Andhra Pradesh - 517502, India*
[b]*Department of Mathematics, Mohan Babu University (Erstwhile Sree Vidyanikethan Eng. Coll.), Tirupati Andhra Pradesh-517 102, India*
[c]*Multi-Physical Engineering Sciences Group, Aeronautical/Mechanical Engineering, Salford University, Corrosion Lab, 3-08, SEE Building, Manchester, M54WT, UK*
[d]*Department of Mathematics, School of Advanced Sciences, Vellore Institute of Technology, Vellore, Tamil Nadu 632014, India*
**Corresponding Author e-mail: venkatadri.venki@gmail.com*
Received March 1, 2025; revised May 11, 2025; accepted May 15, 2025

In the current paper, a comprehensive examination is carried out to investigate heat transmission under the influence of several factors that include magnetic field, moving lid, porous medium, and joule heating within a lid-driven cavity (LDC). The cavity features a moving lid, vertical walls with thermally insulated boundaries, and horizontal walls kept at uniform temperatures T_h (bottom) and T_c (top). The objective of the study is to analyze mixed convective heat transfer behavior of the system using contour plots to visualize the flow and thermal pattern under the various considered parameters: Richardson numbers ($0.01 \leq Ri \leq 10$), and Joule heating parameters ($0 \leq J \leq 10^{-5}$), Hartmann numbers ($0 \leq Ha \leq 30$), and Darcy numbers ($0.001 \leq Da \leq 0.1$). The lattice Boltzmann method (LBM) is applied to employ the governing transport equations. The Joule heating effects are critical in systems where internal heat generation must be controlled, such as in electrical systems or battery cooling, where resistive heating may either aid or hinder the desired thermal dynamics.
Keywords: *Lattice Boltzmann method (LBM); Lid-driven Cavity; Magnetohydrodynamics; Mixed convection; Joule heating; Porous medium*
PACS: 44.05.+e, 47.11.-j, 41.20.−q, 47.15.Rq, 47.65.-d, 47.55.pb, 44.30.+v

1. INTRODUCTION

Convective heat transfer has been the focus of extensive research by scientists and engineers seeking fluids with enhanced thermophysical properties. Recent studies have concentrated on innovative techniques to improve heat transfer systems, with the development of nanofluids emerging as a pivotal strategy. Nanofluids are fluids that contain suspended nanoparticles smaller than 100 nanometres, which contribute to several advantageous characteristics, such as increased thermal conductivity and stability, as well as improved heat transfer capabilities compared to traditional fluids. Addressing the issue of overheating during operation is crucial, as it can significantly shorten the lifespan of modern electronic devices and, in extreme cases, lead to system failures. Therefore, implementing effective heat transfer solutions to efficiently dissipate excess heat from these devices is vital. Nanofluids show great promise as coolants and Fluids used for heat transfer in various electronic applications, featuring computer chips, LED lights, and solar cells, ultimately enhancing their performance and reliability.

One of the significant areas of study has been the influence of magnetic fields on mixed convection in enclosures. Turabi and Munir [1] conducted CFD simulations to inspect the effects of magnetohydrodynamics (MHD) on combined convection of thermal flow in a LDC equipped with cylinder using Casson fluid. As a result of their study the application of a field of magnetism suppresses convective currents due to the Lorentz forces reduce the rate of motion due to their generation in heat transfer efficiency. Similarly, as a result of Oztop and Dagtekin's [2] study, mixed convection occurred in an enclosure driven by both sides of the cavity under differential heating and found that Richardson and Hartmann numbers play crucial roles in controlling the fluid flow structure and thermal distribution. In a more advanced study, the study was reported by Parveen et al. [3] investigated magnetohydrodynamic (MHD) mixed thermal flow within an oblique wavy enclosure packed with ferrofluid under lid-driven conditions, incorporating heat generation and absorption effects. Their findings indicated that wavy geometries enhance thermal mixing, but stronger magnetic fields dampen convective currents, leading to a decline in heat transfer. Further insights into the impact of strong magnetic fields were provided by Zikanov et al. [4], who examined mixed convection in duct and pipe flows, highlighting turbulence suppression and reduced convective heat transfer under intense MHD conditions.

The effect of nanofluids in mixed convection systems has also been extensively studied to leverage their superior thermal conductivity properties. Devi et al. [5] conducted an insightful exploration of thermal flow behavior within an enclosure. Their study examines the influence of applied magnetic field and the presence of a heated square blockage, contributing valuable knowledge to the field. Their numerical simulations revealed that the buoyancy ratio and nanoparticle volume fraction significantly affect the heat and mass transfer characteristics. Mondal et al. [6] explored

Cite as: C.V. Lakshmi, A. Aravapalli, K. Venkatadri, O.A. Bég, V.R. Prasad, East Eur. J. Phys. 2, 383 (2025), https://doi.org/10.26565/2312-4334-2025-2-47

similar phenomena in a trapezoidal enclosure and emphasized the role of heat generation and absorption in modulating temperature gradients. In another study, Parveen and Mahapatra [7] examined entropy generation in a nanofluid-filled curved chamber, demonstrating that increasing the magnetic field strength suppresses convective currents, resulting in higher thermal irreversibility. Yu et al. [8] extended this research by incorporating Buongiorno's nanofluid model to analyze the effects of Brownian motion and thermophoresis on heat transfer in an inclined lid-driven cavity, concluding that these mechanisms enhance thermal conductivity but alter velocity profiles in complex ways. Mahmood and Khan [9] further contributed by assessing the Darcy-Forchheimer effect in mixed convection of nanofluids, showing that nanoparticle aggregation leads to significant changes in flow stability and heat transfer performance.

Geometrical modifications and internal obstructions in LDC's have been another focus area. Munshi et al. [10] analyzed mixed convection within square cavity containing elliptic heated blocks with corner heaters, observing that heat sources at the corners create asymmetric flow patterns that influence convective heat transport. Similarly, Sivasankaran et al. [11] studied forced convection in an oblique LDC with partially heated elements, reporting that inclination angles significantly impact fluid circulation and overall heat dissipation rates. Khanafer and Chamkha [12] inspected combined convection in a porous LDC, concluding that permeability parameters, such as the Darcy number, govern the dominance of either conduction or convection-driven heat transfer. Additionally, Munshi et al. [13] focused on Mixed convection within a square enclosure containing a porous medium and featuring pairs of heat sources and sinks, demonstrating that the arrangement of heat sources strongly affects temperature distribution and vortex formation within the cavity.

Several recent studies have focused on advancing numerical methodologies to Make the computations more accurate and efficient of mixed convection simulations. Nawaz et al. [14] explore an analysis of Williamson non-Newtonian nanofluid flow over oscillatory sheets using a two-stage multi-step numerical technique, achieving improved convergence and stability. Qaiser et al. [15] performed a numerical assessment of Walters-B nanofluid over a elongating sheet incorporating Newtonian heating and mass transfer, utilizing finite difference methods to obtain precise predictions of temperature and velocity fields. These advancements in numerical techniques play a crucial role in solving complex mixed convection problems, particularly in configurations involving nanofluids, MHD, and non-Newtonian fluids. The transient behavior of MHD convection has been significantly enhanced through the contributions of various researchers. Sheremet et al. [16] utilized finite element techniques to analyze time-dependent flows, highlighting the crucial role of computational precision in accurately capturing dynamic phenomena, particularly in the context of geothermal viscosity. Building on this, Alam et al. [17] effectively applied the Finite Element Method to investigate MHD natural convection, demonstrating the method's capability in managing complex geometries and heat sources on base walls. Geridonmez et al. [18] made valuable contributions by examining mixed thermal flow in a driven cavity influenced by a partial magnetic field, thus enriching the understanding of cavity flows in the presence of combined convection fields. Furthermore, Suchana et al. [19] explored the effects of Lorentz force and non-uniform thermal conditions on convection in trapezoidal enclosures, employing FEM to shed light on these interactions. Mohan et al. [20] analyzed double-diffusive convection in porous cavities under MHD effects using an FVM approach, further expanding the field's knowledge base. Additionally, Bakar et al. [21] and Moria [22] have investigated specific configurations, such as inclined magnetic fields and heat-generating blocks respectively, which contributed to a deeper understanding of unique cavity designs. Meanwhile, researchers like Wang et al. [23] and Nee [24] have adopted spectral methods and hybrid FDM-LBM techniques to improve computational accuracy in modeling MHD convection, demonstrating a collaborative effort to advance the field comprehensively.

The extensive research into MHD convection in porous cavities provides valuable insights into the complex interactions among magnetic fields, the properties of porous media, and boundary conditions that influence heat transfer. The application of advanced numerical techniques such as FEM, LBM, FVM, and hybrid approaches has significantly improved the accuracy and relevance of these studies. This progress offers a deeper understanding of transient, steady-state, and double-diffusive behaviours in various configurations. Nonetheless, there are promising opportunities for further exploration. In particular, more comprehensive studies that integrate Joule heating effects, hydro-magnetic mixed convection, and porous medium interactions under realistic boundary and operational conditions are needed. Investigating the effects of internal heat generation due to Joule heating, alongside the complex dynamics of buoyancy-driven convection, forced convection, and magnetic fields, presents a crucial area for future research. Moreover, while the Lattice Boltzmann Method has demonstrated its effectiveness across numerous studies, its application in simulating multi-physics scenarios remains underexplored. To bridge these gaps, the current study intends to utilize Thermal Lattice Boltzmann simulations to examine hydro-magnetic mixed convective transport phenomena in a square cavity filled with a porous medium and subjected to an inclined magnetic field. The configuration involves air-filled cavities that are with heat applied to the lower side and cooling on the upper side, with Joule heating effects incorporated. This research aims to enhance our understanding of the intricate interactions between magnetic and thermal forces, ultimately contributing to the optimization of thermal management systems.

Research Gaps and Motivation for The Current Study

Despite extensive research on MHD mixed convection in porous enclosures, several critical gaps remain in understanding the complex interactions between magnetic fields, porous media, lid-driven forces, and Joule heating effects:

- The combined effects of Joule heating, inclined magnetic fields, and lid-driven forces in a porous enclosure have not been fully explored.
- Existing studies (e.g., [4, 7, 15]) have investigated entropy generation and thermal transport in nanofluid-based MHD systems but overlooked Joule heating effects.
- Existing studies on nanofluid convection focus primarily on Brownian motion and thermophoresis, with limited investigations into electromagnetic heating effects.
- While some studies (e.g., [14]) have explored LBM for nanofluid convection, its application to MHD mixed convection with Joule heating and porous media interactions remains limited.
- While LBM has demonstrated effectiveness in modelling MHD flows, its potential for simulating Joule heating-driven mixed convection remains underutilized.

To address these gaps, the present study focuses on Thermal Lattice Boltzmann simulation of hydro-magnetic mixed convective transport phenomena in a square cavity filled with a porous medium, subjected to an inclined magnetic field. The bottom-heated and top-cooled configuration is chosen to mimic practical thermal management scenarios, while Joule heating effects are incorporated to analyze their impact on heat and fluid transport.

3. MATHEMATICAL FORMULATION

The computational model of the lid-driven square cavity, as illustrated in **Figure 1**, presents an intriguing study of fluid dynamics. This cavity, characterized by equal height and width (H), features a top boundary sustained at a fixed temperature (T_c) while moving to the right at a steady velocity (U_0). The bottom boundary is kept at a constant elevated temperature (T_h), while the vertical side boundaries are thermally insulated to maintain heat distribution within the system. To enhance the practicality of numerical simulations, several assumptions have been implemented. The fluid flow within the cavity is analyzed as a two-dimensional, laminar, and incompressible flow. Additionally, an inclined field of magnetism (B_0) is imposed across the cavity, complemented by a downward gravitational force (g). This model innovatively utilizes a lid-driven cavity with permeable characteristics, treating it as an isotropic and homogeneous porous medium. This medium is defined by constant permeability and porosity, allowing for uniform fluid passage through it. The thermal gradients present across the cavity walls result in density differentials that, along with the lid motion, facilitate the fluid movement within the cavity. The operational effectiveness of the permeable zone is governed by the principle of local thermal equilibrium, a critical condition for its functionality. Furthermore, under the Boussinesq approximation, the analysis intentionally excludes factors such as radiation, viscous dissipation and internal heat generation as a joule heating.

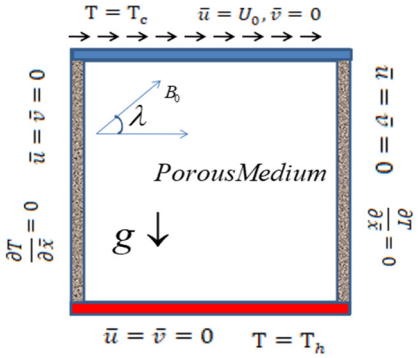

Figure 1. Physical model of the geometry

3. LATTICE BOLTZMANN METHOD

The Lattice Boltzmann Method (LBM) offers a highly versatile and efficient framework for simulating fluid dynamics and related phenomena. Its mesoscopic approach, coupled with computational efficiency and adaptability, positions it as a preferred option for a wide range of scientific and engineering applications. Among the various collision operators available in LBM, the BGK (Bhatnagar-Gross-Krook) model is particularly noteworthy for its simplicity and extensive use in the field. When applied to a D2Q9 lattice—a two-dimensional grid comprising nine discrete velocity directions—the BGK model serves as a solid foundation for fluid dynamics simulations in two dimensions. This method effectively balances computational efficiency with accuracy, making it a valuable tool for researchers and engineers engaged in two-dimensional fluid dynamics studies. The flow field and distribution function of the SRT (single relaxation time) model within the BGK LBM, especially when incorporating external forces, can be articulated as follows [25-27]: f and g, refers for the flow and temperature fields of distribution functions, respectively

$$f_i\left(x+c_i\Delta t,t+\Delta t\right)=f_i\left(x,t\right)-\frac{1}{\tau_f}\left(f_i\left(x,t\right)-f_i^{eq}\left(x,t\right)\right)+\Delta tF_i, \tag{1}$$

$$g_i\left(x+c_i\Delta t,t+\Delta t\right)=g_i\left(x,t\right)-\frac{1}{\tau_g}\left(g_i\left(x,t\right)-g_i^{eq}\left(x,t\right)\right)+S_i, \tag{2}$$

the local equilibrium particle distribution function for flow and temperature are calculated from Eqs. (3) and (4).

$$f_i^{eq} = w_i \rho \left[1 + \frac{3}{c^2}(c_i \bullet u) + \frac{9}{2c^4}(c_i \bullet u)^2 - \frac{3}{2c^2}(u \bullet u) \right], \tag{3}$$

$$g_i^{eq} = w_i T \left[1 + \frac{1}{c^2}(c_i \bullet u) \right]. \tag{4}$$

The D2Q9 model is utilized in this study for analyzing flow and temperature; The lattice weights are calculated as follows;

$$w_i = \begin{cases} \frac{4}{9}, i = 0 \\ \frac{1}{9}, i = 1,2,3,4 \\ \frac{1}{36}, i = 5,6,7,8 \end{cases} \tag{5}$$

The discrete velocities are obtained from the eq. (6).

$$c_{\mathbf{i}} = \begin{cases} 0 & i = 0 \\ \left(\cos\left[\frac{(i-1)\pi}{4} \right], \sin\left[\frac{(i-1)\pi}{4} \right] \right) & i = 1,2,3,4 \\ \sqrt{2}\left(\cos\left[\frac{(i-1)\pi}{4} \right], \sin\left[\frac{(i-1)\pi}{4} \right] \right) & i = 5,6,7,8 \end{cases} \tag{6}$$

Here $c = \frac{\Delta x}{\Delta t}$ is the lattice speed.

macroscopic pressure is determined for incompressible fluid flow by

$$P = \rho c_s^2, (c_s^2 = \frac{c^2}{3}) \tag{7}$$

The single relaxation times are given by

$$\upsilon = \left[\tau_f - \frac{1}{2} \right] {c_s}^2 \Delta t \text{ and } \alpha = \left[\tau_g - \frac{1}{2} \right] {c_s}^2 \Delta t \tag{8}$$

The external body force with LBM as

$$F_i = w_i . F . \frac{c_i}{c_s^2} \tag{9}$$

The value $c_s^2 = \frac{c^2}{3}$, Joule heating acts as an external source term:

$$S_i = w_i \sigma B_0^2 v^2 \ , \ F_i = w_i . F \tag{10}$$

$$F = Fx + Fy$$

$$Fx = -w_k 9 \rho \frac{\upsilon}{K} u + 3 w_k \rho A \left(v \sin\lambda \cos\lambda - u \sin^2\lambda \right), \tag{11}$$

$$Fy = -w_k 9 \rho \frac{\upsilon}{K} v + 3 w_k \rho \left(g\beta \left(T - T_c \right) + A \left(u \sin\lambda \cos\lambda - v \cos^2\lambda \right) \right)$$

Here $A = Ha^2 \frac{\nu}{M^2}$ and $K = DaM^2$

Finally, Macroscopic variables are expressed as:

$$\rho = \sum_i f_i \tag{12}$$

$$\rho u = \sum_i f_i \mathbf{c_i} \tag{13}$$

$$T = \sum_i g_i \tag{14}$$

3.1 Method of mixed convection

The Mach number is considered as 0.1for this simulation. Since, the Mach number for the incompressible flow is Ma < 0.3.

By taking the Mach number, Prandtl number, thermal Grashof number and the thermal diffusivity are employed from definition of:

$$\upsilon = \frac{1}{\sqrt{Gr}} MaMc\,. \tag{15}$$

The speed of the lattice is constant and it considered as $c = \frac{1}{\sqrt{3}}$.

The condition for the lid-driven speed is utilized the following:

$$U_0 = \frac{\mathrm{Re}\,\upsilon}{M}\,. \tag{16}$$

Table 1. The analysis of Grid independence for ψ_{min} and Nu_a at $Pr = 0.71, Re = 100$, $Ri = 1$, and $Ha = 0, J = 0$.

Grid size	$\lvert\psi_{\min}\rvert$	% Error	Nu_a	% Error
41×41	0.5992	----	3.1214	----
41×41	0.8430	0.4124	3.0030	0.03793
81×81	1.0580	0.2551	2.9342	0.02291
101×101	1.2491	0.1806	2.8910	0.01472
121×121	1.4196	0.1365	2.8636	0.00948

Table 2. Average Nusselt Number Comparison for a Mixed convection in a Lid-Driven Cavity at Gr = 100 and Pr = 0.71.

Re	Ri	Tiwari and Das [28]	Iwatsu et al. [29]	Present
100	0.01	2.10	1.94	2.09
400	0.00062	3.85	3.84	4.0808
1000	0.0001	6.33	6.33	6.5469

3.2. Boundary Conditions

Solid (or no slip) walls are considered bounce-back boundary conditions. At the top boundary, the particle distributions are considered as follows:

$$\begin{aligned}
\rho_N &= \frac{1}{1+v_N}\left(f_0 + f_2 + f_3 + 2\left(f_2 + f_6 + f_5\right)\right)\\
f_4 &= f_2 - \frac{2}{3}\rho_N v_N\\
f_7 &= f_5 + \frac{1}{2}\left(f_1 - f_3\right) - \frac{1}{6}\rho_N v_N - \frac{1}{2}\rho_N u_N\\
f_8 &= f_6 + \frac{1}{2}\left(f_1 - f_3\right) - \frac{1}{6}\rho_N v_N + \frac{1}{2}\rho_N u_N
\end{aligned} \tag{17}$$

u and v refer horizontal and vertical velocity on the north (top) boundary, respectively.

The adiabatic wall (East and West), bounce back boundary conditions are used. Temperature at bottom and top walls are known in the bottom wall, $T = T_h$. Since we are using D2Q9, the unknowns are computed as follows.

$$\begin{aligned}
g_2 &= \left(T_h - T_c\right)\left(w_2 + w_4\right) - g_4\\
g_5 &= \left(T_h - T_c\right)\left(w_5 + w_7\right) - g_7\\
g_6 &= \left(T_h - T_c\right)\left(w_6 + w_8\right) - g_8
\end{aligned} \tag{18}$$

In terms of the local Nusselt number and the average value on hot wall, they can be calculated as follows:

$$Nu = \frac{L}{\Delta T}\frac{\partial T}{\partial y} \tag{19}$$

$$Nu_a = \frac{1}{L}\int_0^L Nu\,dx \tag{20}$$

Finally, the stream function can be defined in a manner consistent with its standard definition, as outlined below:

$$u = \frac{\partial \psi}{\partial y}, v = -\frac{\partial \psi}{\partial x} \tag{21}$$

The value of the stream function (ψ) on all boundary walls is considered as zero.

3.3. Grid Independence and Validation of LBM

Table 2 presents the results of the grid independence test conducted across various grid sizes: 41×41, 61×61, 81×81, 101×101, and 121×121. The computational grids were systematically refined and optimized to achieve an accurate discretization of the governing equations within the examination domain. Upon analysis, no significant differences were observed between the grid sizes, particularly between the 101×101 and 121×121 configurations. As a result, the 101×101 grid size was chosen for the simulations. This decision aligns with the findings of Moallemi and Jang [30], underscoring the importance of conducting a grid independence test to ensure numerical stability and solution accuracy. By minimizing discretization errors, we can effectively capture critical flow and thermal characteristics in our simulations.

The Thermal LBM used in this study has been effectively validated through simulations of lid-driven mixed convection heat transfer at a Reynolds number Re=1000, Pr = 0.1, and Ri = 0.01. As illustrated in Figure 2, the streamline and isotherm patterns derived from the LBM simulation reveal a high degree of alignment with the findings of Moallemi and Jang [30]. This strong correlation highlights the accuracy of the flow structures and thermal distributions captured within LDC. Such validation not only supports the reliability of the numerical method used but also sets a solid foundation for further investigations into hydro-magnetic mixed convection in porous cavities, particularly under varying thermal conditions and influences including inclined magnetic fields and Joule heating.

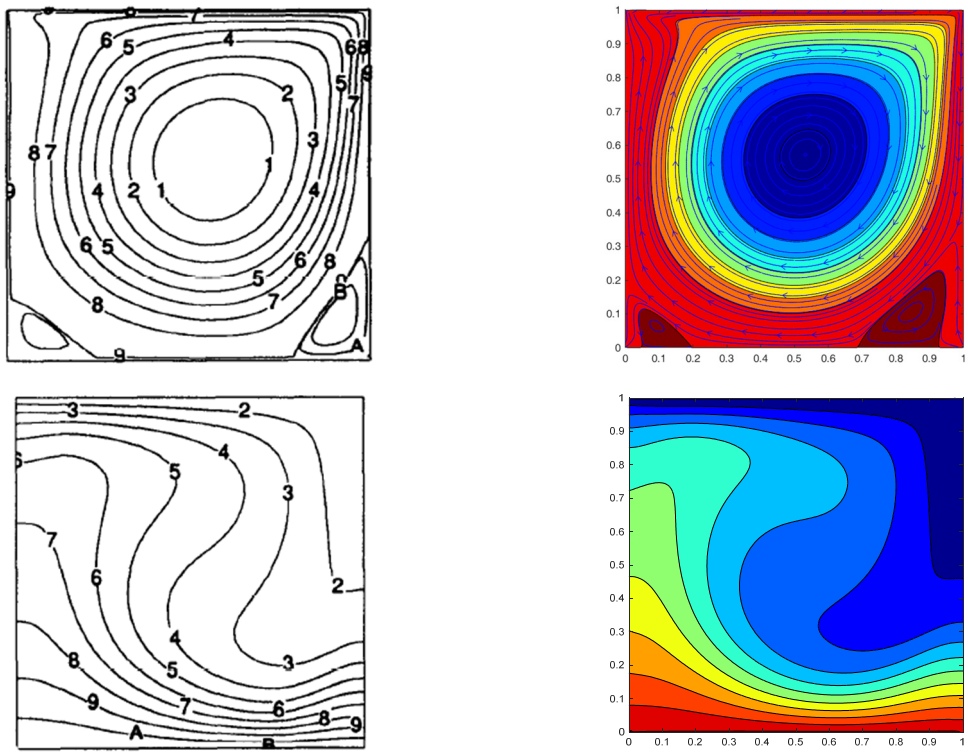

Moallemi et al. [30] Present (LBM)

Figure 2. Comparison results of flow patterns and thermal contours of present and Moallemi et al. [30]

4. RESULTS AND DISCUSSION

This section introduces the graphic diagrams of the simulations concerning the heat and fluid flows of mixed convective flowing in a LDC saturated with porous medium in presence of inclined field of magnetism and joule heating. The density gradients inside the enclosure cause buoyancy forces, leading to the production of streamlines, heatlines, and isotherms. The study investigates the influence of various ranges of involved factors such as Richardson numbers ($0.1 \leq Ri \leq 10$), inclination angle ($0 \leq \lambda \leq 180^0$), Darcy number ($0.001 \leq Da \leq 0.1$), Hartmann number ($0 \leq Ha \leq 30$) and Joule heating parameters ($0 \leq J \leq 10^{-5}$). The $Pr = 0.71$ and $Re = 100$, are kept constant.

Figure 3 presents the influence of the ***Ri*** on the flow and thermal structures within the square cavity. As Ri varies from 0.01 to 10, a clear transition from forced convection to natural convection is observed. At lower Ri values (0.01 and 0.1), inertial forces dominate over buoyancy effects, resulting in strong recirculatory motions and skewed streamlines. The corresponding isotherms exhibit substantial distortion, indicating vigorous convective heat transfer. As Ri increases to 1.0, buoyancy and inertia attain comparative magnitudes, generating more symmetric vortex structures with moderated

thermal gradients. At the highest Ri value considered (Ri = 10), buoyancy forces clearly prevail, leading to weakened circulatory motion and vertically stratified isotherms. The thermal field under these conditions is predominantly governed by conduction, with minimal convective mixing, illustrating the classical characteristics of natural convection dominance.

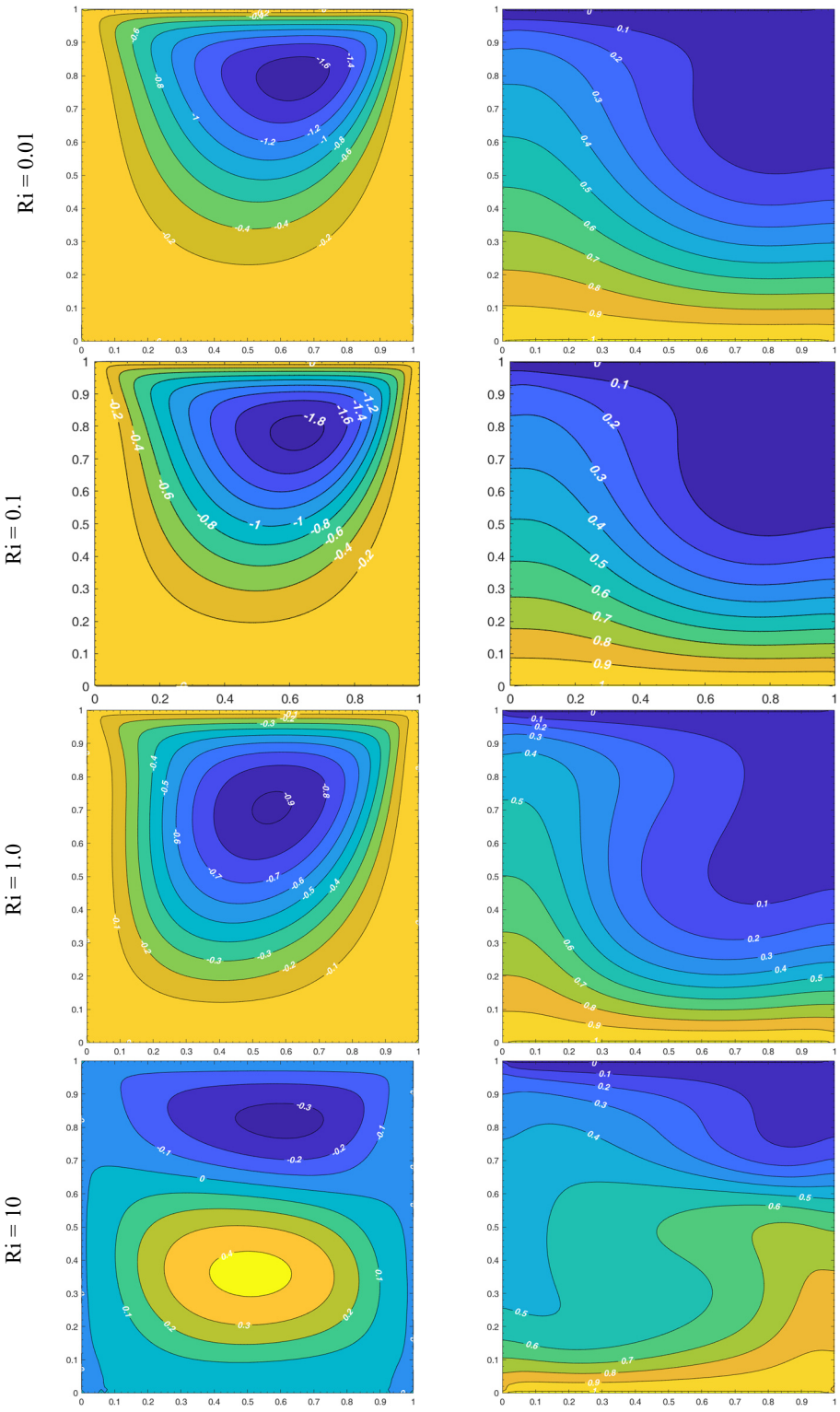

Figure 3. The behavior of streamlines and temperature distribution contour plots for diverse Ri values with fixed Re = 100, $J = 1 \times 10^{-5}$, Ha = 2, Da = 0.1, $\lambda = \pi/4$.

Figure 4 demonstrates the suppressive effect of a magnetic field on the convective flow, illustrated through increasing Hartmann numbers (Ha = 0, 10, 20, 30). In the case Ha = 0, the flow exhibits strong circulation cells, and isotherms show significant distortion due to the active convective transport of heat. Higher Ha values amplify the Lorentz force due to magnetic field-fluid interactions, exerting a decelerating effect. This is evident at Ha = 10 and more

prominently at Ha = 20, where the streamlines become compressed and vortex strength diminishes. At Ha = 30, convective motion is substantially suppressed, and the isotherms tend to align horizontally, marking a shift towards conduction-dominated heat transfer. These results clearly highlight the magnetic field's ability to regulate convective strength and control thermal gradients within the cavity.

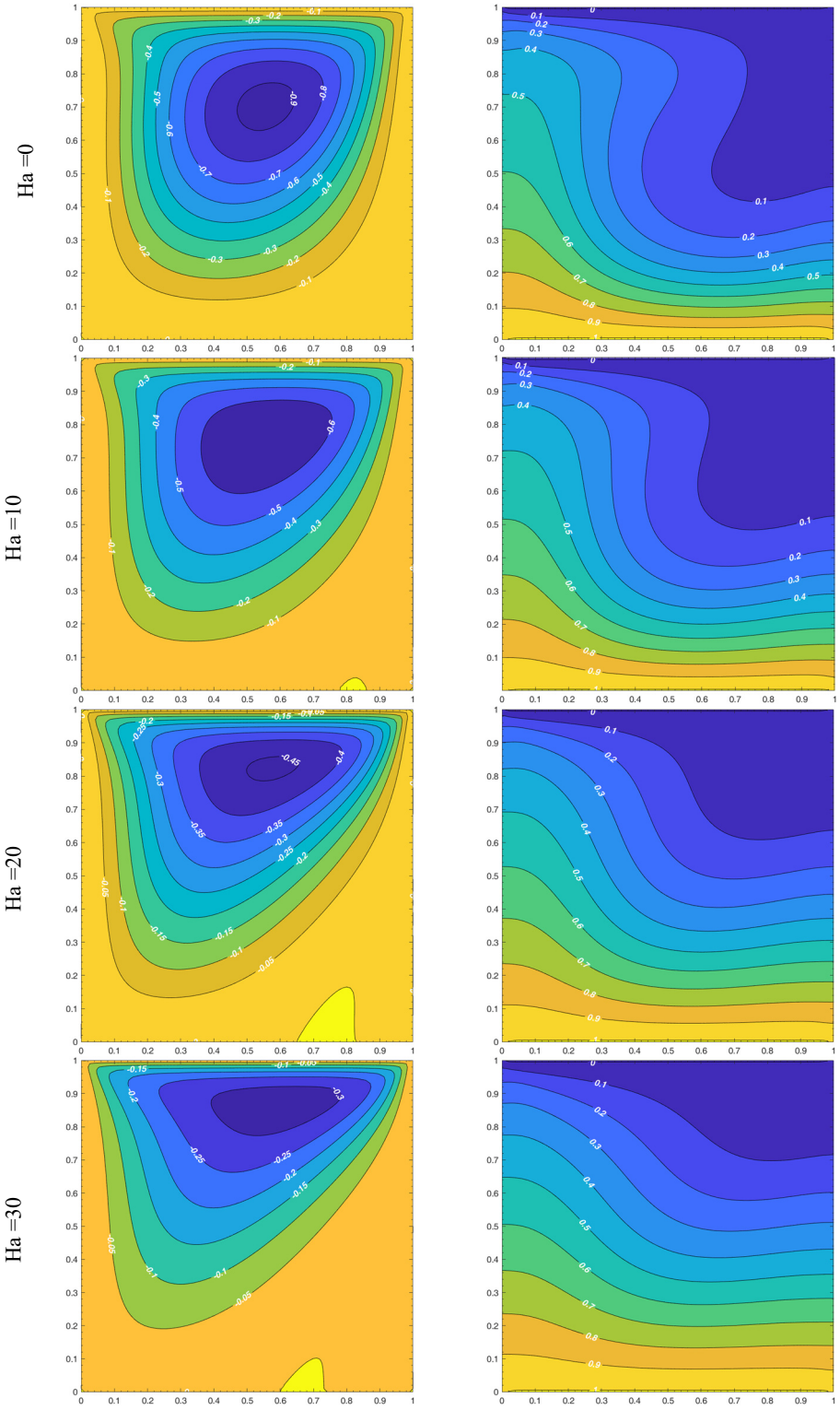

Figure 4. The behavior of streamlines and temperature distribution contour plots for diverse Ha values with fixed Ri = 1, Re = 100, $J = 1 \times 10^{-5}$, Da = 0.1, $\lambda = \pi/4$.

Figure 5 explores the effect of varying the permeability parameter (Da) to assess how the porous medium's permeability influences the transport characteristics. For an effectively non-porous cavity (Da = ∞), the fluid moves freely, yielding strong convection currents and highly perturbed isotherms. As Da is decreased to 0.1 and 0.01, the permeability

of the porous matrix diminishes, increasing the flow resistance. This attenuation in fluid motion results in weaker vortices and a noticeable reduction in isothermal curvature, signifying a gradual suppression of convective heat transport. When Da reaches 0.001, the medium becomes nearly impermeable, and the streamlines collapse into stagnant zones. The isotherms exhibit vertical alignment, characteristic of purely conductive regimes. The observed transition underscores the critical role of porous media in modulating convective intensity and controlling heat flow pathways.

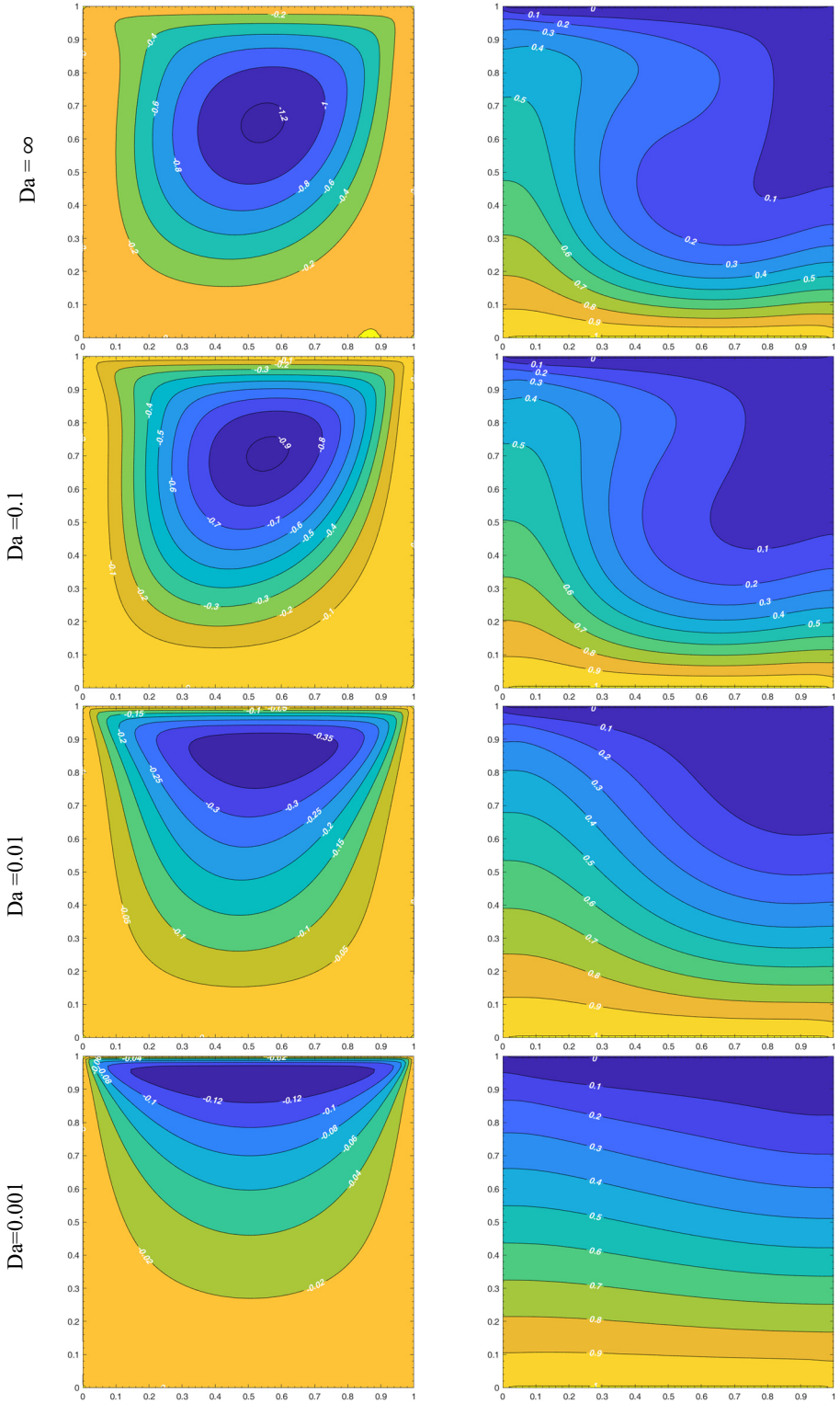

Figure 5. The behavior of streamlines and temperature distribution contour plots for diverse Da values with fixed Ri = 1, Re = 100, $J = 1 \times 10^{-5}$, Ha = 2.0, $\lambda = \pi/4$.

Figure 6 focuses on the impact of the Joule heating parameter (J) on the flow dynamics and temperature distribution. At J = 0, the cavity is unaffected by internal heat generation, and the flow field is governed by buoyancy and inertial

forces alone. The resulting streamline pattern exhibits moderate vortices, and the isotherms reflect smooth, convective bending. As J increases to 0.01 and 0.03, resistive (ohmic) heating due to electromagnetic effects becomes significant. The added thermal energy intensifies buoyancy-driven forces, leading to enhanced vortex strength and increasingly non-uniform isotherm distributions. At J = 0.05, the convective motion becomes even more vigorous, with pronounced distortion in both flow and temperature fields. This escalation of thermal gradients and circulatory activity demonstrates how Joule heating amplifies heat transfer mechanisms by injecting energy directly into the fluid domain, thereby intensifying the hydrothermal interaction under electromagnetic influence.

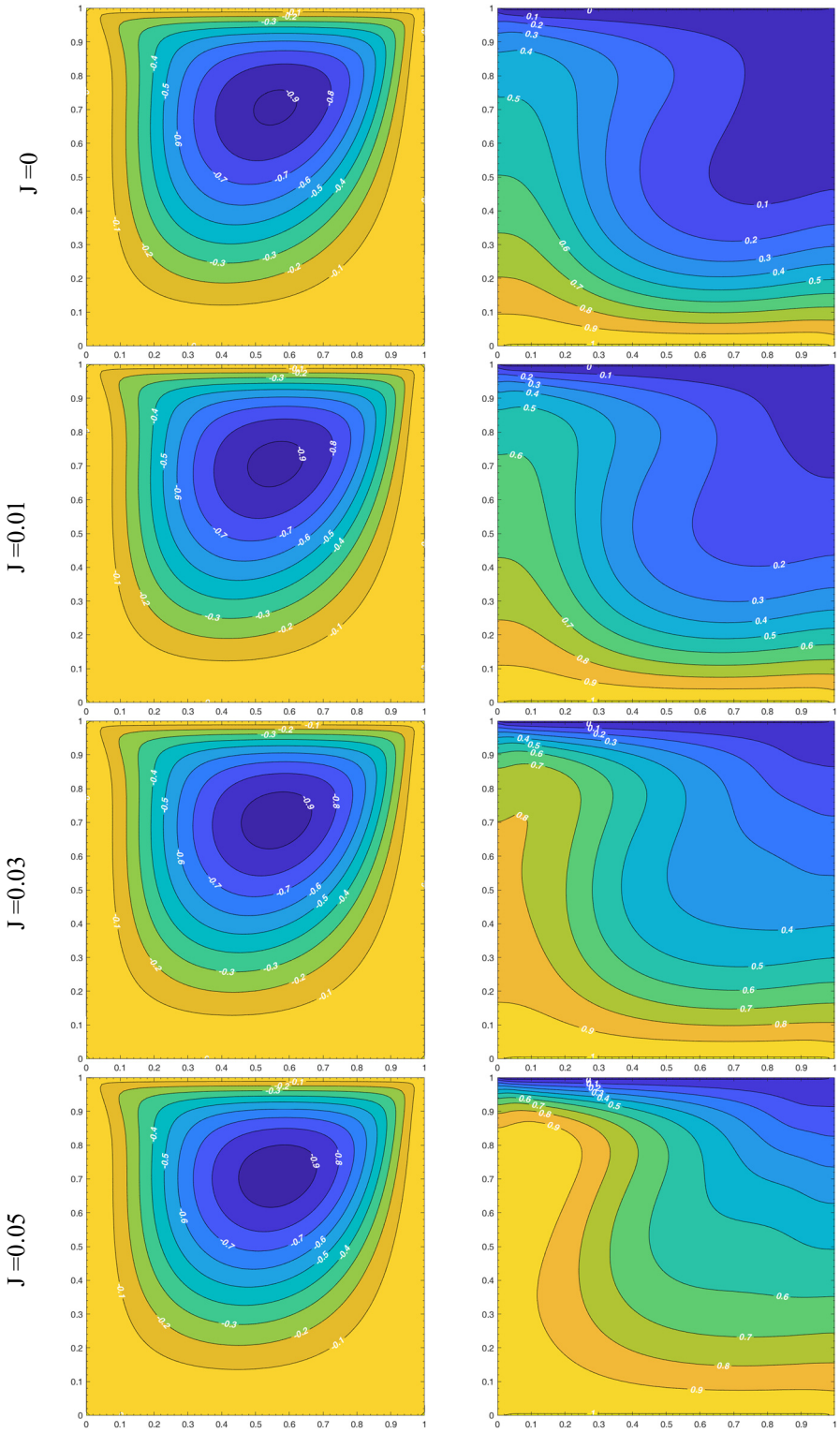

Figure 6. The behavior of streamlines and temperature distribution contour plots for diverse J values with fixed Re = 100, Da = 0.1, Ha = 2, Ri = 1.0, $\lambda = \pi/4$.

Figure 7 depicts how the average Nusselt number (Nu_a) varies with the Hartmann number (Ha) across three distinct Richardson numbers (Ri = 0.1, 1.0, and 10.0). This figure encapsulates the combined effect of magnetic field intensity and buoyancy-to-inertia ratio on thermal transport in the cavity. For all Ri values, it is evident that Nu_a decreases monotonically with increasing Ha, which indicates a progressive suppression of convective heat transfer by the magnetic field. At Ri = 10.0, where buoyancy dominates, Nu_a starts at a significantly higher value (~4.5) and drops steeply as Ha increases, demonstrating that the magnetic damping effect is especially potent when natural convection is dominant. This steep reduction in Nu_a can be attributed to the Lorentz force, which opposes the fluid motion and suppresses thermal plumes that enhance heat transfer in buoyancy-driven flows. For intermediate buoyancy influence (Ri = 1.0), Nu_a also declines with Ha, but the gradient is less severe, reflecting a balance between inertial and buoyancy effects, and a moderated sensitivity to magnetic suppression. At low Ri (0.1), the system is primarily governed by forced convection, and the Nu_a values remain relatively low across all Ha. The impact of increasing Ha under such conditions is more subdued, as the flow is already mechanically driven and less susceptible to Lorentz-induced resistance. The convergence of Nu_a values across different Ri levels at high Ha (>25) suggests that, under strong magnetic fields, conduction becomes the dominant mode of heat transfer, regardless of the initial convective regime.

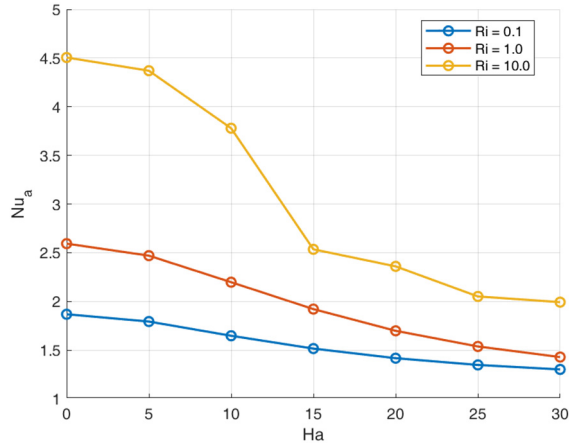

Figure 7. Average Nusselt number (Nu_a) variation with Hartmann number (Ha) with distinct Richardson numbers (Ri).

Figure 8 illustrates the variation Nu_a with respect to the Joule heating parameter (J) for three distinct Ri (Ri = 0.1, 1.0, and 10.0). The results clearly demonstrate a significant decline in Nu_a as J increases, indicating the pronounced influence of resistive (Joule) heating on thermal transport within the cavity. Joule heating acts as an internal volumetric heat source, which leads to temperature homogenization and subsequently diminishes the temperature gradients that drive convective heat transfer.

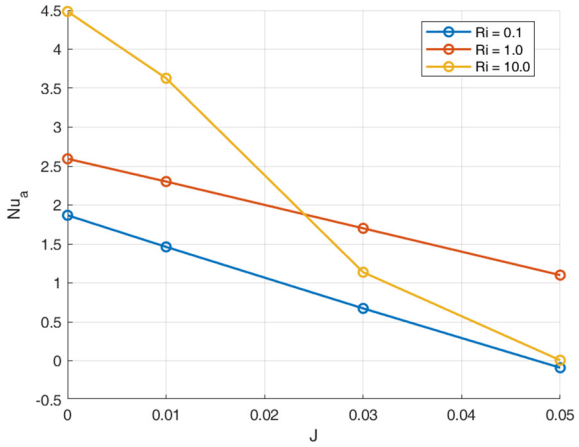

Figure 8. Average Nusselt number (Nu_a) variation with Joule heating parameter (J) with various Richardson numbers (Ri)

For Ri = 10.0, where buoyancy-driven natural convection dominates, the initial Nu_a is notably high (~4.5). However, a sharp decline is observed as J increases, with Nu_a approaching zero at J = 0.05. This underscores the suppressive effect of Joule heating on buoyancy-induced circulation, where thermal diffusion overtakes convective mechanisms. In the case of Ri = 1.0, representing a mixed convection regime, the decrease in Nu_a with increasing J is more gradual, reflecting a competitive balance between forced and natural convection effects being gradually overpowered by Joule heating. For Ri = 0.1, indicative of forced convection dominance, the Nu_a values are the lowest across the board, and exhibit a near-linear decline with J. Notably, at J = 0.05, the Nu_a values for Ri = 0.1 and Ri = 10.0 converge near zero, implying that under

strong internal heating, the nature of convection—whether forced or natural—becomes irrelevant, as conduction becomes the dominant mode of heat transfer. The results collectively reveal that Joule heating can significantly deteriorate convective efficiency, especially in thermally buoyant regimes, due to the suppression of temperature gradients and flow circulation.

Figure 9 presents the variation of the average Nusselt number Nu_a with respect to the inclination angle λ of the applied magnetic field for three different Richardson numbers: Ri=0.1 (forced convection dominant), Ri=1 (mixed convection), and Ri=10 (natural convection dominant). It is observed that for all values of Ri, the average Nusselt number remains nearly constant as λ increases from 0 to π/2. This indicates that the inclination of the non-uniform magnetic field has a minimal impact on the overall heat transfer in the cavity. In particular, the Nu_a values are highest for Ri=10, signifying that natural convection significantly enhances heat transfer independent of the magnetic field's positional alignment. For Ri=0.1, the values of Nu_a are lower, as expected due to the reduced influence of buoyancy, and they too show minimal variation with λ. The negligible slope in each curve suggests that the reorientation of the Lorentz force has little effect on disrupting or altering the thermal boundary layer development and flow structure. This behavior implies that the damping effect imposed by the magnetic field is primarily governed by its magnitude and spatial variation rather than its directional alignment. Therefore, in uniform magnetic strength, altering its inclination angle does not significantly affect convective heat transfer in the cavity under mixed convection conditions.

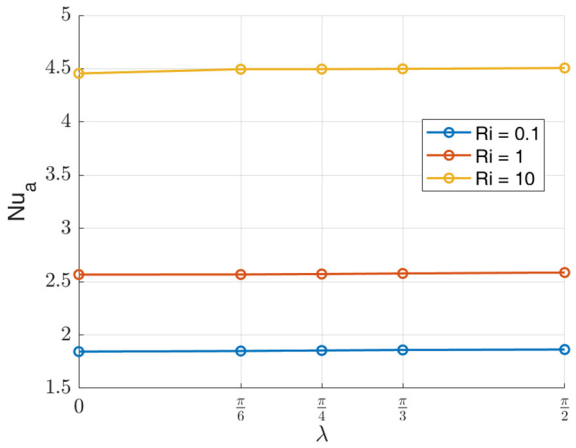

Figure 9. Influence of inclination angle (λ) of magnetic force on average Nusselt number (Nu_a) for different Richardson numbers (Ri)

5. FINAL REMARKS

The study of hydro-magnetic mixed convective transport phenomena in a 2D square cavity, incorporating Joule heating effects and porous media, reveals several critical insights into the underlying physics and parameter interactions. By using the lattice Boltzmann method to simulate fluid dynamics, the study explores the coupling between thermal, flow, and magnetic forces under various dimensionless parameters such as Reynolds number (Re), Hartmann number (Ha), Darcy number (Da), Richardson number (Ri), and the Joule heating parameter (J). The key conclusions are summarized as follows:

- Increasing Ha significantly suppresses fluid motion due to enhanced Lorentz force, which dampens convection and shifts the heat transfer mechanism towards conduction. A higher Ha consistently leads to a lower average Nusselt number.
- As the Hartmann number (Ha) increases from 2 to 30, a significant reduction in fluid circulation is observed. For instance, at **Ha = 30,** streamlines become nearly parallel, indicating **a 70–80%** suppression in convective motion compared to **Ha = 0**, leading to more uniform isotherms and reduced thermal transport.
- At low Ri (e.g., 0.01), forced convection dominates, allowing stronger thermal mixing. As Ri increases, buoyancy becomes more influential, but it is also more susceptible to suppression by magnetic fields and Joule heating.
- An increase in J introduces greater internal heat generation, which intensifies local thermal gradients. However, this effect also increases entropy generation, thereby reducing the overall heat transfer efficiency, especially in buoyancy-driven flows.
- With increasing Joule heating parameter J from 0 to 0.05, internal energy generation enhances local temperature gradients. The peak Nusselt number increases by up to 25%, but spatial uniformity of heat transfer degrades, indicating thermal instability and less efficient global heat transport.
- High Da enables strong convection, producing pronounced vortices and thermal mixing, while, Lower Da reduces permeability, constraining fluid motion. At very low Da, conduction dominates, as indicated by vertical isotherms and diminished flow patterns.
- Changes in the inclination angle of the non-uniform magnetic field (λ) have a relatively minor influence on the overall heat transfer rate, suggesting that the direction of the magnetic field is less critical than its magnitude.

- The highest average Nusselt number is recorded under low Ha (2), low J (0), high Ri (10), and high Da (∞) conditions—signifying strong convective transport. Conversely, Ha = 30, J = 0.05, and Da = 0.001 result in a conduction-dominant regime with significantly reduced heat transfer efficiency.

Limitation.

Some constraints of this examination include that the considered numerical model is based on idealized conditions and may not accurately reflect real-world variability.

Future Research Directions:

The study opens several avenues for future research, particularly in exploring the effects of variable properties such as temperature-dependent viscosity and thermal conductivity, as well as more complex boundary conditions. Additionally, the use of the lattice Boltzmann method provides a valuable framework for extending these investigations to more realistic geometries and larger-scale systems, including those involving non-Newtonian fluids and multi-phase flow.

Conflicts of Interest

The authors declare no conflict of interest.

Data Availability

All data generated or analysed during this study are included in this article.

Notation

Roman

B	*Magnetic field intensity [Tesla]*
$c = \delta x/\delta t$	*streaming speed for LBM code.*
$C_S = c/\sqrt{3}$	*speed of the sound in the fluid flow field for LBM code*
e_i	*velocity in the D2Q9 lattice for the discrete type*
g	*Acceleration due to gravity [m/s²]*
L	*Width and height of square enclosure [m]*
Nu	*Nusselt number [-]*
p	*Dimensional pressure [Pa]*
T	*Dimensional temperature [K]*
$\bar{t}$	*Time (s)*
$\bar{u}, \bar{v},$	*Dimensional velocity components in* $\bar{x}, \bar{y} - coordinates$ *[m/s]*
w_i	*weighting coefficients.*
$\bar{x}, \bar{y},$	*Dimensional coordinates [m]*

Greek

α	*Thermal diffusivity [m²/s]*
β	*Thermal expansion coefficient [K⁻¹]*
μ	*Dynamic viscosity [kg/(ms)]*
ν	*Kinematic viscosity [m²/s]*
ρ	*Density of base fluid (water) [kg/m³]*
λ	Magnetic field inclination angle

Key parameter

Pr	Prandtl number ($\mathrm{Pr} = \upsilon/\alpha$)
Da	Darcy number ($Da = K/H^2$)
Gr	Grashof number ($Gr = g\beta(T_h - T_c)H^3/\upsilon$)
Ha	Hartmann number ($Ha = LB_0\sqrt{\sigma/\mu}$)
J	Joule magnetic parameter ($J = g\beta LHa^2/(c_p Ra)$)
Ri	Richardson number ($Ri = Gr/Re^2$)

ORCID

C. Venkata Lakshmi, https://orcid.org/0000-0003-2921-8129; **Anuradha Aravapalli,** https://orcid.org/0009-0003-5137-8804
K. Venkatadri, https://orcid.org/0000-0001-9248-6180; **O. Anwar Bég,** https://orcid.org/0000-0003-0614-8711
V. Ramachandra Prasad; https://orcid.org/0000-0002-9168-3825

REFERENCES

[1] Y.U.U.B. Turabi, and S. Munir, "CFD simulations of MHD effects on mixed convectional flow in a lid-driven square cavity with square cylinder using Casson fluid,' Numerical Heat Transfer, Part B: Fundamentals, pp.1-16 (2024). https://doi.org/10.1080/10407790.2024.2365890

[2] H.F. Oztop, and I. Dagtekin, "Mixed convection in two-sided lid-driven differentially heated square cavity," International Journal of Heat and Mass Transfer, **47**(8-9), 761-1769 (2004). http://dx.doi.org/10.1016/j.ijheatmasstransfer.2003.10.016

[3] R. Parveen, A.K. Hussein, T.R. Mahapatra, M. Al-Thamir, A. Abidi, M.B.B. Hamida, R.Z. Homod, and F.L. Rashid, "MHD double diffusive mixed convection and heat generation / absorption in a lid-driven inclined wavy enclosure filled with a ferrofluid," Int. J. Thermofluids, **22**, 100698 (2024). https://doi.org/10.1016/j.ijft.2024.100698

[4] O. Zikanov, I. Belyaev, Y. Listratov, P. Frick, N. Razuvanov, and V. Sviridov, "Mixed convection in pipe and duct flows with strong magnetic fields," Appl. Mech. Rev. **73**(1), 010801 (2021). https://doi.org/10.1115/1.4049833
[5] N.R. Devi, M. Gnanasekaran, A. Satheesh, P.R. Kanna, J. Taler, D.S. Kumar, *et al*., "Double-diffusive mixed convection in an inclined square cavity filled with nanofluid: A numerical study with external magnetic field and heated square blockage effects," Case Studies in Thermal Engineering, 56, 104210 (2024). https://doi.org/10.1016/j.csite.2024.104210
[6] P. Mondal, T.R. Mahapatra, R. Parveen, and B.C. Saha, "Heat Generation/Absorption in MHD double diffusive mixed convection of different nanofluids in a Trapezoidal enclosure," J. Nanofluids, **13**(2), 339-349 (2024). https://doi.org/10.1166/jon.2024.2116
[7] R. Parveen, and T. R. Mahapatra, "Heat and mass source effect on MHD double diffusive mixed convection and entropy generation in a curved enclosure filled with nanofluid," Nonlin. Analy. Model. Control, **27**(2) 308-330 (2022). https://doi.org/10.15388/namc.2022.27.25338
[8] Q. Yu, H. Xu, and S. Liao, "Analysis of mixed convection flow in an inclined lid driven enclosure with Buongiorno's nanofluid model," Int. J. Heat Mass Transf. **126**, 221-236 (2018). https://doi.org/10.1016/j.ijheatmasstransfer.2018.05.109
[9] Z. Mahmood, and U. Khan, "Mixed convective flow of nanofluid across exponential surface: A numerical assessment of the impact of Darcy-Forchheimer and nanoparticle aggregation," Numerical Heat Transfer, Part A: Applications, **86**(7), 1-26 (2023). https://doi.org/10.1080/10407782.2023.2288265
[10] M.J.H. Munshi, M.A. Alim, A.H. Bhuiyan, and M. Ali, "Hydrodynamic mixed convection in a lid-driven square cavity including elliptic shape heated block with corner heater," Procedia engineering, **194**, 442-449 (2017). https://doi.org/10.1016/j.proeng.2017.08.169
[11] S. Sivasankaran, V. Sivakumar, and A.K. Hussein, "Numerical study on mixed convection in an inclined lid-driven cavity with discrete heating," International Communications in Heat and Mass Transfer, **46**, 112-125 (2013). https://doi.org/10.1016/j.icheatmasstransfer.2013.05.022
[12] K.M. Khanafer, and J. Chamkha, "Mixed convection flow in a lid-driven enclosure filled with a fluid-saturated porous medium," Int. J. Heat Mass Transf. **42**(13), 2465–2481 (1999). https://doi.org/10.1016/S0017-9310(98)00227-0
[13] M.J.H. Munshi, N. Jahan, and G. Mostafa, "Mixed Convection Heat Transfer of Nanofluid in a Lid-Driven Porous Medium Square Enclosure with Pairs of Heat Source Sinks," Am. J. Eng. Res. (AJER), **8**(6), 59-70 (2019).
[14] Y. Nawaz, M.S. Arif, K. Abodayeh, and A.H. Soori. "A two-stage multi-step numerical scheme for mixed convective Williamson nanofluid flow over flat and oscillatory sheets," International Journal of Modern Physics B, **38**(22), 2450298 (2024). https://doi.org/10.1142/S0217979224502989
[15] D. Qaiser, Z. Zheng, and M.R. Khan, "Numerical assessment of mixed convection flow of Walters-B nanofluid over a stretching surface with Newtonian heating and mass transfer," Thermal Sci. Eng. Prog. 22, 100801 (2021). https://doi.org/10.1016/j.tsep.2020.100801
[16] M.A. Sheremet, M.S. Astanina, and I. Pop, "MHD natural convection in a square porous cavity filled with a water-based magnetic fluid in the presence of geothermal viscosity," International Journal of Numerical Methods for Heat & Fluid Flow, **28**(9), 2111-2131 (2018). https://doi.org/10.1108/HFF-12-2017-0503
[17] M.S. Alam, M.S.H. Mollah, M.A. Alim, and M.K.H. Kabir, «Finite Element Analysis of MHD Natural Convection in a Rectangular Cavity and Partially Heated Wall," Engineering and Applied Sciences, **10**(4), 53-58 (2017). https://doi.org/10.11648/j.eas.20170203.12
[18] B.P. Geridonmez, and H.F. Oztop, "Mixed Convection Heat Transfer in a Lid-Driven Cavity under the Effect of a Partial Magnetic Field," Heat Transfer Engineering, **42**(10), 875–887 (2020). https://doi.org/10.1080/01457632.2020.1792622
[19] S.S. Suchana, and M.M. Ali, "Finite Element Analysis of Convective Heat Transfer in a Linearly Heated Porous Trapezoidal Cavity in the Presence of a Magnetic Field," Int. J. Appl. Comput. Math. **10**, 141 (2024). https://doi.org/10.1007/s40819-024-01770-0
[20] C.G. Mohan, and A. Satheesh, "The Numerical Simulation of Double-Diffusive Mixed Convection Flow in a Lid-Driven Porous Cavity with Magnetohydrodynamic Effect," Arab. J. Sci. Eng. **41**, 1867–1882 (2016). https://doi.org/10.1007/s13369-015-1998-x
[21] N.A. Bakar, R. Roslan, A. Karimipour, and I. Hashim, "Mixed convection in lid-driven cavity with inclined magnetic field," Sains Malaysiana, **48**(2), 451-471 (2019). http://dx.doi.org/10.17576/jsm-2019-4802-24
[22] H. Moria, "Natural convection in an L-shape cavity equipped with heating blocks and porous layers," International Communications in Heat and Mass Transfer, **126**, 105375 (2021). https://doi.org/10.1016/j.icheatmasstransfer.2021.105375
[23] Y. Wang, G. Qin, W. He, and Z. Bao, "Chebyshev spectral element method for natural convection in a porous cavity under local thermal non-equilibrium model," International Journal of Heat and Mass Transfer, **121**, 1055-1072 (2018). https://doi.org/10.1016/j.ijheatmasstransfer.2018.01.024
[24] A. Nee, "Hybrid Lattice Boltzmann Simulation of Three-Dimensional Natural Convection," Journal of Computational and Theoretical Transport, **50**(4), 280–296 (2021). https://doi.org/10.1080/23324309.2021.1942061
[25] S.A. Fanaee, A. Shahriari, and S. Nikpour, "The Lattice Boltzmann Simulation of Free Convection Heat Transfer of a Carbon-Nanotube Nanofluid in a Triangular Cavity with a Solar Heater," Journal of Nanofluids, **13**(3), 694-709 (2024). https://doi.org/10.1166/jon.2024.2159
[26] A. Mahmoudi, I. Mejri, M.A. Abbassi, and A. Omri, "Lattice Boltzmann simulation of MHD natural convection in a nanofluid-filled cavity with linear temperature distribution," Powder Technology, **256**, 257-271 (2014). https://doi.org/10.1016/j.powtec.2014.02.032
[27] G.R. Kefayati, "Lattice Boltzmann simulation of natural convection in a square cavity with a linearly heated wall using nanofluid," Arabian Journal for Science and Engineering, **39**(3), 2143-2156 (2014). https://doi.org/10.1007/s13369-013-0748-1
[28] R.K. Tiwari, and M.K. Das, "Heat transfer augmentation in a two-sided lid-driven differentially heated square cavity utilizing nanofluids." Int. J. Heat Mass. Transf. **50**, 2002–2018 (2007). https://doi.org/10.1016/j.ijheatmasstransfer.2006.09.034
[29] R. Iwatsu, J.M. Hyun, and K. Kuwahara, "Mixed convection in a driven cavity with a stable vertical temperature gradient," Int. J. Heat Mass Transf. **36**, 1601–1608 (1993). https://doi.org/10.1016/S0017-9310(05)80069-9
[30] M.K. Moallemi, and K.S. Jang, "Prandtl number effects on laminar mixed convection heat transfer in a lid-driven cavity," International Journal of Heat and Mass Transfer, **35**(8), 1881-1892 (1992). https://doi.org/10.1016/0017-9310(92)90191-T

ВПЛИВ ДЖОУЛЕВОГО НАГРІВАННЯ ТА ГІДРОМАГНІТНИХ ЕФЕКТІВ НА ЗМІШАНУ КОНВЕКЦІЮ В ПОРИСТІЙ ПОРОЖНИНІ З ВИКОРИСТАННЯМ МЕТОДУ БОЛЬЦМАНА З ГРАТКОЮ

С. Венката Лакшмі[a], Анурадха Аравапаллі[a], К. Венкатадрі[b], О. Анвар Бег[c], В. Рамачандра Прасад[d]

[a]Кафедра прикладної математики, Шрі Падмаваті Махіла Вішвавідьялаям, Тірупаті, Андхра-Прадеш - 517502, Індія

[b]Кафедра математики, Університет Мохана Бабу (колишній інженерний коледж Шрі Відьянікетан), Тірупаті, Андхра-Прадеш - 517 102, Індія

[c]Група багатофізичних інженерних наук, Аеронавтика/Машинобудування, Університет Солфорда, Лабораторія корозії, 3-08, будівля SEE, Манчестер, M54WT, Велика Британія

[d]Кафедра математики, Школа передових наук, Технологічний інститут Веллор, Веллор, Таміл Наду 632014, Індія

У цій статті проводиться комплексне дослідження теплопередачі під впливом кількох факторів, включаючи магнітне поле, рухому кришку, пористе середовище та джоулеве нагрівання в порожнині з кришкою (LDC). Порожнина має рухому кришку, вертикальні стінки з теплоізольованими межами та горизонтальні стінки, що підтримуються при рівномірних температурах Th (внизу) та Tc (вгорі). Метою дослідження є аналіз поведінки змішаної конвективної теплопередачі системи за допомогою контурних діаграм для візуалізації потоку та теплової картини за різних розглянутих параметрів: числа Річардсона ($0{,}01 \le Ri \le 10$) та параметри джоулеве нагрівання ($0 \le J \le 10^{-5}$), числа Гартмана ($0 \le Ha \le 30$) та числа Дарсі ($0{,}001 \le Da \le 0{,}1$). Для використання основних рівнянь переносу застосовується метод ґратчастого Больцмана (LBM). Ефекти джоулевої термічної обробки є критично важливими в системах, де необхідно контролювати внутрішнє теплоутворення, наприклад, в електричних системах або охолодженні акумуляторів, де резистивна термічна обробка може як сприяти, так і перешкоджати бажаній тепловій динаміці.

Ключові слова: *метод Больцмана з ґраткою (LBM); порожнина з кришкою; магнітогідродинаміка; змішана конвекція; джоулева термічна обробка; пористе середовище*

East European Journal of Physics. 2. 398-404 (2025)
DOI:10.26565/2312-4334-2025-2-48 ISSN 2312-4334

COMPUTATIONAL STUDY OF DRUG DELIVERY SYSTEMS WITH RADIONUCLIDE AND FLUORESCENCE IMAGING MODALITIES. III. DOXORUBICIN DELIVERY SYSTEMS BASED ON ALBUMIN AND LYSOZYME

V. Trusova[a]*, U. Malovytsia[a], P. Kuznietsov[b], I. Yakymenko[b], I. Karnaukhov[c], A. Zelinsky[c], B. Borts[c], I. Ushakov[c], L. Sidenko[c], G. Gorbenko[a]

[a]*Department of Medical Physics and Biomedical Nanotechnologies, V.N. Karazin Kharkiv National University 4 Svobody Sq., Kharkiv, 61022, Ukraine*

[b]*O.I. Akhiezer Department for Nuclear Physics and High Energy Physics, V.N. Karazin Kharkiv National University 4 Svobody Sq., Kharkiv, 61022, Ukraine*

[c]*National Science Center "Kharkiv Institute of Physics and Technology", 1, Akademichna Str., Kharkiv, Ukraine*

**Corresponding Author e-mail: valerija.trusova@karazin.ua*

Received March 1, 2025, revised April 24, 2025; accepted May 17, 2025

This study investigates the development of advanced protein-based drug delivery systems for doxorubicin (DOX) by integrating lysozyme into albumin-based carriers, incorporating both radionuclide (technetium-99m complexes) and fluorescence (near-infrared dyes) imaging modalities. Utilizing molecular docking simulations, we examined the binding affinities and sites of technetium-99m complexes and near-infrared fluorescent dyes within these hybrid protein systems. The results demonstrate that the incorporation of lysozyme significantly modulates the binding landscape, enhancing the specificity and stability of technetium complexes and fluorescent dyes. Notably, the binding affinities of indocyanine green were markedly higher in lysozyme-containing systems, suggesting improved imaging capabilities. Additionally, our analysis revealed distinct binding sites for doxorubicin in the presence of different technetium complexes, which could influence drug release and therapeutic efficacy. These findings support the potential of albumin-lysozyme hybrid systems as nanocarriers with dual imaging capabilities for DOX delivery, offering a promising approach to enhance therapeutic efficacy while reducing systemic toxicity in anticancer treatment and contributing to the design of more sophisticated and targeted delivery platforms for cancer therapy.

Keywords: *Protein-based drug delivery nanosystems; Human serum albumin; Lysozyme; Doxorubicin; Technetium complexes; Near infrared dyes; Molecular docking*

PACS: 87.14.C++c, 87.16.Dg

The development of multifunctional effective drug delivery systems remains a critical challenge in modern oncology, where the need for improved therapeutic efficacy must be balanced against the risk of systemic toxicity, particularly for potent but toxic agents like doxorubicin (DOX). Protein-based carriers have emerged as promising platforms due to their intrinsic biocompatibility, structural versatility, and capacity for targeted drug transport [1,2]. These characteristics enable precise control over drug pharmacokinetics and biodistribution while allowing for the incorporation of imaging agents that facilitate real-time monitoring of drug delivery. Among the various proteins explored for this purpose, human serum albumin (HSA) has been extensively studied for its ability to enhance drug solubility, prolong circulation time, and promote tumor accumulation through passive targeting mechanisms [3]. Our previous works established transferrin-albumin hybrids as effective DOX delivery vehicles with integrated imaging capabilities [4,5]. However, lysosomal entrapment and extracellular matrix viscosity may limit the translational potential of such systems in hypoxic solid tumors [6,7]. In response to these potential clinical challenges, we are compelled to explore alternative protein combinations that can overcome these barriers, and in the present contribution we introduce lysozyme (Lz), cationic, membrane-permeabilizing protein with inherent glycosidase activity [8,9], as a strategic partner to HSA in designing the next-generation theranostic platforms. Unlike transferrin receptor-mediated targeting, lysozyme confers unique advantages through pH-dependent structural reconfiguration and enzymatic degradation of bacterial cell wall analogs, a property exploitable in tumor microenvironments enriched with peptidoglycan-mimetic glycoproteins. Using computational modeling approaches, this study aims to characterize the molecular interactions between DOX, albumin, and lysozyme to assess the structural and energetic factors influencing drug loading and stability. Additionally, we explore the potential of these hybrid protein carriers for applications in multimodal imaging, where the incorporation of radiopharmaceutical and fluorescent labels could provide new opportunities for non-invasive tracking of drug biodistribution.

METHODS

Dimeric conformation of human serum albumin (HSA) (PDB ID: 1AO6) was selected as the principal constituent of the constructed protein-based drug delivery systems (PDDS). For PDDS formulation, twelve radiopharmaceuticals

Cite as: V. Trusova, U. Malovytsia, P. Kuznietsov, I. Yakymenko, I. Karnaukhov, A. Zelinsky, B. Borts, I. Ushakov, L. Sidenko, G. Gorbenko, East Eur. J. Phys. 2, 398 (2025), https://doi.org/10.26565/2312-4334-2025-2-48

based on technetium-99m (TCC) were selected [4,5]: [^{99m}Tc]Tc-Sestamibi (TcSES), [^{99m}Tc]Tc-Tetrofosmin (TcTET), [^{99m}Tc]Tc-Medronate (TcMED), [^{99m}Tc]Tc-dimercaptosuccinic acid (TcDMSA), [^{99m}Tc]Tc-diethylenetriaminepentaacetate (TcDTPA), [^{99m}Tc]Tc-mercaptoacetyltriglycine (TcMAG), Pertechnetate [^{99m}Tc]TcO_4^- (TcPER), [^{99m}Tc]Tc-Exametazime (TcEXA), [^{99m}Tc]Tc-diisopropyl iminodiacetic acid (TcDIS), [^{99m}Tc]Tc-ethylene cysteine dimer (TcECD), [^{99m}Tc]Tc-hydrazinonicotinic acid-H6F (TcHYN), and [^{99m}Tc]Tc-Mebrofenin (TcMEB). To enable multimodal imaging with both radionuclide and optical tracking capabilities, these [^{99m}Tc] complexes were combined with four near-infrared (NIR) fluorescent dyes: Methylene Blue (MB), Indocyanine Green (IG), cyanine AK7-5, and squaraine SQ1. Molecular docking analyses were conducted using the HDOCK server to determine the optimal binding sites for technetium-labeled agents, DOX, and fluorescent dyes in HSA-Lz protein assemblies. Prior to docking, molecular dynamics (MD) simulations of 1 ns were performed to refine the structures of HSA dimers and their complexes with lysozyme (Lz). Ligand structures were created in MarvinSketch (version 18.10.0) and underwent geometry optimization using Avogadro (version 1.1.0). The best docking conformations were visualized with UCSF Chimera (version 1.14) and analyzed via the Protein-Ligand Interaction Profiler [10].

RESULTS AND DISCUSSION

Our previous studies have explored the potential of albumin-based drug delivery systems for doxorubicin (DOX) with integrated radionuclide and fluorescence imaging modalities [4,5]. Specifically, our first work demonstrated that human serum albumin (HSA) can serve as an effective carrier for DOX, forming stable complexes with technetium-99m-based radiopharmaceuticals and near-infrared fluorescent (NIR) dyes. Molecular docking and molecular dynamics simulations revealed that these multimodal nanocarriers exhibit strong binding affinities and structural stability, supporting their potential use in theranostic applications. Expanding on this approach, our second paper from this series introduced transferrin (TRF) as an additional protein component, investigating its role in enhancing the targeting capabilities of albumin-based drug delivery platforms. The findings indicated that HSA-TRF complexes maintain favorable interactions with TCC and fluorescent dyes, highlighting their promise for improving the therapeutic efficacy and specificity of DOX delivery. The present study focuses on drug delivery systems based on albumin and lysozyme, aiming to further refine the design of protein-based carriers by evaluating their binding interactions and stability in multimodal imaging.

As illustrated in Fig. 1, left panel, the best docking scores (BDS) for TCC binding to the albumin-lysozyme (HAS-Lz) complexes reveal a hierarchy of affinities: HSA + Lz - TcHYN > TcDIS > TcMEB > TcDTPA ~ TcTET ~ TcDMSA ~ TcSES ~ TcMED ~ TcECD ~ TcMAG ~ TcEXA > TcPER.

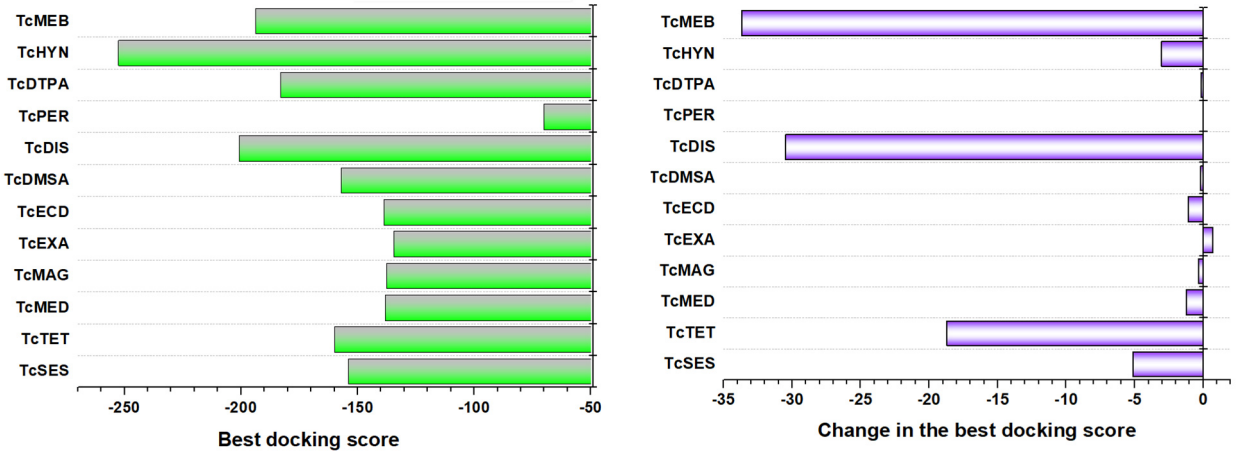

Figure 1. Absolute values (left panel) and changes (right panel) in the best docking score values obtained for the TCC complexes with HSA in the absence and presence of Lz

Interestingly, the BDS value for the HSA-Lz complex was estimated to be -205.2, corresponding to 71 interface residues, involved into the complexation (Table 1). This indicates a strong interaction between HSA and Lz, suggesting a potential stabilizing effect of Lz on the albumin structure and its ligand-binding properties. The formation of HSA-Lz complexes resulted in a reconfiguration of the ligand binding domains, thereby modulating the binding affinity for specific TCC molecules.

Table 1. Interfacial amino acids and interaction modes for TCC binding in albumin-lysozyme complexes

TCC	HSA-Lz-TCC interface residues		Type of interactions
	HSA	Lz	
TcSES	THR_{420B*}, PRO_{421B}, GLU_{505B}, THR_{506B}, PHE_{507B}, THR_{508B}, PHE_{509B}, ASP_{512B}, LEU_{516B}, GLU_{520B}, ILE_{523B}, LYS_{524B}, THR_{527B}, ALA_{528B}, GLU_{531B}, PHE_{551B}	LYS_{33}, TRP_{34}, ARG_{115}, GLN_{123}, TYR_{124}	Hydrophobic interactions, hydrogen bonds

TCC	HSA-Lz-TCC interface residues		Type of interactions
	HSA	Lz	
TcTET	ASN_{109B}, ARG_{114B}, LEU_{115B}, GLU_{425B}, GLU_{520B}, ILE_{523B}, LYS_{524B}	TRP_{34}, ARG_{115}	Hydrophobic interactions, hydrogen bonds
TcMED	VAL_{116B}	GLU_{35}, ASN_{44}, ASN_{46}, SER_{51}, ASP_{53}, GLN_{58}, ILE_{59}, ASN_{60}, TRP_{64}, ALA_{108}, TRP_{109}, VAL_{110}, ALA_{111}	Hydrogen bonds
TcMAG	ASP_{107A}, ASP_{108A}, ASN_{109A}, ARG_{145A}, HSD_{146A}, PRO_{147A}, TYR_{148A}, LYS_{190A}, ALA_{191A}, SER_{193A}, ALA_{194A}, ARG_{197A}, GLU_{425A}, ASN_{458A}, GLN_{459A}		Hydrogen bonds, salt bridges
TcEXA	LEU_{115A}, VAL_{116A}, ARG_{117A}, PRO_{118A}, MET_{123A}, PHE_{134A}, LYS_{137A}, TYR_{138A}, LEU_{139A}, GLU_{141A}, ILE_{142A}, ARG_{145A}, TYR_{161A}, PHE_{165A}, LEU_{182A}, ARG_{186A}		Hydrophobic interactions, hydrogen bonds
TcECD	LEU_{115B}, ARG_{117B}, PRO_{118B}, MET_{123B}, PHE_{134B}, LYS_{137B}, TYR_{138B}, GLU_{141B}, ILE_{142B}, TYR_{161B}, LEU_{182B}, ASP_{183B}, LEU_{185B}, ARG_{186B}	ALA_{47}	Hydrophobic interactions, hydrogen bonds, salt bridges
TcDMSA	LEU_{115A}, VAL_{116A}, ARG_{117A}, PRO_{118A}, MET_{123A}, TYR_{138A}, ILE_{142A}, HSD_{146A}, PHE_{149A}, LEU_{154A}, PHE_{157A}, TYR_{161A}, LEU_{182A}, LEU_{185A}, ARG_{186A}, ASP_{187A}, GLY_{189A}, LYS_{190A}		Hydrogen bonds, salt bridges
TcDIS	GLU_{505B}, HSD_{510B}, LYS_{524B}, THR_{527B}	ARG_5, LYS_{33}, TRP_{34}, TYR_{38}, GLN_{123}, TYR_{124}	Hydrophobic interactions, hydrogen bonds, salt bridges
TcPER	TYR_{30B}, HSD_{67B}, THR_{68B}, PHE_{70B}, GLY_{71B}, LEU_{74B}, GLU_{95B}, ARG_{98B}, ASN_{99B}, PHE_{102B}		Hydrogen bonds
TcDTPA	LEU_{115A}, VAL_{116A}, ARG_{117A}, PRO_{118A}, MET_{123A}, PHE_{134A}, LEU_{135A}, LYS_{137A}, TYR_{138A}, GLU_{141A}, ILE_{142A}, TYR_{161A}, LEU_{182A}, ARG_{186A}		Hydrogen bonds, salt bridges
TcHYN	GLU_{383A}, LEU_{387A}, ASN_{391A}, LEU_{394A}, ALA_{406A}, LEU_{407A}, VAL_{409A}, ARG_{410A}, TYR_{411A}, LYS_{414A}, LEU_{430A}, LEU_{453A}, SER_{489A}, GLU_{492A}, LYS_{541A}, GLU_{542B}, LYS_{545A}		Hydrogen bonds, π-stacking, salt bridges
TcMEB	THR_{420B}, PRO_{421B}, ASN_{503B}, GLU_{505B}, THR_{506B}, HSD_{510B}, LYS_{524B}, THR_{527B}, GLU_{531B}	ARG_5, LYS_{33}, TRP_{34}, TYR_{38}, ARG_{115}, GLN_{123}, TYR_{124}	Hydrophobic interactions, hydrogen bonds, salt bridges

*-A and B denote monomer subunits of the HSA dimer

As illustrated in Fig. 1, right panel, the most pronounced changes in binding affinity were observed for TcMEB, with a less pronounced effect for TcDTPA. This suggests that the presence of Lz may induce conformational perturbations in HSA, exposing or altering binding sites that favor specific TCCs.

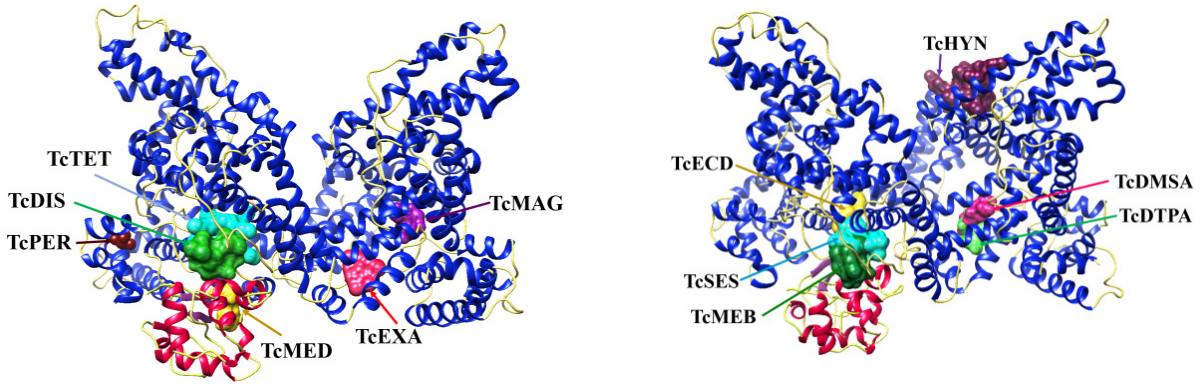

Figure 2. Structures of the most stable TCC complexes with HSA-Lz assemblies

The binding sites for TcMEB and TcDIS in the HSA-Lz complexes differ significantly from those on albumin alone, involving residues from both HSA and Lz. Specifically, interaction domain involves GLU_{505}, HSD_{510}, LYS_{524}, THR_{527} of HSA and ARG_5, LYS_{33}, TRP_{34}, TYR_{38}, GLN_{123}, TYR_{124} of Lz (Fig. 2). These findings imply that Lz may act as a structural modulator of HSA, potentially facilitating cooperative binding interactions between the two proteins and their ligands.

To further investigate the impact of Lz on drug delivery systems, we employed a multiple ligand docking approach to explore ternary ((HSA/HSA-Lz)-TCC-DOX) and quaternary (protein-TCC-DOX-FD) protein-ligand systems. The ternary systems were obtained by docking doxorubicin (DOX) to the best-score complexes of TCC with HSA and HSA-Lz (Fig. 3).

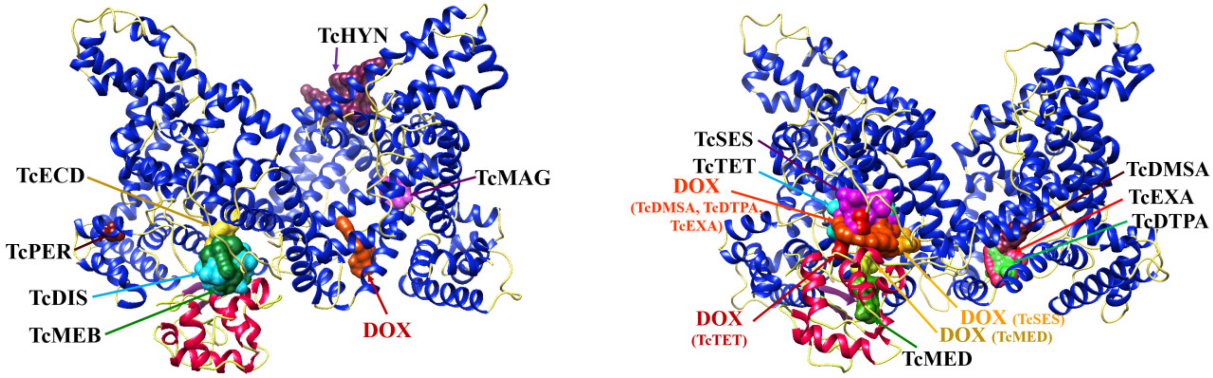

Figure 3. The highest affinity binding sites for DOX in the HSA-Lz-TCC systems

The following features of the ternary systems are worthy of mention: i) when the binding sites for TCC and DOX on HSA do not overlap, DOX binds to a site within domain I of the HSA molecule, spanning 16 residues between PRO_{113} and ARG_{186} (designated as site $HSA_{113\text{-}186}$); ii) when the binding sites overlap, as seen with TcMED, TcEXA, TcDMSA, and TcDTPA, DOX binds to an alternative site on HSA that includes 23 amino acid residues between ASP_{107} and GLN_{459}; iii) presence of Lz slightly enhances DOX binding affinity only in systems with TcTET and TcMED; iv) in systems containing Lz, DOX binds to site HSA113-186 in the absence of TCC and with TcMAG, TcECD, TcDIS, TcPER, TcHYN, and TcMEB. However, with other TCCs, the DOX binding site involves residues from both HSA and Lz. These results suggest that Lz may have a stabilizing effect on specific DOX binding sites, possibly due to alterations in protein conformational dynamics or indirect allosteric effects. The presence of Lz appears to promote a more defined and stable binding environment for DOX in certain ternary complexes, potentially influencing drug release kinetics and bioavailability. Further molecular dynamics simulations would be required to elucidate whether these observed changes are due to direct electrostatic interactions, hydrogen bonding stabilization, or shifts in protein secondary structure upon complex formation.

To achieve systems with dual imaging modalities, the best-score protein-TCC-DOX complexes were docked with NIR fluorophores, including methylene blue (MB), indocyanine green (IG), heptamethine cyanine dye AK7-5, and squaraine dye SQ1. Comparison of the docking results for quaternary systems (protein + TCC + DOX + FD) shows that the affinities of the examined dyes for HSA/HSA-DOX decrease in the following order: IG (BDS = -207.2 / -190.3) > SQ1 (BDS = -186.1 / -185.9) > AK7-5 (BDS = -162.4 / -162.9) > MB (BDS = -127.1 / -117.3). While the amino acid composition of FD binding sites varies among different TCCs and protein components, key residues that predominantly interact with FD can be identified. Notably, the albumin site spanning 12 residues between LEU_{115} and ARG_{186} (site $HSA_{115\text{-}186}$) is the preferred site for MB binding in HSA-DOX, HSA-TCC-DOX, and HSA-Lz-DOX complexes. In contrast, MB binding sites in HSA-Lz-TCC-DOX systems involve residues from both HSA and Lz (Table 2).

Table 2. The interface amino acid residues and the types of interactions involved in the binding of MB to HSA-Lz-TCC-DOX complexes

Complex	HSA-Lz-TCC- DOX-MB interface residues		Type of interactions
	HSA	LYS	
HSA-Lz-MB	LEU_{115A*}, VAL_{116A}, ARG_{117A}, PRO_{118A}, VAL_{122A}, MET_{123A}, ALA_{126A}, PHE_{134A}, LYS_{137A}, TYR_{138A}, GLU_{141A}, ILE_{142A}, TYR_{161A}, ARG_{186A}		Hydrophobic interactions, π-stacking
HSA-Lz-DOX-MB	VAL_{116B}, ARG_{117B}, PRO_{118B}	GLU_{35}, ASN_{44}, ASN_{46}, ASP_{53}, GLN_{58}, ASN_{60}, ARG_{62}, TYR_{63}, TRP_{64}, ALA_{108}, TRP_{109}, VAL_{110}	Hydrophobic interactions, π-stacking
HSA-Lz-TcSES-DOX-MB	ARG_{117B}, MET_{123B}, PHE_{134B}, LYS_{137B}, TYR_{138B}, GLU_{141B}, ILE_{142B}		Hydrophobic interactions
HSA-Lz-TcTET-DOX-MB	THR_{243B}, GLY_{248B}	LYS_{33}	Hydrophobic interactions
HSA-Lz-TcMED-DOX-MB	VAL_{116B}, ARG_{117B}, PRO_{118B}	GLU_{35}, ASN_{44}, ASN_{46}, ASP_{53}, GLN_{58}, ASN_{60}, ARG_{62}, TYR_{63}, TRP_{64}, ALA_{108}, TRP_{109}, VAL_{110}	Hydrophobic interactions, π-stacking
HSA-Lz-TcMAG-DOX-MB	VAL_{116B}, ARG_{117B}, PRO_{118B}	GLU_{35}, ASN_{44}, ASN_{46}, ASP_{53}, GLN_{58}, ASN_{60}, ARG_{62}, TYR_{63}, TRP_{64}, ALA_{108}, TRP_{109}, VAL_{110}	Hydrophobic interactions, π-stacking
HSA-Lz-TcEXA-DOX-MB	PRO_{421B}, HSD_{510B}, LYS_{524B}		Hydrophobic interactions

Complex	HSA-Lz-TCC- DOX-MB interface residues		Type of interactions
	HSA	LYS	
HSA-Lz-TcECD-DOX-MB	VAL_{116B}, ARG_{117B}, PRO_{118B}	GLU_{35}, ASN_{44}, ASN_{46}, ASP_{53}, GLN_{58}, ASN_{60}, ARG_{62}, TYR_{63}, TRP_{64}, ALA_{108}, TRP_{109}, VAL_{110}	Hydrophobic interactions, π-stacking
HSA-Lz-TcDMSA-DOX-MB	VAL_{116B}, ARG_{117B}, PRO_{118B}	GLU_{35}, ASN_{44}, ASN_{46}, ASP_{53}, GLN_{58}, ASN_{60}, ARG_{62}, TYR_{63}, TRP_{64}, ALA_{108}, TRP_{109}, VAL_{110}	Hydrophobic interactions, π-stacking
HSA-Lz-TcDIS-DOX-MB	VAL_{116B}, ARG_{117B}, PRO_{118B}	GLU_{35}, ASN_{44}, ASN_{46}, ASP_{53}, GLN_{58}, ASN_{60}, ARG_{62}, TYR_{63}, TRP_{64}, ALA_{108}, TRP_{109}, VAL_{110}	Hydrophobic interactions, π-stacking
HSA-Lz-TcPER-DOX-MB	VAL_{116B}, PRO_{118B}	GLU_{35}, ASN_{44}, ASN_{46}, ASP_{53}, GLN_{58}, ASN_{60}, ARG_{62}, TYR_{63}, TRP_{64}, ALA_{108}, TRP_{109}, VAL_{110}	Hydrophobic interactions, π-stacking
HSA-Lz-TcDTPA-DOX-MB	PRO_{421B}, HSD_{510B}, LYS_{524B}		Hydrophobic interactions
HSA-Lz-TcHYN-DOX-MB	VAL_{116B}, ARG_{117B}, PRO_{118B}	GLU_{35}, ASN_{44}, ASN_{46}, ASP_{53}, GLN_{58}, ASN_{60}, ARG_{62}, TYR_{63}, TRP_{64}, ALA_{108}, TRP_{109}, VAL_{110}	Hydrophobic interactions, π-stacking
HSA-Lz-TcMEB-DOX-MB	VAL_{116B}, ARG_{117B}, PRO_{118B}	GLU_{35}, ASN_{44}, ASN_{46}, ASP_{53}, GLN_{58}, ASN_{60}, ARG_{62}, TYR_{63}, TRP_{64}, ALA_{108}, TRP_{109}, VAL_{110}	Hydrophobic interactions, π-stacking

*-A and B denote monomer subunits of the HSA dimer

A remarkable characteristic of the HSA binding sites for IG is the consistent presence of three identical amino acid residues: ARG_{114A}, PRO_{421A} (with the exception of the system involving TcEXA), and ILE_{523A}. In contrast, the IG binding sites within HSA-Lz-TCC-DOX systems exhibit a higher degree of heterogeneity (Fig. 4). This observation suggests that Lz may introduce variability in fluorophore binding preferences, possibly due to subtle changes in local electrostatic potential or steric hindrance effects.

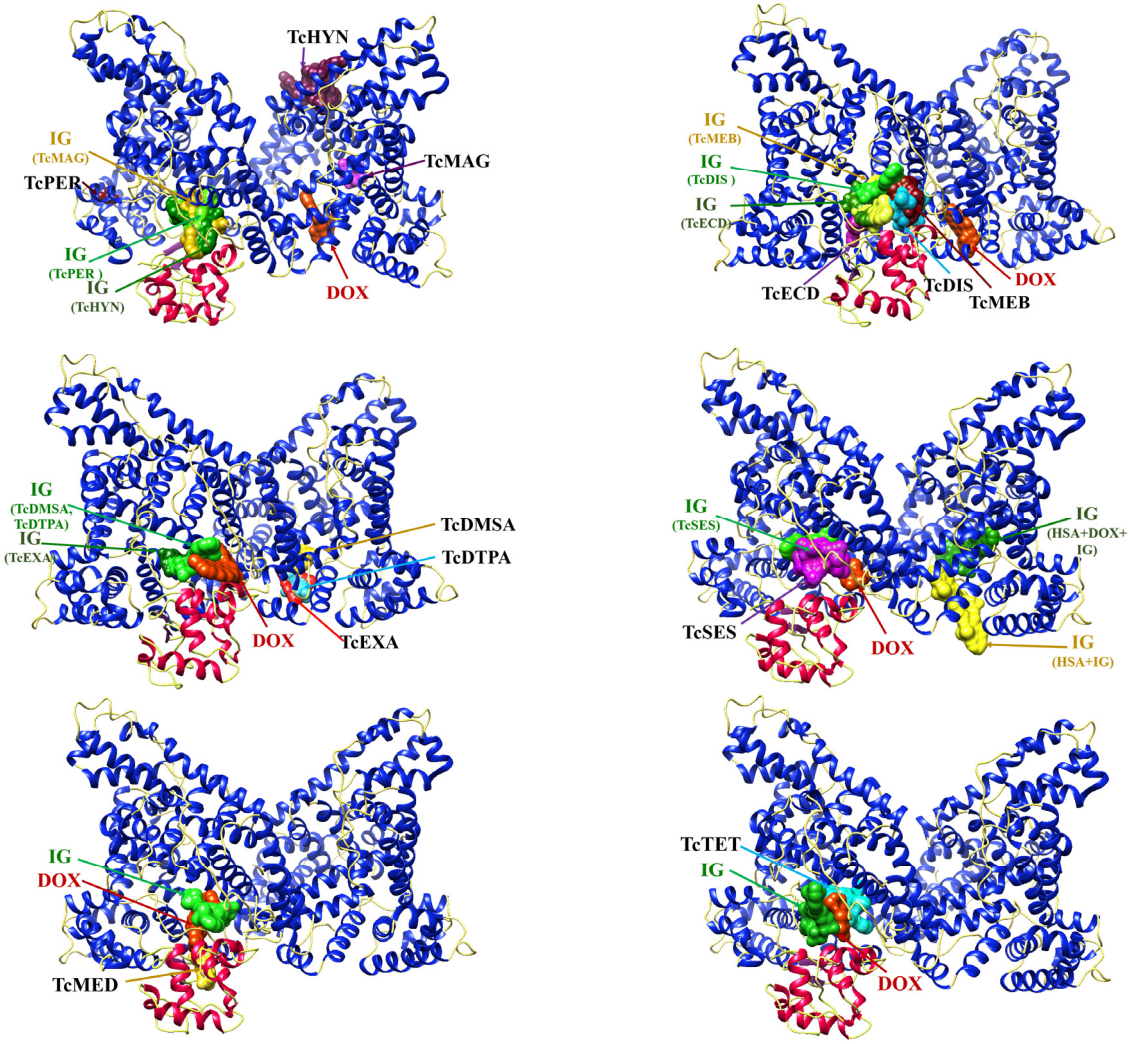

Figure 4. The most energetically favorable docking poses in the complexes HSA-Lz-TCC-DOX-IG

Notably, IG binding affinities are markedly higher in Lz-containing systems compared to HSA alone. This enhanced affinity could be attributed to the structural modifications induced by Lz, which may expose additional binding sites or alter the electrostatic properties of the protein surface. The interaction of AK7-5 with HSA occurs through sites composed of 18 (site HSA115-523) or 12 amino acid residues from albumin domains I and III, with the most pronounced increases in binding affinity observed in the systems HSA-Lz-TcSES-DOX and HSA-Lz-TcTET-DOX. These findings highlight the potential role of Lz in modulating fluorescence imaging properties within dual-modality drug delivery systems, opening avenues for further optimization and experimental validation.

Our findings support the hypothesis that the incorporation of lysozyme into albumin-based drug delivery systems can enhance the specificity and stability of TCC and NIR fluorophore binding. The observed changes in binding affinities and sites may be attributed to the structural and electrostatic modifications induced by Lz, which could influence the pharmacokinetics and targeting efficiency of these systems. Further experimental validation is necessary to confirm these hypotheses and explore the potential therapeutic benefits of these hybrid systems. The molecular mechanisms underlying these interactions may involve conformational changes in the protein structure upon complexation with Lz, which could expose new binding sites or alter the accessibility of existing ones. Additionally, the electrostatic properties of the protein surface may be modified, influencing the binding affinities of TCC and NIR fluorophores. These modifications could enhance the stability and specificity of the delivery system, potentially improving its therapeutic efficacy and reducing systemic toxicity.

CONCLUSIONS

Taken together, the results of this study suggest that Lz-containing drug delivery systems may offer enhanced stability and altered binding characteristics for both radionuclide and fluorescent imaging agents. The cooperative interactions observed between HSA and Lz could be further explored to develop novel multimodal nanocarriers with improved pharmacokinetics and targeting capabilities. Future work should focus on molecular dynamics simulations and experimental binding assays to validate the observed docking trends and assess the potential of these systems for clinical translation.

Acknowledgements

This work was supported by the Ministry of Education and Science of Ukraine (the project № ДЗ/174-2025).

ORCID IDs

Valeriya Trusova, https://orcid.org/0000-0002-7087-071X; **Uliana Malovytsia,** https://orcid.org/0000-0002-7677-0779
Galyna Gorbenko, https://orcid.org/0000-0002-0954-5053; **Andrey Zelinsky,** https://orcid.org/0000-0002-4110-8523
Borys Borts, https://orcid.org/0000-0002-1492-4066; **Pylyp Kuznietsov,** https://orcid.org/0000-0001-8477-1395
Ivan Yakymenko, https://orcid.org/0000-0001-8477-1395

REFERENCES

[1] C. Li, Z. Wang, H. Lei, and D. Zhang, Drug Deliv. **30**, 2174206 (2023). https://doi.org/10.1080/10717544.2023.2174206
[2] P. Trucillo, Processes **9**, 470 (2021). https://doi.org/10.3390/pr9030470
[3] A. Spada, J. Emami, J. Tuszynski, and A. Lavasanifar, The uniqueness of albumin as a carrier in nanodrug delivery, Mol. Pharmaceut. 18, 1862. https://doi.org/10.1021/acs.molpharmaceut.1c00046
[4] V. Trusova, U. Tarabara, I. Karnaukhov, A. Zelinsky, B. Borts, I. Ushakov, L. Sidenko, and G. Gorbenko, East Eur. J. Phys. (4), 447 (2024). https://doi.org/10.26565/2312-4334-2024-4-54
[5] V. Trusova, U. Malovytsia, P. Kuznietsov, I. Karnaukhov, A. Zelinsky, B. Borts, I. Ushakov, *et al*., East Eur. J. Phys. (1), 376 (2025). https://doi.org/10.26565/2312-4334-2025-1-46
[6] R. Halaby, Cancer Drug Resist. **2**, 31 (2019). http://dx.doi.org/10.20517/cdr.2018.23
[7] B. Zhitomirsky, and Y. Assaraf, Oncotarget, **8**, 45117 (2017). http://dx.doi.org/10.18632/oncotarget.15155
[8] I. Schadt, and V. Marino, Curr. Res. Cmpl. Alt. Med. **7**, 188 (2023). https://doi.org/10.29011/2577-2201.100088
[9] P. Ojha, N. Kar, H. Behera, M. Parija, S. Nayak, S. Singh, A. Patra, and K. Sahoo, Biotech. **13**, 240 (2023). https://doi.org/10.29011/2577-2201.100088
[10] M.F. Adasme, K.L. Linnemann, S.N. Bolz, F. Kaiser, S. Salentin, V.J. Haupt, and M. Schroeder, Nucl. Acids Res. **49**, W530-W534 (2021). https://doi.org/10.1093/nar/gkab294

КОМП'ЮТЕРНЕ ДОСЛІДЖЕННЯ СИСТЕМ ДОСТАВКИ ЛІКІВ З РАДІОНУКЛІДНИМИ ТА ФЛУОРЕСЦЕНТНИМИ МОДАЛЬНОСТЯМИ ВІЗУАЛІЗАЦІЇ. ІІІ. СИСТЕМИ НА ОСНОВІ АЛЬБУМІНУ ТА ЛІЗОЦИМУ ДЛЯ ДОСТАВКИ ДОКСОРУБІЦИНУ

В. Трусова[a], У. Маловиця[a], П. Кузнєцов[b], І. Якименко[b], І. Карнаухов[c], А. Зелінський[c], Б. Борц[c], І. Ушаков[c], Л. Сіденко[c], Г. Горбенко[a]

[a]Кафедра медичної фізики та біомедичних нанотехнологій, Харківський національний університет імені В.Н. Каразіна м. Свободи 4, Харків, 61022, Україна
[b]Кафедра фізики ядра та високих енергій імені О.І. Ахієзера, Харківський національний університет імені В.Н. Каразіна м. Свободи 4, Харків, 61022, Україна
[c]Національний науковий центр «Харківський фізико - технічний інститут», Харків, вул. Академічна, 1, 61108, Україна

Дане дослідження присвячене розробці білкових систем доставки лікарських засобів для доксорубіцину (DOX) шляхом інтеграції лізоциму в носії на основі альбуміну, що включають як радіонуклідні (комплекси технецію-99m), так і флуоресцентні (барвники ближнього інфрачервоного діапазону) методи візуалізації. Використовуючи метод молекулярного докінгу, було досліджено спорідненість зв'язування та сайти комплексів технецію-99m і флуоресцентних барвників ближнього інфрачервоного діапазону в гібридних білкових системах. Результати демонструють, що включення лізоциму суттєво модулює ландшафт зв'язування, підвищуючи специфічність і стабільність комплексів технецію та флуоресцентних барвників. Зокрема, спорідненість зв'язування індоціаніну зеленого була значно вищою в системах, що містять лізоцим, що свідчить про покращення можливостей візуалізації. Крім того, аналіз виявив різні сайти зв'язування для доксорубіцину в присутності різних комплексів технецію, що може впливати на вивільнення препарату та його терапевтичну ефективність. Ці результати підтверджують потенціал гібридних систем альбумін-лізоцим як наноносіїв із подвійними можливостями візуалізації для доставки DOX, пропонуючи перспективний підхід до підвищення терапевтичної ефективності при одночасному зниженні системної токсичності в протиракову лікуванні та сприяючи розробці більш складних і цільових платформ доставки для терапії раку.

Ключові слова: *наносистеми доставки ліків на основі білків; людський сироватковий альбумін; лізоцим; доксорубіцин; комплекси технецію; інфрачервоні барвники; молекулярний докінг*

East European Journal of Physics. 2. 405-411 (2025)
DOI:10.26565/2312-4334-2025-2-49 ISSN 2312-4334

IN SILICO CHARACTERIZATION OF TECHNETIUM-99M RADIOTRACERS: ADMET PROPERTIES AND PROTEIN INTERACTION PROFILES

V. Trusova[a]*, U. Malovytsia[a], P. Kuznietsov[b], I. Yakymenko[b], G. Gorbenko[a]
[a]*Department of Medical Physics and Biomedical Nanotechnologies, V.N. Karazin Kharkiv National University 4 Svobody Sq., Kharkiv, 61022, Ukraine*
[b]*O.I. Akhiezer Department for Nuclear Physics and High Energy Physics, V.N. Karazin Kharkiv National University 4 Svobody Sq., Kharkiv, 61022, Ukraine*
**Corresponding Author: valerija.trusova@karazin.ua*
Received February 28, 2025, revised March 17, 2025; accepted April 30, 2025

The rational design of technetium-99m (^{99m}Tc)-based radiopharmaceuticals requires a nuanced understanding of how physicochemical properties influence *in vivo* behavior and molecular interactions. In this study, we employed an integrated *in silico* framework to characterize ten clinically relevant ^{99m}Tc-labeled tracers using ADMET prediction, molecular docking with functional proteins (albumin, insulin, lysozyme), and multivariate statistical analysis. The results revealed that polarity, hydrogen bonding capacity, and molecular flexibility critically govern both pharmacokinetic properties and protein-binding profiles. Tracers such as TcSES and TcTET, with low topological polar surface area and minimal binding affinity, were associated with rapid clearance and are well suited for dynamic imaging protocols. In contrast, compounds like TcDTPA and TcDIS demonstrated strong albumin interaction and metabolic stability, supporting their use in delayed-phase imaging. TcHYN emerged as a unique tracer, exhibiting extreme polarity and promiscuous high-affinity binding across multiple protein targets. Principal component analysis and hierarchical clustering grouped tracers into functionally distinct categories, highlighting structure-dependent design trends. Collectively, these findings suggest that combined ADMET-docking profiling offers a scalable strategy for preclinical evaluation and supports the development of safer, more targeted ^{99m}Tc-based radiopharmaceuticals.
Keywords: *Technetium-based radiotracers; Human serum albumin; Lysozyme; Insulin; Molecular docking; SPECT imaging*
PACS: 87.14.C++c, 87.16.Dg

Radiotracers based on technetium-99m (^{99m}Tc) remain at the forefront of diagnostic nuclear medicine, enabling non-invasive visualization of physiological and pathological processes across a broad spectrum of clinical applications [1]. Their widespread use is underpinned by favorable nuclear properties, well-established radiochemistry, and ability to tailor molecular structures for targeted imaging of specific organs and disease states. However, the continual evolution of molecular imaging demands rigorous preclinical evaluation of new and existing radiotracers to optimize their pharmacokinetic behavior, safety, and diagnostic efficacy. Along with high target specificity, the effective design of radiopharmaceuticals necessitates optimal biodistribution, metabolic stability, minimal off-target toxicity, and favorable protein-binding characteristics. In particular, interactions with transport and carrier proteins, such as serum albumin, insulin, and lysozyme, can profoundly influence plasma retention, tissue delivery, and imaging contrast [2]. However, systematic molecular-level comparisons across multiple ^{99m}Tc compounds are rarely undertaken, in part due to the cost and complexity of experimental pharmacological profiling. In this context, *in silico* methodologies offer a compelling alternative. In particular, advanced platforms such as ADMETlab 3.0 enable high-throughput prediction of absorption, distribution, metabolism, excretion, and toxicity (ADMET) properties [3], while molecular docking allows for detailed interrogation of tracer-protein interactions at atomic resolution. When used in concert, these tools provide a multidimensional framework for evaluating the safety, efficacy, and mechanistic underpinnings of radiopharmaceuticals. The present work is directed at comprehensive *in silico* characterization of clinically relevant ^{99m}Tc-based tracers, integrating ADMET predictions with molecular docking against three functionally relevant proteins, human serum albumin, insulin, and lysozyme. Our aim is to uncover structure-dependent trends in pharmacokinetics and binding profiles, offering mechanistic insights that may guide future tracer design and optimization strategies.

METHODS

A representative set of ten clinically utilized technetium-99m (^{99m}Tc)-based radiopharmaceuticals was selected to capture structural diversity across approved diagnostic agents. The compounds analyzed included [^{99m}Tc]Tc-Sestamibi (TcSES), [^{99m}Tc]Tc-Tetrofosmin (TcTET), [^{99m}Tc]Tc-Medronate (TcMED), [^{99m}Tc]Tc-dimercaptosuccinic acid (TcDMSA), [^{99m}Tc]Tc-diethylenetriaminepentaacetate (TcDTPA), [^{99m}Tc]Tc-mercaptoacetyltriglycine (TcMAG), [^{99m}Tc]Tc-diisopropyl iminodiacetic acid (TcDIS), [^{99m}Tc]Tc-ethylene cysteine dimer (TcECD), [^{99m}Tc]Tc-Mebrofenin (TcMEB), and [^{99m}Tc]Tc-hydrazinonicotinic acid conjugate-H6F (TcHYN). Physicochemical and pharmacokinetic parameters were predicted using ADMETlab 3.0 (https://admetlab3.scbdd.com/), an integrated platform for the data-driven prediction of ADME and toxicity profiles. Each compound was converted to a canonical SMILES representation

Cite as: V. Trusova, U. Malovytsia, P. Kuznietsov, I. Yakymenko, G. Gorbenko, East Eur. J. Phys. 2, 405 (2025), https://doi.org/10.26565/2312-4334-2025-2-49

and processed through the platform to retrieve a comprehensive panel of descriptors. Predicted parameters included molecular weight, topological polar surface area (TPSA), partition coefficient (logP), hydrogen bond donors and acceptors, number of rotatable bonds, and absorption-related features such as human intestinal absorption (HIA) and Caco-2 permeability. Additional metrics included plasma protein binding (PPB), volume of distribution (VDss), blood-brain barrier (BBB) penetration, hepatic microsomal stability (HLM), total plasma clearance (CL), and biological half-life ($T_{1/2}$). Toxicity endpoints, including AMES mutagenicity, hERG inhibition, drug-induced liver injury (DILI), skin sensitization, and carcinogenicity, were also assessed. Three biologically relevant proteins, human serum albumin (PDB ID 1AO6), human insulin (PDB ID 4EYN), and human lysozyme (PDB ID 8Y9W), were selected as docking targets to evaluate potential interactions of ^{99m}Tc-tracers with endogenous carrier and regulatory proteins. Prior to docking, each protein structure was subjected to 10 ns molecular dynamics relaxation using a standard explicit solvent protocol to ensure conformational stabilization. Relaxation simulations were performed with position restraints applied to backbone atoms and standard temperature and pressure conditions. Molecular docking simulations were performed using the HDOCK server (https://hdock.phys.hust.edu.cn/) [4], a hybrid docking platform integrating template-based modeling and free docking via a fast FFT-based algorithm. All ligands were submitted as energy-minimized structures. For each protein-ligand pair, blind docking was conducted to explore global interaction surfaces.

RESULTS AND DISCUSSION

Due to the diversity of their chelating ligands and pharmacophore groups, TCC exhibit substantial chemical heterogeneity. This complexity underlies their varying pharmacokinetics, biodistribution, and safety profiles. To systematize this variability, we conducted a high-throughput computational analysis of ten clinically employed ^{99m}Tc-labeled compounds using the ADMETlab 3.0 platform, focusing on key descriptors of absorption, distribution, metabolism, excretion, and toxicity (ADMET). The results are given in Table 1.

Table 1. ADMET properties of ^{99m}Tc-based radiopharmaceuticals

		TcSES	**TcTET**	**TcMED**	**TcDMSA**	**TcDTPA**	**TcMAG**	**TcDIS**	**TcECD**	**TcMEB**	**TcHYN**
Physicochemical properties	Molecular weight	113.08	382.24	173.95	181.97	393.14	259.03	350.18	321.1	386.05	1252.6
	TPSA	13.59	36.92	120.72	74.6	196.22	133.64	106.94	78.73	106.94	438.63
	logP	1.084	2.179	-2.092	0.4	-0.914	0.34	0.055	1.561	-0.003	1.334
	Number of hydrogen bond acceptors	2	4	6	4	13	8	7	6	7	27
	Number of hydrogen bond donors	0	0	2	2	5	0	3	1	3	16
	Number of rotatable bonds	2	19	2	3	16	10	10	13	8	45
Absorption	HIA	0.018	0.028	0.964	0.317	1	0.016	0.798	0.009	0.445	0.606
	Caco-2 permeability	-4.727	-5.189	-5.94	-4.884	-5.195	-4.821	-5.16	-5.542	-5.305	-6.215
	P-gp substrate	0.063	0.094	0	0.002	0	0.001	0	0	0	0.003
Distribution	VDss	0.115	0.028	-0.26	-0.171	-0.54	-0.413	-0.278	0.199	0.075	-0.578
	BBB permeability	0.285	0.096	0	0.001	0	0.216	0	0	0	0
	PPB	27.95	12.97	12.224	94.613	14.538	7.819	92.556	57.144	97.438	77.494
Metabolism	CYP2D6 inhibitor	0	0.38	0	0	0	0	0	0	0	0
	CYP3A4 inhibitor	0	0.408	0	0	0	0	0	0.59	0	0
	HLM stability	0	0.755	0.003	0.286	0.077	0.002	0.953	0.989	0.21	0
Excretion	CL_{plasma}	10.213	8.257	1.518	1.953	1.464	2.021	2.346	5.701	2.088	0.844
	$T_{1/2}$	1.739	0.797	2.224	1.97	1.528	1.801	1.158	0.784	1.264	1.563
Toxicity	AMES	1	0.023	0.078	0.332	0.514	0.782	0.149	0.935	0.172	0.046
	hERG	1	0.728	0.269	0.181	0.033	0.013	0.165	0.004	0.093	0.052
	DILI	0.116	0.006	0.467	0.974	0.331	0.779	0.142	1	0.222	0.91
	Skin sensitization	1	0.991	0.997	0.857	0.774	1	0.951	1	0.98	0.557
	Carcinogenicity	1	0.409	0.987	0.009	0.138	0.196	0.853	0.032	0.883	0.574

As seen from this table, the examined TCC are characterized by a broad distribution in molecular weight (113.08-1252.6 Da), topological polar surface area (TPSA 13.59-438.63 Å^2), and lipophilicity (logP; from -2.092 to 2.179). As expected, two cationic, lipophilic agents used for myocardial perfusion imaging, TcSES and TcTET, exhibited low polarity (TPSA < 40 Å^2), moderate lipophilicity, and minimal hydrogen bonding potential. These values align closely with their

experimentally established passive membrane permeability and mitochondrial accumulation [5]. In contrast, highly polar tracers such as TcDTPA and TcHYNIC demonstrated elevated TPSA and rotatable bond counts, aligning with their renal clearance and low membrane permeability [6]. Predicted absorption characteristics were found to correlate also with the reported clinical behavior of TCC. High human intestinal absorption (HIA > 0.75) was observed for TcDIS and TcMED, the tracers previously evaluated for enteral administration under experimental protocols. In contrast, TCC with reduced HIA and Caco-2 permeability (e.g., TcHYNIC, TcDTPA) are administered strictly via intravenous routes, consistent with their poor predicted epithelial transport.

Analysis of the systemic distribution revealed general low tissue accumulation, as can be judged from the values of VDss which are ranged from -0.578 to 0.199 L/kg. Notably, only TcSES and TcMAG exhibited predicted blood-brain barrier (BBB) penetration probabilities above the threshold of 0.2, being in partial agreement with prior studies reporting minimal but detectable cerebral uptake for lipophilic cationic complexes. Predicted plasma protein binding (PPB) was also dependent in TCC chemical structure. Specifically, TcMEB, TcDIS and TcDMSA showed PPB > 90%, which is in line with empirical data confirming strong affinity to serum albumin [7], whereas TcMAG and TcTET exhibited lower predicted values (<15%), suggesting more rapid plasma clearance.

Predicted hepatic microsomal stability (HLM) also varied markedly across tracers. TcDIS and TcECD exhibited high metabolic stability (HLM > 0.95), consistent with renal excretion, whereas TcSES and TcMAG showed minimal stability, aligning with their known hepatobiliary clearance [8,9]. These metabolic trends were reflected in plasma clearance values, with TcSES demonstrating the highest systemic turnover (10.2 mL/min/kg). All compounds exhibited half-lives within the clinically favorable range (0.78-2.22 h), balancing imaging efficiency and radiation safety. TcTET and TcECD showed the shortest predicted half-lives, supporting their utility in dynamic protocols. Toxicity predictions revealed elevated hERG inhibition risk for TcSES and TcTET, likely due to their cationic lipophilicity and mitochondrial affinity. TcECD and TcHYNIC were associated with high DILI risk, while TcMED and TcMEB showed increased carcinogenicity potential. These findings warrant further *in vivo* validation, particularly for tracers considered for repeated or high-dose use.

To explore molecular determinants of tracer-protein interactions, we next conducted docking simulations against human serum albumin (HSA), lysozyme (HLz), and insulin (HIns). The best scored docking poses of the protein-TCC complexes are presented in Fig. 1.

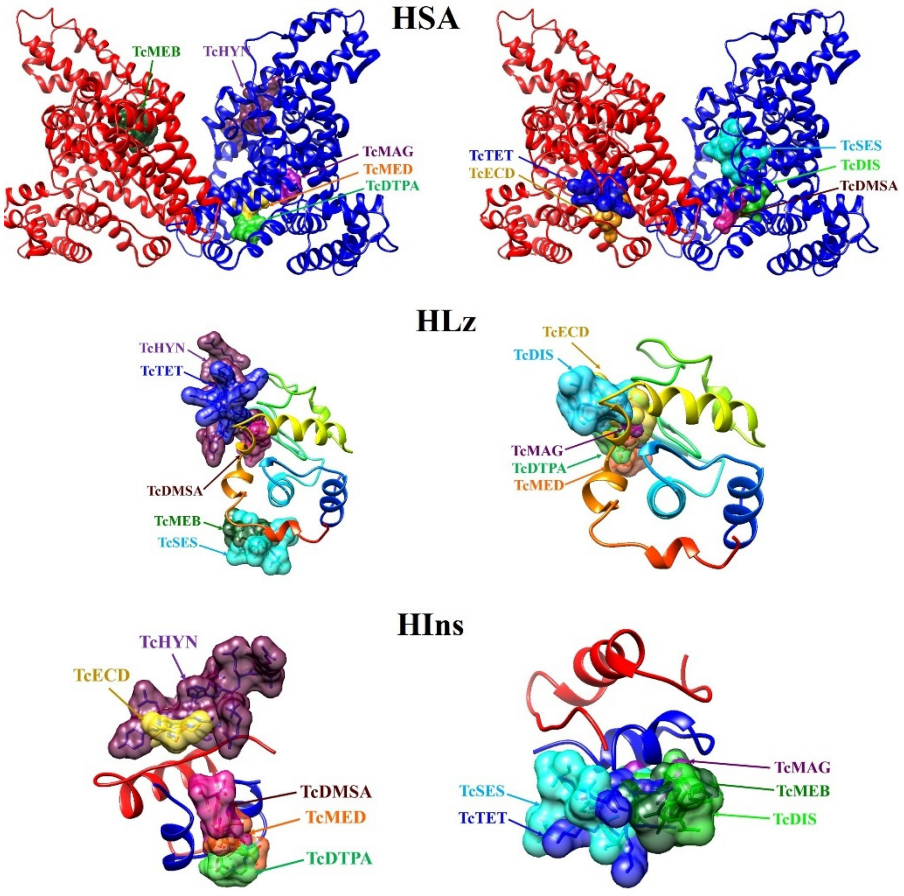

Figure 1. Best docking poses of the protein-TCC complexes

The resulting interaction scores and interface maps revealed compound-specific trends in affinity, interaction types, and binding site architecture (Tables 2-5). The analysis of the obtained data revealed marked differences in binding

affinity, interaction type, and binding site localization. Accordingly, TcHYN exhibited the strongest affinity across all targets (-249.5 for HSA, -194.8 for HLz, and -163.7 for HIns), driven by its extended π-system, high polar surface area, and flexible coordination geometry. TcDTPA and TcDIS also showed strong binding, particularly to albumin, reflecting their polyanionic nature and multivalent hydrogen bonding. In contrast, TcSES and TcTET displayed weaker binding, particularly to insulin, suggesting passive diffusion may be their dominant transport mechanism.

Table 2. Binding affinities of technetium-99m radiopharmaceuticals for functional proteins

TCC	Albumin	Lysozyme	Insulin
TcSES	-148.84	-138.37	-116.92
TcTET	-141.24	-126.06	-121.66
TcMED	-137.01	-133.67	-96.81
TcMAG	-137.33	-127.38	-105.69
TcECD	-137.71	-120.27	-99.43
TcDMSA	-156.73	-132.46	-100.25
TcDIS	-170.32	-162.07	-143.44
TcDTPA	-182.8	-149.79	-129.09
TcHYN	-249.51	-194.79	-163.74
TcMEB	-159.93	-153.45	-137.67

Table 3. Interface residues in the complexes of technetium-99m radiopharmaceuticals with human serum albumin

TCC	**HSA-TCC interface residues**	**Type of interactions**
TcSES	TYR_{150A}, GLU_{153A}, PHE_{156A}, PHE_{157A}, ARG_{160A}, GLU_{188A}, ALA_{191A}, SER_{192A}, LYS_{195A}, GLN_{196A}, LYS_{199A}, ARG_{218A}, ARG_{222A}, HSD_{288A}, GLU_{292A}, VAL_{293A}, LYS_{436A}, HSD_{440A}, TYR_{452A}	Hydrophobic interactions, hydrogen bonds
TcTET	ASN_{109B}, ARG_{114B}, LEU_{115B}, ARG_{145B}, LYS_{190B}, GLU_{425B}, ARG_{428B}, GLU_{520B}, ILE_{523B}	Hydrophobic interactions, hydrogen bonds
TcMED	LEU_{115A}, ARG_{117A}, TYR_{138A}, ILE_{142A}, HSD_{146A}, PHE_{149A}, LEU_{154A}, PHE_{157A}, TYR_{161A}, LEU_{182A}, ASP_{183A}, LEU_{185A}, ARG_{186A}, ASP_{187A}, GLY_{189A}, LYS_{190A}	Hydrogen bonds
TcMAG	ASP_{107A}, ASP_{108A}, ASN_{109A}, ARG_{145A}, HSD_{146A}, PRO_{147A}, TYR_{148A}, LYS_{190A}, ALA_{191A}, SER_{193A}, ALA_{194A}, ARG_{197A}, GLU_{425A}, ASN_{458A}, GLN_{459A}	Hydrogen bonds, salt bridges
TcECD	LEU_{115B}, ARG_{117B}, PRO_{118B}, MET_{123B}, PHE_{134B}, LYS_{137B}, TYR_{138B}, GLU_{141B}, ILE_{142B}, TYR_{161B}, LEU_{182B}, ASP_{183B}, LEU_{185B}, ARG_{186B}	Hydrophobic interactions, hydrogen bonds, salt bridges
TcDMSA	LEU_{115A}, VAL_{116A}, ARG_{117A}, PRO_{118A}, MET_{123A}, TYR_{138A}, ILE_{142A}, HSD_{146A}, PHE_{149A}, LEU_{154A}, PHE_{157A}, TYR_{161A}, LEU_{182A}, LEU_{185A}, ARG_{186A}, ASP_{187A}, GLU_{188A}, GLY_{189A}, LYS_{190A}	Hydrogen bonds, salt bridges
TcDIS	ASN_{109A}, PRO_{110A}, LEU_{112A}, ARG_{114A}, LEU_{115A}, ARG_{145A}, HSD_{146A}, ARG_{186A}, LYS_{190A}, PRO_{421A}, GLU_{425A}, GLU_{520A}, ILE_{523A}	Hydrophobic interactions, hydrogen bonds
TcDTPA	LEU_{115A}, VAL_{116A}, ARG_{117A}, PRO_{118A}, MET_{123A}, PHE_{134A}, LEU_{135A}, LYS_{137A}, TYR_{138A}, GLU_{141A}, ILE_{142A}, TYR_{161A}, LEU_{182A}, ARG_{186A}	Hydrogen bonds, salt bridges
TcHYN	GLU_{383A}, LEU_{387A}, ASN_{391A}, LEU_{394A}, LEU_{407A}, VAL_{409A}, ARG_{410A}, TYR_{411A}, LEU_{430A}, LEU_{453A}, GLU_{492A}, SER_{489A}, LYS_{541A}, GLU_{542A}, LYS_{545A}	Hydrogen bonds, π-stacking, salt bridges
TcMEB	GLU_{188B}, LYS_{195B}, TRP_{214B}, ARG_{218B}, GLN_{221B}, ARG_{222B}, GLU_{292B}, VAL_{293B}, GLU_{294B}, ASN_{295B}, LYS_{436B}, HSD_{440B}, LYS_{444B}, PRO_{447B}, CYS_{448B}, ALA_{449B}, ASP_{451B}, TYR_{452B}	Hydrophobic interactions, hydrogen bonds, salt bridges

Table 4. Interface residues in the complexes of technetium-99m radiopharmaceuticals with human lysozyme

TCC	**HLz-TCC interface residues**	**Type of interactions**
TcSES	ARG_5 CYS_{30} LYS_{33} TRP_{34} TYR_{38} ARG_{115} CYS_{116} ARG_{119} ASP_{120} VAL_{121} ARG_{122} GLN_{123} TYR_{124}	Hydrogen bonds, hydrophobic interactions
TcTET	TYR_{63}, VAL_{74}, ASN_{75}, ARG_{107}	Hydrophobic interactions
TcMED	GLU_{35} ASN_{44} ASN_{46} SER_{51} ASP_{53} GLN_{58} ILE_{59} ASN_{60} ALA_{108} TRP_{109} VAL_{110} ALA_{111}	Hydrogen bonds
TcMAG	GLU_{35} ASN_{46} ASP_{49} SER_{51} ASP_{53} GLN_{58} ILE_{59} ASN_{60} ARG_{62} TYR_{63} TRP_{64} ALA_{108} TRP_{109}	Hydrogen bonds
TcECD	GLU_{35} ASN_{44} ASN_{46} ASP_{49} ASP_{53} GLN_{58} ILE_{59} ASN_{60} SER_{61} ARG_{62} TYR_{63} TRP_{64} VAL_{99} GLY_{105} ALA_{108} TRP_{109} VAL_{110}	Hydrogen bonds

TCC	HLz-TCC interface residues	Type of interactions
TcDMSA	GLU_{35} ASN_{44} ASN_{46} ASP_{53} GLN_{58} ILE_{59} ASN_{60} SER_{61} ARG_{62} TYR_{63} TRP_{64} VAL_{99} GLY_{105} ALA_{108} TRP_{109} VAL_{110} ALA_{111}	Hydrogen bonds
TcDIS	ASP_{49}, SER_{51}, ASN_{60}, ARG_{62}, TYR63, ASN_{75}, GLY_{105}, ALA_{108}	Hydrogen bonds, hydrophobic interactions
TcDTPA	GLU_{35} ASN_{44} ASN_{46} ASP_{49} SER_{51} ASP_{53} PHE_{57} GLN_{58} ILE_{59} ASN_{60} ARG_{62} TYR_{63} TRP_{64} ALA_{108} TRP_{109} VAL_{110} ALA_{111}	Hydrogen bonds
TcHYN	TYR_{1}, TYR_{63}, ASN_{75}	Hydrogen bonds, hydrophobic interactions, π-stacking
TcMEB	LYS_{33} TRP_{34} ASN_{114} ARG_{115} ARG_{119} ASP_{120} VAL_{121} ARG_{122} GLN_{123} TYR_{124}	Hydrophobic interactions, hydrogen bonds, salt bridges

Table 5. Interface residues in the complexes of technetium-99m radiopharmaceuticals with human insulin

TCC	HIns-TCC interface residues	Type of interactions
TcSES	GLY_{1A} ILE_{2A} GLN_{5A} TYR_{14A} GLN_{15A} ASN_{18A} TYR_{19A} CYS_{20A} ASN_{21A} PHE_{24B} PHE_{25B}	Hydrophobic interactions, hydrogen bonds
TcTET	GLN_{5A}, TYR_{14A}, ASN_{18A}, CYS_{7B}, GLU_{13B}, ALA_{14B}	Hydrophobic interactions, hydrogen bonds
TcMED	ILE_{2A} GLN_{5A} CYS_{6A} SER_{9A} ILE_{10A} TYR_{14A} GLN_{15A} ASN_{18A} TYR_{19A}	Hydrogen bonds
TcMAG	GLN_{5A} SER_{9A} ILE_{10A} CYS_{11A} SER_{12A} TYR_{14A} GLN_{15A} ASN_{18A} TYR_{19A}	Hydrogen bonds
TcECD	SER_{9B} $VAL1_{2B}$ TYR_{16B} PHE_{24B} PHE_{25B} TYR_{26B}	Hydrophobic interactions, hydrogen bonds
TcDMSA	ILE_{2A} GLN_{5A} TYR_{14A} GLN_{15A} ASN_{18A} TYR_{19A} CYS_{20A} ASN_{21A} PHE_{25B}	Hydrogen bonds
TcDIS	GLN_{5A}, SER_{9A}, SER_{12A}, TYR_{14A}, GLN_{15A}, ASN_{18A}, TYR_{19A}, CYS_{7B}, GLU_{13B}, ALA_{14B}	Hydrophobic interactions, hydrogen bonds
TcDTPA	GLN_{5A} CYS_{6A} SER_{9A} ILE_{10A} CYS_{11A} SER_{12A} TYR_{14A} GLN_{15A} ASN_{18A} TYR_{19A}	Hydrogen bonds
TcHYN	TYR_{1A}, CYS_{7B}, GLU_{13B}, ALA_{14B}, TYR_{26B}, THR_{27B}	Hydrogen bonds, hydrophobic interactions, π-stacking
TcMEB	GLU_{4A} GLN_{5A} CYS_{6A} THR_{8A} SER_{9A} ILE_{10A} CYS_{11A} SER_{12A} TYR_{14A} GLN_{15A} ASN_{18A} TYR_{19A}	Hydrophobic interactions, hydrogen bonds

All TCC were characterized by different binding sites within the protein molecules. Specifically, TcHYN was shown to bind to HSA in the Sudlow site II [10] via TYR_{411A} and ARG_{410A} through hydrogen bonding and π-stacking. TcDIS engaged the GLU_{520A}–ILE_{523A} region through hydrophobic and hydrogen bonds contacts. In turn, TcMEB was found to be localized within the chain B of the protein (residues ARG_{218B}–ARG_{222B}, LYS_{436B}–TYR_{452B}), consistent with its known *in vivo* albumin affinity and prolonged circulation. Such interactions are beneficial for stabilizing tracers in the bloodstream and facilitating organ-specific targeting.

Lysozyme binding followed a conserved pattern across high-affinity tracers, with GLU35, $ASN_{44\text{-}60}$, and TYR_{63} commonly involved in hydrogen bonding. TcHYN displayed additional π–π stacking interactions with TYR63 and formed hydrophobic contacts with ASN_{75}, further stabilizing the complex. These interactions appear to be driven by shape complementarity and the presence of polar and aromatic functional groups on the tracer surface, rather than by strong site-specific recognition.

Insulin presented a more selective interaction interface compared to transport proteins, with docking localized to structurally and functionally relevant surface regions. TcHYN and TcDIS demonstrated the highest binding affinities, forming interactions with residues located on the B-chain surface, though not directly with core receptor-binding residues such as PHE_{24B}. Some tracers, including TcSES and TcDMSA, formed hydrogen bonds with TYR_{14A} and GLN_{15A} of the A-chain, situated near the receptor-binding groove. While the low concentrations of radiotracers used in SPECT imaging are unlikely to perturb insulin function, the engagement of tracers with surface-accessible residues adjacent to biologically critical domains reinforces the need for careful evaluation of biochemical neutrality, particularly in the context of metabolic disorders.

To emerge the above findings into a predictive framework, we applied principal component analysis and hierarchical clustering to the combined ADMET and docking dataset. The resulting PCA plot (Fig. 2, left panel) revealed a structured spatial distribution of tracers, with distinct segregation according to molecular polarity, flexibility, metabolic stability, and protein-binding capacity. Hierarchical clustering (Fig. 2, right panel) confirmed the existence of three robust tracer groups, each characterized by a specific pharmacological profile.

The first cluster involves TcDTPA, TcDIS, TcMAG, TcMEB, TcMED, TcDMSA, and TcECD. These tracers demonstrated balanced pharmacokinetic and interaction profiles, characterized by moderate to high polarity, generally favorable hepatic microsomal stability, and intermediate levels of protein binding, primarily to albumin. Their ADMET features support suitability for renal, hepatobiliary, and soft tissue imaging, offering flexibility in both administration protocols and imaging time windows. In turn, cluster 2 includes TcSES and TcTET, which were distinguished by low

topological polar surface area, high lipophilicity, minimal protein interaction, and rapid predicted systemic clearance. These properties reflect their optimization for myocardial perfusion imaging, where fast tracer redistribution and early acquisition are essential for diagnostic accuracy. Their distinct separation in PCA space further reinforces the pharmacological coherence of this cluster and its alignment with established clinical applications. Finally, cluster 3 contains only TcHYN, which was markedly separated from the rest in both PCA and hierarchical clustering analyses. This compound exhibited the highest polarity, the greatest number of hydrogen bond donors and acceptors, extensive conformational flexibility, and strong multivalent protein-binding potential. While these characteristics suggest utility for targeted or long-circulating applications, they also raise concerns regarding non-specific interactions and off-target effects. As such, TcHYN represents a structurally and functionally distinct tracer that warrants further experimental validation *in vivo* before broader application.

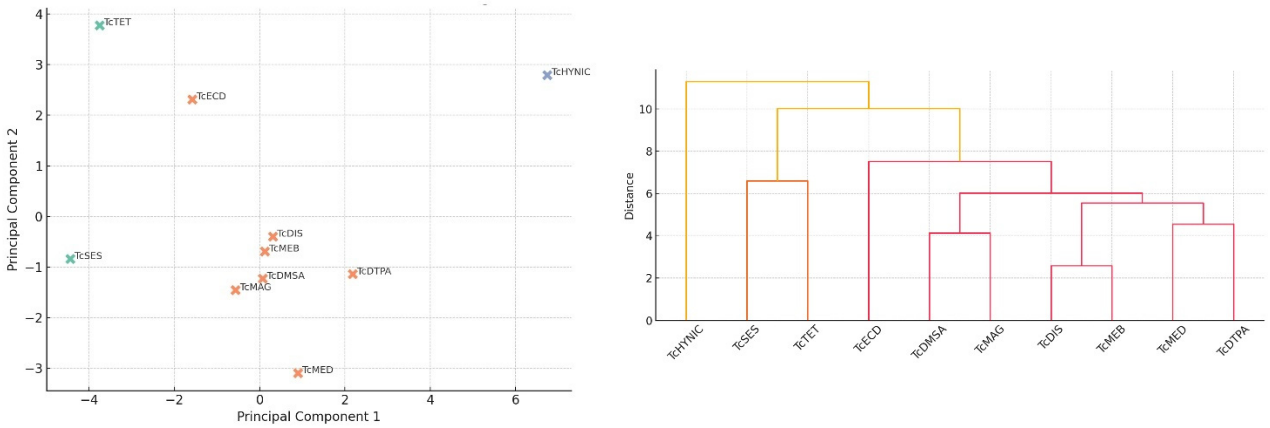

Figure 2. Cluster analysis of TCC. Left panel represents Principal Component Analysis (PCA) biplot showing tracer distribution in the space of the first two principal components. Right panel shows the dendrogram of hierarchical clustering using Ward linkage and Euclidean distance.

The integrated analysis of physicochemical descriptors, ADMET properties, and protein-binding profiles presented in this study yields several design rules for the rational development of ^{99m}Tc-labeled radiopharmaceuticals. First, polarity and permeability must be carefully matched to the intended imaging kinetics. Tracers characterized by low topological polar surface area and limited hydrogen bonding potential, such as TcSES and TcTET, demonstrate rapid systemic clearance and minimal protein binding, which make them particularly suitable for perfusion imaging or early-phase dynamic acquisitions. In contrast, compounds with moderate to high polarity, exemplified by TcDTPA and TcDIS, display extended plasma residence times and are better suited for delayed-phase protocols, including renal or hepatobiliary imaging. Another key parameter influencing *in vivo* performance is the degree of albumin interaction. Incorporation of chemical motifs that promote reversible albumin binding, such as hydrophilic chelators or carboxylate groups, can enhance plasma half-life and systemic stability. This strategy is advantageous when sustained blood pool activity is desirable; however, excessive or non-specific binding may increase background signal or delay tissue clearance, thereby complicating image interpretation in protocols that rely on rapid kinetics. Moreover, our data underscores the importance of limiting molecular flexibility and avoiding extreme polarity unless such features are deliberately employed for targeted delivery to plasma protein-rich compartments. Tracers like TcHYN, with high polar surface area and a large number of rotatable bonds, exhibit promiscuous binding across multiple protein classes, including transport and regulatory proteins. While such interactions can be beneficial in specialized contexts, they may also lead to off-target accumulation or biological interference, particularly in metabolically compromised individuals. The results outlined here also demonstrates that strong and selective binding to functional proteins, such as insulin, must be carefully evaluated *in silico* during early design stages. Although the docking-predicted affinities observed here are unlikely to disrupt hormonal function at diagnostic doses, repeated exposure or application in sensitive patient populations could present a non-negligible safety concern.

CONCLUSIONS

Taken together, the results of the present study revealed that the pharmacokinetics and protein interaction profiles of TCC are strongly influenced by their physicochemical properties. It was shown that tracers with low polarity and weak protein binding, such as TcSES and TcTET, are well suited for dynamic imaging due to their rapid clearance. In contrast, compounds like TcDTPA and TcDIS exhibited strong albumin binding and extended circulation, supporting their use in delayed-phase protocols. The analysis also identified TcHYN as a structurally distinct radiotracer with broad, high-affinity protein interactions, suggesting a higher risk of off-target effects. Multivariate classification further demonstrated that tracers could be grouped into functionally meaningful clusters, reflecting shared ADMET and binding characteristics. Overall, the findings suggest that integrated ADMET profiling and docking can provide a predictive framework for the rational design and optimization of technetium-based radiotracers.

Acknowledgements
This work was supported by the Ministry of Education and Science of Ukraine (the project № Д3/174-2025).

ORCID
Valeriya Trusova, https://orcid.org/0000-0002-7087-071X; **Uliana Malovytsia,** https://orcid.org/0000-0002-7677-0779
Galyna Gorbenko, http://orcid.org/0000-0002-0954-5053; **Pylyp Kuznietsov,** http://orcid.org/0000-0001-8477-1395
Ivan Yakymenko, http://orcid.org/0000-0001-8477-1395

REFERENCES

[1] N. Ahmed, and M. Zia, "Diagnostic modalities and radiopharmaceuticals with particular importance of technetium-99m (^{99m}Tc)," Chin. J. Acad. Radiol. **6**, 143 (2023). https://doi.org/10.1007/s42058-023-00128-7
[2] Y. Arano, "Recent advances in ^{99m}Tc radiopharmaceuticals," Ann. Nucl. Med. **16**, 79 (2002). https://doi.org/10.1007/BF02993710
[3] G. Xiong, Z. Wu, and J. Yi, "ADMETlab 2.0: an integrated online platform for accurate and comprehensive predictions of ADMET properties," Nucleic Acids Res. **49**, W5 (2021). https://doi.org/10.1093/nar/gkab255
[4] Y. Yan, H. Tao, J. He, and S. Huang, "The HDOCK server for integrated protein–protein docking," Nature Protocols, **15**, 1829 (2020). https://doi.org/10.1038/s41596-020-0312-x
[5] A. Alkandari, Y. Alsayed, and A. El-Hanbaly, "Enhanced efficacy of radiopharmaceuticals when using technetium-99m-labeled liposomal agents: synthesis and pharmacokinetic properties," Biomedicines, **10**, 2994 (2022). https://doi.org/10.3390/biomedicines10112994
[6] S. Rathmann, Z. Ahmad, S. Slikboer, H. Bilton, D. Snider, and J. Valliant, "The radiopharmaceutical chemistry of technetium-99m," in: *Radiopharmaceutical Chemistry*, edited by J. Lewis, A. Windhorst, and B. Zeglis, (Springer, Cham., 2019). http://dx.doi.org/10.1007/978-3-319-98947-1_18
[7] B. Lee, J. Yeh, N. Chiu, G. Liu, H. Yu, M. Wang, and L. Shen, "Evaluation of Tc-99m (V) DMSA binding to human plasma proteins," Kaohsiung J. Med. Sci. **24**, 1 (2008). http://dx.doi.org/10.1016/S1607-551X(08)70066-4
[8] L. Shattuck, D. Eshima, A. Taylor, *et al*., "Evaluation of the hepatobiliary excretion of technetium-99m-MAG3 and reconstitution factors affecting radiochemical purity," J. Nucl. Med. **35**, 349 (1994). https://doi.org/10.29011/2577-2201.100088
[9] A. Mori, Y. Saito, and K. Nakamura, "Microcalcification and ^{99m}Tc-pyrophosphate uptake without increased bone metabolism in cardiac tissue from patients with transthyretin cardiac amyloidosis," Int. J. Mol. Sci. **24**, 1921 (2023). https://doi.org/10.3390/ijms24031921
[10] J. Smith, and J. Pfaendtner, "Elucidating the molecular interactions between uremic toxins and the Sudlow II binding site of human serum albumin," J. Phys. Chem. B, **14**, 3922 (2020). https://doi.org/10.1021/acs.jpcb.0c02015

КОМП'ЮТЕРНЕ МОДЕЛЮВАННЯ РАДІОФАРМПРЕПАРАТІВ ТЕХНЕЦІЮ-99М: ОЦІНКА ADMET-ВЛАСТИВОСТЕЙ ТА ВЗАЄМОДІЇ З БІЛКАМИ

В. Трусова[a], У. Маловиця[a], П. Кузнєцов[b], І. Якименко[b], Г. Горбенко[a]
[a]Кафедра медичної фізики та біомедичних нанотехнологій, Харківський національний університет імені В.Н. Каразіна м. Свободи 4, Харків, 61022, Україна
[b]Кафедра фізики ядра та високих енергій імені О.І. Ахієзера, Харківський національний університет імені В.Н. Каразіна м. Свободи 4, Харків, 61022, Україна

Раціональний дизайн радіофармацевтичних препаратів на основі технецію-99m (^{99m}Tc) вимагає глибокого розуміння того, як фізико-хімічні властивості впливають на поведінку сполук *in vivo* та їхні біомолекулярні взаємодії. У даному дослідженні застосовано інтегроване комп'ютерне моделювання для характеристики десяти клінічно релевантних радіофармпрепаратів на основі технецію. Дослідження включало оцінювання ADMET-параметрів, молекулярний докінг з функціональними білками (альбуміном, інсуліном і лізоцимом), а також багатовимірний статистичний аналіз. Отримані результати показали, що полярність, здатність до утворення водневих зв'язків та молекулярна гнучкість суттєво впливають як на фармакокінетичні властивості, так і на профілі зв'язування з білками. Трейсери типу TcSES і TcTET, які характеризуються низькою топологічною полярною поверхнею та мінімальною спорідненістю до білків, продемонстрували швидке виведення з організму та виявилися придатними для динамічних протоколів візуалізації. Натомість, сполуки TcDTPA і TcDIS мали високу спорідненість до альбуміну та стабільність до продуктів метаболізму, що робить їх перспективними для візуалізації у відтерміновані фази. TcHYN, що має унікальну структуру, характеризується надмірною полярністю із широким спектром білкових взаємодій високої афінності. Аналіз головних компонент і ієрархічна кластеризація дозволили класифікувати радіофармпрепарати на функціонально відмінні групи, що підкреслює структурно-залежні закономірності дизайну. Сукупність отриманих результатів свідчать про те, що поєднання ADMET-прогнозування та молекулярного докінгу формує релевантну стратегію передклінічного скринінгу та сприяє розробці більш безпечних і таргетованих ^{99m}Tc-радіофармацевтичних препаратів.

Ключові слова: *радіофармпрепарати на основі технецію; людський сироватковий альбумін; лізоцим; інсулін; молекулярний докінг; ОФЕКТ візуалізація*

EAST EUROPEAN JOURNAL OF PHYSICS. **2.** 412-417 (2025)
DOI:10.26565/2312-4334-2025-2-50 ISSN 2312-4334

STRUCTURE AND TENSILE PROPERTIES OF Pb–0.3%Sn–0.1%Ca NEGATIVE GRID ALLOY FOR LEAD-ACID BATTERIES

Victor O. Dzenzerskiy, Serhii V. Tarasov, Olena V. Sukhova*, Dmytro O. Redchyts, Volodymyr A. Ivanov
Institute of Transport Systems and Technologies of National Academy of Sciences of Ukraine
5, Pisarzhevsky St., Dnipro, 49005, Ukraine
**Corresponding Author e-mail: sukhovaya@ukr.net*
Received January 16, 2025; revised April 14, 2025; accepted May 12, 2025

The structure and tensile properties of Pb–0.3%Sn–0.1%Ca alloy for negative grids of lead-acid batteries have been characterised as functions of mould preheating temperature during casting and ageing time during storage under atmospheric conditions. Several techniques have been used to study microstructure, including quantitative metallography, scanning electron microscopy, and energy dispersive analysis. Tensile properties such as ultimate tensile strength, yield strength, Young's modulus, and elongation have been determined at room temperature. The increase of mould preheating temperature in the range between 60 °C and 170 °C causes the decrease in ultimate tensile strength (by ~25 %) and increase in elongation (by ~50 %) due to twofold increase in the grain size of the alloy. Whereas natural ageing for 35 days influences neither grain size nor tensile properties markedly.
Keywords: *Lead-acid batteries; Negative grids; Lead-tin-calcium alloy; Casting conditions; Mould temperature; Natural ageing; Grain size; Tensile properties*
PACS: 61.82.Bg, 61.66.Dk, 62.20.-x, 62.20.Fe, 62.20.Mk, 64.70.Dv, 81.70.Bt, 81.40.Cd, 81.40.Lm

Over the last years, there has been substantial interest in lead-acid batteries which require no further maintenance throughout the expected life of the battery [1,2]. This type of maintenance-free batteries is currently in widespread use [3,4]. A considerable amount of attention over the years has been given to the type of alloys used for manufacturing negative grids in such maintenance-free batteries [5,6]. Much interest has centered around the use of lead-tin-calcium alloys for making such grids [7-9].

The properties of lead-tin-calcium alloys depend mainly on the ratio of tin-to-calcium content (Sn/Ca) [10,11]. Often, the materials of choice for the negative grids have been alloys with low tin-to-calcium ratios (Sn/Ca<9) [12,13]. The calcium content in such alloys has been at least about 0.1 % by weight while the tin has generally been at about 0.3 % [14,15]. These ternary alloys are classic precipitation-strengthening alloys which derive mechanical strength due to a dispersion of very fine intermetallic precipitates in a lead-based matrix [16-19]. For lead-tin-calcium alloys with ratios below 9, the strengthening process is similar to that of lead-calcium alloys [20,21]. Strengthening occurs very rapidly with the formation of stable Pb_3Ca precipitates [22,23]. But due to tin additives to the binary Pb–Ca alloys the mode of precipitation changes from Pb_3Ca to more stable and stronger $(Pb,Sn)_3Ca$ precipitates [24,25].

The service life requirements for negative grid alloys are diverse [26,27]. Service conditions heighten the importance of grid strength to avoid premature failure of performance. Accordingly, enhancing the structure and tensile properties stability of the negative grids is an important demand. Excessive negative grid dimensional changes can result in premature failure in service and thus must be carefully controlled.

Production equipment to fabricate negative grids is now commercially available by which battery grids can be made by a variety of casting technologies [12]. Potentially, the use of any casting process to make negative grids is capable of minimizing problems associated with structural and dimensional stability. Several methods can be used at the casting step to control the microstructure of negative grid alloys. Most of these methods operate by exercising strict control of cooling rate from the melt [28-30]. For example, simple changes in such parameter as mould preheating temperature have been commonly used over the years to control grain size and precipitated phase dispersion [31,32].

Thus, proven methods to increase tensile properties required in negative grid alloys for efficient processing are to control casting procedure and monitor ageing processes. However, the tensile properties of the negative grids, which are among important factors limiting the life of the lead-acid battery, have not been intensively investigated. Over the last 30 years a vast range of research has been focused on the additives into lead-tin-calcium alloys, strengthening mechanisms, hardness and/or resistivity measurements etc. Therefore, the aim of this work is to investigate effects of mould preheating temperature during casting and ageing time during storage under atmospheric conditions on such mechanical properties as ultimate tensile strength, yield strength, elongation, and Young's modulus of Pb–0.3%Sn–0.1%Ca negative grid alloy.

Cite as: V.O. Dzenzerskiy, S.V. Tarasov, O.V. Sukhova, D.O. Redchyts, V.A. Ivanov, East Eur. J. Phys. 2, 412 (2025), https://doi.org/10.26565/2312-4334-2025-2-50

MATERIALS AND METHODS

The Pb–0.3%Sn–0.1%Ca (in wt. %) grid alloy was commercially produced in the C.O.S. melting pot of production line for negative grids of lead-acid batteries of *BM* Company (Austria) at *Westa* Corp. (City of Dnipro, Ukraine). Molten metal at the temperature of 465±5 °C was poured into a casting mould preheated in the range between 60 °C and 170 °C to prepare specimens for the tensile tests. The temperature was measured by chromel-alumel thermocouple and temperature variation during casting did not exceed ±3°C. Chemical composition of the alloy was determined using an ARL 3460 optical emission spectrometer. Trace amounts of major impurities, such as Al and Bi, amounted to less than 0.017 wt. %. The natural ageing of the alloy was carried out by keeping the samples in storage for 35 days under atmospheric conditions.

Microstructure of the Pb–0.3%Sn–0.1%Ca negative grid alloy was observed by JEOL JSM-6490 LV scanning electron microscope (SEM) equipped with an energy dispersive spectrometer (EDS). The operating voltage of the equipment was set to 20 kV and 30 nA, where the electron beam size was ~2 μm. Spectra of certain areas of the sample surface was also obtained to analyse the distribution of alloying elements within the alpha-lead solid solution. Grain size of the alloy was determined using an EPIQUANT image analyser with measurement error ±3 %.

The alloy specimens were tested in unaged (immediately after casting) and aged conditions (with intervals of 2–7 days) at room temperature. Tensile tests were conducted using a computer controlled TIRAtest 2300 universal testing machine at a constant crosshead speed of 10 mm/min. The stretching force was applied stepwise with a step of 100 N. Standard flat samples with a total length of 60 mm, a gage length of 45 mm, and a thickness of 3 mm from the as-cast alloy and each ageing group were prepared. Ultimate tensile strength (σ_U), yield strength (σ_Y), Young's modulus (Y), and elongation (γ) were calculated from the nominal stress (P_H) versus strain elongation ($\Delta l/l$) curves obtained from the tensile test. The results were the average value of six samples in each test group.

RESULTS AND DISCUSSION

The studied Pb–0.3%Sn–0.1%Ca alloy produces fine grains with serrated grain boundaries, as seen in Fig. 1. Fig. 1b is a higher magnification image of Fig. 1a revealing the intermetallic compounds that are suggested to be primary Pb_3Ca particles. This phase is also precipitated during cooling at the grain boundaries from the supersaturated alpha-lead solid solution by the process of cellular precipitation [12,33]. Then calcium precipitation can be converted from cellular to continuous precipitation to form more stable and strong $(Pb,Sn)_3Ca$ particles.

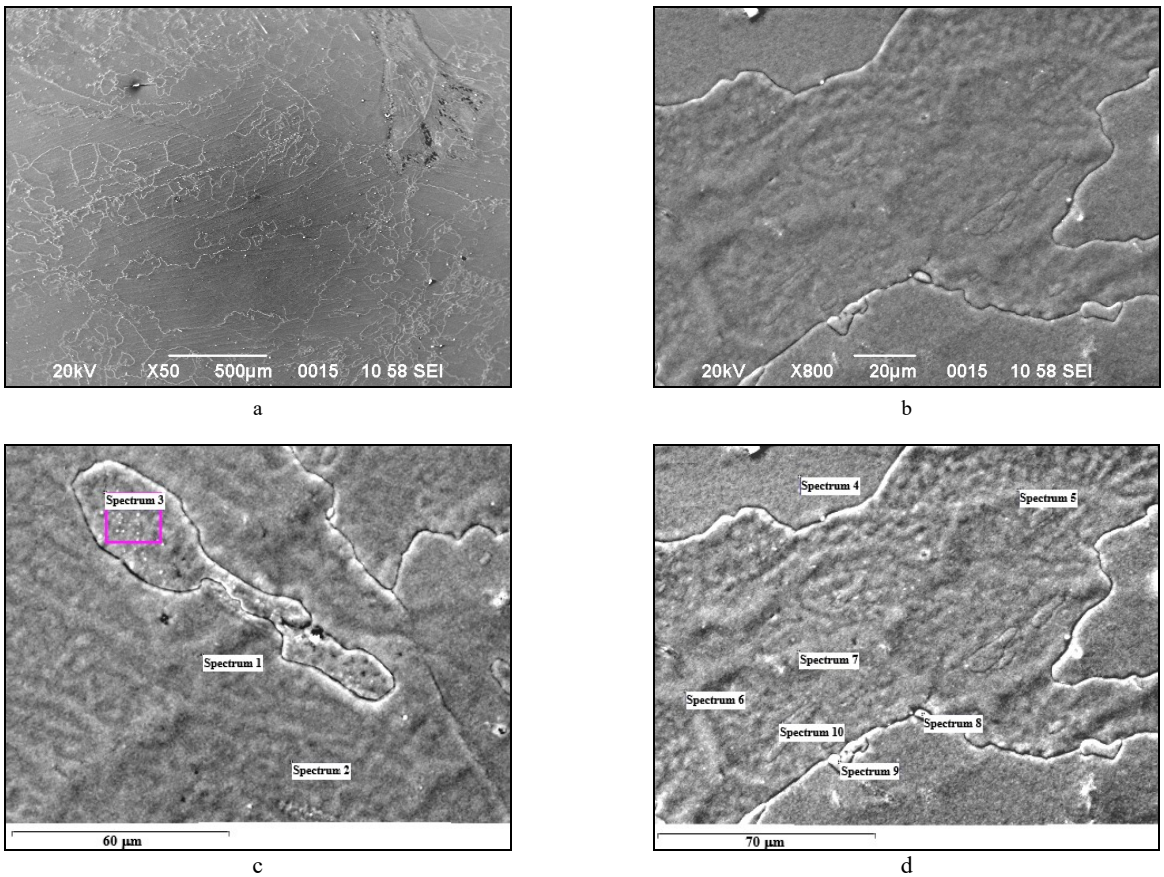

Figure 1. Microstructure of Pb–0.3%Sn–0.1%Ca grid alloy: a,b – SEM images at different magnifications; c,d – EDS analysis points across the surface

EDS analyses carried out in the lead-rich matrix of the Pb–0.3%Sn–0.1%Ca alloy (spectra corresponding to the white rectangles in Fig. 1cd) show that calcium can barely be detected around precipitated intermetallic particles, which indicates that calcium is enriched in these precipitates. It is not possible to determine exactly the composition for the intermetallic phases since electron diffraction spectrum comes from both the precipitates and the matrix. Considering the related literature [24,25], it is assumed that the fine phases appearing in the SEM images are the Pb_3Ca and $(Pb,Sn)_3Ca$ precipitates.

SEM images combined with EDS results confirm the segregation of some tin at grain boundaries [12]. EDS analysis points across surface of the studied alloy reveal on average 0.45 wt. % Sn at the grain boundaries and in their vicinity (see Spectra 1,3 in Fig. 1c and Spectrum 4 in Fig. 1d). Average tin content near subgrain boundaries increases up to 0.63 wt. % (see Spectrum 5 in Fig. 1d) as compared with that near grain boundaries. But Spectra 8,9,10 in Fig. 1d show that there is no tin at some grain boundaries indicating that the $(Pb,Sn)_3Ca$ phase has been nucleated here. This means that the alloy does not contain sufficient tin to remain at all grain boundaries. Sometimes, in the grain centre traces of Sn are also not revealed (see Spectrum 2 in Fig. 1c and Spectrum 7 in Fig. 1d).

The average grain size of the Pb–0.3%Sn–0.1%Ca alloy can be significantly increased by rising mould preheating temperature during casting procedure. Higher mould temperature enlarges the grain size from 45±5 μm at 60 °C up to 67±8 μm at 125 °C, and then up to 92±11 μm at 170 °C (by 104 % in all). The increase in grain size is very favourable [34,35] since fine-grained structure is a serious detriment in terms of intergranular corrosion [36-38] which prevails in the lead-tin-calcium grid alloys for lead-acid batteries.

In this investigation, it has been observed that larger grain size of the Pb–0.3%Sn–0.1%Ca negative grid alloy produces lower ultimate tensile strength (by ~25 %) and higher elongation (by ~50 %), as shown in Fig. 2. The temperature dependencies of ultimate tensile strength and elongation are approximately 0.1 MPa/ºC and 0.09 %/ºC, respectively. At mould temperatures higher than 160±5 °C, there are little variations in the values of these properties.

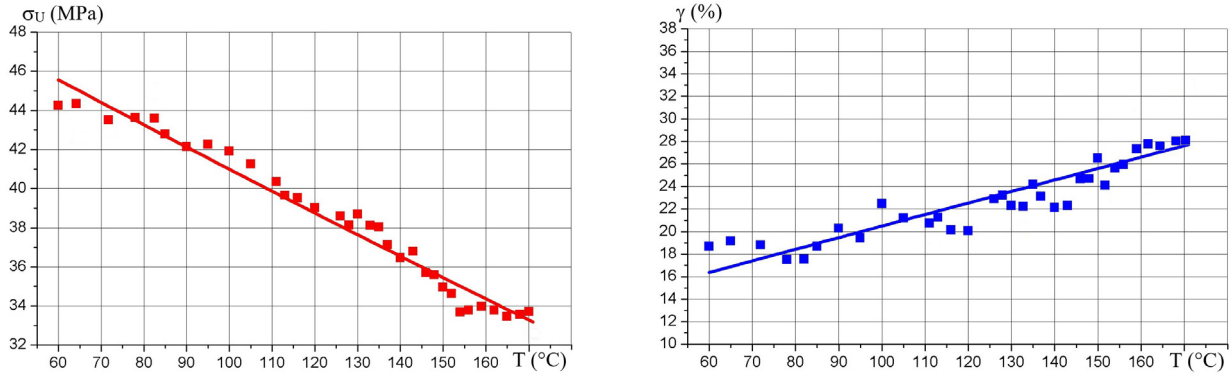

a b

Figure 2. Effects of casting mould temperature on tensile properties of Pb–0.3%Sn–0.1%Ca negative grid alloy: a – ultimate tensile strength; b – elongation

Described changes in the values of ultimate tensile strength and elongation are assumed to be due to the formation of larger grains in the alloy's structure as mould preheating temperature increases. The area of grain boundaries impeding dislocation movement decreases, which increases elongation. But when mould temperature related to the cooling rate is higher, cooling conditions are closer to an equilibrium kinetic, resulting in less uniform structure within the lead grains. As known, calcium segregates in the grain centre while tin segregates at the grain boundaries [2]. As a result, the grain boundaries have different composition as that of the grain centre, which reduces values of ultimate tensile strength.

Mould preheating temperature has less effect on ultimate tensile strength as compared with that on elongation due to formation of greater amounts of uniformly dispersed primary Pb_3Ca particles in the slower cooled alloy that strengthen lead matrix. Formation of these particles is presumed to partially compensate the reduction in the tensile strength. The change in elongation is relatively large since both the resistance to dislocation motion and the promotion of inhomogeneous dislocation multiplication by the precipitates are relatively low [39,40].

Thus, slower cooling can produce two times larger grains in the Pb–0.3%Sn–0.1%Ca grid alloy structure. Whereas natural ageing during storage for 35 days under atmospheric conditions has no appreciable effect on increasing grain size. Furthermore, the alloy has been fully strengthened by ageing during first 1–3 days and cannot be further strengthened by ageing. Such conclusion follows from the stress-strain curves that show a good convergence of tensile test results for specimens aged over a period of 35 days, as illustrated in Fig. 3a.

Ageing of the Pb–0.3%Sn–0.1%Ca grid alloy for 1–3 days increases ultimate tensile strength by 8.8 % and decreases elongation by 7.1 % over their values determined immediately after casting into the mould preheated up to 160±5 °C and air cooling. More stable and strong $(Pb,Sn)_3Ca$ precipitates are believed to form and strengthen alpha-lead matrix during this ageing stage. The movable capacity of the dislocations decreases resulting in an increase in the alloy's ultimate tensile strength and a decrease in the elongation. But as the formation of these precipitates which can

effectively impede dislocation movement is suggested to occur at a very slow rate, relatively slight changes in these properties are found.

After first 3 days of storage, ageing has insignificant effect on tensile properties, which is confirmed by calculated values of ultimate tensile and yield strengths, Young's modulus, and elongation, as shown in Fig. 3bcd. The changes in values are negligible since ultimate tensile and yield strengths increase from 37.0 MPa to 37.2 MPa (by 0.5 %) and from 10.0 MPa to 10.1 MPa (by 1 %), respectively. Young's modulus also remains almost unchanged and equals to 12.9 GPa on average. Elongation decreases from 26.1 % to 21.5 % (by 17.6 %), which corresponds to embrittlement due to ageing result of the interaction between dislocation and precipitate particles.

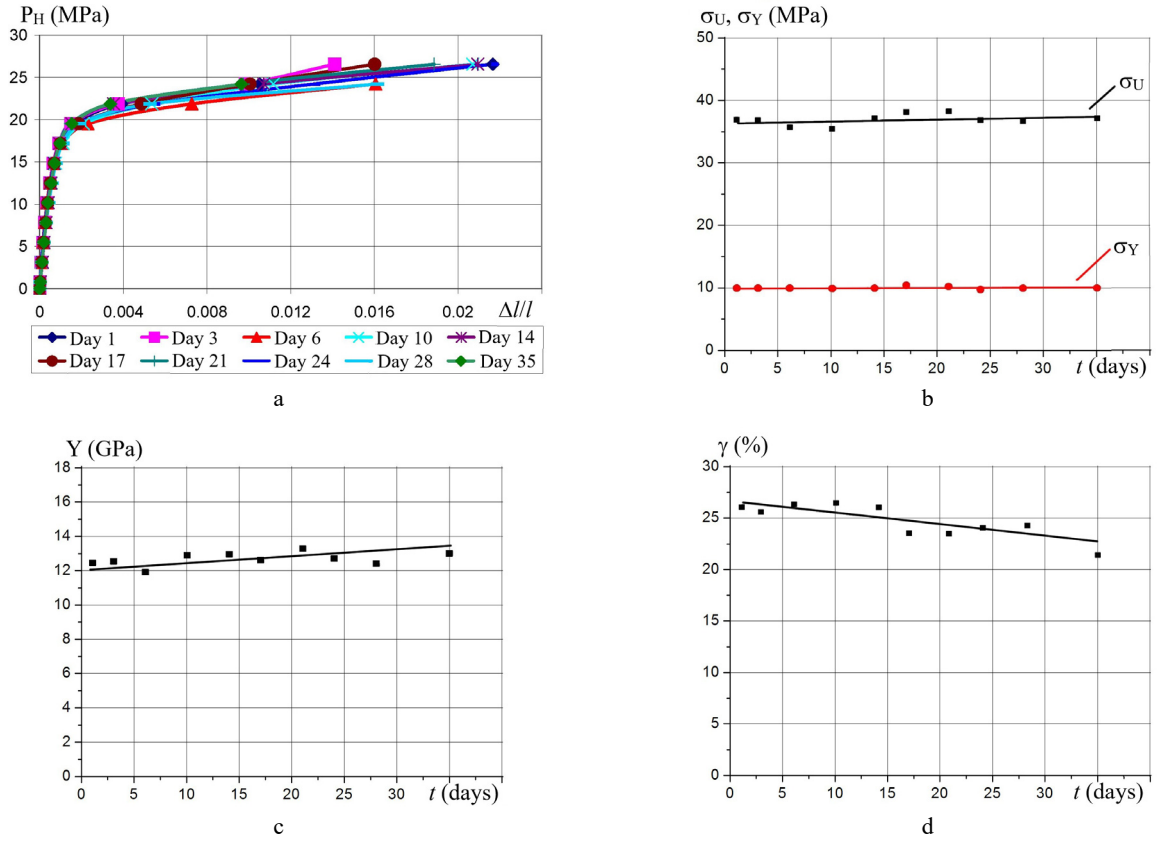

Figure 3. Effects of ageing time on tensile properties of Pb–0.3%Sn–0.1%Ca negative grid alloy:
a – stress-strain curves; b – ultimate tensile (σ_U) and yield (σ_Y) strengths; c – Young's modulus; d – elongation

Thus, as expected, the Pb–0.3%Sn–0.1%Ca grid alloy strengthens very rapidly, which is in good agreement with previous observations [14,15]. The strength and plasticity of the alloy are closely correlated with the changes in the microstructure. Since the ageing time has little influence on the grain size of the alloy, no significant differences in the values of the tensile properties are found due to the slow precipitation processes with the extension of ageing time. Generally, the characteristics of microstructure evolved in different ageing stages during 35 days in storage contribute to a significant flat tendency in most tensile properties, especially after the ageing time of 1–3 days.

The lower values of yield strength as compared with those of ultimate tensile strength can be attributed to the precipitation of the strengthening phases which consume alloying elements present in the alpha-lead solid solution. As a result, distribution of these elements is less effective in blocking the motion of dislocations within the lead grains and thus weakens the strengthening effects. Ageing also causes a reduction in elongation due to the precipitates formed on the dislocations. As dislocations are pinned by precipitates, higher stress is required for the dislocations to escape the blockage of the precipitates to proceed moving. As a result, dislocations are less uniformly distributed, and deformation is localized, causing a loss of ductility. The ageing time for 35 days is sufficient for dislocations to get locked because the Pb_3Ca and $(Pb,Sn)_3Ca$ precipitates, stable against dissolving and coarsening, constitute an effective obstacle for restricting the movable capacity of the dislocations.

So, tin and calcium contents in the studied Pb–0.3%Sn–0.1%Ca negative grid alloy are presumed to form strengthening precipitates, which produces tensile properties required for further processing. Ageing alone contributes very little to the strength of the alloys yet provides more effective level of strengthening when combined with casting conditions. Casting procedure that comprises preheating of the casting mould up to 160±5 °C and further air cooling to room temperature changes ageing kinetics of the Pb–0.3%Sn–0.1%Ca grid alloy. The change is attributed to a decrease in the calcium supersaturation, i.e., the driving force of the precipitation of the strengthening phases after cooling at the

slower rate. Strengthening occurs very rapidly within 1–3 days with the formation of stable Pb_3Ca and $(Pb,Sn)_3Ca$ precipitates. The decrease in precipitation rate is believed to be mainly related to the saturation of precipitation because the actual amounts of calcium and tin in the lead-based solution are reduced due to slower cooling and ageing. Thus, in this alloy cast negative grids can be processed within short period after production, which significantly reduces inventory in the enterprise.

CONCLUSIONS

In this work, the effects of mould preheating temperature and ageing time on grain structure and tensile properties of Pb–0.3%Sn–0.1%Ca alloy for negative grids of lead-acid batteries have been studied. The alloy's grains become two times larger as the mould preheating temperature during casting increases in the range between 60 °C and 170 °C. This is accompanied by the decrease in ultimate tensile strength by ~25 % and the increase in elongation by ~50 %.

The microstructure of the Pb–0.3%Sn–0.1%Ca negative grid alloy remains stable during natural ageing for 35 days, with no noticeable changes in grain size revealed. For the alloy, the age strengthening occurs very quickly since stable values of most tensile properties are reached within 1–3 days. After this period, the alloy continues to strengthen at a negligible rate since a slight decrease in elongation is observed. So, as compared with the effect of mould temperature, ageing time has a minor effect on the Pb–0.3%Sn–0.1%Ca grid alloy microstructure and tensile properties during a period exceeding 3 days.

The Pb–0.3%Sn–0.1%Ca alloy possesses acceptable combination of tensile properties for processability so that the alloy can be made into negative grids using the chosen casting method and be subjected to various lead-acid battery processing and assembly steps.

The work was performed within the framework of research projects of National Academy of Sciences of Ukraine No. 1.3.6.18 "Development of new methods and improvement of known ones to investigate mechanics of transport and energetic systems" (2017-2021) and No. 1.3.6.22 "Development of mathematical models and investigation of ground transport and energetic systems" (2022-2026).

ORCID

Victor O. Dzenzerskiy, https://orcid.org/0000-0002-9722-1920; **Sergei V. Tarasov,** https://orcid.org/0000-0002-9254-1503
Olena V. Sukhova, https://orcid.org/0000-0001-8002-0906; **Dmytro O. Redchyts,** https://orcid.org/0000-0001-8538-6026
Volodymyr A. Ivanov, https://orcid.org/0009-0008-9836-6508

REFERENCES

[1] S. Guruswamy, *Engineering Properties and Applications of Lead Alloys*, (CRC Press, New York, 2000). https://doi.org/10.1201/9781482276909
[2] D.A.J. Rand, T. Moseley, J. Garche, and C.D. Parker, *Valve-Regulated Lead-Acid Batteries*, (Elsevier, Amsterdam, 2004). https://doi.org/10.1016/B978-0-444-50746-4.X5000-4
[3] V.O. Dzenzerskiy, S.V. Tarasov, D.O. Redchyts, V.A. Ivanov, and O.V. Sukhova, J. Nano- Electron. Phys. **16**(1), 01003 (2024). https://doi.org/10.21272/jnep.16(1).01003
[4] J. Jung, L. Zhang, and J. Zhang, *Lead-acid battery technologies: fundamentals, materials, and applications*, (CRC Press, Boca Ranton, 2015), https://doi.org/10.1201/b18665
[5] V.O. Dzenzerskiy, S.V. Tarasov, O.V. Sukhova, and V.A. Ivanov, East Eur. J. Phys. **2023**(4), 182 (2023). https://doi.org/10.26565/2312-4334-2023-4-21
[6] V.O. Dzenzerskiy, S.V. Tarasov, O.V. Sukhova, D.O. Redchyts, and V.A. Ivanov, Kovove Mater. **62**(3), 153 (2024). https://doi.org/10.31577/km.2024.3.153
[7] E. Gullian, L. Albert, and J.L. Caillerie, J. Power Sources. **116**(1-2), 185 (2003). http://dx.doi.org/10.1016/S0378-7753(02)00705-X
[8] M.T. Wall, Y. Ren, T. Hesterberg, T. Ellis, and M.L. Young, J. Energy Storage. **55**, 105569 (2022). https://doi.org/10.1016/j.est.2022.105569
[9] Y.B. Zhou, C.X. Yang, W.F. Zhou, and H.T. Liu, J. Alloys Compd. **365**(1-2), 108 (2004). https://doi.org/10.1016/S0925-8388(03)00649-2
[10] R.K. Shervedani, A.Z. Isfahani, R. Khodavisy, and A. Hatefi-Mehrjardi, J. Power Sources. **164**(2), 890 (2007). https://doi.org/10.1016/j.jpowsour.2006.10.105
[11] D. Slavkov, B.S. Haran, B.N. Popov, and F. Fleming, J. Power Sources. **112**(1), 199 (2002). https://doi.org/10.1016/S0378-7753(02)00368-3
[12] R.D. Prengaman, J. Power Sources. **67**(1-2), 267 (1997). https://doi.org/10.1016/S0378-7753(97)02512-3
[13] E. Rocca, G. Bourguignon, and J. Steinmetz, J. Power Sources. **161**(2), 666 (2006). http://dx.doi.org/10.1016/j.jpowsour.2006.04.140
[14] Z.W. Chen, J.B. See, W.F. Gillian, and D.M. Rice, J. Power Sources. **42**(1-2), 35 (1993). https://doi.org/10.1016/0378-7753(93)80135-c
[15] L. Muras, P.R. Munroe, S. Blairs, P. Krauklis, Z.W. Chen, and J.B. See, J. Power Sources. **55**(1), 119 (1995). https://doi.org/10.1016/0378-7753(94)02171-x
[16] C. Camurri, C. Carrasco, O. Prat, R. Mangalaraja, A. Pagliero, and R. Colàs, Mater. Sci. Technol. **26**(2), 210 (2010). https://doi.org/10.1179/174328409x443245

[17] M. Dehmas, A. Maitre, J.B. Richir, and P. Archambault, J. Power Sources, **159**(1), 721 (2006). https://doi.org/10.1016/j.jpowsour.2005.07.094
[18] A. Maitre, G. Bourguignon, G. Medjahdi, E. McRae, and M.H. Mathon, Scr. Mater. **50**(5), 685 (2004). https://doi.org/10.1016/j.scriptamat.2003.11.013
[19] Y.A. Yassine, M. Lakhal, N. Labchir, E. Zantalla, E. Saad, and M. Sannad, Coat. **13**(9), 1534 (2023). https://doi.org/10.3390/coatings13091534
[20] L. Bouirden, J.P. Hilger, and J. Hertz, J. Power Sources, **33**(1-4), 27 (1991). https://doi.org/10.1016/0378-7753(91)85046-Y
[21] C.S. Lakshmi, J.E. Manders, and D.M. Rice, J. Power Sources, **73**(1), 23 (1998). https://doi.org/10.1016/S0378-7753(98)00018-4
[22] J. Hilger, J. Power Sources, **72**(2), 184 (1998). https://doi.org/10.1016/s0378-7753(97)02711-0
[23] H. Li, W.X. Guo, H.Y. Chen, D.E. Finlow, H.W. Zhou, C.L. Dou, G.M. Xiao, S.G. Peng, W.W. Wei, and H. Wang, J. Power Sources, **191**(1), 111 (2009). https://doi.org/10.1016/j.jpowsour.2008.10.059
[24] R.D. Prengaman, J. Power Sources, **95**(1-2), 224-233 (2001). https://doi.org/10.1016/S0378-7753(00)00620-0
[25] H. Tsubakino, M. Tagami, S. Ioku, and A. Yamamoto, Metall. Mater. Trans. A, **27**(6), 1675 (1996). https://doi.org/10.1007/BF02649824
[26] K. Sawai, Y. Tsuboi, Y. Okada, M. Shiomi, and S. Osumi, J. Power Sources. **179**(2), 799 (2008). https://doi.org/10.1016/j.jpowsour.2007.12.106
[27] D.A.J. Rand, D.P. Boden, C.S. Lakshmi, R.R. Nelson, and R.D. Prengaman, J. Power Sources, **107**(2), 280 (2002). https://doi.org/10.1016/S0378-7753(01)01083-7
[28] B.O. Trembach, Yu.A. Silchenko, M.G. Sukov, N.B. Ratska, Z.A. Duriagina, I.V. Krasnoshapka, O.V. Kabatskyi, and O.M. Rebrova, Mater. Sci. **59**(6), 733 (2024) https://doi.org/10.1007/s11003-024-00834-2
[29] B. Trembach, Y. Silchenko, O. Balenko, D. Hlachev, K. Kulahin, H. Heiko, O. Bellorin-Herrera, *et al*., Int. J. Adv. Manuf. Technol. **134**, 309 (2024). https://doi.org/10.1007/s00170-024-14115-4
[30] I.M. Spyrydonova, O.V. Sukhova, and G.V. Zinkovskij, Metall. Min. Ind. **4**(4), 2 (2012). (in Russian)
[31] Yu.G. Chabak, K. Shimizu, V.G. Efremenko, M.A. Golinskyi, K. Kusumoto, V.I. Zurnadzhy, and A.V. Efremenko. Int. J. Miner. Metall. Mater. **29**(1), 78 (2022). https://doi.org/10.1007/s12613-020-2135-8
[32] O.V. Sukhova, Probl. At. Sci. Technol. **128**(4), 77 (2020). https://doi.org/10.46813/2020-128-077.
[33] F. Rossi, M. Lambertin, L. Delfaut-Durut, A. Maitre, and M. Vilasi, J. Power Sources. **188**(1), 296 (2009). https://doi.org/10.1016/j.jpowsour.2008.11.049
[34] O.V. Sukhova, V.A. Polonskyy, and K.V. Ustinova, Voprosy Khimii i Khimicheskoi Tekhnologii. (3), 46 (2019). http://dx.doi.org/10.32434/0321-4095-2019-124-3-46-52 (in Ukrainian)
[35] O.V. Sukhova, V.A. Polonskyy, and K.V. Ustinova, Voprosy Khimii i Khimicheskoi Technologii. (6), 77 (2018). https://doi.org/10.32434/0321-4095-2018-121-6-77-83 (in Ukrainian)
[36] O.V. Sukhova, and V.A. Polonskyy, East Eur. J. Phys. (3), 5 (2020). https://doi.org/10.26565/2312-4334-2020-3-01
[37] O.V. Sukhova, V.A. Polons'kyi, and K.V. Ustinova, Mater. Sci. **55**(2), 291 (2019). https://doi.org/10.1007/s11003-019-00302-2
[38] O.V. Sukhova, V.A. Polonskyy, and K.V. Ustinova, Metallofiz. Noveishie Technol. **40**(11), 1475 (2018). https://doi.org/10.15407/mfint.40.11.1475 (in Ukrainian)
[39] V. Lozynskyi, B. Trembach, M.M. Hossain, M.H. Kabir, Y. Silchenko, M. Krbata, K. Sadovyi, O. Kolomiitse, and L. Ropyak, Heliyon, **10**(3), e25199 (2024). https://doi.org/10.1016/j.heliyon.2024.e25199
[40] V.G. Efremenko, A.G. Lekatou, Yu.G. Chabak, B.V. Efremenko, I. Petryshynets, V.I. Zurnadzhy, S. Emmanouilidou, and M. Vojtko, Mater. Today Commun. **35**, 105936 (2023). https://doi.org/10.1016/j.mtcomm.2023.105936.1

СТРУКТУРА ТА МЕХАНІЧНІ ВЛАСТИВОСТІ ПРИ РОЗТЯГУВАННІ СПЛАВУ Pb–0,3%Sn–0,1%Ca ДЛЯ НЕГАТИВНИХ СТРУМОВІДВОДІВ СВИНЦЕВО-КИСЛОТНИХ АКУМУЛЯТОРІВ

Віктор О. Дзензерський, Сергій В. Тарасов, Олена В. Сухова, Дмитро О. Редчиць, Володимир А. Іванов
Інститут транспортних систем і технологій Національної Академії наук України
вул. Писаржевського, 5, 49005, Дніпро, Україна

Встановлено залежності структури і механічних властивостей при розтягуванні сплаву Pb–0,3%Sn–0,1%Ca для негативних струмовідводів свинцево-кислотних акумуляторів від температури підігріву ливарної форми та тривалості старіння за атмосферних умов. Мікроструктуру сплаву досліджено методами кількісної металографії, скануючої електронної мікроскопії та рентгеноспектрального мікроаналізу. Механічні властивості при розтягуванні, а саме межу міцності на розрив, межу текучості, модуль Юнга і відносне подовження, визначено за кімнатної температури. В разі підвищення температури підігріву ливарної форми в діапазоні від 60 °C до 170 °C межа міцності на розрив зменшується (на ~25 %), а відносне подовження збільшується (на ~50 %) завдяки дворазовому збільшенню розміру зерна в структурі сплаву. Тоді як природнє старіння впродовж 35 діб не має суттєвого впливу ні на розмір зерна, ні на механічні властивості при розтягуванні.

Ключові слова: *свинцево-кислотні акумулятори; негативні струмовідводи; сплав свинець-олово-кальцій; ливарні умови; температура підігріву ливарної форми; природнє старіння; розмір зерна; механічні властивості при розтягуванні*

East European Journal of Physics. 2. 418-423 (2025)
DOI:10.26565/2312-4334-2025-2-51 ISSN 2312-4334

POLYPHENOL INTERACTIONS WITH FUNCTIONAL PROTEINS: A MOLECULAR DOCKING STUDY

U. Malovytsia[a]*, V. Trusova[a], M. Thomsen[b], K. Vus[a], O. Zhyntniakivska[a], G. Gorbenko[a]
Department of Medical Physics and Biomedical Nanotechnologies, V.N. Karazin Kharkiv National University
4 Svobody Sq., Kharkiv, 61022, Ukraine
[b]AAU Energy, Aalborg University, Niels Bohrs Vej 8, 6700 Esbjerg, Denmark
**Corresponding Author email: uliana.tarabara@karazin.ua*
Received February 15, 2025, revised April 22, 2025; accepted May 12, 2025

Polyphenols, bioactive phytochemicals with anticancer, immunomodulating, antioxidative, anti-inflammatory, antimicrobial and many other favorable properties currently attract considerable attention due to their promising therapeutic potential. Biomolecular interactions of polyphenolic compounds, particularly, their association with physiologically important proteins may largely account for their biological effects. In the present study the molecular docking technique was employed to characterize the binding of curcumin (enol and keto forms), resveratrol, sesamin, salycilyc and gallic acids to the functional proteins such as serum albumin, hemoglobin (deoxy and oxy forms), cytochrome c (oxidized and reduced forms). It was found that all examined polyphenols possess the highest affinities for serum albumin and deoxyhemoglobin, while the lowest affinities are observed for cytochrome c. The analysis of the protein-ligand interfacial amino acid residues revealed that there exist specific amino acids with the highest occurrence frequency in the polyphenol binding sites among which are lysine, arginine and tyrosine.
Keywords: *Polyphenols; Serum albumin; Hemoglobin; Cytochrome c; Molecular docking*
PACS: 87.14.C++c, 87.16.Dg

Polyphenols are a chemically diverse class of secondary plant metabolites found in fruits and vegetables, that display a wide spectrum of biological effects beneficial for human health among which are anticancer [1], immunomodulating, antioxidative, anti-inflammatory, antimicrobial and anticoagulant properties [2]. These biological activities are determined to a large extent by polyphenol interactions with various types of functionally important proteins [3, 4]. In particular, it has been demonstrated that polyphenols can form stable complexes with salivary and plasma proteins [5, 6], digestive enzymes [7], amyloidogenic proteins [8], etc. Hydrogen bonding and hydrophobic interactions between polyphenols and proteins are thought to be the main determinants of the specificity of the forming complexes [3]. Despite extensive research efforts, the molecular-level details of polyphenol-protein complexation are far from being fully understood. In view of this, the aim of the present study was to gain deeper insights into the mechanisms of polyphenol association with human serum albumin, hemoglobin and cytochrome c using the molecular docking approach. The choice of the functional proteins was dictated by the following considerations. Being the major protein in human plasma, albumin has multiple functions among which are maintaining the osmotic pressure, transporting various molecules, and modulating the immune response. A diversity of binding sites and multiple hydrophobic pockets account for a high loading and entrapment capacity of human serum albumin (HSA) for a wide variety of substances [9]. Hemoglobin (Hb), representing about 10% of the total proteins of the human organism, accounts for transport of oxygen and carbon dioxide, modulation of erythrocyte metabolism, heat transduction via oxygenation-deoxygenation reactions, etc. [10]. Cytochrome c (cyt c), is a mitochondrial heme protein playing a key role in cellular energetics and metabolism. The redox state of iron atom in the heme group is critical for cyt c functioning as a component of electron transfer chain and its ability to induce the apoptotic cell death [11]. The group of polyphenols under study included curcumin, salicylic acid, gallic acid, sesamin and resveratrol, possessing anti-inflammatory, antioxidant, antimicrobial and neuroprotective activities [12-16].

METHODS

The blind docking of polyphenols to functional proteins was conducted with the HDOCK server using the FFT-based hierarchical algorithm of rigid-body docking [17]. While implementing this algorithm, the receptor and ligand molecules are mapped onto grids and the possible binding modes are ranked according to their binding energy with the shape complementarity scoring method in which one molecule is fixed, while the second one adopts evenly distributed orientations in rotational Euler space and translational space within a grid. The three-dimensional X-ray crystal structures of the investigated proteins were obtained from the Protein Data Bank (https://www.rcsb.org/) using the following PDB IDs 2N9J (human cytochrome c oxidized, cyt c oxy), 2N9I (human cytochrome c reduced, cyt c red), 2DN2 (human deoxyhemoglobin, deoxyHb), 1LFQ (human oxyhemoglobin, oxyHb), 1AO6 (human serum albumin). The structures of polyphenols were prepared in MarvinSketch software, v.18.10, ChemAxon with subsequent geometry optimization in Avogadro 1.1.0 software. The top-scored protein-polyphenol complexes were visualized with the UCSF Chimera software (version 1.14) and analyzed in the protein–ligand interaction profiler (PLIP) [18].

Cite as: U. Malovytsia, V. Trusova, M. Thomsen, K. Vus, O. Zhyntniakivska, G. Gorbenko, East Eur. J. Phys. 2, 418 (2025), https://doi.org/10.26565/2312-4334-2025-2-51

RESULTS AND DISCUSSION

The analysis of the best score values obtained for the complexes of polyphenols with functional proteins (Table 1) revealed that PF binding affinities decrease in the order: ***Curcumin enol***: Hbdeoxy > HSA > Hboxy > Cyt c red > Cyt c oxy; ***Curcumin keto***: deoxyHb > HSA > oxyHb > > Cyt c oxy > Cyt c red; ***Salicylic acid***: HSA > deoxyHb > Cyt c oxy > oxyHb > Cyt c red; ***Gallic acid***: HSA > deoxyHb > > Cyt c oxy > oxyHb >Cyt c red; ***Sesamin***: HSA > deoxyHb > oxyHb > Cyt c oxy > Cyt c red; ***Resveratrol***: HSA > deoxyHb > oxy Hb> > Cyt c red > Cyt c oxy. Remarkably, all polyphenols possess the highest and comparable affinities for HSA and deoxyHb, while the lowest affinities are observed for cytochrome c.

Table 1. The best score values for the complexes of polyphenols with functional proteins

Polyphenol/Protein	Cyt c oxy	Cyt c red	HSA	deoxyHb	oxyHb
Curcumin enol	-117.68	-125.00	-158.27	-163.65	-148.40
Curcumin keto	-126.71	-120.10	-182.88	-188.42	-145.22
Salicylic (phenolic) acid	-93.14	-74.57	-102.34	-95.84	-83.50
Gallic acid	-104.21	-85.28	-124.03	-112.55	-99.64
Sesamin	-115.33	-126.21	-173.97	-163.87	-145.15
Resveratrol	-89.80	-92.91	-131.52	-125.79	-109.65

While comparing the affinities of different PF to a certain protein it was found that the HSA, deoxyHb and cyt c oxy contain the highest affinity sites for curcumin keto, oxy Hb – for curcumin enol, and cyt c red – for sesamin and curcumin enol. Shown in Figs. 1-3 are the best score docking poses predicted by HDOCK for polyphenol-protein interactions.

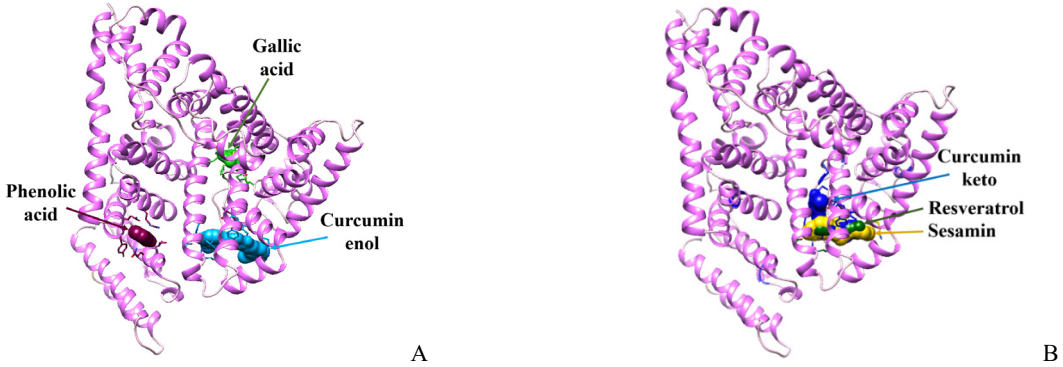

Figure 1. The most energetically favorable complexes between human serum albumin and polyphenols predicted by HDOCK.

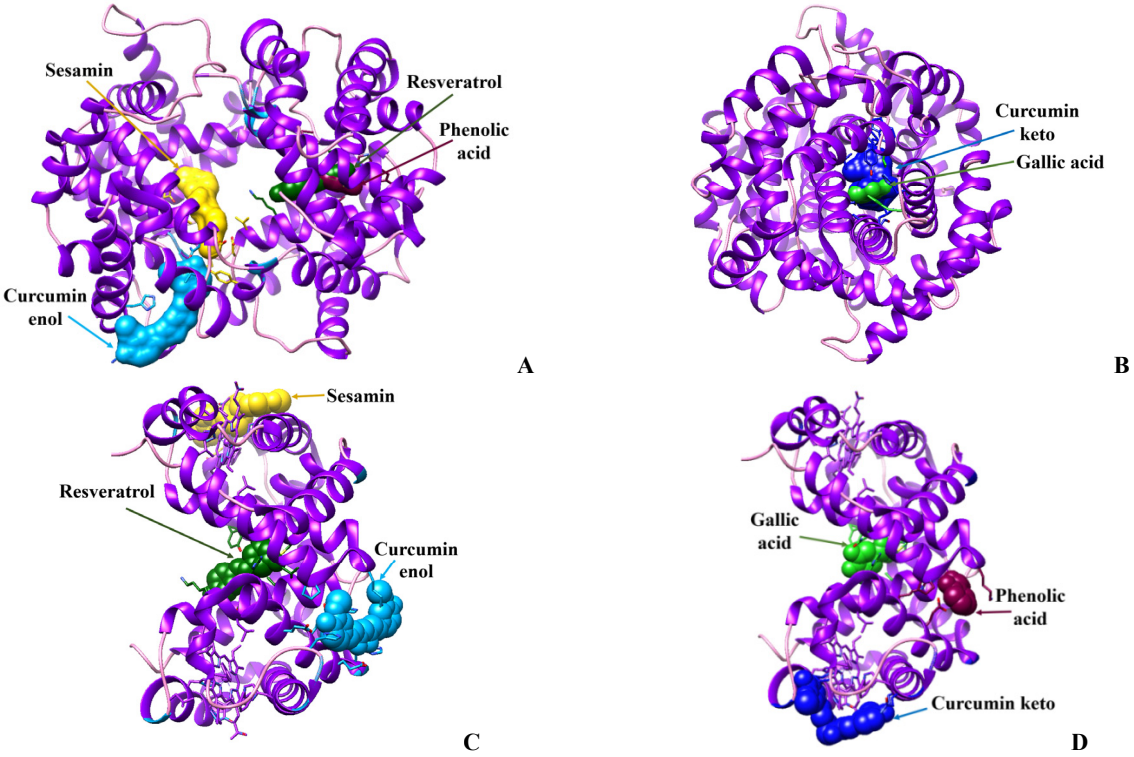

Figure 2. The most energetically favorable complexes between deoxyhemoglobin (A, B) or oxyhemoglobin (C, D) and polyphenols predicted by HDOCK

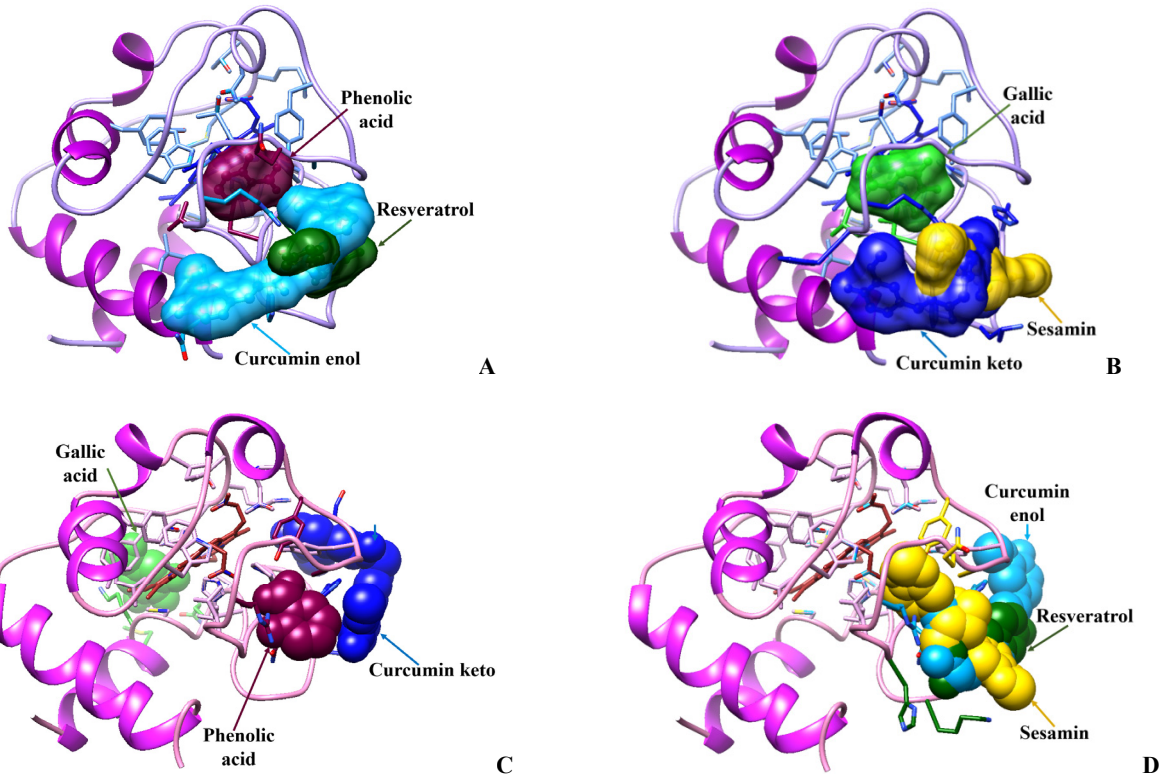

Figure 3. The most energetically favorable complexes between cytochrome c oxy (A, B) or cytochrome c red (C, D) and polyphenols predicted by HDOCK

The amino acid compositions of the binding sites appear to have both similarities and distinctions for different FP-PF systems (Tables 2-6). More specifically, the residues LEU_{115}, ARG_{117}, PRO_{118}, MET_{123}, PHE_{134}, LYS_{137}, TYR_{138}, GLU_{141}, TYR_{161}, LEU_{182}, ASP_{183}, ARG_{186} account for the binding of most polyphenols (except salicylic and gallic acids) to HSA , while the binding sites for SA and GA are quite different (Table 2).

Table 2. The interface residues in the complexes of polyphenols with human serum albumin

HSA +	Amino acid residues forming the HSA binding sites for polyphenols	Type of interactions
Salicylic acid	GLU_{400}, TYR_{401}, GLN_{404}, ARG_{428}, LYS_{519}, GLU_{520}, GLN_{522}, ILE_{523}, GLN_{526}	Hydrophobic interactions, hydrogen bonds, salt bridges
Resveratrol	LEU_{115}, ARG_{117}, PRO_{118}, PHE_{134}, LEU_{135}, LYS_{137}, TYR_{138}, GLU_{141}, TYR_{161}, LEU_{182}, ASP_{183}, ARG_{186}	Hydrophobic interactions, hydrogen bonds
Curcumin (enol form)	PHE_{36}, LEU_{115}, VAL_{116}, ARG_{117}, PRO_{118}, PHE_{134}, LYS_{137}, TYR_{138}, GLU_{141}, TYR_{161}, LEU_{182}, ASP_{183}, ARG_{186}	Hydrophobic interactions, hydrogen bonds
Curcumin (keto form)	LEU_{115}, VAL_{116}, ARG_{117}, PRO_{118}, PHE_{134}, LYS_{137}, TYR_{138}, GLU_{141}, ILE_{142}, HSD_{146}, PHE_{149}, PHE_{157}, TYR_{161}, LEU_{182}, LEU_{185}, ARG_{186}, GLY_{189}, LYS_{190}	Hydrophobic interactions, hydrogen bonds
Sesamin	LEU_{115}, ARG_{117}, PRO_{118}, MET_{123}, PHE_{134}, LYS_{137}, TYR_{138}, GLU_{141}, ILE_{142}, TYR_{161}, LEU_{182}, ASP_{183}, LEU_{185}, ARG_{186}	Hydrophobic interactions, hydrogen bonds
Gallic acid	GLN_{29}, LEU_{103}, LYS_{106}, PRO_{147}, TYR_{148}, PHE_{149}, TYR_{150}, ALA_{151}, GLN_{196}, ARG_{197}, CYS_{200}, CYS_{245}, CYS_{246}, HSD_{247}, GLY_{248}, LEU_{250}	Hydrophobic interactions, hydrogen bonds, salt bridges

The binding sites for curcumin enol and sesamin on deoxyHb have only three similar residues (ASP_{99D}, ASN_{102D}, PHE_{103D}), while the sites for curcumin keto, resveratrol, salicylic and gallic acids contain 14 similar residues from the A and B protein chains (LYS_{99A}, SER_{102A}, HSD_{103A}, LEU_{106A}, PHE_{117A}, HSD_{122A}, ALA_{123A}, ASP_{126A}, VAL_{34B}, TYR_{35B}, LEU_{105B}, ASN_{108B}, VAL_{109B}, CYS_{112B}) (Table 3).

Table 3. The interface residues in the complexes of polyphenols with deoxyhemoglobin

Hb deoxy+	Amino acid residues forming the deoxyHb binding sites for polyphenols	Type of interactions
Salicylic acid	HSD_{103A}, LEU_{106A}, VAL_{107A}, ALA_{110A}, PHE_{117A}, HSD_{122A}, ALA_{123A}, ASP_{126A}, VAL_{34B}, TYR_{35B}, ASN_{108B}, VAL_{109B}, CYS_{112B}	Hydrophobic interactions, hydrogen bonds
Resveratrol	LYS_{99A}, LEU_{100A}, SER_{102A}, HSD_{103A}, LEU_{106A}, PHE_{117A}, HSD_{122A}, ALA_{123A}, ASP_{126A}, VAL_{34B}, TYR_{35B}, LEU_{105B}, ASN_{108B}, VAL_{109B}, CYS_{112B}, VAL_{113B}	Hydrophobic interactions

Hb deoxy+	Amino acid residues forming the deoxyHb binding sites for polyphenols	Type of interactions
Curcumin (enol form)	THR_{41A}, LEU_{28D}, PHE_{41D}, PHE_{42D}, PHE_{45D}, LYS_{59D}, ALA_{62D}, HSD_{63D}, VAL_{67D}, HSD_{97D}, VAL_{98D}, ASP_{99D}, ASN_{102D}, PHE_{103D}	Hydrophobic interactions, hydrogen bonds, π-stacking
Curcumin (keto form)	LYS_{99A}, LEU_{100A}, SER_{102A}, HSD_{103A}, LEU_{106A}, PHE_{117A}, HSD_{122A}, ALA_{123A}, ASP_{126A}, LYS_{127A}, LEU_{129A}, ALA_{130A}, VAL_{34B}, TYR_{35B}, TRP_{37B}, GLU_{101B}, LEU_{105B}, ASN_{108B}, VAL_{109B}, CYS_{112B}, ASP_{94C}, PRO_{95C}, ARG_{141C}	Hydrophobic interactions, hydrogen bonds, π-stacking
Sesamin	TYR_{42A}, ASP_{94A}, PRO_{95A}, VAL_{96A}, ARG_{141A}, LYS_{99C}, SER_{102C}, ASP_{126C}, LEU_{129C}, ALA_{130C}, SER_{133C}, TYR_{35D}, TRP_{37D}, THR_{38D}, ASP_{99D}, GLU_{101D}, ASN_{102D}, LEU_{105D}, ASN_{108D}	Hydrophobic interactions, hydrogen bonds, π-cation interactions
Gallic acid	HSD_{103A}, LEU_{106A}, PHE_{117A}, HSD_{122A}, ALA_{123A}, ASP_{126A}, VAL_{34B}, TYR_{35B}, ASN_{108B}, VAL_{109B}, CYS_{112B}, VAL_{113B}	Hydrophobic interactions, hydrogen bonds

In the case of oxyHb there are 9 similar amino acid residues (LYS_{99A}, SER_{102A}, HIS_{103A}, LEU_{106A}, HIS_{122A}, ASP_{126A}, TYR_{35B}, LEU_{105B}, ASN_{108B}) which are involved in the interactions of resveratrol and gallic caid with the protein, the sites for curcumin enol and salicylic acid contain 4 similar residues (GLU_{27A}, ARG_{31A}, ALA_{111A}, HIS_{112A}), while the sites for curcumin keto and sesamin are completely different from each other (Table 4).

Table 4. The interface residues in the complexes of polyphenols with oxyhemoglobin

Hb oxy +	Amino acid residues forming the oxyHb binding sites for polyphenols	Type of interactions
Salicylic acid	GLU_{27A}, ARG_{31A}, ALA_{111A}, HIS_{112A}, GLY_{119B}, LYS_{120B}, PHE_{122B}, THR_{123B}, PRO_{124B}	Hydrophobic interactions, hydrogen bonds, salt bridges
Resveratrol	PHE_{98A}, LYS_{99A}, SER_{102A}, HIS_{103A}, LEU_{106A}, VAL_{107A}, HIS_{122A}, ASP_{126A}, LEU_{129A}, ALA_{130A}, SER_{133A}, TYR_{35B}, LEU_{105B}, ASN_{108B}, VAL_{109B}, CYS_{112B}	Hydrophobic interactions, hydrogen bonds
Curcumin (enol form)	HIS_{20A}, GLU_{23A}, TYR_{24A}, GLU_{27A}, GLU_{30A}, ARG_{31A}, HIS_{50A}, LYS_{56A}, ALA_{111A}, HIS_{112A}, LEU_{113A}, PRO_{114A}, LYS_{120B}, THR_{123B}, PRO_{124B}	Hydrophobic interactions, hydrogen bonds
Curcumin (keto form)	THR_{41A}, TYR_{42A}, PHE_{43A}, PRO_{44A}, HIS_{45A}, PHE_{46A}, GLN_{54A}, HIS_{58A}, LYS_{61A}, LYS_{90A}, LEU_{91A}	Hydrophobic interactions, hydrogen bonds
Sesamin	ARG_{40B}, PHE_{41B}, PHE_{42B}, GLU_{43B}, SER_{44B}, PHE_{45B}, LYS_{59B}, ALA_{62B}, HIS_{63B}, LYS_{66B}	Hydrophobic interactions, hydrogen bonds
Gallic acid	LYS_{99A}, SER_{102A}, HIS_{103A}, LEU_{106A}, HIS_{122A}, ASP_{126A}, TYR_{35B}, LEU_{105B}, ASN_{108B}, VAL_{109B}, CYS_{112B}	Hydrophobic interactions, salt bridges

An interesting peculiarity of the cyt c oxy – PF complexes is the fact that four amino acid residues, *viz.* ASN_{31}, HIS_{33}, GLY_{34}, and ARG_{38} are present in the binding sites for all polyphenols. Likewise, the high extent of similarity (nine similar residues) was observed for the binding sites of quercetin and resveratrol, curcumin enol and curcumin keto (Table 5).

Table 5. The interface residues in the complexes of polyphenols with oxidized cytochrome c

Cyt c oxy+	Amino acid residues forming the cyt c oxy binding sites for polyphenols	Type of interactions
Salicylic acid	PRO_{30}, ASN_{31}, LEU_{32}, HIS_{33}, GLY_{34}, LEU_{35}, ARG_{38}, LYS_{39}, THR_{40}, GLY_{41}, GLN_{42}, ALA_{43}, TYR_{48}, TRP_{59}	Hydrophobic interactions, hydrogen bonds, π-cation interactions, salt bridges
Resveratrol	VAL_{20}, GLU_{21}, LYS_{22}, GLY_{23}, GLY_{24}, LYS_{25}, HIS_{26}, ASN_{31}, HIS_{33}, GLY_{34}, ARG_{38}	Hydrogen bonds, π-cation interactions
Curcumin (enol form)	HIS_{26}, PRO_{30}, ASN_{31}, LEU_{32}, HIS_{33}, GLY_{34}, LEU_{35}, PHE_{36}, ARG_{38}, GLN_{42}, ALA_{43}, PRO_{44}, GLY_{45}, TYR_{46}, TYR_{48}, THR_{102}, ASN_{103}	Hydrogen bonds
Curcumin (keto form)	VAL_{20}, GLU_{21}, LYS_{22}, GLY_{24}, HIS_{26}, ASN_{31}, HIS_{33}, GLY_{34}, LEU_{35}, PHE_{36}, GLY_{37}, ARG_{38}, THR_{102}, ASN_{103}	Hydrophobic interactions
Sesamin	VAL_{20}, GLU_{21}, LYS_{22}, GLY_{23}, GLY_{24}, LYS_{25}, HIS_{26}, ASN_{31}, HIS_{33}, GLY_{34}, ARG_{38}	Hydrophobic interactions, hydrogen bonds, π-cation interactions
Gallic acid	PRO_{30}, ASN_{31}, LEU_{32}, HIS_{33}, GLY_{34}, LEU_{35}, PHE_{36}, ARG_{38}, LYS_{39}, THR_{40}, GLY_{41}, GLN_{42}, ALA_{43}, TYR_{48}, ILE_{57}, ILE_{58}, TRP_{59}	Hydrophobic interactions, hydrogen bonds, π-cation interactions

The conformational changes of cyt c upon its reduction seem to underlie the observed differences in amino acid composition of PF binding sites compared to cyt c oxy. For the majority of polyphenols the binding sites of cyt c red and cyt c oxy are essentially similar, but for gallic acid they are completely distinct (Table 6). To exemplify, the binding sites for salicylic acid contain the core residues such as PRO_{30}, ASN_{31}, LEU_{32}, HIS_{33}, LEU_{35}, ARG_{38}, ALA_{43} and TYR_{48} that

are conserved across both redox states, suggesting a substantial similarity in the binding mode of salicylic acid to the oxidized and reduced forms of cytochrome c.

Table 6. The interface residues in the complexes of polyphenols with reduced cytochrome c

Cyt c red +	Amino acid residues forming the cyt c red binding sites for polyphenols	Type of interactions
Salicylic acid	HIS_{26}, PRO_{30}, ASN_{31}, LEU_{32}, HIS_{33}, LEU_{35}, ARG_{38}, ALA_{43}, PRO_{44}, TYR_{46}, TYR_{48}	Hydrophobic interactions, Hydrogen bonds, salt bridges
Resveratrol	LYS_{22}, GLY_{23}, GLY_{24}, LYS_{25}, HIS_{26}, ASN_{31}, HIS_{33}, ARG_{38}, ALA_{43}	Hydrophobic interactions, hydrogen bonds
Curcumin (enol form)	LYS_{22}, GLY_{23}, GLY_{24}, LYS_{25}, HIS_{26}, ASN_{31}, HIS_{33}, GLY_{34}, ARG_{38}, ALA_{43}, GLY_{45}, TYR_{46}, SER_{47}, TYR_{48}	Hydrophobic interactions, hydrogen bonds
Curcumin (keto form)	GLY_{23}, GLY_{24}, LYS_{25}, HIS_{26}, LYS_{27}, THR_{28}, GLY_{29}, PRO_{44}, GLY_{45}, TYR_{46}, SER_{47}, TYR_{48}, LYS_{79}	Hydrophobic interactions, hydrogen bonds
Sesamin	LYS_{22}, GLY_{23}, GLY_{24}, HIS_{26}, PRO_{30}, ASN_{31}, LEU_{32}, HIS_{33}, LEU_{35}, ARG_{38}, LYS_{39}, THR_{40}, GLY_{41}, GLN_{42}, ALA_{43}, PRO_{44}, TYR_{48}, TRP_{59}	Hydrophobic interactions, hydrogen bonds, π-stacking, π-cation interactions
Gallic acid	MET_{12}, LYS_{13}, GLN_{16}, CYS_{17}, ILE_{81}, PHE_{82}, VAL_{83}	Hydrophobic interactions, hydrogen bonds, salt bridges

The additional involvement of HIS_{26}, PRO_{44} and TYR_{46} in the reduced form may reflect subtle conformational or electronic differences between the two oxidation states of cyt c. These differences are supposedly affect the dynamics and stability of the PF-cytochrome *c* complexes. To ascertain whether there exist some specific amino acids in the protein binding sites of a given polyphenolic compound we performed the cumulative analysis of the data presented in the Tables 2-6 aimed at determining the occurrence frequency of amino acid residue in the polyphenol binding sites. It appeared that salicylic acid the highest occurrence frequency was observed for tyrosine and arginine (80 %); resveratrol – lysine (100 %); curcumin, enol form – arginine, lysine, tyrosine, leucine (80 %); curcumin, keto form – lysine, histidine (100 %), leucine, tyrosine, proline, phenylalanine (80 %); sesamine – arginine, lysine (100 %), glutamic acid (80 %); gallic acid – leucine, tyrosine, cysteine, phenylalanine, histidine (80 %). Remarkably, most protein binding sites for polyphenols contain positively charged amino acid residues (lysine or arginine) and aromatic residue (tyrosine), while histidine and phenylalanine seem to be essential for the interactions of curcumin keto and gallic acid with proteins. The analysis of the molecular docking data with PLIP showed that most complexes are stabilized by hydrophobic interactions and hydrogen bonds, but salt bridges, π-stacking and π-cation interactions may also contribute to polyphenol association with functional proteins (Tables 2-6).

CONCLUSIONS

In conclusion, the molecular docking study of the complexes between the functional proteins including serum albumin, hemoglobin (deoxy and oxy forms), cytochrome c (oxidized and reduced forms), and representatives of five groups of polyphenolic compounds such as phenolic acids and derivatives (salicylic acid), stilbenes (resveratrol), curcuminoids (curcumin), lignans (sesamin) and tannins (gallic acid) revealed that all polyphenols display the highest affinities for serum albumin and deoxyHb, while the lowest affinities are observed for cytochrome c. The protein-polyphenol binding sites have been characterized in terms of their amino acid composition, the binding energy and the types of protein-ligand interactions. The importance of specific amino acid residues for the association of polyphenols with proteins has been demonstrated, with the highest occurrence frequency in the protein binding sites being found for lysine, arginine and tyrosine.

Acknowledgements

This project has received funding through the EURIZON project, which is funded by the European Union under grant agreement No. 3049.

ORCID

Uliana Malovytsia, https://orcid.org/0000-0002-7677-0779; **Valeriya Trusova,** https://orcid.org/0000-0002-7087-071X;
Mette Hedegaard Thomsen, https://orcid.org/0000-0001-6805-7247; **Kateryna Vus,** https://orcid.org/0000-0003-4738-4016
Olga Zhytniakivska, https://orcid.org/0000-0002-2068-5823; **Galyna Gorbenko,** https://orcid.org/0000-0002-0954-5053

REFERENCES

[1] C. Weng, and G. Yen, Canc. Treat. Rev. **38**, 76 (2012), https://doi.org/10.1016/j.ctrv.2011.03.001
[2] T. Ozdal, E. Capanoglu, and F. Altay, Food Res. Int. **51**, 954 (2013). https://doi.org/10.1016/j.foodres.2013.02.009
[3] N. Poklar Ulrih, Crit. Rev. Food Sci. Nutr. **57**, 2144 (2017). https://doi.org/10.1080/10408398.2015.1052040
[4] F. Shahidi, and C. Dissanayaka, Food Prod. Process and Nutr. **5**, 2 (2023). https://doi.org/10.1186/s43014-022-00121-0
[5] A. Bennick, Crit. Rev. Oral Biol. Med. **13**, 184-196 (2002). https://doi.org/10.1177/154411130201300208
[6] P. Xue, G. Zhang, J. Zhang, and L. Ren, Curr. Protein Pept. Sci. **22**, 217 (2021). https://doi.org/10.2174/1389203721666201109112220
[7] V. de Freitas, and N. Mateus, Curr. Organ. Chem. **16**, 724 (2012). https://doi.org/10.2174/138527212799958002
[8] T. Raja, W. Raja, V. Duraipandiyan, S. Ignacimuthu, U. Janakiraman, and S. Packiam, Curr. Med. Chem. **30**, 4032 (2023). https://doi.org/10.2174/0929867330666221202152540

[9] T. Xu, J. Na, Q. Liu, G. Kuang, Q. Zhang, and Y. Zhao, Mater. Today Commun. **41**, 110575 (2024). https://doi.org/10.1016/j.mtcomm.2024.110575
[10] B. Giardina, I. Messana, R. Scatena, and M. Castagnola, Crit. Rev. Biochem. Mol. Biol. **30**, 165 (1995). https://doi.org/10.3109/10409239509085142
[11] Y. Ow, D. Green, Z. Hao, and T. Mak, Nat. Rev. Mol. Cell. Biol. **9**, 532 (2008). https://doi.org/10.1038/nrm2434
[12] S.J. Hewlings, and D.S. Kalman, Foods, **6**, 92 (2017). https://doi.org/10.3390/foods6100092
[13] L. Frémont, Life Sci. **66**, 663 (2000). https://doi.org/10.1016/S0024-3205(99)00410-5
[14] Y. Zhang, F. Liu, Y. Lin, L. Li, M. Chen, and L. Ni, J. Chem. **1**, 4236525 (2022). https://doi.org/10.1155/2022/4236525
[15] Rosheen, S. Sharma, and D. Utreja, ChemistrySelect, **8**, e202204614 (2023). https://doi.org/10.1002/slct.202204614
[16] B. Badhani, N. Sharmaa, and R. Kakkar, RSC Adv. **5**, 27540 (2015). https://doi.org/10.1039/C5RA01911G
[17] Y. Yan, H. Tao, J. He, and S-Y. Huang, Nat. Protoc. **15**, 1829 (2020). https://doi.org/10.1038/s41596-020-0312-x
[18] S. Salentin, S. Schreiber, V. Haupt, M. Adasme, and M. Schroeder, Nucleic Acids Res. **43**, W443 (2015). https://doi.org/10.1093/nar/gkv315

ВЗАЄМОДІЯ ПОЛІФЕНОЛІВ З ФУНКЦІОНАЛЬНИМИ БІЛКАМИ: ДОСЛІДЖЕННЯ МЕТОДОМ МОЛЕКУЛЯРНОГО ДОКІНГУ

У. Маловиця[a], В. Трусова[a], М. Томсен[b], К. Вус[a], О. Житняківська[a], Г. Горбенко[a]

[a]Кафедра медичної фізики та біомедичних нанотехнологій, Харківський національний університет імені В.Н. Каразіна м. Свободи 4, Харків, 61022, Україна

[b]Університет Аалборг, вул. Нільса Бора 8,6700 Есб'єрг, Данія

Поліфеноли, біоактивні речовини рослинного походження з протипухлинними, імуномоделюючими, антиоксидантними, протизапальними, протимікробними та багатьма іншими властивостями наразі привертають значну увагу завдяки їхньому високому терапевтичному потенціалу. Біомолекулярні взаємодії поліфенольних сполук, зокрема, асоціація з фізіологічно важливими білками, можуть у значній мірі визначати їхні біологічні ефекти. У даній роботі метод молекулярного докінгу був застосований для характеризації зв'язування куркуміну (єнольна та кето форми), ресвератролу, сесаміну, саліцилової та галової кислот з функціональними білками, такими як сироватковий альбумін, гемоглобін (дезокси та окси форми), цитохром с (окислена та відновлена форми). Встановлено, що всі досліджені поліфеноли мають найвищу спорідненість до сироваткового альбуміну та дезоксигемоглобіну, тоді як найнижча спорідненість була виявлена до цитохрому с. Аналіз амінокислотних залишків в контактній області між білком і лігандом показав, що існують специфічні амінокислоти, які найчастіше входять до складу сайтів зв'язування поліфенолів, серед яких лізин, аргінін та тирозин.

Ключові слова: *поліфеноли; сироватковий альбумін; гемоглобін; цитохром с; молекулярний докінг*

East European Journal of Physics. **2.** 424-430 (2025)
DOI:10.26565/2312-4334-2025-2-52 ISSN 2312-4334

REDUCING INFLUENCE OF HARDWARE OF COMMUNICATION STATION ON CHARACTERISTICS OF ASYMMETRIC BICONICAL DIPOLE USING MAGNETO-DIELECTRIC SUBSTRATE ON FINITE-SIZE METAL SCREEN

Mikhail V. Nesterenko*, Victor A. Katrich, Svetlana V. Pshenichnaya, Sergey A. Pogarsky
V.N. Karazin Kharkiv National University, 4, Svobody Sq., Kharkiv, Ukraine, 61022
**Corresponding Author e-mail: mikhail.v.nesterenko@gmail.com*
Received February 2, 2025; revised April 17, 2025; accepted May 3, 2025

Based on the approximate analytical solution previously obtained by the authors to the problem of excitation (radiation, scattering) of electromagnetic waves by an asymmetric biconical dipole with distributed surface impedance (constant and variable) in a free space, the recommendations are proposed for reducing the influence of the hardware of a communication station on the characteristics of the such dipole using a magneto-dielectric substrate on a finite-size metal screen. Comparison of numerical and experimental results for a dipole in free space confirms the adequacy of the proposed mathematical model to the real physical process. Numerical results are given for the input characteristics and radiation fields of the dipole with magneto-dielectric substrate in the case of its asymmetric feeding by a point source.
Keywords: *Biconical dipole; Distributed surface impedance; Magneto-dielectric substrate; Finite-size metal screen; Asymmetric excitation; Current distribution; Input characteristics*
PACS: 02.70.Pt; 78.70Gq; 84.40.-x

INTRODUCTION

Among modern communication systems (both mobile and stationary), the leading place is occupied by multi-frequency (multi-channel) structures. The main functional element of such devices are antennas, which differ from each other in their design features, for example, they can be single-element structures (mono-frequency) or multi-element (multi-frequency) structures [1]. At the same time, the operation of a multi-frequency antenna, implemented by expanding the operating band (broadband antenna), in turn, can lead to a significant weakening of its noise-immune interference immunity properties. Typically, designers take the path of combining several antennas operating at different frequencies into one structure [2-8]. This approach significantly complicates the design of the antenna device and this is a difficult factor to overcome on the path to its miniaturization. Note, that since in the abovementioned publications and other similar ones, the antennas are located outside the phone body, so the influence of the phone's internals on their characteristics is significantly minimized.

In recent decades, a large number of publications have appeared devoted to multi-band printed antennas directly integrated into communication devices, for example [9-21] and references therein. In this case, the electrodynamic characteristics of the antennas are obtained using commercial programs such as ANSYS HFSS, CST Microwave Studio, FEKO and others. Calculating and optimizing the antenna characteristics using this approach requires enumeration of a large number of options, and, hence, huge amount of computer time and resources. However, it is not always clear from the text of the publications: 1) how the influence of the phone hardware on the antenna characteristics is minimized? 2) how the experimental studies were carried out, namely, together with the filling or only the case with the antenna?
The use of dipoles with an asymmetric excitation, i.e. with an arbitrary position feeding point along their length, for creating multi-band antennas has been repeatedly proposed by researchers in various publications [5], [7], [22-29]. However, in these literary sources only perfectly conducting dipoles were considered. Another solution makes use of a dipole antenna with an asymmetric excitation and distributed surface impedance, directly integrated into the body of the communication device [25-28]. In this case, the frequency response of the antenna may have several resonances that prevent the radiation (receiving) of electromagnetic waves outside the resonant frequency bands.

On the other hand, one of the additional parameters for obtaining the special characteristics of antennas in the form of a cylindrical dipole can be a change of the radius of the cross section of the dipole along its length. In the case of a linear increase in the radius of the vibrator from the feeding point of the antenna to its ends (biconical dipole), this antenna resonates at a smaller geometric length, and is also more broadband compared to a dipole of constant radius (see, for example, [27], [28], [30–41] and references in them). However, all of them are devoted to calculating the electrodynamic characteristics of perfectly conducting dipoles excited at the geometric center by a concentrated electromotive force (EMF). Also, as is known, to analyze receiving antennas it is necessary to know the current in the scattering dipole excited by the incident electromagnetic wave [38]. It is worth to notice that in [41] for operation in the three-frequency range it is offered to use three antennas in the form of symmetrical patch biconical dipoles. Moreover, it is proposed to make both the antennas themselves and the rather complex supply system from pure gold.

Cite as: M.V. Nesterenko, V.A. Katrich, S.V. Pshenichnaya, S.A. Pogarsky, East Eur. J. Phys. 2, 424 (2025), https://doi.org/10.26565/2312-4334-2025-2-52

The purpose of this paper is to study a multiband antenna for communication systems based on an asymmetric biconical dipole with a distributed surface impedance and arbitrary excitation, in particular, by feeding the antenna with a voltage source at a point arbitrary along the length of the dipole to create a multi-frequency operating mode. Thus, we will combine in one design all the advantages of asymmetric excitation, biconical geometry and the presence of a distributed surface impedance. Based on the approximate analytical solution previously obtained by the authors to the problem of excitation of electromagnetic waves by an asymmetric biconical dipole with distributed surface impedance (constant and variable) in a free space, the recommendations are proposed for reducing the influence of the hardware of a communication station on the characteristics of the such dipole using a magneto-dielectric substrate on a finite-size metal screen.

CHARACTERISTICS OF THE ASYMMETRIC BICONICAL DIPOLE IN A FREE SPACE

Let us limit ourselves by the linear law of the radius change $r(s)$ along the dipole with the $2L$ length and located in free space. It has the distributed internal linear impedance z_i and is excited by the electrical field $E_{0s}(s)$ of the given sources (tangential component). We assume that the dipole stays electrically thin in the operating frequency band, i.e. $kr(s)<<1$, $r(s)<<2L$, where $k=2\pi/\lambda$, λ is the wavelength in free space. Then the integral equation relatively to the $J(s)$ current for the impedance boundary condition on the dipole surface can be written as [38]:

$$\left(\frac{\mathrm{d}^2}{\mathrm{d}s^2}+k^2\right)\int_{-L}^{L} J(s')\frac{e^{-ik\tilde{R}(s,s')}}{\tilde{R}(s,s')}\mathrm{d}s' = -\frac{i\omega}{\cos\psi}\left[E_{0s}(s)-z_i J(s)\right], \tag{1}$$

where $\tilde{R}(s,s')=\sqrt{(s-s')^2+r^2(s)}$, $\psi=(\psi_1+\psi_2)/2$ ($\frac{\psi}{2\pi}<<1$), s and s' are the local coordinates related to the dipole axis and surface (Fig. 1).

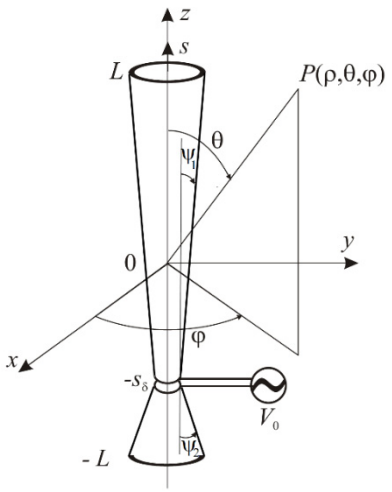

Figure 1. The geometry of structure and notations

An approximate analytical solutions of equation (1) was obtained in [27] (z_i is the constant along the dipole length) and in [28] (z_i is the variable along the dipole length) for an arbitrary field of external sources $E_{0s}(s)$ and the case of dipole feeding by the voltage generator with amplitude V_0 in the point $s=-s_\delta$ was investigated. As a result of solving equation (1), the following expressions were obtained: for the input impedance $Z_{in}=R_{in}+iX_{in}$, module of reflection coefficient in the antenna feeder with the wave impedance W $|S_{11}|=|(Z_{in}-\mathrm{W})|/|(Z_{in}+\mathrm{W})|$, the voltage standing wave ratio $\mathrm{VSWR}=(1+|S_{11}|)/(1-|S_{11}|)$ and radiation fields of the dipole.

As it is well known [25], the condition for resonance of any antenna structure is the equality on average over the period of harmonic oscillations of the near-range reactive fields of electric and magnetic types. The fulfillment of this condition mainly depends on the geometric dimensions of the antenna. In our case, we define it as the minimum value of the modulus of the reflection coefficient in the feeder line (hereinafter W =50 Ohm). The dependences of the $|S_{11}|$ versus frequency for different positions of the feeding point s_δ are presented in Fig. 2 (hereinafter z_i =0).

As can be seen, when moving s_δ from the geometric center of the dipole, there are several resonant frequencies at $2L$ =132 mm, r_δ =0.5 mm, r_L =3 mm (r_δ and r_L are the radii of the dipole in point $s=-s_\delta$ and in its end). This choice of the dipole length is due to the condition of the first resonance at the frequency f =0.850 GHz (GSM 850). One can notice that for a regular dipole with a radius r =2 mm, its length would be equal to $2L$ =156 mm.

The spatial distribution of the dipole radiation field in a free space in comparison with experimental data presented in Fig. 3. Due to the complexity of the antenna structures considered below, we will use software FEKO.

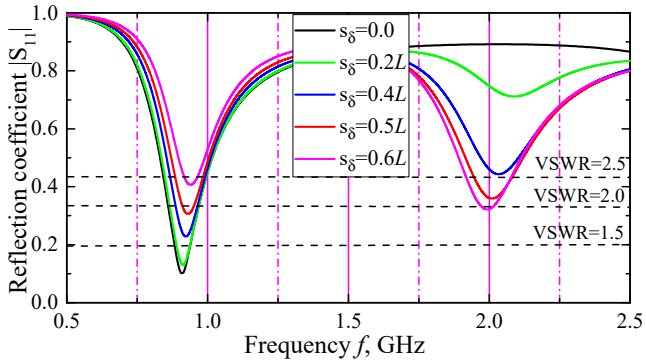

Figure 2. The dependences of the $|S_{11}|$ versus frequency for dipole in a free space for different positions of the feeding point s_δ at $2L$ =132 mm, r_δ =0.5 mm, r_L =3 mm

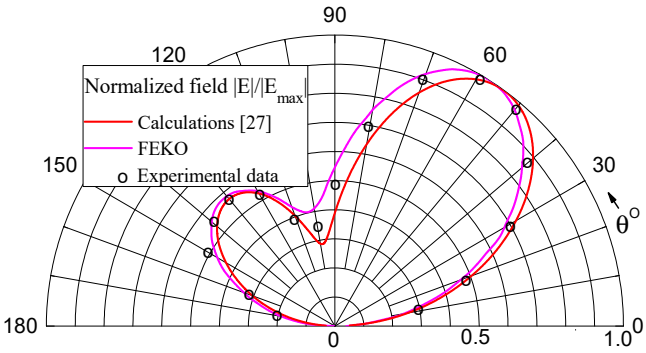

Figure 3. The spatial distribution of the dipole radiation field in a free space at $f = 0.85$GHz, $s_\delta = 0.2L$, $2L$ =138 mm, r_δ =1 mm, r_L =3 mm

INFLUENCE OF SUBSTRATE PARAMETERS ON DIPOLE CHARACTERISTICS

1. Dipole above metal screen of finite dimensions and on dielectric substrate

Fig. 4 shows the results of calculations for the cases of a dipole in free space, a dipole above a metal screen (herein after screen length L_{scr} = 140 mm, width W_{scr} = 6 mm) and on a dielectric substrate made of a material FR4 ($\varepsilon = \varepsilon' - i\varepsilon'' = 4.4 - i0.115$) with thickness d =2 mm. As it can be seen, the presence of a metal screen of finite dimensions, as well as a purely dielectric substrate, significantly worsens the resonant characteristics of the dipole.

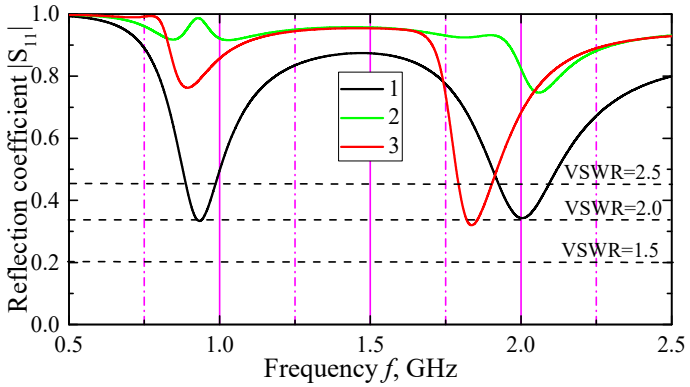

Figure 4. The dependences of the $|S_{11}|$ versus frequency at $s_\delta = 0.55L$, $2L$ =132 mm, r_δ=0.5 mm, r_L =3 mm: 1-dipole in a free space, 2- dipole above a metal screen, 3- dipole on a dielectric substrate (d =2 mm) on a metal screen.

2. Dipole with variable feeding point on dielectric substrate on screen

Fig. 5 Shows the dependences of the $|S_{11}|$ versus frequency for dipole on a dielectric substrate on a screen. As follows from the graphs, changing the position of the feeding point in this case has small effect on the resonant characteristics of the dipole.

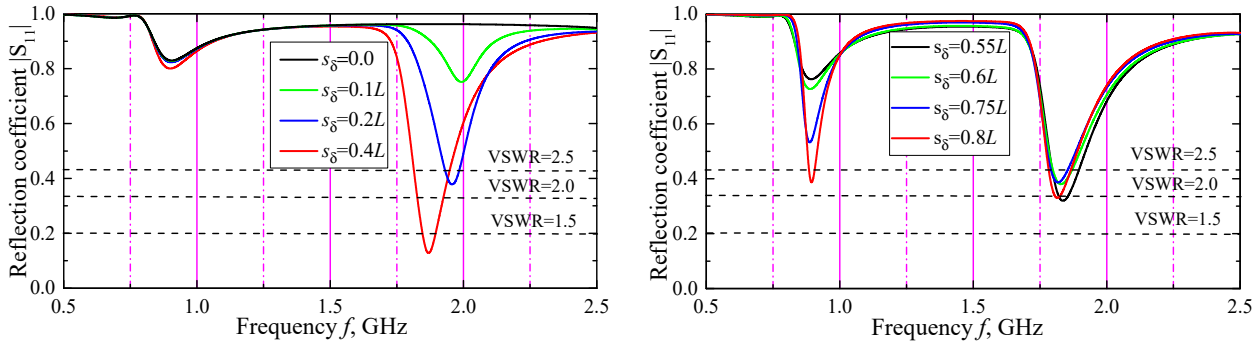

Figure 5. The dependences of the $|S_{11}|$ versus frequency for dipole on a dielectric substrate (d =2 mm) on a screen for the different positions of the feeding point s_δ at $2L$ =132 mm, r_δ=0.5 mm, r_L =3 mm

3. Dipole on magneto-dielectric substrate on screen with variable feeding point

As follows from general physical principles (mainly based on impedance concept [42]), to improve the characteristics of the dipole it is necessary to use the magnetic material as a substrate. Let us use the magneto-dielectric TDK-IR-A095 with the following electrophysical parameters in the frequency range $f = 0.5 \div 10.0$ GHz are $\varepsilon = 6.2 - i0.32$, $\mu = 0.60 - i0.32$ [43].

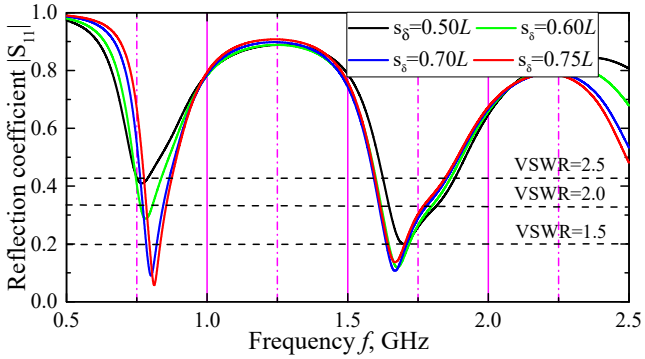

Figure 6. The dependences of the $|S_{11}|$ versus frequency for dipole on a magneto-dielectric substrate on a screen (TDK with thickness d_1 =1 mm on a screen and FR4 with thickness d_2 =1 mm under the dipole) for different positions of the feeding point s_δ at $2L$ =132 mm, r_δ=0.5 mm, r_L =3 mm.

As can be seen from the presented curves in Fig. 6, it is possible to achieve a significant decrease in the value of the reflection coefficient by changing the position of the feeding point in the given frequency range. However, the values of the resonant frequencies differ significantly from the original ones (see Fig. 2). To correct this drawback, the next step must be realized.

4. Finding the resonant length of dipole on magneto-dielectric substrate on screen

Graphs for the final resonant length $2L$ =117 mm of the dipole (in accordance with Fig. 2) are presented in Fig. 7. As can be seen, the resonant frequencies of the dipole correspond to the ranges of GSM 850 and GSM 1900.

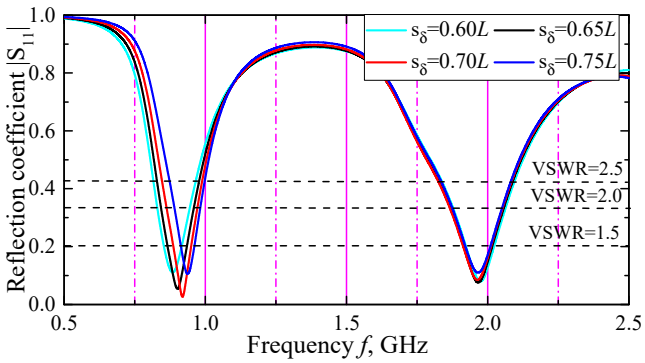

Figure 7. The dependences of the $|S_{11}|$ versus frequency for dipole on a magneto-dielectric substrate on a screen (TDK with thickness d_1 =1 mm on a screen and FR4 with thickness d_2 =1 mm under the dipole) on a screen for different positions of the feeding point s_δ at $2L$ =117 mm, r_δ=0.5 mm, r_L =3 mm (part 1).

The corresponding spatial distributions of the dipole radiation field for the resonant frequencies are represented in Fig. 8. Although the spatial distributions presented are somewhat different, this does not impair the user properties of the radiating system presented because the direction of the main maximum remains almost unchanged.

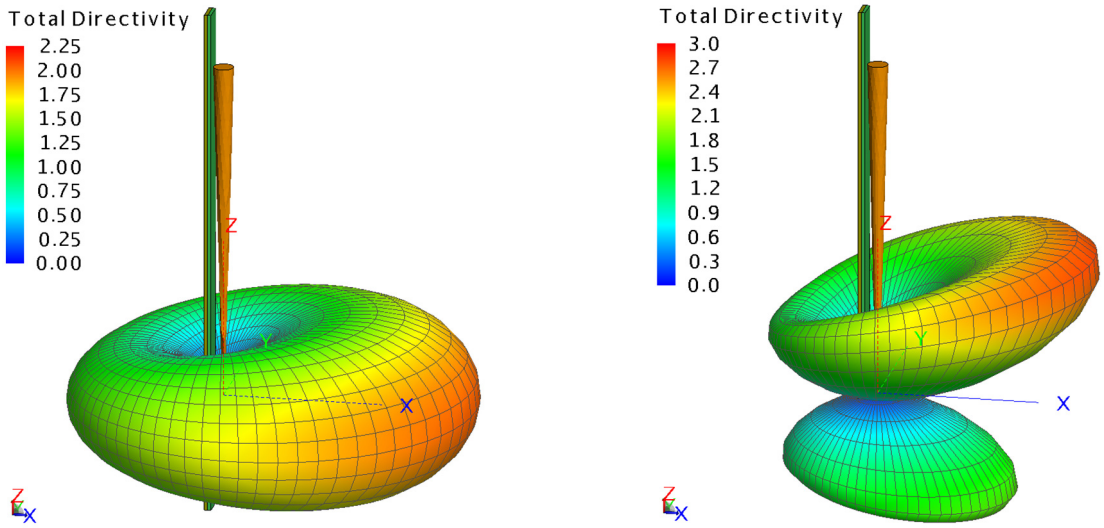

(a) $f = 0.850$ GHz (b) $f = 1.900$ GHz

Figure 8. Spatial distributions for dipole on a magneto-dielectric substrate (TDK with thickness d_1 =1 mm on a screen and FR4 with thickness d_2 =1 mm under the dipole) on a screen at $s_\delta = 0.7L$, $2L$ =117 mm, r_δ=0.5 mm, r_L =3 mm

With a further increase in the frequency range, another resonance occurs (Fig. 9). In this case, the ratio of resonant frequencies for $s_\delta = 0.7L$ is approximately 1 : 2.2 : 3.6. However, if we look at the figure more closely, we can see that this ratio is not exactly fulfilled under the influence of a change in the feeding point, so this gives reasons for an independent change in the center frequency of each of the operating frequency bands within certain limits.

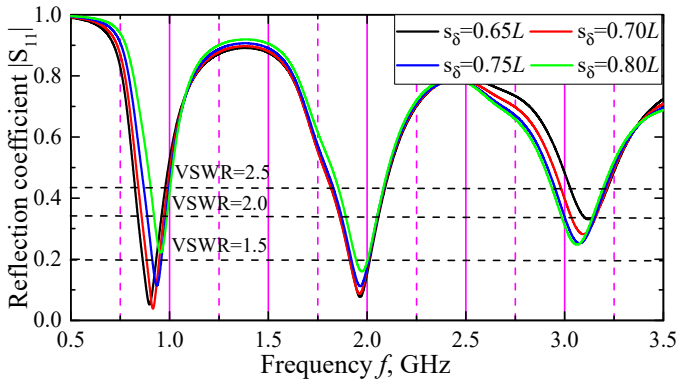

Figure 9. The dependences of the $|S_{11}|$ versus frequency for dipole on a magneto-dielectric substrate on a screen (TDK with thickness d_1 =1 mm on a screen and FR4 with thickness d_2 =1 mm under the dipole) on a screen for different positions of the feeding point s_δ at $2L$ =117 mm, r_δ=0.5 mm, r_L =3 mm (part 2).

CONCLUSION

Based on the approximate analytical solution previously obtained by the authors to the problem of excitation (radiation, scattering) of electromagnetic waves by an asymmetric biconical dipole with distributed surface impedance (constant and variable) in a free space, the recommendations are proposed for reducing the influence of the hardware of a communication station on the characteristics of the such dipole using a magneto-dielectric substrate on a finite-size metal screen. Solution correctness is confirmed by satisfactory agreement of numerical results received using the commercial software FEKO and experimental data. Numerical results are given for the input characteristics and radiation field of the dipole in the case of its asymmetric feeding by a point source. In order to reduce the interaction of the antenna with the phone hardware, the influence of the electrophysical parameters of the magneto-dielectric substrate on the characteristics of the dipole was comprehensively studied. The distinctive property of the antenna is the possibility of resonant tuning to the selected frequencies, depending on the geometric and electro-physical parameters of the dipole and substrate, which does not deteriorate the noise-immune interference immunity properties in comparison with broadband antennas. In this case, the reduction in the length of the antenna on a magneto-dielectric substrate compared to a biconical

dipole in free space is 11%, and the shortening compared to a regular dipole in free space is 25%. It can be seen that the center frequencies of the channels in which the antenna operates can be independently adjusted within small limits by changing the size of the cones and the position of the feeding point. It is possible to calculate the dimensions of the dipole and the substrate parameters for other resonant frequencies. It is also planned to further study the gain and radiation efficiency of such a structure. Analysis of radiation characteristics of the proposed dipole antenna has proved the possibility of practical applications of this antenna for multiband portable radio stations, smartphones, electronic gadgets, base stations and different antenna systems, for example, multi-channel UAV communication systems.

ORCID

Mikhail V. Nesterenko, https://orcid.org/0000-0002-1297-9119; **Victor A. Katrich**, https://orcid.org/0000-0001-5429-6124;
Svetlana V. Pshenichnaya, https://orcid.org/0000-0002-6212-7280; **Sergey A. Pogarsky**, https://orcid.org/0000-0003-0833-1421

REFERENCES

[1] Z. Zhang, *Antenna design for mobile devices*, (London, England: Wiley, 2017).
[2] G. Zhou, and B. Yildirim, "A multi-band fixed cellular phone antenna," in: Proc. IEEE AP-S Int. Symp. **1**, 112 (1999). https://doi.org/10.1109/APS.1999.789095
[3] N. Odachi, S. Sekine, H. Shoki, and Y. Suzuki, "A rod antenna with a meander element for hand-held phone," in: *IEEE Antennas and Propagation Society International Symposium. Transmitting Waves of Progress to the Next Millennium. 2000 Digest. Held in conjunction with: USNC/URSI National Radio Science Meeting*, vol.3, (Salt Lake City, UT, USA, 2000), pp. 1682-1685, https://doi.org/10.1109/APS.2000.874565
[4] H.-C. Tung, C.-Y. Fang, and K.-L. Wong, "Dual-band inverted-L monopole antenna for GSM/DCS mobile phone," in: *IEEE Antennas and Propagation Society International Symposium (IEEE Cat. No.02CH37313),* (San Antonio, TX, USA, 2002), (2002). pp. 30-33, https://doi.org/10.1109/APS.2002.1018149
[5] C. Song, Y. Huang, J. Zhou, P. Carter, S. Yuan, Q. Xu, and Z. Fei, "Matching network elimination in broadband rectennas for high-efficiency wireless power transfer and energy harvesting," IEEE Trans. Industrial Electronics, **64**, 3950-3961 (2017). https://doi.org/10.1109/TIE.2016.2645505
[6] K. Paramayudha, S. J. Chen, T. Kaufmann, W. Withayachumnankul, and C. Fumeaux, "Triple-band reconfigurable low-profile monopolar antenna with independent tenability," IEEE Open J. Antennas Propag. **1**, 47-56 (2020). https://doi.org/10.1109/OJAP.2020.2977662
[7] W. Hu, T. Feng, S. Gao, L. Wen, Q. Luo, P. Fei, Y. Liu, and X. Yang, "Wideband circularly polarized antenna using single-arm coupled asymmetric dipoles," IEEE Trans. Antennas Propag. **68**, 5104-5113 (2020). https://doi.org/10.1109/TAP.2020.2975275
[8] Y. Luo, and Y. Liu, "Nona-band antenna with small nonground portion for full-view display mobile phones," IEEE Trans. Antennas Propag. **68**, 7624-7629 (2020). https://doi.org/10.1109/TAP.2020.2989874
[9] S. Wang, and Z. Du, "A dual-antenna system for LTE/WWAN/WLAN/WiMAX smartphone applications," IEEE Antennas Wireless Propag. Lett. **14**, 1443-1446 (2015). https://doi.org/10.1109/LAWP.2015.2411253
[10] R. Tang, and Z. Du, "Wideband monopole without lumped elements for octa-band narrow-frame LTE smartphone," IEEE Antennas Wireless Propag. Lett. **16**, 720-723 (2017). https://doi.org/10.1109/LAWP.2016.2600761
[11] Y. Yang, Z. Zhao, W. Yang, Z. Nie, and Q.-H. Liu, "Compact multimode monopole antenna for metal-rimmed mobile phones," IEEE Trans. Antennas Propag. **65**, 2297-2304 (2017). https://doi.org/10.1109/TAP.2017.2679059
[12] Y. Liu, P. Liu, Z. Meng, L. Wang, and Y. Li, "A planar printed nona-band loop-monopole reconfigurable antenna for mobile handsets," IEEE Antennas Wireless Propag. Lett. **17**, 1575-1579 (2018). https://doi.org/10.1109/LAWP.2018.2856459
[13] D. Huang, Z. Du, and Y. Wang, "A quad-antenna system for 4G/5G/GPS metal frame mobile phones," IEEE Antennas Wireless Propag. Lett. **18**, 1586-1590 (2019). https://doi.org/10.1109/LAWP.2019.2924322
[14] Q. Tan, and F-C. Chen, "Triband circularly polarized antenna using a single patch," IEEE Antennas Wireless Propag. Lett. **19**, 2013-2017 (2020). https://doi.org/10.1109/LAWP.2020.3014961
[15] R.M. Moreno, J. Kurvinen, J. Ala-Laurinaho, A. Khripkov, J. Ilvonen, J. van Wonterghem, and V. Viikari, "Dual-polarized mm-wave endfire chain-slot antenna for mobile devices," IEEE Trans. Antennas Propag. **69**, 25-34 (2021). https://doi.org/10.1109/TAP.2020.3001434
[16] L. Chang, G. Zhang, and H. Wang, "Triple-band microstrip patch antenna and its four-antenna module based on half-mode patch for 5Gx4 MIMO operation," IEEE Trans. Antennas Propag. **70**, 67-74 (2022). https://doi.org/10.1109/TAP.2021.3090572
[17] C. Sahana, D. Nirmala, and M. Jayakumar, "Dual-band circularly polarized annular ring patch antenna for GPS-aided GEO-augmented navigation receivers," IEEE Antennas Wireless Propag. Lett. **21**, 1737-1741 (2022). https://doi.org/10.1109/LAWP.2022.3178980
[18] Z. Wan, Y. He, Y. Bai, and H. Sun, "Miniaturized, low-profile, triple-band microstrip antenna and its four-antenna module for smartphone applications," IEEE Trans. Antennas Propag., **71**, 9950-9955 (2023). https://doi.org/10.1109/TAP.2023.3315471
[19] R. Lakshmanan, S. Mridula, A. Pradeep, and K. Neema, "Ultra compact flexible monopole antennas for tri-band applications," Prog. Electromagn. Res. C, **130**, 43-55 (2023). http://dx.doi.org/10.2528/PIERC22110906
[20] A. Khade, M. Trimukhe, S. Verblkar, and R. K. Gupta, "Miniaturization of printed rectangular monopole antenna by using slots for triple band applications," Prog. Electromagn. Res. C, **130**, 155-167 (2023). http://dx.doi.org/10.2528/PIERC22122401
[21] R. Xu, and Z. Shen, "Dual-band circularly polarized RFID reader antenna with combined dipole and monopoles," IEEE Trans. Antennas Propag., **71**, 9593-9600, (2023). https://doi.org/10.1109/TAP.2023.3326945
[22] R.W.P. King, and T.T. Wu, "The cylindrical antenna with arbitrary driving point," IEEE Trans. Antennas Propag. **13**, 710-718 (1965). https://doi.org/10.1109/TAP.1965.1138531
[23] B. D. Popovic, "On polynomial approximation of current along thin asymmetrical cylindrical dipoles," IEEE Trans. Antennas Propag. **19**, 117-120 (1971). https://doi.org/10.1109/TAP.1971.1139879

[24] Y. Wang, S. Xu, and D. H. Werner, "1 bit dual-polarized reconfigurable transmitarray antenna using asymmetric dipole elements with parasitic bypass dipoles," IEEE Trans. Antennas Propag. **69**, 1188-1192 (2021). https://doi.org/10.1109/TAP.2020.3005713
[25] M. V. Nesterenko, V. A. Katrich, Y M. Penkin, V. M. Dakhov, and S. L. Berdnik, *Thin Impedance Vibrators. Theory and Applications*, (Springer Science+Business Media, New York, 2011).
[26] M. V. Nesterenko, V. A. Katrich, S. L. Berdnik, O. M. Dumin, and Y. O. Antonenko, "Asymmetric impedance vibrator for multi-band communication systems," Prog. Electromagn. Res. M, **102**, 81-89 (2021). http://dx.doi.org/10.2528/PIERM21031207
[27] M. V. Nesterenko, V. A. Katrich, and S. V. Pshenichnaya, "Multyband asymmetric biconical dipole antenna with distributed surface impedance and arbitrary excitation," East European J. Physics, (2), 450-455 (2024). https://doi.org/10.26565/2312-4334-2024-2-59
[28] M. V. Nesterenko, V. A. Katrich, Yu. V. Arkusha, and V. V. Katrich, "Radiation of electromagnetic waves by regular and biconical dipoles with variable distributed surface impedance and arbitrary excitation," East European J. Physics, (3), 465-474 (2024). https://doi.org/10.26565/2312-4334-2024-3-56
[29] X. Liu, K. Ning, S. Xue, L. Ge, K. W. Leung, and J.-F. Mao, "Printed filtering dipole antenna with compact size and high selectivity," IEEE Trans. Antennas Propag., **72**, 2355-2367, (2024). https://doi.org/10.1109/TAP.2024.3356176
[30] S. A. Schelkunoff, "Theory of antennas of arbitrary size and shape," Proc. IRE, **29**, 493-521 (1941). https://doi.org/10.1109/JRPROC.1941.231669
[31] C.T. Tai, "On the theory of biconical antennas," Journal Applied Phys., **19**, 1155-1160 (1948). https://doi.org/10.1063/1.1715036
[32] T.T. Wu, and R.W.P. King, "The tapered antenna and its application to the junction problem for thin wires," IEEE Trans. Antennas Propag. **24**, 42-45 (1976). https://doi.org/10.1109/TAP.1976.1141274
[33] S.A. Saoudy, and M. Hamid, "Input admittance of a biconical antenna with wide feed gap," IEEE Trans. Antennas Propag. **38**, 1784-1790 (1990). https://doi.org/10.1109/8.102740
[34] S. S. Sandler, and R. W. P. King, "Compact conical antennas for wide-band coverage," IEEE Trans. Antennas Propag. **42**, 436-439 (1994). https://doi.org/10.1109/8.280735
[35] K.-L. Wong, and S.-L. Chien, "Wide-band cylindrical monopole antenna for mobile phone," IEEE Trans. Antennas Propag. **53**, 2756-2758 (2005). https://doi.org/10.1109/TAP.2005.851784
[36] O. Dumin, P. Fomin, V. Plakhtii, and M. Nesterenko, "Ultrawideband combined monopole-slot radiator of Clavin type," in: *Proc. XXVth Int. Sem. Direct Inverse Problems of Electromagn. and Acoustic Wave Theory*, (Tbilisi, Georgia, 2020). pp. 32-36, https://doi.org/10.1109/DIPED49797.2020.9273399
[37] P. Fomin, O. Dumin, V. Plakhtii, and M. Nesterenko, "UWB antenna arrays with the monopole-slot radiator of Clavin type," in: *Proc. IIIth Ukraine Conf. on Electrical and Computer Engineering*, (Lviv, Ukraine, 2021). pp. 258-261, https://doi.org/10.1109/UKRCON53503.2021.9575282
[38] M. V. Nesterenko, A. V. Gomozov, V. A. Katrich, S. L. Berdnik, and V. I. Kijko, "Scattering of electromagnetic waves by impedance biconical vibrators in a free space and in a rectangular waveguide," Prog. Electromagn. Res. C, **119**, 275-285 (2022). http://dx.doi.org/10.2528/PIERC22020304
[39] F. F. Dubrovka, S. Piltyay, M. Movchan, and I. Zakharchuk, "Ultrawideband compact lightweight biconical antenna with capability of various polarizations reception for modern UAV applications," IEEE Trans. Antennas Propag., **71**, 2922-2929 (2023). https://doi.org/10.1109/TAP.2023.3247145
[40] J.M. Platt, L.B. Boskovic, and D.S. Filipovic, "Wideband biconical antenna with embedded band-notch resonator," IEEE Trans. Antennas Propag., **72**, 2921-2925 (2024). https://doi.org/10.1109/TAP.2024.3349785
[41] I. D. Chiele, M. Donelli, J. Iannacci, and K. Guha, "On chip modulated scattering tag operating at millimetric frequency band," Prog. Electromagn. Res. M, **124**, 71-77 (2024). http://dx.doi.org/10.2528/PIERM23102707
[42] M. V. Nesterenko, S. L. Berdnik, A. V. Gomozov, D. V. Gretskih, and V. A. Katrich, "Approximate boundary conditions for electromagnetic fields in electromagnetics. Radioelectronic and Computer Systems," No 3(103), 141-160, (2022). https://doi.org/10.32620/reks.2022.3.11
[43] K. Yoshitomi, "Radiation from a slot in an impedance surface," IEEE Trans. Antennas Propag. **49**, 1370-1376 (2001). https://doi.org/10.1109/8.954925

ЗМЕНШЕННЯ ВПЛИВУ АПАРАТНОГО ЗАБЕЗПЕЧЕННЯ СТАНЦІЇ ЗВ'ЯЗКУ НА ХАРАКТЕРИСТИКИ АСИМЕТРИЧНОГО БІКОНІЧНОГО ДИПОЛЯ З ВИКОРИСТАННЯМ МАГНІТО-ДІЕЛЕКТРИЧНОЇ ПІДКЛАДКИ НА СКІНЧЕННО-РОЗМІРНОМУ МЕТАЛЕВОМУ ЕКРАНІ

М. В. Нестеренко, Віктор А. Катрич, Світлана В. Пшеничная, Сергій О. Погарський
Харківський національний університет імені В.Н. Каразіна, майдан Свободи, 4, Харків, Україна, 61022

На основі попередньо отриманого авторами наближеного аналітичного розв'язку задачі збудження (випромінювання, розсіювання) електромагнітних хвиль асиметричним біконічним диполем з розподіленим поверхневим імпедансом (постійним і змінним) у вільному просторі запропоновано рекомендації щодо зменшення впливу апаратного забезпечення станції зв'язку на характеристики такого диполя за допомогою магніто-діелектричної підкладки на металевий екран кінцевого розміру. Порівняння чисельних та експериментальних результатів для диполя у вільному просторі підтверджує адекватність запропонованої математичної моделі реальному фізичному процесу. Наведено чисельні результати для вхідних характеристик і полів випромінювання диполя з магніто-діелектричною підкладкою за умови його несиметричного живлення точковим джерелом.

Ключові слова: *біконічний диполь; розподілений поверхневий імпеданс; магніто-діелектрична підкладка; кінцевий металевий екран; асиметричне збудження; розподіл струму; вхідні характеристики*

EAST EUROPEAN JOURNAL OF PHYSICS. 2. 431-435 (2025)
DOI:10.26565/2312-4334-2025-2-53 ISSN 2312-4334

ELECTROPHYSICAL NATURE OF DEFECTS IN SILICON CAUSED BY IMPLANTED PLATINUM ATOMS

Akramjon Y. Boboev*, Biloliddin M. Ergashev, Nuritdin Y. Yunusaliyev, Jamshidbek S. Madaminjonov
Andijan state university named after Z.M. Babur, Andijan, Uzbekistan
**Corresponding Author e-mail: aboboevscp@gmail.com*
Received March 2, 2025; accepted May 15, 2025

The article of this study focuses on the defects caused by the platinum (Pt) atoms implanted in the silicon (Si) with the changes of their electrophysical properties after the high temperature thermal treatments. The introduction of the platinum atom into the silicon crystal lattice creates deep-level defect centers where the sensitive electrical properties and phenomena caused by temperature changes can be observed more clearly than in intrinsic defects. Of particular focus on platinum atoms incorporation, extensive studies have demonstrated significant changes of the defect structure in silicon and substantial transformation of its electrophysical properties related to the electrical conduction mechanisms and carrier scattering phenomena. Exclusive electrophysical effects were observed for platinum-doped silicon samples, which underwent high-temperature thermal annealing at 1050 °C and 1150 °C, primarily associated with the clustering of boron and platinum atoms, and the formation of complex defect aggregates. These thermal treatments enhance the interaction of isolated defects leading to the formation of clusters and complex defect entities, which greatly enhances the scattering mechanisms. These interactive effects of defects were found to be dominant in changing charge carrier transport and recombination processes in silicon crystals. Furthermore, experimental results showed a combination of scattering mechanisms that includes neutral defects, deep energy levels induced by platinum impurities, and their respective charged states. Platinum-induced defects thus enable multiple scattering mechanisms, and such hybrid mechanisms play a critical role in a silicon electrical and electronic behaviors, which influence the semiconductor applicability of the materials in high-temperature or high-performance, etc.
Keywords: *Charge carrier mobility; Conductivity; Thermal treatment; Temperature coefficient; Acceptor impurities; van der Pauw method; Vacancies; Crystallography*
PACS: 78.30.Am

INTRODUCTION

In semiconductor technology, the thermal treatment at a high temperature and the metal-diffusion into silicon are important for changing the electrophysical characteristics of the material. They have a great influence over silicon crystallographic structure, charge carriers' concentration and mobility, and recombination processes. They are also chosen to improve the reliability of silicon-based microelectronic devices, provide a controlled spatial distribution of charge carriers, and enhance the thermal stability of the material. Among semiconductors, silicon (Si) is the dominant material, as it is cheap, mechanically strong, and can be synthesized in a sufficiently pure state to form high-quality monocrystals. An acceptor energy level is located near the top of a valence band [1] when an acceptor atom (B, Ga, or Al in the case of silicon) is located in the silicon crystal. These acceptor levels promote carrier generation (holes), thus helping to form p-type semiconductors. As a result, adjusting distribution and ionization energy of acceptor atoms in silicon is extremely important in microelectronics.

Also, when heavy metals like platinum (Pt), gold (Au), iron (Fe) and nickel (Ni) are incorporated in silicon, deep energy levels and defects form in this material [2]. These metals can introduce deep trap centers in the energy spectrum of silicon, which can have a profound impact on the mobility of charge carriers and mechanisms for conductivity. In particular, platinum atoms introduce deep energy levels in the band structure of silicon, thereby speeding up the recombination processes of charge carriers [3-5] In addition, at high-temperature processing, platinum atoms penetrate into the silicon lattice and occupy vacancies and interstitial defects [6]. Moreover, metallic atoms present in silicon act as electron and hole traps, which can either diminish their mobility, or, conversely, enhance their bulk conductivity. Those semiconductor processes are used in the production of silicon-based integrated circuits (ICs), high-speed transistors and sensor devices. Therefore, knowing the effect of the acceptor and/or metal atoms used to dope the silicon and studying their energy levels are paramount for accurate tuning of the electromagnetic properties of this material. This article presents the analysis of electrophysical changes arising from p-type silicon dopant by Pt atoms and high-temperature thermal processing conducted in this respect.

MATERIALS AND METHODS

Samples measuring 1×10×10 mm³, prepared from monocrystalline silicon with a resistivity of 5 Ω·cm and p-type conductivity, were used as the initial material [7]. Doping of silicon with platinum atoms was performed by gas-phase diffusion at temperatures of 950°C, 1050°C, and 1150°C for 5 hours in quartz ampoules evacuated to a vacuum of approximately 10^{-4} Torr. Afterward, the samples underwent a gradual cooling process to determine the resistivity,

Cite as: A.Y. Boboev, B.M. Ergashev, N.Y. Yunusaliyev, J.S. Madaminjonov, East Eur. J. Phys. 2, 431 (2025), https://doi.org/10.26565/2312-4334-2025-2-53

concentration and the mobility of the majority charge carriers in the grown films, the Van der Pauw method was used on a *HMS-7000* Hall effect measurement unit.

RESULTS AND DISCUSSION

It is known that in semiconductors, the temperature dependence of the mobility of charge carriers is given by the following expression:

$$\mu \sim T^m \cdot e^{-\frac{E_a}{kT}}.$$

Here, μ is the charge carriers' mobility, T is the absolute temperature, E_a is the activation energy, and k is the Boltzmann constant. In many cases, to achieve a linear relationship from equation (1), it is necessary to take the logarithm of both sides of the equation. Additionally, the mobility μ of charge carriers in monocrystalline silicon decreases with increasing temperature, exhibiting an inverse relationship [8]:

$$\mu \sim T^m.$$

Here, m is the temperature coefficient.

Charge carrier mobility in common p-type silicon samples doped with boron (p-Si<B>) normally retains such temperature dependence: informal of low temperatures (T < 150 K), it shows a weak or medium increase due to neighboring ionized impurities [9] scattering, whereas in the case of high temperatures (T > 150 K) - a highly mobility drops as a consequence of phonon [10] scattering. Which mechanism dominates depends on the doping concentration of the silicon where impurity atoms are incorporated, and the crystalline quality of the sample [11]. For instance, in the case of p-Si<B> samples, we noticed a temperature dependent charge carrier mobility in the range of 200–300 K with a temperature coefficient m = 0.4 (illustrated in the Figure 1). This implies that, beyond the acoustic phonon scattering at high temperature observed in the curve, further scattering mechanisms associated with structural imperfections (defects, clusters, dislocation points etc.) are being activated in samples treated by 5 h at 950 °C [12].

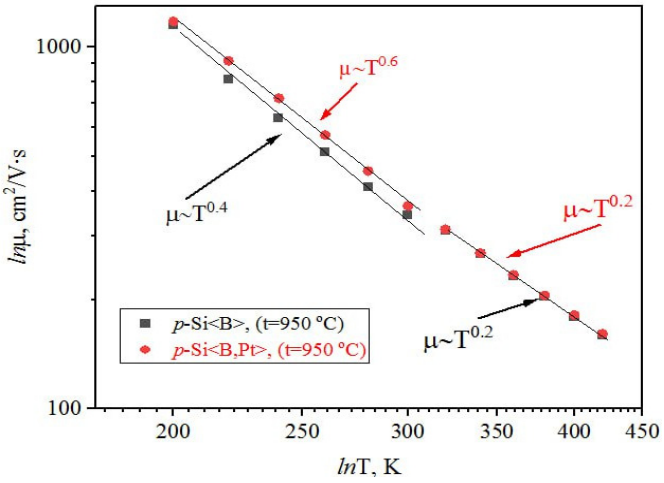

Figure 1. Logarithmic dependence of charge carrier mobility μ on temperature in p-Si<B> samples subjected to thermal treatment at 950°C and doped with Pt atoms.

Regarding the 200–300 K region, the temperature coefficient of charge carrier mobility rises from m = 0.4 to m = 0.6 in the sample of p-Si<B> when Pt atoms are diffusing in the substrate at high temperature of 950°C for 5 hours (see figure). This indicates that the Pt atoms, diffused into the silicon crystal lattice as a result of high-temperature processing, generate more complex structural damage and deep-level trap centers in silicon crystal, resulting in enhanced and temperature-dependent scattering mechanisms.

Between 300–450 K, the mobility of the charge carriers in p-Si<B> samples showed temperature dependence with a coefficient of m = 0.2 (figure shown). A quick recap of the underlying physical mechanisms behind this behavior is in order. Silicon possesses a moderate temperature regime at 300–450 K, as phonon scattering to charge carrier mobility prevails in this temperature range. We suspect scattering due to neutral defects or neutral impurity atoms in this case is more important due to the relatively low mobility coefficient m = 0.2 [13] Furthermore, because the boron atom concentration of the samples is very high (N_A>1018÷1019cm-3), this may also cause similar behaviors as reducing carrier mobility in heavily doped samples depends primarily on the scattering at impurity atoms and structural defects [14]. Finally, the presence of dislocations or other structural imperfections can also give rise to this reduction in temperature coefficient of mobility (e.g. (m = 0.2). It is more likely that this happens in the 300–450 K range where, in general, the interaction between charge carriers and defect structures is weakly temperature dependent.

A similar temperature dependence (μ~T0. 2) was also detected for p-Si<B,Pt> samples at the temperature range from 300 to 450 K (Figure 1). It is well known that in the case of p-Si<B> samples, the incorporation of transition metal

atoms such as Pt produces energy levels deep in the bandgap treated as deep-level impurities. These levels are related to defects that may be present in both neutral and positively charged forms [15]. These defects often exhibit neutral scattering center-like behavior – especially when related to Pt atoms – resulting in a weak temperature dependence of mobility. Moreover, Pt atoms serve as deep-level traps in the energy spectrum of the silicon crystal, being almost unchanged in a neutral state at high temperature due to the difficulty of entering a charged state [16]. As these defects stay in place in the neutral state during the temperature increases, they will serve as a scattering mechanism that is mostly independent of the temperature producing low value of mobility coefficient (m = 0.1÷0.3).

In addition, as can be found in the literature, low temperature coefficients, like the ones discussed here, are often how those of Si doped with Pt and other transition metals, such as Fe, Au, and Ni, are reported. The underlying cause of this behavior can mainly be ascribed to the generation of deep-level defects in silicon crystals by Pt atoms in turn activated by neutral scattering mechanisms. Thus, the equal temperature coefficient found in p-Si<B> and p-Si<B,Pt> samples (m = 0.2), proves that the dominant factor which causes scattering in this temperature range is neutral defect scattering. As we know, prolonged high-temperature thermal treatment leads to the redistribution of boron (B) and oxygen (O) atoms in the silicon lattice structure, resulting in the formation of small clusters or complexes. Therefore, as the concentration of intrinsic defects increases, so does the concentration of various intrinsic defects like vacancies, dislocations, and complex defect structures (e.g., double defects, clustered defects). Here in our case for p-Si<B> samples subjected to thermal treatment at 1050°C for 5 hours, we have seen the temperature dependence of charge carrier mobility in the full 200–450 K range with a temperature coefficient of m = 2.6 (Fig. 2). Such a large value cannot be accounted for by typical scattering mechanisms such as phonon or ionized impurity scattering. Instead, it suggests, at these high temperatures, boron atoms and other defects aggregate together to build complex defect centers, their effect in scattering not only remains high at high temperatures but may actually amplify [17]. Similarly, the addition of Pt atoms onto p-Si<B> samples at 1050°C for 5 hours led to a mobility coefficient of m = 2.3 in the 200–300 K range and m = 2.5 in the 300–450 K range. Traditional scattering mechanisms alone cannot explain these large values. They are rather rationalized by strong scattering from deep-level defects (trap centers) and cluster defects, and by related localized strain fields created by Pt inclusion. The defects provide ever stronger scattering centers for charge carriers at elevated temperatures.

For p-Si<B> samples heat-treated at 1150°C for 5 hours temperature-dependent mobility of charge carriers exhibited coefficients of m = 0.55 and m = 0.56 in the temperature ranges of 200–300 K and 300–450 K respectively (see Figure 3). These values (m=0.55÷0.6) are characteristic of a mixed scattering mechanism that arises from the joint contribution of acoustic phonon scattering (for which m ≈ 1.5) and neutral defect scattering (for which m ≈ 0.1÷0.3) [18]. This means that boron atoms and thus intrinsic defects in the silicon lattice redistribute due to the long-term high-temperature treatment, forming complex defects and clusters liable to exist both in neutral and charged states. This leads to temperature dependence of mobility that is significant, but smaller than what is commonly related to phonon scattering only.

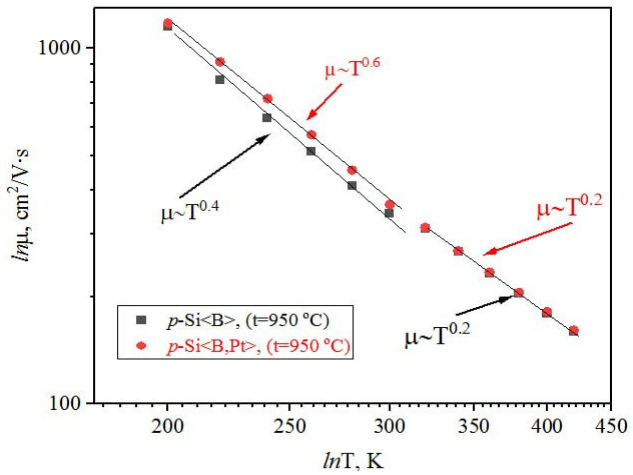

Figure 2. Logarithmic dependence of charge carrier mobility (μ) on temperature in p-Si<B> samples subjected to thermal treatment at 1050°C and doped with Pt atoms.

The charge carrier mobility in p-Si<B> samples with Pt atom doping at 1150°C for 5 hours showed a m = 0.6 temperature dependence in the 200–450 K range. It is well known that Pt atoms can create deep-level energy states in silicon, which create defect centers with neutral and charged states. The influence of such defects provides mostly larger temperature coefficients (m ≈ 0.5÷0.7) as compared to the scattering with the only neutral defects. This is because, in this case, the carrier mobility is determined not only by the neutral defects but also by the charged states of deep-level defects and trap centers. Hence, the intermediate value of m = 0.6 seen here, across the 200–450 K mid-range, signifies a combination of scattering mechanisms. Scattering is dominated instead by the joint action of neutral defects, deep-level energy states, and their ensuing localized strain fields in this regime. These defect centers are generally more thermally active at higher temperatures, thus perturbating more of the mobility of the charge carriers. Leading to a moderately strong temperature dependence of the mobility, typical of such a mixed scattering mechanism.

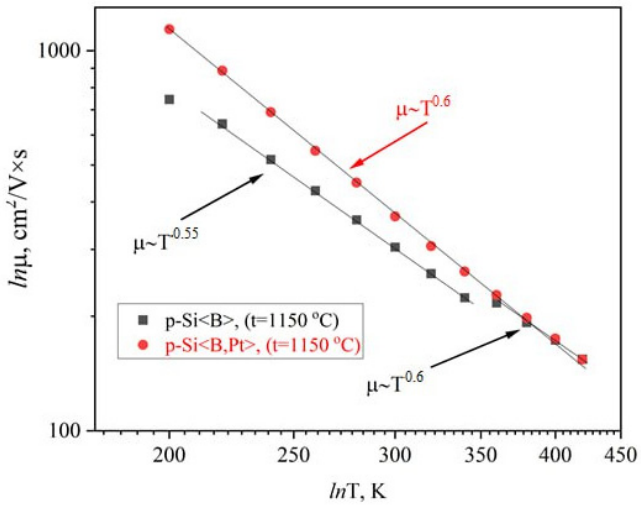

Figure 3. Logarithmic dependence of charge carrier mobility (μ) on temperature in p-Si<B> samples subjected to thermal treatment at 1150°C and doped with Pt atoms.

CONCLUSIONS

The following conclusions were established by the result of electrophysical changes observed in p-type silicon as a result of platinum (Pt) atom incorporation and subsequent high-temperature thermal treatments.

- Estimate of p-Si<B> samples collected from 200-300 K, which showed that the temperature coefficient of charge carrier mobility in p-Si<B> samples increased from m = 0.4 (before incorporation of Pt) to m = 0.6 (after Pt doping). This increase is maintained by the fact that Pt atoms in the silicon crystal forms deeper and more temperature-sensitive defect centers.

- The temperature coefficient (m = 0.2) for the p-Si<B> and Pt-doped p-Si<B,Pt> samples was obtained in the 300-450 K temperature range. This tendency is attributed to the superiority of scatterings of high concentration of boron and neutral crystalline defects.

- at the 1050°C, 5 hours thermal treatment, the value of the temperature coefficient reached the m=2.6 for the p-Si<B> samples showing the additional potential for propagation strong scattering mechanisms. These are mainly ascribed to boron atoms clustering and complex defect structures formation at high temperatures.

- In p-Si<B> samples doped with Pt atoms and annealed at 1150 °C, the mobility temperature coefficient in the range of 200–450 K is found equal to m = 0.60. This is ascribed to a combination scattering mechanism by neutral defects, deep-level energy states created by the Pt atoms, and their charged configurations.

Conflict of Interests

The authors declare that they have no conflict of interests

Funding

The present research work was financed under the project FZ-292154210 granted by the Ministry of Innovative Development of the Republic of Uzbekistan

ORCID

Akramjon Y. Boboev, https://orcid.org/0000-0002-3963-708X
Biloliddin M. Ergashev, https://orcid.org/0009-0007-9392-6548
Nuritdin Y. Yunusaliyev, https://orcid.org/0000-0003-3766-5420
Jamshidbek S. Madaminjonov, https://orcid.org/0009-0001-3786-4457

REFERENCES

[1] B. Pramanik, A. Al Rakib, A. Siddik, and Sh. Bhuiyan, "Doping Effects and Relationship between EnergyBand Gaps, Impact of Ionization Coefficient and Light Absorption Coefficient in Semiconductors," European Journal of Engineering and Technology Research, **9**(1), 10-15 (2024). https://doi.org/10.24018%2Fejeng.2024.9.1.3118

[2] S. Ibrahim, "Effect of temperature on silicon carriers mobilitiesusing.Res Article," Al-Mustansiriyah J. Sci. **28**(3), 214–21 (2018). http://dx.doi.org/10.23851/mjs.v28i3.185

[3] S. Reggiani, A. Valdinoci, L. Colalongo, and et al., "Surface mobility in silicon at large operating temperature," in: *International Conference on Simulation of Semiconductor Processes and Devices*, (Kobe, Japan, 2002), pp. 15-20. https://doi.org/10.1109/SISPAD.2002.1034506

[4] G. Ghibaudo, and Q. Rafhay, "Electron and Hole Mobility in Semiconductor Devices," in: *Wiley Encyclopedia of Electrical and Electronics Engineering*, (France, 2014), pp 1-13. https://doi.org/10.1002/047134608X.W3148.pub2

[5] J.A. Solovjov, and V.A. Pilipenko, "Effect of rapid thermal treatment temperature on electrophysical properties of nickel films on silicon," Doklady Bguir. **18**(1), 81-88 (2020). http://dx.doi.org/10.35596/1729-7648-2020-18-1-81-88

[6] A.I. Prostomolotov, Yu.B. Vasiliev, and A.N. Petlitsky, "Mechanics of defect formation during growth and heat treatment of singlecrystal silicon," **4**, 1716–1718 (2011). http://www.unn.ru/pages/e-library/vestnik/19931778_2011_-_4-4_unicode/147.pdf (in Russian)
[7] S.Z. Zainabidinov, Sh.Kh. Yulchiev, A.Y. Boboev, B.D. Gulomov, N.Y. Yunusaliyev, and "Structural properties of Al-doped ZnO films," Eur. J. Phys. (3), 282 (2024). https://doi.org/10.26565/2312-4334-2024-3-28
[8] K. Ali, S. Khan, M. Zubir, and M.Z.M. Jafri, "Spin-on doping (SOD) and diffusion temperature effect on re-combinations/ideality factor for solar cell applications," Chalcogenide Letters, **9**, 457–463 (2012). https://www.chalcogen.ro/457_KhuramAli.pdf
[9] Sh.B. Utamuradova, Kh.J. Matchonov, J.J. Khamdamov, and Kh.Y. Utemuratova, "X-ray diffraction study of the phase state ofsilicon single crystals doped with manganese," New Materials, Compounds and Applications, **7**(2), 93-99 (2023). http://jomardpublishing.com/UploadFiles/Files/journals/NMCA/v7n2/Utamuradova_et_al.pdf
[10] M.A. Lourenço, Z. Mustafa, W. Luduczak, L. Wong, R.M. Gwilliam, and K.P. Homewood, "High temperature dependence Dy3+ in crystalline silicon in the optical communication and eye-safe spectral regions," Optics Letters, **38**(18), 3669-3672 (2013). https://doi.org/10.1364/OL.38.003669
[11] M. Li, Y. Liu, Y. Zhang, X. Han, T. Zhang, Y. Zuo, C. Xie, et al., "Effect of the Annealing Atmosphere on Crystal Phase and Thermoelectric Properties of Copper Sulfide," ACS Nano, **15**(3), 4967-4978 (2021). https://doi.org/10.1021/acsnano.0c09866
[12] S.Z. Zainabidinov, A.Y. Boboev, M.B. Rasulova, N.Y. Yunusaliyev, "X-ray diffraction analysis, optical characteristics, and electro-physical properties of the n-ZnO/p-NiO structure grown by the spray pyrolysis method," New Materials, Compounds and Applications, **8**(3) 411-421 (2024). https://doi.org/10.62476/nmca83411
[13] S.Z. Zainabidinov, A.Y. Boboev, and N.Y. Yunusaliyev, "Effect of γ-irradiation on structure and lectrophysical properties of S-doped ZnO films," East Eur. J. Phys, (2), 321-326 (2024). https://doi.org/10.26565/2312-4334-2024-2-37
[14] N.Y. Yunusaliyev, "The Gas-Sensitive Properties of Tin Dioxide Films," Eur. J. Phys. (4), 439-442 (2024). https://doi.org/10.26565/2312-4334-2024-4-52
[15] K. Valalaki, and A. Nassiopoulou, "Thermal conductivity of highly porous Si in the temperature range 4.2 to 20 K," Nanoscale Research Letters, **9,** 318 (2014). https://doi.org/10.1186/1556-276X-9-318
[16] D. Goustouridis, G. Kaltsas, and A. Nassiopoulou, "A silicon thermal accelerometer without solid proof mass using porous silicon thermal isolation," IEEE Sens. J. **7**, 983–989 (2007). https://doi.org/10.1109/JSEN.2007.896559
[17] J-H. Lee, G.A. Galli, and J.C. Grossman, "Nanoporous Si as an efficient thermoelectric material," Nano Lett, **8,** 3750-3754 (2008). https://doi.org/10.1021/nl802045f

ЕЛЕКТРОФІЗИЧНА ПРИРОДА ДЕФЕКТІВ У КРЕМНІЇ, СПРИЧИНЕНИХ ІМПЛАНТОВАНИМИ АТОМАМИ ПЛАТИНИ

Акрамджон Й. Бобоєв, Білоліддін М. Ергашев, Нурітдін Й. Юнусалієв, Джамшидбек С. Мадамінжонов
Андижанський державний університет імені З.М. Бабура, Андижан, Узбекистан

У статті цього дослідження розглядаються дефекти, спричинені атомами платини (Pt), імплантованими в кремній (Si), зі змінами їх електрофізичних властивостей після високотемпературної термічної обробки. Введення атома платини в кристалічну решітку кремнію створює глибокі центри дефектів, де чутливі електричні властивості та явища, спричинені змінами температури, можна спостерігати чіткіше, ніж у власних дефектах. Зосереджуючись на включенні атомів платини, масштабні дослідження продемонстрували значні зміни дефектної структури кремнію та суттєву трансформацію його електрофізичних властивостей, пов'язаних з механізмами електропровідності та явищами розсіювання носіїв заряду. Ексклюзивні електрофізичні ефекти спостерігалися для зразків кремнію, легованого платиною, які пройшли високотемпературний термічний відпал при 1050°C та 1150°C, головним чином пов'язані з кластеризацією атомів бору та платини, а також утворенням складних агрегатів дефектів. Ці термічні обробки посилюють взаємодію ізольованих дефектів, що призводить до утворення кластерів та складних дефектних утворень, що значно посилює механізми розсіювання. Було виявлено, що ці інтерактивні ефекти дефектів домінують у зміні процесів переносу носіїв заряду та рекомбінації в кристалах кремнію. Крім того, експериментальні результати показали комбінацію механізмів розсіювання, яка включає нейтральні дефекти, глибокі енергетичні рівні, індуковані домішками платини, та їх відповідні заряджені стани. Таким чином, дефекти, індуковані платиною, дозволяють реалізувати множинні механізми розсіювання, і такі гібридні механізми відіграють вирішальну роль в електричній та електронній поведінці кремнію, що впливає на напівпровідникову застосовність матеріалів у високотемпературних або високопродуктивних умовах тощо.

Ключові слова: *рухливість носіїв заряду; провідність; термічна обробка; температурний коефіцієнт; акцепторні домішки; метод Ван-дер-Паува; вакансії; кристалографія*

East European Journal of Physics. 2. 436-440 (2025)
DOI:10.26565/2312-4334-2025-2-54 ISSN 2312-4334

LONG-TERM RELAXATION PROCESSES OF ELECTRICAL CONDUCTIVITY IN COMPENSATED Si<B,S> AND Si<B,Rh> MONOCRYSTALS

Akramjon Y. Boboev[a], Khushroy A. Makhmudov[b], Ziyodjon M. Ibrokhimov[a], Avaz K. Rafikov[c], Nuritdin Y. Yunusaliyev[a], Sarvarbek Kh. Ibrokhimov[a]
[a]*Andijan State University named after Z.M. Babur, Andijan, Uzbekistan*
[b]*Kokand university Andijan branch, Andijan, Uzbekistan*
[c]*Institute of Nuclear Physics Academy of Sciences of the Republic of Uzbekistan*
**Corresponding Author e-mail: aboboevscp@gmail.com*
Received March 2, 2025; revised March 29, 2025; accepted May 19, 2025

In this paper, the processes of conductivity relaxation in Si<B,S> and Si<B,Rh> single crystals under different compensation conditions and concentrations are investigated. It is found that the relaxation process of photoconductivity in compensated Si<B,S> and Si<B,Rh> single crystals is described by a two-step exponential dependence with characteristic times of fast (τ_1) and slow (τ_2) relaxation, and these relaxation processes depend on the type of compensating impurity and its concentration. The relaxation parameters (τ_1, τ_2) were determined and it was found that the characteristic relaxation time of the photocurrent in the Si<B,Rh> sample is much shorter compared to the Si<B,S> sample. With increasing γ-irradiation dose, the second characteristic relaxation time (τ_2) first sharply increases and then reaches the saturation state at a certain high dose, which is explained by the limited number of deep energy defects formed under irradiation. The dependence of the relaxation time (τ_2) on the γ-radiation fluence increases with decreasing temperature (up to 77 K). The influence of fluctuations in the concentration of charge carriers on the relaxation process is investigated, and it is found that with a decrease in the resistivity of the starting material, i.e. at higher concentrations, the amplitude of fluctuations increases, which leads to an increase in the relaxation time.
Keywords: *Film; Si<B,S>; Si<B,Rh>; γ-radiation; Photoconductivity; Relaxation time; Temperature; Concentration*
PACS: 78.30.Am

INTRODUCTION

Modern electronics and solar energy together with photonics require an increasing demand for high-efficiency semiconductor materials. Compensated semiconductors represent an effective method for the development of these materials. The compensation method adds dopants with opposite charges to semiconductors, which allows scientists to control electrical properties and photoelectric characteristics and conductivity type and carrier concentration. Boron-doped silicon, which receives compensation through sulfur (S) or rhodium (Rh) atoms, emerges as the most critical silicon-based compensated material [1,2]. Compensated Si<B,S> and Si<B,Rh> monocrystals demonstrate high photosensitivity properties that make them suitable for solar energy systems and photodetectors and radiation-resistant electronic devices [3]. Such materials demonstrate changing electrical conductivities through time due to the occurrence of relaxation processes. The nature of relaxation processes needs thorough analysis because it enables enhancements in material properties including photosensitivity and electrical conductivity as well as radiation resistance [4]. The long-term relaxation behavior of electrical conductivity in Si<B,S> and Si<B,Rh> materials demands scientific investigation due to its practical value. The current research analyzes the electrical conductivity relaxation characteristics of Si<B,S> and Si<B,Rh> monocrystals under different compensation conditions and impurity concentration levels.

RESEARCH METHODS

The researchers used boron-doped p-type silicon (Si) monocrystals because they selected them as starting materials. The starting Si<B,S> samples displayed specific resistivity values between 1 to 10 Ω·cm while Si<B,Rh> samples showed specific resistivity between 7 to 10 Ω·cm. The implement of thermodiffusion enabled compound creation through the specified temperature range from 1250 to 1290°C for a complete duration of 20 hours. The concentration development of compensating sulfur (S) atoms in Si<B,S> samples reached N_S between $(0.2\text{-}2)\cdot10^{16}$ cm^{-3} and Si<B,Rh> samples contained rhodium (Rh) atoms at $N_{Rh} \approx 5\cdot10^{15}$ cm^{-3}. The specific resistivity rose dramatically through compensation in both sample types which led to the creation of high-resistivity silicon monocrystals with $\rho = (8\text{-}10)\cdot10^4$ Ω·cm.

RESULTS AND DISCUSSION

Relaxation Processes of Electrical Conductivity

It is well established that photoconductivity relaxation refers to the decay of photocurrent in semiconductor materials after the cessation of photoexcitation. This process is a key parameter characterizing the electro-optical properties of the material. For the Si<B,S> and Si<B,Rh> monocrystals under investigation, this relaxation process can be accurately described by a two-stage exponential law [5]:

Cite as: A.Y. Boboev, Kh.A. Makhmudov, Z.M. Ibrokhimov, A.K. Rafikov, Y.N. Yunusaliyev, S.Kh. Ibrokhimov, East Eur. J. Phys. 2, 436 (2025), https://doi.org/10.26565/2312-4334-2025-2-54

$$I_\Phi = A_1 e^{-t/\tau_1} + A_2 e^{-t/\tau_2} \quad (1)$$

In this context, I_Φ – denotes the time-dependent photocurrent, while A_1 and $A_{2\ 2}$ represent the initial amplitudes of the photocurrent components. The parameters, τ_1 and $\tau_{2\ 2}$ are the characteristic time constants of the relaxation process [6]. According to the authors of [6], these parameters are strongly dependent on the type and concentration of the compensating impurity. Typically, the condition $A_1 \gg A_2$ and $\tau_1 \ll \tau_2$ is fulfilled, indicating the presence of two distinct mechanisms involved in the relaxation process—one fast and one slow. Table 1 presents the characteristic values of the relaxation parameters determined from experimental investigations conducted on Si<B,S> and Si<B,Rh> monocrystals. These values reflect the unique properties of the compensated materials. The data in the table provide a basis for evaluating the photosensitivity and response speed of the materials, and demonstrate the potential of creating highly photosensitive semiconductors through compensation techniques for practical applications [7].

Table 1. Photoconductivity Relaxation Parameters

Sample type	Expression	τ_1	τ_2
Si<B,S> (1)	$I_\Phi = 4 \cdot 10^{-2} e^{\frac{t}{9}} + 2{,}5 \cdot 10^{-2} e^{\frac{t}{6184}}$	9	6184
Si<B,S> (2)	$I_\Phi = 1 \cdot 10^{-7} e^{\frac{t}{261}} + 2 \cdot 10^{-8} e^{\frac{t}{4121}}$	261	4121
Si<B,S> (3)	$I_\Phi = 1 \cdot 10^{-3} e^{\frac{t}{160}} + 5 \cdot 10^{-5} e^{\frac{t}{1060}}$	160	1060
Si<B,Rh>	$I_\Phi = 2 \cdot 10^{-5} e^{\frac{t}{0.72}} + 4{,}5 \cdot 10^{-8} e^{\frac{t}{53}}$	0.72	53

The Si<B,Rh> sample exhibits a considerably reduced relaxation time than the Si<B,S> sample. The different materials exhibit different potential barrier heights because of this observation. The scientific importance of studying how external gamma radiation doses affect photoconductivity relaxation processes is widely acknowledged as a fundamental concept. Semiconductor materials undergo such radiation analysis to evaluate their resistance to radiation according to research in [8]. This research analyzed the effect of different γ-irradiation doses on the photocurrent relaxation behavior in Si<B,S> and Si<B,Rh> material samples. Figure 1 displays the second characteristic relaxation time (τ₂) variations with increasing γ-irradiation dose according to graphical results.

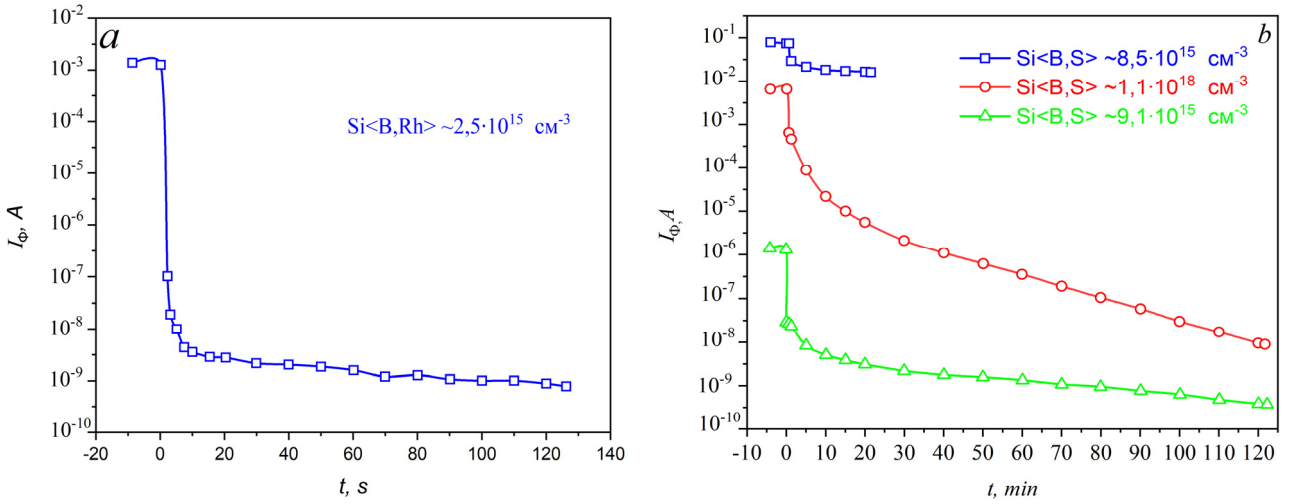

Figure 1. Dependence of photoconductivity relaxation kinetics on γ-radiation dose
a) Si<B,Rh> sample $N_{Rh}^{d} \sim 2.5 \cdot 10^{15}\ cm^{-3}$; b) Si<B,S> sample 1 – $8.5 \cdot 10^{15}\ cm^{-3}$, 2 – $\sim 9.1 \cdot 10^{15} cm^{-3}$, 3 – $\sim 1.1 \cdot 10^{18}\ cm^{-3}$

Results analysis demonstrated that the second characteristic relaxation time (τ₂) started with substantial growth until it stabilized at a saturation point under high dose exposure of γ-irradiation. The saturation amount depends on atom type Rh or S together with atom concentration. The two slow recombination pathways for photo-generated carriers in compensated Si<B,S> and Si<B,Rh> monocrystals emerge as the result of these experimental findings [9].

The slow decay of photocurrent follows the second characteristic relaxation time (τ₂) primarily because deep energy centers exist within the semiconductor. Different types of deep-level energy traps known as defect centers are generated or their concentration grows within Si<B,S> and Si<B,Rh> materials when the γ-irradiation dosage increases [10]. The charge carriers become trapped by these defects, which decelerates their recombination rate until the relaxation time τ₂ extends. When the dose of irradiation reaches, its critical level the creation and density of these defects will become saturated [11]. The total number of deep-level centers reaches its maximum limit at the same time as their carrier capture capability reaches saturation. After reaching this saturation point the additional dose becomes ineffective since it fails to modify the relaxation time value of τ₂—and this stage is referred to as the saturation regime. The evolution of this process depends on both the type and amount of compensating impurity because each impurity atom affects the silicon crystal

lattice structure and the carrier recombination patterns differently according to literature [12]. The research findings establish essential evaluation criteria for assessing radiation resistance in compensated Si<B,S> and Si<B,Rh> samples making them suitable materials for building radiation-resistant photosensitive semiconductors [13].

Analysis of the Influence of Radiation and Temperature on the Relaxation Process

In order to gain a deeper understanding of the photoconductivity relaxation process in semiconductors, it is essential to consider the impact of external factors such as radiation fluence and temperature. As γ-irradiation dose increases, the number of defects in the semiconductor also rises, which in turn modifies the recombination processes of charge carriers [14]. Figure 2 presents the influence of γ-radiation doses on the photocurrent relaxation time in the Si<B,Rh> sample as a function of temperature.

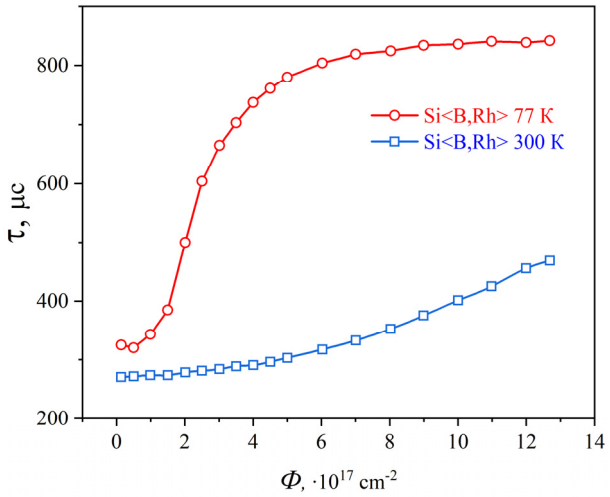

Figure 2. Dependence of Relaxation Time τ_2 on γ-radiation and temperature in the Si<B,Rh> Sample: 1 – 77 K; 2 – 300 K

Results in Figure 2 show that the relaxation time changes at a faster rate when γ-radiation increases at 77 K low temperature conditions. When temperatures decrease the number of thermally activated charge carriers decreases so recombination happens mostly through deep-level defect centers produced by irradiation [15]. Each defect center plays a stronger role because of which the relaxation process experiences a more noticeable slowdown.

The number of thermally activated carriers rises at 300 K leading to weakened interactions between charge carriers and defects that causes the relaxation time to change more slowly [16]. The temperature increase reduces the fluence-dependence of relaxation times. The necessity of high fluence sensitivity in relaxation time comes forth as fundamental for creating radiation-tolerant photoelectronics designed to operate at cold temperatures.

Effect of Concentration Fluctuations on the Relaxation Process

During the compensation of semiconductor materials, fluctuations in charge carrier concentration-i.e., variability in carrier density-can have a significant impact on electrical conductivity and photocurrent relaxation. These fluctuations lead to local distortions in the energy bands of compensated semiconductors, resulting in the formation of potential barriers [17]. Consequently, the mobility of charge carriers decreases, and their recombination process slows down, which leads to an increase in relaxation time.

Table 2 presents the amplitude of charge carrier concentration fluctuations and their relative variation with respect to the mean value for Si<B,S> materials at a compensation level of $K = 1$.

Table 2. Dependence of Concentration Fluctuations on Material Type in Si<B,S> Samples with a Compensation Level of K = 1

#	P^{max}, cm^{-3}	P^{min}, cm^{-3}	$\bar{P}, cm^{-3}$	$\frac{P^{max} - P^{min}}{\bar{P}} \cdot 100\%$	$\bar{N}_S, cm^{-3}$
1	$2.1 \cdot 10^{16}$	$1.9 \cdot 10^{16}$	$2 \cdot 10^{16}$	10	$2 \cdot 10^{16}$
2	$2.1 \cdot 10^{15}$	$1.9 \cdot 10^{15}$	$2 \cdot 10^{15}$	10	$2 \cdot 10^{15}$

The data shows that higher carrier concentrations lead to larger absolute fluctuations of charge carrier concentrations that correspond to lower specific resistivity values of initial materials. The process produces enhanced potential barriers, which grow in both height and quantity. Lower specific resistivity values in the material result in increased recombination times for charge carriers according to the table data analysis. During the process, time the number of barriers and height, increase simultaneously. The reduction of specific resistivity extends charge carrier recombination time because photoconductivity relaxation duration stretches out.

The relaxation time length becomes extended when the initial material has lower specific resistivity levels as this produces higher charge carrier concentration fluctuations to enhance photosensitivity. This research discovery has immense potential to improve the creation of photodetectors while creating high-sensitivity sensor devices.

CONCLUSIONS

Scientific and practical findings from the research evaluation enabled researchers to establish these main conclusions:

Compensated Si<B,S> and Si<B,Rh> monocrystals exhibit two-stage exponential relaxation which proceeds through fast (τ_1) and slow (τ_2) relaxation times during photoconductivity decay. The relaxation processes showed significant dependence on the type together with the concentration level of the compensating impurity used.

The experimental results revealed that the Si<B,Rh> sample had a substantially reduced characteristic relaxation time of its photocurrent compared to the Si<B,S> sample.

γ-radiation doses lead to an abrupt upswing of the second characteristic relaxation time (τ_2) before it reaches an equilibrium state at a particular high dose level. The saturation occurs because radiation exposure creates only a limited number of deep-level energy defects.

When the γ-radiation flux was assessed at 77 K the dependency of relaxation time (τ_2) became more significant. Low temperatures lead to mostly recombination through defect centers that form due to irradiation. Thus, a decrease in the specific resistivity of the initial material enhances the concentration fluctuations of charge carriers and creates the potential to improve the material's photosensitivity through the prolongation of the relaxation time.

This finding is particularly important for the development of photodetectors and highly sensitive sensor devices.

Conflict of Interests

The authors declare that they have no conflict of interests

Funding

The present research work was financed under the project FZ-292154210 granted by the Ministry of Innovative Development of the Republic of Uzbekistan

ORCID

Akramjon Y. Boboev, https://orcid.org/0000-0002-3963-708X
Khushroy A. Makhmudov, https://orcid.org/0009-0004-8845-8741
Ziyodjon M. Ibrokhimov, https://orcid.org/0009-0003-6931-661X
Avaz K. Rafikov, https://orcid.org/0000-0001-9199-2428
Nuritdin Y. Yunusaliyev, https://orcid.org/0000-0003-3766-5420
Sarvarbek Kh. Ibrokhimov, https://orcid.org/0009-0004-6907-8129

REFERENCES

[1] V.N. Krivoruchko, and A.S. Tkachenko, "Defect engineering in compensated silicon: The role of boron-sulfur and boron-rhodium complexes," J. Appl. Phys. **131**, 084501 (2022). https://doi.org/10.1063/5.0083721
[2] A. García-Loureiro, *et al*., "First-principles study of rhodium-induced deep levels in compensated silicon," J. Phys.: Condens. Matter, **35**, 225701 (2023). https://doi.org/10.1088/1361-648X/acc5a2
[3] S.Z. Zainabidinov, *et al*., "Effect of γ-Irradiation on Structure and Electrophysical Properties of S-Doped ZnO Films," East Eur. J. Phys. (2), 321 (2024). https://doi.org/10.26565/2312-4334-2024-2-37
[4] A.A. Istratov, H. Chen, and J. Yang, "Long-term relaxation effects in compensated Si<B,S> monocrystals: Implications for photodetectors," Phys. Rev. Appl. **16**, 044032 (2021). https://doi.org/10.1103/PhysRevApplied.16.044032
[5] M. Stavola, *et al*., "Defect metastability in sulfur-compensated silicon," Appl. Phys. Lett. **104**, 042101 (2014). https://doi.org/10.1063/1.4862799
[6] N. Yarykin, *et al*., "Deep-level transformations in Si<B,S> under illumination," Phys. Status Solidi b, **258**, 2100032 (2021). https://doi.org/10.1002/pssb.202100032
[7] Sh.B. Utamuradova, *et al*., "Research of the impact of silicon doping with holmium on its structure and properties using Raman scattering spectroscopy methods," East Eur. J. Phys. (2), 274 (2024). https://doi.org/10.26565/2312-4334-2024-2-28
[8] L. Vines, *et al*., "Radiation-hard Si<B,Rh> photodetectors: Relaxation dynamics under γ-irradiation," Nucl. Instrum. Methods Phys. Res. B, **540**, 100 (2023). https://doi.org/10.1016/j.nimb.2023.03.010
[9] M.J. Puska, *et al*., "Divacancy-mediated carrier lifetime saturation in irradiated Si<B,S>," Phys. Rev. Materials, **7**, 014603 (2023). https://doi.org/10.1103/PhysRevMaterials.7.014603
[10] V.P. Markevich, *et al*., "Defect saturation in Rh-doped silicon under irradiation," Appl. Phys. Lett. **118**, 242103 (2021). https://doi.org/10.1063/5.0052627
[11] A. Kuznetsov, *et al*., "Radiation-induced defect evolution in S-compensated silicon," J. Appl. Phys. **128**, 155701 (2020). https://doi.org/10.1063/5.0023418
[12] J.W. Farmer, *et al*., "Impurity-controlled defect saturation in irradiated silicon," Phys. Rev. Appl. **18**, 014045 (2022). https://doi.org/10.1103/PhysRevApplied.18.014045
[13] K.M. Itoh, "Compensated silicon for radiation-hard electronics: Progress and prospects," Chem. Mater. **34**, 6123 (2022). https://doi.org/10.1021/acs.chemmater.2c01108
[14] S. Zaynabidinov, *et al*., "X-ray diffraction and electron microscopic studies of the ZnO(S) metal oxide films obtained by the ultrasonic spray pyrolysis method," Herald of the Bauman Moscow State Tech. Univ., Ser. Nat. Sci. **1**, 78 (2024). https://doi.org/10.18698/1812-3368-2024-1-78-92
[15] G.D. Watkins, "Radiation-induced defects in Rh-doped silicon," Phys. Rev. B, **105**, 195205 (2022). https://doi.org/10.1103/PhysRevB.105.195205
[16] M.T. Lusk, *et al*., "Temperature-dependent defect interactions in compensated Si," Phys. Rev. Appl. **19**, 034045 (2023). https://doi.org/10.1103/PhysRevApplied.19.034045

[17] U.O. Kutliev, M.U. Otabaev, and M.K. Karimov, "Investigation Ne ions scattering from the stepped InP(001)<$\bar{1}$10> surface," J. Phys.: Conf. Ser. **2388**, 012092 (2022). https://doi.org/10.1088/1742-6596/2388/1/012092

ДОВГОТРИВАЛІ ПРОЦЕСИ РЕЛАКСАЦІЇ ЕЛЕКТРОПРОВІДНОСТІ В КОМПЕНСОВАНИХ МОНОКРИСТАЛАХ Si<B,S> ТА Si<B,Rh>

Акрамджон Й. Бобоєв[a], Хушрой А. Махмудов[b], Зійоджон М. Іброхімов[a], Аваз К. Рафіков[c], Ю.Н. Юнусалієв[a], Сарварбек Х. Іброхімов[a]

[a]*Андижанський державний університет імені З.М. Бабура, Андижан, Узбекистан*
[b]*Кокандський університет, Андижанська філія, Андижан, Узбекистан*
[c]*Інститут ядерної фізики Академії наук Республіки Узбекистан*

У цій статті досліджуються процеси релаксації провідності в монокристалах Si<B,S> та Si<B,Rh> за різних умов компенсації та концентрацій. Встановлено, що процес релаксації фотопровідності в компенсованих монокристалах Si<B,S> та Si<B,Rh> описується двоступеневою експоненціальною залежністю з характерними часами швидкої (τ_1) та повільної (τ_2) релаксації, причому ці процеси релаксації залежать від типу компенсуючої домішки та її концентрації. Визначено параметри релаксації (τ_1, τ_2) та виявлено, що характерний час релаксації фотоструму у зразку Si<B,Rh> значно коротший порівняно зі зразком Si<B,S>. Зі збільшенням дози γ-опромінення другий характерний час релаксації (τ_2) спочатку різко збільшується, а потім досягає стану насичення при певній високій дозі, що пояснюється обмеженою кількістю глибоких енергетичних дефектів, що утворюються під час опромінення. Залежність часу релаксації (τ_2) від флюенсу γ-випромінювання зростає зі зниженням температури (до 77 K). Досліджено вплив флуктуацій концентрації носіїв заряду на процес релаксації та виявлено, що зі зменшенням питомого опору вихідного матеріалу, тобто при вищих концентраціях, амплітуда флуктуацій збільшується, що призводить до збільшення часу релаксації.

Ключові слова: *плівка; Si<B,S>; Si<B,Rh>; γ-випромінювання; фотопровідність; час релаксації; температура; концентрація*

EAST EUROPEAN JOURNAL OF PHYSICS. **2.** 441-451 (2025)
DOI:10.26565/2312-4334-2025-2-55 ISSN 2312-4334

ON THE THEORY OF THE INTRABAND MECHANISM OF SINGLE-PHOTON ABSORPTION IN SEMICONDUCTORS, TAKING INTO ACCOUNT THE EFFECT OF COHERENT SATURATION

Rustam Y. Rasulov[a], Vokhob R. Rasulov[a]*, Forrukh U. Kasimov[b], Mardonbek Kh. Nasirov[a,c], Islam A. Muminov[a]
[a]*Fergana State University, Fergana, Uzbekistan*
[b]*Andijan State University, Andijan, Uzbekistan*
[c]*Fergana Polytechnic Institute, Fergana, Uzbekistan*
**Corresponding Author e-mail: vrrasulov83@gmail.com*
Received August 6, 2024; revised May 11, 2025; accepted May 20, 2025

A theoretical analysis of the frequency–temperature dependence of the single-photon absorption coefficient of polarized radiation in narrow- and wide-bandgap semiconductors is conducted, considering intraband optical transitions and including the coherent saturation effect. It is shown that with a fixed radiation frequency, the single-photon absorption coefficient initially increases with temperature, reaches a maximum, and then decreases. The position of this maximum shifts to lower frequencies for both narrow- and wide-bandgap semiconductors when the temperature dependence of the bandgap width and the effective masses of holes are taken into account. In semiconductors with a zinc-blende lattice structure, accounting for the temperature variation of band parameters leads to a reduction in the amplitude of the frequency and temperature response of the single-photon absorption coefficient. As temperature rises, the absorption threshold diminishes, an effect which is especially noticeable when using the Passler bandgap model. Each type of intraband optical transition contributes differently to the frequency, temperature, and polarization dependence of the absorption coefficient $K^{(1)}(\omega, T)$ for transitions involving the split-off band (SO) and light-hole (LH) band.
Keywords: *Probability of single-photon transitions; Coefficients of single-photon absorption and linear-circular dichroism, Coherent saturation effect; Temperature dependence of the band gap*
PACS: 71.20.Nr, 71.70.Ej, 42.50.Nn

INTRODUCTION

The absorption of light associated with optical transitions between the heavy-hole and light-hole subbands of the valence band in cubic symmetry has long been studied both theoretically and experimentally (see, for example, [1-3] and the references therein).

In studies [4-9], theoretical investigations were conducted on one- and multi-photon absorption caused by both interband and intraband optical transitions. In [8], multi-photon intraband Larmor cyclotron resonance (LCR) in *p-Ge* was examined under conditions of strong nonlinearity, where multi-photon processes contribute comparably to the absorption. In [4, 6-9], the spectral and temperature dependences of the multi-photon absorption coefficient and LCR in semiconductors with complex band structures were described. In [10, 11], saturation of the vertical optical transition rate in regions of higher intensity and nonlinear light-intensity-dependent photocurrents induced by direct optical transitions between topological surface and bulk states in three-dimensional topological insulators were observed. In [12], a microscopic theory of nonlinear edge photocurrent in graphene illuminated by terahertz radiation was developed, while in [13], single- and multi-photon interband optical transitions in monolayers of transition metal dichalcogenides were analyzed. Studies [14-17] experimentally investigated two-photon absorption of unpolarized light in *GaAs, InP, GaInAs, InSb, InAsP*.

The analysis of our calculations for the LCR coefficient (the probability of light absorption with linear and circular polarization) indicates that accounting for the effect of coherent saturation leads to a distinctive polarization dependence. Therefore, it is of interest to theoretically investigate the LCR coefficient and light absorption as a function of the angle between the wave vectors of charge carriers and photons. This is related to optical transitions from the light-hole and heavy-hole subbands to the spin-orbit split-off subband, as well as the contribution of the coherent saturation effect [5-9] to the LCR coefficient and light absorption, considering the temperature dependence of band parameters (bandgap width and effective masses of charge carriers). The present work is dedicated to studying these phenomena.

In direct-gap semiconductors with a degenerate valence band, single-photon absorption can occur not only via interband transitions but also via intraband transitions between different valence subbands. In a zinc-blende semiconductor, the top of the valence band (comprising the heavy-hole and light-hole bands, which are degenerate at $k = 0$) is split by spin–orbit coupling: a lower-lying split-off valence band is separated from the heavy/light-hole valence band by an energy Δ_{so} [13]. Here Δ_{so} (often called the spin–orbit splitting energy) denotes the energy gap between the split-off (SO) band and the top of the valence band. Intraband single-photon absorption refers to optical transitions that take place *within* the valence band, for example between the heavy-hole (HH) band and the split-off band (SO). These transitions require the presence

Cite as: R.Y. Rasulov, V.R. Rasulov, F.U. Kasimov, M.Kh. Nasirov, I.A. Muminov, East Eur. J. Phys. 2, 441 (2025), https://doi.org/10.26565/2312-4334-2025-2-55

of initial carriers (holes) in one of the bands; in p-type or intrinsic material at finite temperature, a certain fraction of the valence band states are empty (holes are present) allowing such absorptions to occur. Because the intraband transition energies are generally lower than the fundamental bandgap E_g, they are manifested as absorption in the infrared or far-infrared range (for instance, the HH→SO transition in GaAs with $\Delta_{so} \approx 0.34$ eV would correspond to a ~3.6μm photon).

Previous studies of one-photon absorption have mostly focused on **interband** processes and associated phenomena such as optical orientation of carriers [14] and nonlinear absorption saturation. Nonlinear light absorption in semiconductors with degenerate bands, caused by direct optical transitions between subbands of heavy and light holes, and its dependence on radiation polarization, was examined in a number of works [15]. However, the intraband single-photon absorption mechanism – especially including the effects of *coherent saturation* at high light intensities – has remained less explored. The coherent saturation effect refers to the reduction of absorption at high photon flux, due to depletion of initial-state carriers and other many-body effects that saturate the optical transition probability [16]. In the context of intraband transitions, this means that beyond a certain intensity, the absorption of additional photons is diminished because the available holes in the initial band are being exhausted (or the population distribution is driven towards equilibrium between the bands).

In this work, we develop a theoretical description of intraband single-photon absorption in direct-gap semiconductors of the zinc-blende type, explicitly including the coherent saturation effect. We consider both narrow-bandgap and wide-bandgap materials to highlight how Δ_{so} and other band parameters influence the absorption behavior. We also take into account the temperature dependence of the band structure parameters (such as E_g and effective masses), since temperature can significantly affect the absorption coefficient spectrum. Our aim is to derive analytic expressions for the polarized absorption coefficient $K^{(1)}(\omega, T)$ for intraband transitions, and to analyze how this coefficient depends on temperature, photon frequency, and light polarization in both low- and high-intensity regimes.

The polarization dependence of the probability of intraband optical transitions in A3B5 semiconductors with a degenerate valence band

It is known [2] that the absorption coefficient of N -photon light is $K^{(N)}$determined in the following form:

$$K^{(N)} = N\hbar\omega \frac{W^{(N)}}{I},, \tag{1}$$

where $W^{(N)}$ is the probability of N -photon absorption per unit volume of light, defined as [2, 5-9]. For the intraband case, we consider transitions from the HH or LH subbands to the split-off (SO) subband, whose energy dispersion is given by

$$E_{lh}(k) = \frac{\hbar^2 k^2}{2\, m_{lh}}, \quad E_{hh}(k) = \frac{\hbar^2 k^2}{2\, m_{hh}}, \quad E_{\mathrm{SO}}(k) = \Delta_{so} + \frac{\hbar^2 k^2}{2\, m_{\mathrm{SO}}}.$$

here m_{lh}, m_{hh}, and m_{SO} are the effective mass. m_{SO} is effective mass in the spin-orbit (SO) valence subband. As noted above, m_{so} is the energy gap between the top most valence edge (HH/LH) and the SO band at $k = 0$. The squared matrix elements governing these intraband transitions depend on polarization. For single-photon absorption, transitions from valence band to spin-orbit band, with relative strengths determined by angular momentum selection rules [2,5-9]. Accounting for Coherent Saturation Effects in Single-Photon Intraband Absorption To include the coherent saturation effect, we adopt the approach of Refs. [5-9],

$$W^{(N)} = \frac{2\pi}{\hbar}\sum_{n,n',\vec{k}} \left\langle \sum_{m,m'} \left| M^{(N)}_{n,m;n',m'}(\vec{k}) \right|^2 \right\rangle \left(f_{n\vec{k}} - f_{n'\vec{k}}\right)\delta\left(E_{n'\vec{k}} - E_{n\vec{k}} - N\hbar\omega\right),, \tag{2}$$

where $m, m' = \pm 1/2$ corresponds to states in the light-hole and spin-orbit split-off subbands, $m, m' = \pm 3/2$ corresponds to states in the heavy-hole subband [18, 19], $\left\langle \sum_{m,m'} \left| M^{(N)}_{n,m;n',m'}(\vec{k}) \right|^2 \right\rangle$ is the value of the squared modulus of the composite matrix element of the optical transition, averaged over the solid angles of the hole $(\vec{k})$ wave vector, for a transition from state $|n\vec{k}\rangle$ to $|n'\vec{k}\rangle$ ($|n\vec{k}\rangle \to |n'\vec{k}\rangle$), $E_{n'\vec{k}}(E_{n\vec{k}})$ and $f_{n\vec{k}}(f_{n'\vec{k}})$ are the energy and distribution function of charge carriers in the initial (or final) state, and $\vec{A}$ is the vector potential of the electromagnetic wave:

$$\vec{A}(\vec{x}, t) = A_0 \vec{e} e^{-i\omega t + i\vec{q}\vec{x}} + A_0 \vec{e}^{*} e^{i\omega t - i\vec{q}\vec{x}}, \tag{3}$$

$\hbar\omega(\hbar\vec{q})$ is the energy (momentum) of the photon, $\vec{e}$ and A_0 are the polarization vector and the amplitude of the vector potential, respectively:

$$\left(\frac{eA_0}{m_0 c}\right)^2 = \frac{2\pi e^2 I}{c\omega^2 m_0^2 n_\omega}, \tag{4}$$

I is the light intensity, $n_\omega = \frac{cq}{\omega}$ is the refractive index of the semiconductor, and the remaining terms are well-known quantities.

It should be noted that when calculating, for example, the frequency or temperature dependence of $W^{(N)}$ for both intraband and interband N-photon optical transitions, the choice of the electron-photon interaction operator, which is part of the composite matrix element of the transition, is crucial [5-9]. Depending on the chosen operator, the relative contribution of various optical transition channels, $W^{(N)}$which differ in their virtual states, may increase or decrease.

Let us analyze the optical transitions occurring from the hole subbands to the spin-orbit split-off subband (see Fig. 1), where the energy dispersion for light and heavy holes can be expressed as: $E_{lh}(\vec{k}) = \frac{\hbar^2 k^2}{(2m_{lh})}$ and $E_{hh}(\vec{k}) = \frac{\hbar^2 k^2}{(2m_{hh})}$, respectively, and for the spin-orbit split-off subband as: $E_{SO}(\vec{k}) = \Delta_{SO} + \frac{\hbar^2 k^2}{(2m_{SO})}$. Here, $m_{lh}(m_{hh})$ represents the effective mass of light (heavy) holes, and Δ_{SO} is the spin-orbit splitting energy, the numerical values of which for several semiconductors are provided in [20].

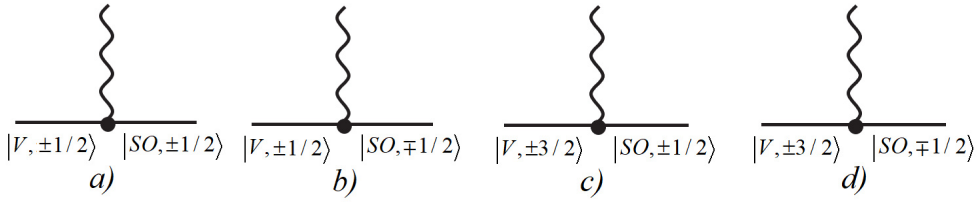

Figure 1. Feynman diagrams describing intraband optical transitions in semiconductors

It should be noted that when the photon energy satisfies the condition $\Delta_{SO} \leq \hbar\omega$, then: a) In wide-bandgap semiconductors (e.g., GaAs, where $\Delta_{SO}\langle E_g$, and E_g is the bandgap width), optical transitions from the heavy- and light-hole branches to the spin-orbit split-off subband are allowed. b) In narrow-bandgap semiconductors (e.g., InSb, where $\Delta_{SO}\rangle E_g$), optical transitions occur in two stages. First, transitions take place between the valence and conduction subbands (interband transitions) in the frequency range $E_g \leq \hbar\omega\langle\Delta_{SO}$. Subsequently, optical transitions proceed simultaneously from the heavy- and light-hole branches to the spin-orbit split-off subband (intraband transitions) as well as interband transitions in the frequency range $\hbar\omega\rangle\Delta_{SO}$. c) In intermediate-bandgap semiconductors (e.g., InAs, where $\Delta_{SO} \simeq E_g$), both intraband and interband optical transitions are allowed.

As seen from equations (1) and (2), the light absorption coefficient is determined by the squared modulus of the composite matrix element, whose polarization dependence is defined by the type of optical transitions. In particular, according to the Luttinger-Kohn Hamiltonian approximation [18, 19], the composite matrix elements for single-photon transitions $|V,\pm1/2\rangle \rightarrow |SO,\pm1/2\rangle$ a (see Fig. 1a) and $|V,\pm1/2\rangle \rightarrow |SO,\mp1/2\rangle$ (see Fig. 1b), occurring from the light-hole branch to the spin-orbit split-off subband, are defined by the relation:

$$\left|M^{(1)}_{SO,+1/2;V,+1/2} + M^{(1)}_{SO,-1/2;V,+1/2}\right|^2 = \left(\frac{eA_0}{c\hbar}\right)^2 2B^2k^2\left[\frac{9}{4}e'_-e'_+ + e'_z\frac{3}{2}(e'_+ + e'_-) + e'^2_z\right],$$

$$\left|M^{(1)}_{SO,-1/2;V,-1/2} + M^{(1)}_{SO,+1/2;V,-1/2}\right|^2 = \left(\frac{eA_0}{c\hbar}\right)^2 2B^2k^2\left[\frac{9}{4}e'^2_\perp - \frac{3}{2}(e'_+ + e'_-)e'_z + e'^2_z\right], \quad (5)$$

where $e'_\pm = e_{x'} \pm e_{y'}$, $e_{x'}, e_{y'}$, $\vec{e}$represents the projections of the polarization vector onto the Ox', Oy' axes, which are perpendicular to the wave vector of the holes $\vec{k}4B = \frac{\hbar^2 m_{lh}m_{hh}}{(m_{hh}-m_{lh})}$.

In this case, the sum of the squared moduli of the composite matrix elements is determined as:

$$\left|M^{(1)}_{SO,-1/2;V,-1/2} + M^{(1)}_{SO,+1/2;V,-1/2}\right|^2 + \left|M^{(1)}_{SO,+1/2;V,+1/2} + M^{(1)}_{SO,-1/2;V,+1/2}\right|^2 = \left(\frac{eA_0}{c\hbar}\right)^2 2B^2k^2\left(\frac{9}{2}e'^2_\perp + 2e'^2_z\right). \quad (6)$$

The composite matrix elements of single-photon transitions, $|V,\pm3/2\rangle \rightarrow |SO,\pm1/2\rangle$ i.e., optical transitions from the heavy-hole branch to the spin-orbit split-off subband (see Fig. 1c and 1d), are expressed as follows:

$$\hat{M}^{(1)}_{SO;V,hh} = \left(\frac{eA_0}{c\hbar}\right)\sqrt{\frac{3}{2}}Bk\begin{bmatrix} e'_- & 0 \\ 0 & -e'_+ \end{bmatrix}. \quad (7)$$

from which:

$$\left|M^{(1)}_{SO,\pm1/2;V,\pm3/2}\right|^2 = \left(\frac{eA_0}{c\hbar}\right)^2\frac{3}{2}B^2\left|e'_\mp\right|^2. \quad (8)$$

It should be noted that, according to the law of energy conservation, $\frac{\hbar^2k^2}{2m_{SO}} + \Delta_{SO} - \frac{\hbar^2k^2}{2m_L} - \hbar\omega = 0$ ($L = lh$for light holes) and $L = hh$ (for heavy holes), for transitions $|V,\pm1/2\rangle \rightarrow |SO,\pm1/2\rangle$ and $|V,\pm1/2\rangle \rightarrow |SO,\mp1/2\rangle$, it is

straightforward to derive an expression for the wave vector: $k^2 = k^2_{SO,hh} = 2\mu_-^{(SO,hh)}\hbar^{-2}(\hbar\omega - \Delta_{SO})$. For transitions of type $|V,\pm1/2\rangle \to |SO,\pm1/2\rangle$ and $|V,\pm1/2\rangle \to |SO,\mp1/2\rangle$, we have $k^2 = k^2_{SO,lh} = 2\mu_-^{(SO,lh)}\hbar^{-2}(\hbar\omega - \Delta_{SO})$, where $\mu_-^{(SO,hh)} = \frac{m_{SO}m_{hh}}{(m_{SO}-m_{hh})}$, $\mu_-^{(SO,lh)} = \frac{m_{SO}m_{lh}}{m_{SO}-m_{lh}}$. Thus, it follows that the polarization dependence of the matrix element for transitions of type $|V,\pm3/2\rangle \to |SO,\pm1/2\rangle$ and $|V,\pm3/2\rangle \to |SO,\mp1/2\rangle$ is described by the quantity $|e'_-|^2 + |e'_+|^2$, while optical transitions $|V,\pm1/2\rangle \to |SO,\pm1/2\rangle$ and $|V,\pm1/2\rangle \to |SO,\mp1/2\rangle$ are characterized by the quantity $4{,}5e'^2_\perp + 2e'^2_z$. Therefore, the polarization dependence of the single-photon absorption coefficient $\left(K^{(N=1)}\right)$, as well as the probability of the considered transition $\left(W^{(N=1)}\right)$, is determined by these quantities. To calculate the spectral and temperature dependence, these quantities must be averaged over the solid angles $\vec{k}$.

It should be noted that for single-photon absorption occurring between the branches of light and heavy holes and the spin-orbit split-off subband, single-photon LCR is not observed in diamond-like semiconductors or semiconductors of the zinc blende type. To observe single-photon LCR, it is necessary to account for the contribution of the coherent saturation effect to the transition probability, which will be analyzed further.

Light Absorption Induced by Single-Photon Optical Transitions from the Heavy- and Light-Hole Branches to the Spin-Orbit Split-Off Subband

By integrating over **k** and using the density of states in the valence bands, one obtains

$$K^{(1)}(\omega) \;=\; \frac{2\pi}{\hbar}\,\frac{\hbar\omega}{I}\sum_{\mathbf{k}}\;(f^{(1)}_{\mathrm{lh},\mathbf{k}} - f^{(1)}_{\mathrm{SO},\mathbf{k}})\;|\mathbf{M}^{(1)}_{\mathrm{lh}\to\mathrm{SO}}(\mathbf{k})|^2\,\delta(E_{\mathrm{SO},\mathbf{k}} - E_{\mathrm{lh},\mathbf{k}} - \hbar\omega),$$

with analogous expressions for transitions originating from the heavy-hole subband. In wide-gap semiconductors such as GaAs, $\Delta_{so} < E_g$, so the intraband HH→SO or LH→SO transitions occur at mid-infrared frequencies. In certain narrow-gap materials (InSb) one may have $\Delta_{so} > E_g$, meaning that the SO band sits "below" the HH/LH edges but by a larger energy difference than E_g itself. Numerically, this can place the intraband transition frequency in the near-infrared or even overlapping with interband transitions.

When Δ_{so} exceeds $\mathrm{E_g}$, the calculated transition energy $\hbar\omega = \Delta_{\mathrm{so}}$ can lie in a range above the conduction-band edge, making it appear as if $\mathrm{E_{SO}}$ has become "too high." However, physically, $\mathrm{E_{SO}}$ remains part of the valence band manifold; it just so happens that $\Delta_{\mathrm{so}} > \mathrm{E_g}$ places the SO subband closer to or even above the conduction band minimum on an absolute energy scale. This does not contradict the fact that Δ_{so} is specifically the energy splitting within the valence band.

Linear-Circular Dichroism of Single-Photon Optical Transitions from the Light- and Heavy-Hole Branches to the Spin-Orbit Split-Off Subband

In this case, the probability of single-photon optical transitions is determined using the following relation (see, for example, [5-9] and the references therein):

$$W^{(1)} = \frac{2\pi}{\hbar}\left(\frac{eA_0}{m_0c}\right)^2\left\langle\sum_{n,n',\vec{k}}\left|\vec{e}\vec{p}_{nn'}(\vec{k})\right|^2\sum_{n,n',\vec{k}}\left[1+\frac{\alpha_\omega}{\hbar^2\omega^2}\left(\frac{eA_0}{m_0c}\right)^2\left|\vec{e}\vec{p}_{nn'}(\vec{k})\right|^2\right]^{-1/2}\right\rangle\times$$
$$\times\left(f_{n\vec{k}} - f_{n'\vec{k}}\right)\delta\left(E_{n'\vec{k}} - E_{n\vec{k}} - \hbar\omega\right), \tag{9}$$

where the term $\frac{\alpha_\omega}{\hbar^2\omega^2}\left(\frac{eA_0}{m_0c}\right)^2\left|\vec{e}\vec{p}_{nn'}(\vec{k})\right|^2$ arises due to the consideration of the coherent saturation effect [21], $\alpha_\omega = \frac{6\omega^2 T_n^{(1)} T_{n'}^{(1)} I}{I_0}$, $T_n^{(1)}$ is the time spent by photoexcited charge carriers in state $|n,\vec{k}\rangle$, $\vec{p}_{nn'}(\vec{k}) = m_0\hbar^{-1}\vec{\nabla}_{\vec{k}}H(\vec{k})$ is the matrix element of the momentum operator, $H(\vec{k})$ is the Hamiltonian of the charge carriers, which is described by the Luttinger-Kohn Hamiltonian for intraband single-photon optical transitions and by the Kane Hamiltonian for interband light absorption [18, 19], and $I_0 = \frac{cn_\omega\hbar^3\omega^3}{2\pi|B|}$ is a parameter that, for zinc blende semiconductors, takes on values in the range of several gigawatts/cm² [3]. In cases where it is impossible to analytically determine, for example, the polarization, frequency, or temperature dependence of multi-photon absorption or LCR, an approximation can be used where $\frac{I}{I_0} << 1$. In this approximation, the radical can be expanded into a series in terms of $\frac{I}{I_0}$, and only the first few terms of the series can be retained.

Then, substituting (7, 8) into (9), it is straightforward to determine that the angular dependence of the probability of single-photon absorption of linearly polarized light $\left(W^{(1)}_{lin}\right)$ for the first-type transitions $|V,\pm1/2\rangle \to |SO,\pm1/2\rangle$ and $|V,\pm1/2\rangle \to |SO,\mp1/2\rangle$, shown in Fig. 2a and 2b, is described as:

$$\Im_{lin}^{(2)} = (2 + 2{,}5\,sin^2\,\phi)[1 + \zeta_\omega(4 + 5\,sin^2\,\phi)]^{-1/2}, \tag{11}$$

and for second-type transitions $|V, \pm 3/2\rangle \to |SO, \pm 1/2\rangle$and $|V, \pm 3/2\rangle \to |SO, \mp 1/2\rangle$, shown in Fig. 1c and 1d, it is described as:

$$\Im_{lin}^{(1)} = \frac{2\,sin^2\,\phi}{[1+3\zeta_\omega\,sin^2\,\phi]}^{-1/2}, \tag{12}$$

where ϕ is the angle between the wave vector of the holes and the light polarization vector, $\zeta_\omega = \alpha_\omega \left(\frac{eA_0}{c\hbar}\right)^2 B^2k^2$ is the Rabi parameter, and the wave vector k, as mentioned above, depends on the light frequency and the band parameters of the semiconductor.

For circularly polarized light, the angular dependence of the probability of optical transitions $\left(W_{circ}^{(1)}\right)$ from the heavy-hole branch to the spin-orbit split-off subband is determined by the expression:

$$\Im_{circ}^{(1)} = \left\langle \frac{2\left[\frac{1}{2}(1+cos^2\,\phi')\mp P_{circ}\,cos\,\phi'\right]}{\sqrt{1+3\zeta_\omega\left[\frac{1}{2}(1+cos^2\,\phi')\mp P_{circ}\,cos\,\phi'\right]}} \right\rangle, \tag{13}$$

The angular dependence of the probability of optical transitions $\left(W_{circ}^{(2)}\right)$ from the light-hole branch to the spin-orbit split-off subband will be represented as:

$$\Im_{circ}^{(2)} = \frac{1}{2}\left\langle \frac{9\left[\frac{1}{2}(1+cos^2\,\phi')\mp P_{circ}\,cos\,\phi'\right]+2\,sin^2\phi'}{\sqrt{1+\zeta_\omega\left(9\left[\frac{1}{2}(1+cos^2\,\phi')\mp P_{circ}\,cos\,\phi'\right]+2\,sin^2\phi'\right)}} \right\rangle, \tag{14}$$

where $\phi'$is the angle between the wave vectors of the holes and the photon, and $P_{circ}$is the degree of circular polarization of the light.

From Figs. 2 and 3, it can be seen that the angular dependences of the quantities $\Im_{lin}^{(1)}$, $\Im_{lin}^{(2)}$, and $\Im_{circ}^{(2)}$, i.e., the corresponding probabilities of single-photon light absorption, exhibit oscillatory behavior. The minimum values of $\Im_{lin}^{(1)}$and $\Im_{lin}^{(2)}$, as well as $\Im_{circ}^{(1)}$ and $\Im_{circ}^{(2)}$, coincide in their angular dependence, while their maximum values depend on the type of optical transitions. Specifically: a) The probabilities of optical transitions originating from the light-hole branch (see Figs. 1a and 1b) are approximately 2.5 (for linearly polarized light) to 4.5 (for circularly polarized light) times greater than the probabilities of transitions originating from the heavy-hole branch (see Figs. 1c and 1d). b) The maximum value of the probability for second-type transitions is always greater than that for first-type transitions, regardless of the degree of polarization or the value of the Rabi parameter (ζ_ω).

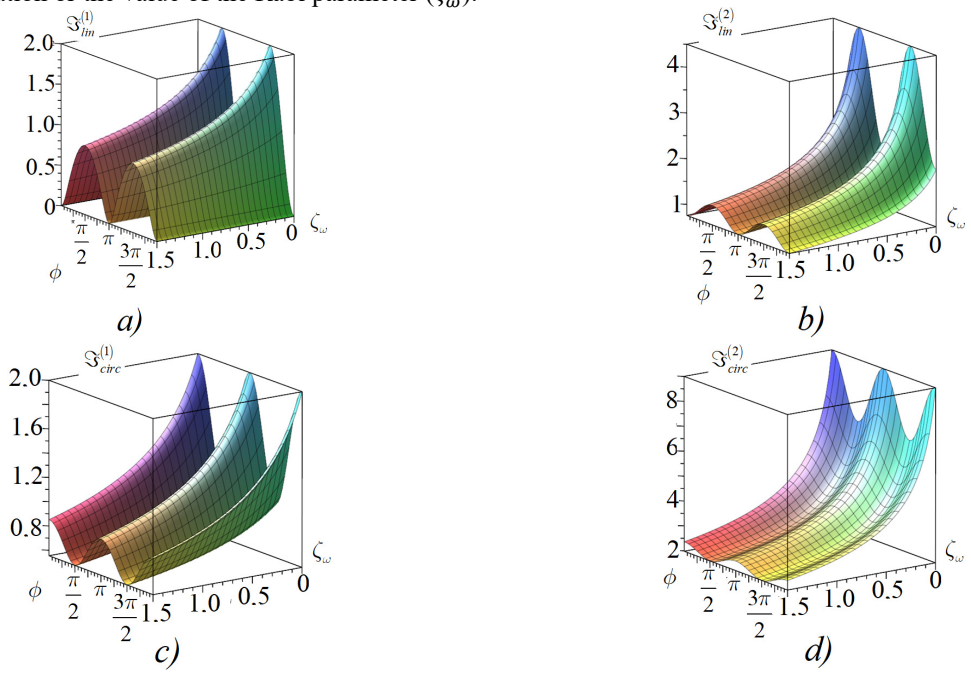

Figure 2. Graphs of the quantities $\Im_{lin}^{(1)}$ (*a*), $\Im_{lin}^{(2)}$ (*b*), $\Im_{circ}^{(1)}$_c (c), and $\Im_{circ}^{(2)}$ (d), which determine the contributions to the angular dependences and Rabi parameter dependences of the probabilities of single-photon optical transitions from the heavy-hole (a, c) and light-hole (b, d) branches to the spin-orbit split-off subband of the valence band for linearly (a, b) and circularly (c, d) polarized light

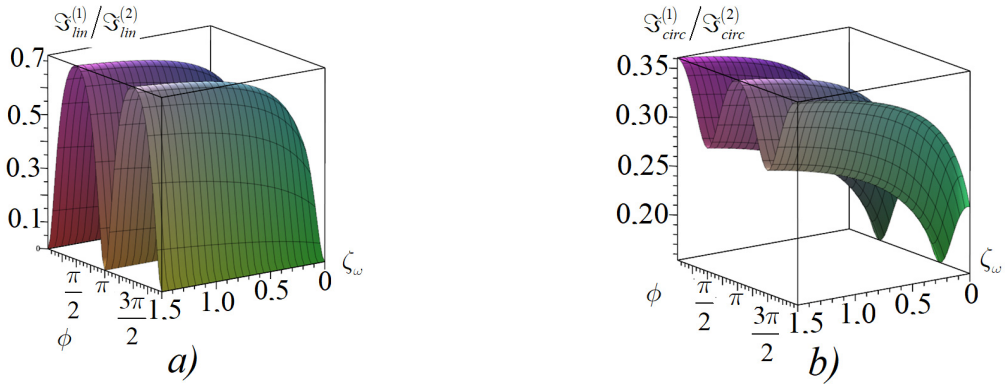

Figure 3. Graphs of the ratios $\Im_{circ}^{(1)}$ and $\Im_{circ}^{(2)}$, which allow determining the contribution of the optical transitions shown in Fig. 2 to the angular dependences and Rabi parameter dependences of the probabilities of single-photon optical transitions from the heavy- and light-hole branches to the spin-orbit split-off subband of the valence band for linearly (a) and circularly (b) polarized light.

The probabilities of optical transitions shown in Fig. 1 decrease with an increase in ζ_ω: if ζ_ω increases by 1.5 times, $\Im_{lin}^{(1)}$decreases by approximately 3.3 times, $\Im_{lin}^{(2)}$by 5 times, $\Im_{circ}^{(1)}$by 2.1 times, and $\Im_{circ}^{(2)}$by 4.5 times. It should also be noted that with increasing ζ_ω, the ratio of the probabilities of first-type optical transitions for linearly polarized light increases sharply in the range of ζ_ω $(0; 0{,}4)$values, followed by an almost imperceptible growth. For circularly polarized light, $\frac{\Im_{circ}^{(1)}}{\Im_{circ}^{(2)}}$ noticeably increases with ζ_ω across all its values.

From Fig. 3, it is evident that the primary contribution to the angular dependences and the Rabi parameter dependences of the probabilities of single-photon optical transitions from the heavy-hole (a, c) and light-hole (b, d) branches to the spin-orbit split-off subband of the valence band, for both linearly (a, b) and circularly (c, d) polarized light, is made by optical transitions involving light holes.

Thus, we have confirmed that accounting for the coherent saturation effect significantly alters the polarization dependence of the LCR coefficient.

Next, we examine the single-photon LCR coefficient, defined as the ratio $\eta = \frac{W_{lin}^{(1)}}{W_{circ}^{(1)}}$, i.e., $\eta = \frac{\Im_{lin}}{\Im_{circ}}$, as a function of the angle and the Rabi parameter, where $\eta = \eta^{(1)} + \eta^{(2)}$ $\eta^{(1)} = \frac{\Im_{lin}^{(1)}}{\Im_{circ}^{(1)}}$, and $\eta^{(2)} = \frac{\Im_{lin}^{(2)}}{\Im_{circ}^{(2)}}$ are the LCR coefficients for the first-type (Fig. 2a and 2b) and second-type (Fig. 2c and 2d) optical transitions (see Fig. 4). From Fig. 4, it is evident that both $\eta^{(1)}$ and $\eta^{(2)}$ exhibit oscillatory angular dependence, and their maximum values decrease with increasing ζ_ω, regardless of the angle between the wave vectors of the holes and the photon. It is noteworthy that the minimum value of the angular dependence of the LCR coefficient for first-type optical transitions is nonzero at $\zeta_\omega > 0$, whereas for second-type optical transitions, the minimum angular dependence $\eta^{(2)}$ equals zero across arbitrary values of ζ_ω.

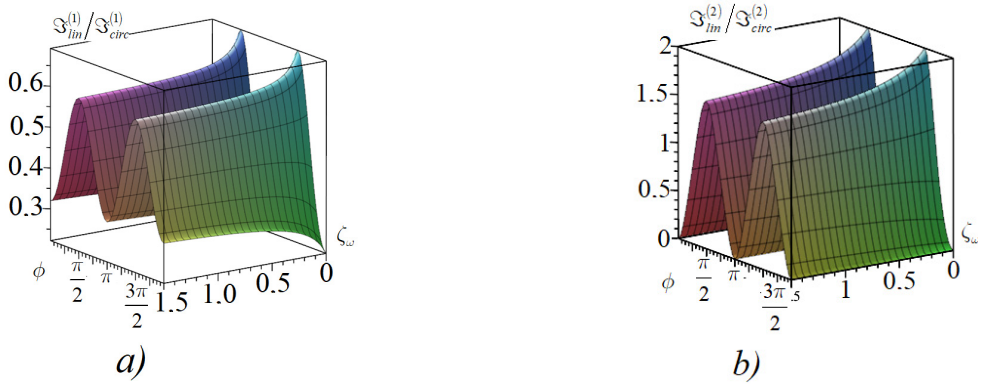

Figure 4. Dependence of the LCR coefficient on the angle and the Rabi parameter for single-photon optical transitions of the first (a) and second (b) types.

Light Absorption Induced by Single-Photon Optical Transitions from the Heavy- and Light-Hole Branches to the Spin-Orbit Split-Off Subband

The spectral, polarization, and temperature dependences of the absorption coefficient due to single-photon optical transitions from the heavy- and light-hole branches of the valence band to the spin-orbit split-off subband are determined by the following expression:

$$K^{(1)} = \frac{2\pi}{\hbar}\frac{\hbar\omega}{I}\sum_{\vec{k}}\left(f^{(1)}_{lh,\vec{k}} - f^{(1)}_{SO,\vec{k}}\right)\left|\sum_{lh,m=\pm1/2;SO,m'=\pm1/2} M^{(2)}_{lh,m;SO,m'}(\vec{k})\right|^2 \delta\left(E_{SO,\vec{k}} - E_{lh,\vec{k}} - \hbar\omega\right), \quad (15)$$

If the coherent saturation effect is taken into account [14], the following expression is obtained:

$$K^{(1)} = \frac{2\pi}{\hbar}\hbar\omega\frac{1}{I}\rho(\hbar\omega)f(T,\omega)(\langle\Re_+\rangle + \langle\Re_-\rangle), \quad (16)$$

where

$$\Re_\pm = \frac{\left|M^{(1)}_{SO,+1/2,lh,\pm1/2}(\vec{k}) + M^{(1)}_{SO,-1/2,lh,\pm1/2}(\vec{k})\right|^2}{\sqrt{1+4\frac{\alpha_\omega}{\hbar^2\omega^2}\left|M^{(1)}_{SO,+1/2,lh,\pm1/2}(\vec{k}) + M^{(1)}_{SO,-1/2,lh,\pm1/2}(\vec{k})\right|^2}}, \quad (17)$$

$\rho(\hbar\omega) = \mu_- k^{(1)}_\omega/(\pi^2\hbar^2)$ is the density of states, $k^{(1)}_\omega = (2\mu_-[\hbar\omega - \Delta_{SO}]/\hbar^2)^{1/2}$, $\left\langle\left|M^{(1)}_{n\vec{k}',n\vec{k}}\right|^2\right\rangle$ is the squared modulus of the composite matrix element $M^{(1)}_{n'\vec{k}',n\vec{k}}$ for an optical transition of type $|n\vec{k}\rangle \to |n'\vec{k}'\rangle$, averaged over the solid angles of the wave vector $\vec{k}$ $\alpha_\omega = 6\omega^2 T_1^{(1)} T_2^{(1)}\frac{I}{I_0}$, $I_0 = \frac{cn_\omega\hbar^3\omega^3}{2\pi|B|}I(\omega)$ is the light intensity (frequency), $f^{(1)}_{L\vec{k}}$ are the distribution functions of charge carriers (L=1L=1 (hh) corresponds to heavy holes, L=2L=2 (lh) to light holes, and L=SO to holes in the spin-orbit split-off subband), $E_{L\vec{k}} = -\hbar^2k^2/2m_L$ is the energy dispersion of holes in the L branch [15, 16] $e'_\pm = e_{x'} \pm e_{y'}$, $e_{x'}, e_{y'}$, $\vec{e}$ are the projections of the polarization vector onto the Ox', Oy' axes perpendicular to the wave vector $\vec{k}$ of the holes, and $\mu_-^{(SO,L)} = \frac{m_{SO}m_L}{(m_{SO}-m_L)}$ is the reduced effective mass of the holes.

In particular, for single-photon optical transitions from the light-hole branch to the spin-orbit split-off subband, the value of $\Re_\pm$ can be expressed as:

$$\Re_+ = 3\left(\frac{eA_0}{c\hbar}\right)^2 B^2k^2|e'_-|^2\left[1 + 4\frac{\alpha_\omega}{\hbar^2\omega^2}\left(\frac{eA_0}{c\hbar}\right)^2 B^2k^2 3|e'_-|^2\right]^{-1/2}, \quad (18)$$

$$\Re_- = \left(\frac{eA_0}{c\hbar}\right)^2 B^2k^2\left(9e'^2_\perp + 4e'^2_z\right)\left[1 + 4\frac{\alpha_\omega}{\hbar^2\omega^2}\left(\frac{eA_0}{c\hbar}\right)^2 B^2k^2\left(9e'^2_\perp + 4e'^2_z\right)\right]^{-1/2}, \quad (19)$$

the $4B = \frac{\hbar^2 m_{lh}m_{hh}}{(m_{hh}-m_{lh})}$.

If the contribution of the coherent saturation effect to light absorption ($\alpha_\omega = 0$) is neglected and averaging over the solid angles is performed, $\vec{k}$ from (18, 19), we obtain:

$$\left\langle\Re^{(0)}_+\right\rangle + \left\langle\Re^{(0)}_-\right\rangle = \left(\frac{eA_0}{c\hbar}\right)^2 B^2k^2\left\langle 9e'^2_\perp + 4e'^2_z\right\rangle = \frac{22}{3}\left(\frac{eA_0}{c\hbar}\right)^2 B^2k^2. \quad (20)$$

Then, (15) takes the form:

$$K^{(1)} = \frac{44\pi}{3\hbar}\left(\frac{eA_0}{c\hbar}\right)^2\frac{\hbar\omega}{I}\rho(\hbar\omega)f(\beta,\omega)B^2k^2. \quad (21)$$

Table 1. Fundamental band-structure parameters for the III–V semiconductors **GaAs, InSb, and InAs** employed in the present modelling of single-photon intraband absorption with coherent saturation.

Parameters	*GaAs*	*InSb*	*InAs*
E_g, eV	1.519	0.235	0.417
Δ_{SO}, eV	0.341	0.81	0.39
m_c/m_0	0.067	0.0135	0.026
m_{SO}/m_0	0.172	0.11	0.14
Δ_{SO}/E_g	0.24b	4.65	1.1
m_{lh}/m_0	0.09009	0.0152	0.027027
m_{hh}/m_0	0.34965	0.26316	0.33333
$\alpha_T, meV/K$	0.5405	0.32	0.276
β_T, K	204	170	93
F	-1.94	-0.23	-2.90

From Table 1, it can be seen that the reduced effective mass of holes $\mu_{-}^{(SO,hh)} = \frac{m_{SO}m_{hh}}{m_{SO}-m_{hh}}$, involved in optical transitions from the heavy-hole branch to the spin-orbit split-off subband, takes on negative values for several A3B5 semiconductors. This, in turn, results in the wave vector of charge carriers involved in such optical transitions $k_{SO,hh}^{(1\omega)} = \left[2\mu_{-}^{(SO,hh)}\hbar^{-2}(\hbar\omega - \Delta_{SO})\right]^{1/2}$ becoming an imaginary quantity. For this reason, unlike optical transitions from the light-hole branch, transitions from the heavy-hole branch to the spin-orbit split-off subband are forbidden.

Since optical transitions are allowed from the light-hole branch to the spin-orbit split-off subband of the valence band, we will further analyze the frequency and temperature dependences of the single-photon absorption coefficient. From the law of energy conservation, $\frac{\hbar^2k^2}{2m_{SO}} + \Delta_{SO} - \frac{\hbar^2k^2}{2m_L} - \hbar\omega = 0$, the wave vector is determined by the expression $k_{SO,L}^{(1\omega)} = \left[2\mu_{-}^{(SO,L)}\hbar^{-2}(\hbar\omega - \Delta_{SO})\right]^{1/2}$.

From (20) and (21), it is evident that the single-photon absorption coefficient does not depend on the degree of light polarization. Therefore, LCR is not observed in single-photon absorption. To observe it, the contribution of the coherent saturation effect to absorption must be taken into account, i.e., calculations need to be performed based on (16) and (17).

Now, we will calculate the frequency-temperature dependencies of the single-photon absorption coefficient using the following expression for the single-photon absorption coefficient, associated with optical transitions from the light hole branch to the spin-orbit split-off subband:

$$K^{(1)} = \frac{4\pi e^2}{c\omega m_0^2 n_\omega}\sum_{nn'\vec{k}}\left|\vec{e}\vec{p}_{SO,lh}(\vec{k})\right|^2\left(f_{lh,\vec{k}} - f_{SO,\vec{k}}\right)\delta\left(E_{SO}(\vec{k}) - E_{lh}(\vec{k}) - \hbar\omega\right). \tag{22}$$

Next, we assume the energy dispersion of light and heavy holes as $E_{lh}(\vec{k}) = -\hbar^2k^2/(2m_{lh})$ and $E_{hh}(\vec{k}) = -\hbar^2k^2/(2m_{hh})$, while in the spin-orbit split-off subband it is $E_{SO}(\vec{k}) = -\Delta_{SO} - \hbar^2k^2/(2m_{SO})$, where m_{lh} (m_{hh}) are the effective masses of light and heavy holes, respectively, and, Δ_{SO}- is the spin-orbit splitting energy, with numerical values for various semiconductors provided in [17]. Then, from (8), we obtain:

$$K_{SO,lh}^{(1)} = \frac{22}{3}\frac{e^2}{c\hbar n_\omega\hbar\omega}\frac{\mu_{-}}{\hbar^2}B^2\left(k_\omega^{(1)}\right)^3 f_{lh,k_\omega^{(1)}}[1 - \exp(-\hbar\omega/k_BT)]$$

or

$$K_{SO,lh}^{(1)} = \frac{11}{12}\frac{e^2}{c\hbar n_\omega}\left(\frac{m_{hh}-m_{lh}}{m_{SO}-m_{lh}}\frac{m_{SO}}{m_{lh}}\right)^2\frac{\hbar\omega-\Delta_{SO}}{\hbar\omega}\left(\frac{m_{hh}-m_{lh}}{m_{hh}}\right)^2 k_\omega^{(1)} f_{lh,k_\omega^{(1)}}\left(1 - e^{-\hbar\omega/k_BT}\right), \tag{23}$$

Where $k_\omega^{(1)} = \left[2\mu_{-}^{(SO,lh)}\hbar^{-2}(\hbar\omega - \Delta_{SO})\right]^{1/2}$, $f_{lh,k_\omega^{(1)}} = \exp\left(\frac{E_F}{k_BT}\right)\cdot\exp\left[-\frac{m_{SO}}{m_{SO}-m_{lh}}\frac{\hbar\omega-\Delta_{SO}}{k_BT}\right]$. The Fermi energy E_F is determined by the relation:

$$e^{\frac{E_F}{k_BT}} = \frac{1}{2}p\left(\frac{k_BT}{2\pi\hbar^2}\right)^{-3/2}\left(m_{hh}^{3/2} + m_{lh}^{3/2} + m_{SO}^{3/2}e^{-\frac{\Delta_{SO}}{k_BT}}\right)^{-1}, \tag{24}$$

where p is the hole concentration. Note that in our case, $\hbar\omega \gg k_BT$, so $e^{-\hbar\omega/k_BT} \ll 1$.

Thus, the frequency $(x = \hbar\omega/\Delta_{SO})$ and temperature $(y = k_BT/\Delta_{SO})$ dependencies of the single-photon absorption coefficient can be written as:

$$K_{SO,lh}^{(1)}(\omega,T) = K_0^{(1)}\frac{x-1}{x}(x-1)^{1/2}\frac{\exp\left[-\frac{m_{SO}}{m_{SO}-m_{lh}}\frac{x-1}{y}\right]}{y^{3/2}\left(m_{hh}^{3/2}+m_{lh}^{3/2}+m_{SO}^{3/2}e^{-1/y}\right)}, \tag{25}$$

where

$$K_0^{(1)} = \frac{11}{6}\frac{\pi^{3/2}e^2}{c\hbar n_\omega}\frac{(m_{hh}-m_{lh})^4}{(m_{SO}-m_{lh})^{5/2}}\frac{m_{SO}^{5/2}}{m_{lh}^{3/2}m_{hh}^2}\frac{\hbar^2p}{\Delta_{SO}}.$$

In further calculations, we assert that the temperature dependence of the bandgap width is determined by the Varshni formula [17]:

$$E_g(T) = E_g(T=0) - \gamma_T\frac{T^2}{T+T_V}, \tag{26}$$

and by the Passler formula [18]:

$$E_g(T) = E_g(T=0) - \frac{\alpha\Theta_p}{2}\left[\left(1 + \left(\frac{2T}{\Theta_p}\right)^p\right)^{1/p} - 1\right]. \tag{27}$$

Then, according to the multi-zone Kane model, the effective masses of electrons in the conduction band (m_c) and holes in the spin-orbit split-off subband (m_{SO}) depend on temperature and are expressed as:

$$m_0/m_c = \left[1 + 2F + \frac{E_P}{3}\left(E_{g0} - \frac{\alpha T}{\beta+T} + \frac{2}{3}\Delta_{SO}\right)\left(E_{g0} - \frac{\alpha T}{\beta+T}\right)^{-1}\left(E_{g0} - \frac{\alpha T}{\beta+T} + \Delta_{SO}\right)^{-1}\right], \quad (28)$$

$$m_0/m_{SO} = \left[\gamma_1 - \frac{E_P}{3}\Delta_{SO}\left(E_{g0} - \frac{\alpha T}{\beta+T}\right)^{-1}\left(E_{g0} - \frac{\alpha T}{\beta+T} + \Delta_{SO}\right)^{-1}\right], \quad (29)$$

where $E_{g0} = E_g(T=0)$. For quantitative calculations, the numerical values of the parameters γ_T, T_V, α, Θ_p, p are taken from [18].

If the numerical values of the band parameters for GaAs and InAs (see Table 1) are used, then as the temperature changes from 10 K to 300 K, the effective mass of electrons in the conduction band decreases by 0.053% and 0.051%, respectively, while the effective mass of holes in the spin-orbit split-off subband decreases by 0.01% and 0.04%, respectively, over this temperature range. At first glance, these changes appear to be very small; $\mathrm{E}_g(T)$ however, accounting for them significantly alters the frequency-temperature dependence of the absorption coefficient.

As seen from equation (8), the temperature dependence of $K_{SO,lh}^{(1)}$ is determined by the temperature dependence of $f_{lh,k_\omega^{(1)}}(\mathrm{T})$, while the frequency dependence is determined by the term $\frac{\hbar\omega-\Delta_{SO}}{\hbar\omega}k_\omega^{(1)}\rho(\hbar\omega)\exp\left(-\frac{m_{SO}}{m_{SO}-m_{lh}}\frac{\hbar\omega-\Delta_{SO}}{k_BT}\right)$. In this context, Figure 5 presents the frequency-temperature dependence of the distribution function of light holes involved in single-photon transitions in GaAs and InAs. It shows that, at a fixed frequency, the distribution function $f_{lh,k_\omega^{(1)}}$ initially increases with temperature, reaches a maximum, and then decreases. Specifically, at $\hbar\omega = 1{,}01\Delta_{SO}$ in GaAs (InAs), the function $f_{lh,k_\omega^{(1)}}$ reaches its maximum at a temperature of 90 K (60 K). Figure 5 also shows that the functions $f_{lh,k_\omega^{(1)}}(\mathrm{T}) = f_{lh,k_\omega^{(1)}}\left(\mathrm{T}, E_g(T)\right)$ and $\tilde{f}_{lh,k_\omega^{(1)}}(\mathrm{T}) = f_{lh,k_\omega^{(1)}}\left(\mathrm{T}, E_g(T)=0\right)$ differ significantly at low frequencies across all temperatures, but converge at high frequencies. Furthermore, the temperature dependence of the band parameters is prominently observed at low frequencies. The calculations do not account for the contribution of the coherent saturation effect in $f_{lh,k_\omega^{(1)}}(\mathrm{T})$ and $\tilde{f}_{lh,k_\omega^{(1)}}(\mathrm{T})$.

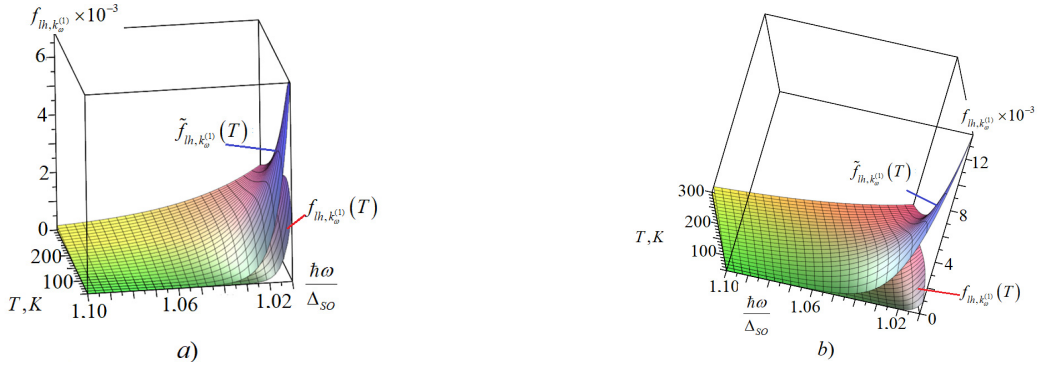

Figure 5. Frequency-temperature dependence of the distribution function of light holes $f_{lh,k_\omega^{(1)}}(\mathrm{T})$, participating in single-photon optical transitions in GaAs (a) and InAs (b) semiconductors, accounting for the temperature dependence of the bandgap width $E_g(\mathrm{T})$ and the effective mass of charge carriers using the Varshni formula, where $\tilde{f}_{lh,k_\omega^{(1)}}(\mathrm{T})$ is the distribution function of light holes at $E_g(\mathrm{T}=0)$.

The frequency-temperature dependence of the single-photon absorption coefficient $K_{SO,lh}^{(1)}(\omega,\mathrm{T})$ $\left(\widetilde{K}_{SO,lh}^{(1)}(\omega,\mathrm{T})\right)$ in InSb (a, b) and GaAs (c, d) (see Fig. 6), calculated using equation (14) with the Varshni formula (graphs a, c in Fig. 6) and the Passler formula (graphs b, d in Fig. 6), considers $\left(\widetilde{K}_{SO,lh}^{(1)}(\omega,\mathrm{T})\right)$ as the absorption coefficient, where the temperature dependence of $E_g(\mathrm{T})$ and the effective masses of holes is (or is not) accounted for. The contribution of the coherent saturation effect is not included, and the amplitude value of $\widetilde{K}_{SO,lh}^{(1)}(\omega,\mathrm{T})$ is assumed to be unity. From Fig. 6, it is evident that at a fixed frequency, $K_{SO,lh}^{(1)}(\mathrm{T})$ increases with temperature, reaches a maximum, and then decreases. This temperature behavior of $\left(\widetilde{K}_{SO,lh}^{(1)}(\omega,\mathrm{T})\right)$ corresponds to the analogous behavior of their distribution functions. Notably, in the frequency range $\Delta_{SO} \le \hbar\omega \le 1.3\Delta_{SO}$, the absorption coefficient $K_{SO,lh}^{(1)}(\omega,\mathrm{T})$ is greater than $\widetilde{K}_{SO,lh}^{(1)}(\omega,\mathrm{T})$, while at $\hbar\omega > 1.3\Delta_{SO}$, the graphs of $K_{SO,lh}^{(1)}(\omega,\mathrm{T})$ and $\widetilde{K}_{SO,lh}^{(1)}(\omega,\mathrm{T})$merge.

It should be noted that in narrow-bandgap crystals, if the dependences of $E_g(\mathrm{T})$, $m_{SO}(\mathrm{T})$, and $m_c(\mathrm{T})$ are taken into account, the dependence of $K_{SO,lh}^{(1)}(\omega,\mathrm{T})$ increases sharply (see Fig. 2). This is explained by the rapid growth of

$\left(\frac{m_{hh}-m_{lh}}{m_{SO}-m_{lh}}\right)^2\left(\frac{m_{hh}-m_{lh}}{m_{hh}}\right)^2\left(\frac{m_{SO}\cdot m_{lh}}{m_{SO}-m_{lh}}\cdot \Delta_{SO}\right)^{1/2}$ with increasing temperature (specifically, in InSb, this value increases by a factor of 10).

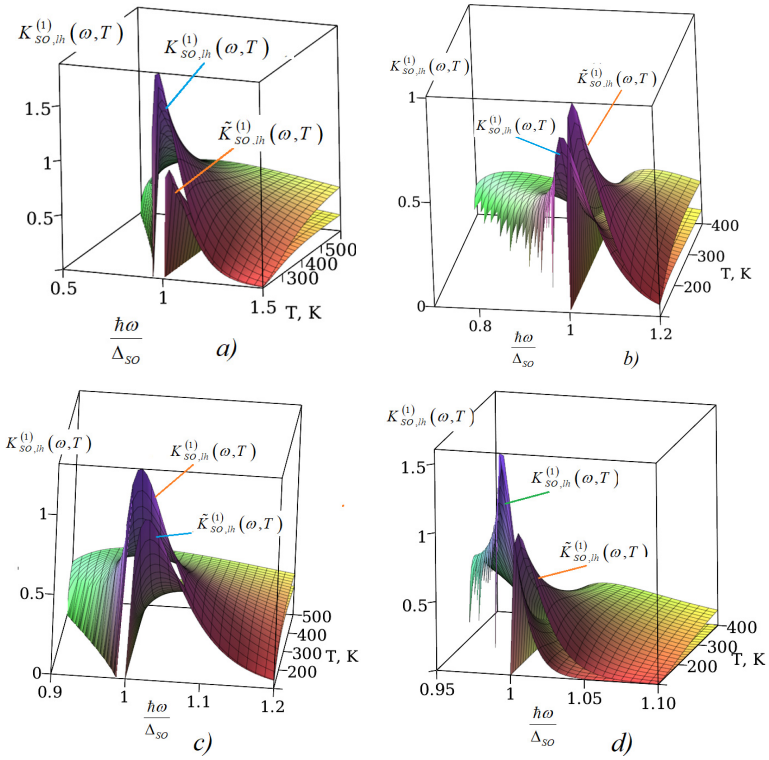

Figure 6. Frequency-temperature dependence of the single-photon absorption coefficient $K^{(1)}_{SO,lh}$ in InSb (a, b) and GaAs (c, d), where $K^{(1)}_{SO,lh}$a is calculated using the Varshni formula (graphs a, c) and the Passler formula (graphs b, d). Here, $\left(\tilde{K}^{(1)}_{SO,lh}(\omega,\mathrm{T})\right)$ represents the absorption coefficient, accounting for (or not accounting for) the temperature dependence of the bandgap width $E_g(\mathrm{T})$ and the effective masses of holes.

CONCLUSIONS

It has been shown that, when accounting for the contribution of the coherent saturation effect, the angular dependences of the probabilities of single-photon optical transitions from the heavy- and light-hole branches to the spin-orbit split-off subband of the valence band exhibit an oscillatory nature for both linearly and circularly polarized light, regardless of the Rabi parameter values (ζ_ω)

The maximum values of the angular dependence of the LCR coefficients for both first- and second-type optical transitions decrease with increasing ζ_ω, regardless of the angle between the wave vectors of the holes and the photon. The minimum value for first-type transitions is nonzero in the low ζ_ω region, while for second-type optical transitions, it is zero regardless of ζ_ω values.

The aforementioned results show that, at a fixed frequency, the single-photon absorption coefficient in GaAs and InAs semiconductors initially increases with rising temperature, reaches a maximum, and then decreases. Its maximum value, when accounting for the temperature dependence of $E_g(\mathrm{T})$, $m_{SO}(\mathrm{T})$, and $m_c(\mathrm{T})$, shifts toward lower frequencies. This shift is particularly pronounced when considering (27), both for narrow- and wide-bandgap semiconductors.

It is also noted that accounting for the temperature dependence of band parameters leads to a reduction in the frequency and temperature dependence of the single-photon absorption coefficient $K^{(1)}_{SO,lh}(\omega,\mathrm{T})$.

The work was carried out at Fergana State University.

ORCID

Rustam Y. Rasulov, https://orcid.org/0000-0002-5512-0654; **Voxob R. Rasulov,** https://orcid.org/0000-0001-5255-5612

REFERENCES

[1] E.L. Ivchenko, "Two-photon absorption of light and optical orientation of free carriers," Physics, St. Petersburg, **14**(12), 3489-3496 (1972). (in Russian)

[2] R.Ya. Rasulov, Polarization optical photovoltaic effects in semiconductors with linear and nonlinear absorption of light," Sc.D. Thesis, Ioffe Institute, 1993.

[3] R.Ya. Rasulov, "Linear-circular dichroism in multiphoton intersubband absorption in semiconductors," Semiconductors, **35**(6), 1674-1678 (1993). https://journals.ioffe.ru/articles/viewPDF/14966 (in Russian).
[4] S.D. Ganichev, E.L. Ivchenko, R. Ya. Rasulov, I.D. Yaroshetsky, and B.Ya. Averbukh, "Linear-circular dichroism of the drag current during nonlinear intersubband absorption of light in p-Ge," FTT, **35**(1), 198-207 (1993). https://journals.ioffe.ru/articles/viewPDF/14762 (in Russian).
[5] R.Ya. Rasulov, G.Kh. Khoshimov, and Kh. Kholitdinov, "Linear-circular dichroism of nonlinear light absorption in n-GaP," Semiconductors, **30**(2), 274-272 (1996). https://journals.ioffe.ru/articles/viewPDF/18345
[6] V.R. Rasulov, R.Ya. Rasulov, I. Eshboltaev, "Linearly and Circular Dichroism in a Semiconductor with a Complex Valence Band with Allowance for Four-Photon Absorption of Light," Physics of the Solid State, **59**, 463 (2017). https://doi.org/10.1134/S1063783417030283
[7] R.Y. Rasulov, V.R. Rasulov, I. Eshboltaev, and R.R. Sultonov, "Two- and Three-Photon Linear Circular Dichroism in Semiconductors of Cubic Symmetry," Russian Physics Journal, **63**(11), 2025–2030 (2021).
[8] R.Ya. Rasulov, V.R. Rasulov, M.Kh. Kuchkarov, and I.M. Eshboltaev, "Interband multiphoton absorption of polarized radiation and its linear circular dichroism in semiconductors in the Kane approximation," Russian Physics Journal, **65**(10), (2023). https://doi.org/10.1007/s11182-023-02825-3
[9] R.Ya. Rasulov, V.R. Rasulov, N.U. Kodirov, and U.M. Isomaddinova, "Interband one photon absorption of light and its linear-circular dichroism in crystals with coherent saturation effect included," Physics of the Solid State, **65**(7), 1173-1179 (2023). https://doi.org/10.61011/PSS.2023.07.56410.77
[10] N.V. Leppenen, E.L. Ivchenko, and L.E. Golub, "Nonlinear optical absorption and photocurrents in topological insulators," Phys. Rev. B, **105**, 115306 (2022). https://doi.org/10.1103/PhysRevB.105.115306
[11] S.N. Danilov, L.E. Golub, T. Mayer, A. Beer, S. Binder, E. Mönch, J. Minár, *et al*., "Superlinear Photogalvanic Effects in (Bi0.3Sb0.7)2(Te0.1Se0.9)3: Probing Three-Dimensional Topological Insulator Surface States at Room Temperature," Phys. Rev. Applied, **15**, 064030 (2021). https://doi.org/https://doi.org/10.1103/PhysRevApplied.16.064030
[12] S. Candussio, L.E. Golub, S. Bernreuter, T. Jötten, T. Rockinger, K. Watanabe, T. Taniguchi, *et al*., "Nonlinear intensity dependence of terahertz edge photocurrents in graphene," Phys. Rev B, **104**, 155404 (2021). https://doi.org/10.1103/PhysRevB.104.155404
[13] R.Y. Rasulov, V.R. Rasulov, K.K. Urinova, M.A. Mamatova, and B.B. Akhmedov, "Single and multiphoton optical transitions in atomically thin layers of transition metal dichalcogenides," East European Journal of Physics, (1), 393–397 (2024). https://doi.org/10.26565/2312-4334-2024-1-40
[14] D.A. Parshin, and A.R. Shabaev, "Theory of linear IR absorption by semiconductors with degenerate bands," Zh. Exp. Teor. Fiz. **92**(4), 1471-1484 (1987). http://jetp.ras.ru/cgi-bin/dn/e_065_04_0827.pdf
[15] G.L. Bir, and G.E. Pikus, *Symmetry and Strain-induced Effects in Semiconductors*, (Wiley, New York, 1972).
[16] E.L. Ivchenko, and R.Ya. Rasulov, *Symmetry and real band structure of semiconductors*, (Tashkent, Fan, 1989). https://koha.lib.tsu.ru/cgi-bin/koha/opac-detail.pl?biblionumber=125752
[17] I. Vurgaftman, J.R. Meyer, and L.R. Ram-Mohan, "Band parameters for III–V compound semiconductors and their alloys," Journal of Applied Physics, **89**, 5815-5875 (2001). https://doi.org/10.1063/1.1368156
[18] R. Paèssler, "Parameter Sets Due to Fittings of the Temperature Dependencies of Fundamental Bandgaps in Semiconductors," Phys. Stat. Sol. (b), **216**, 975-1007 (1999). https://doi.org/10.1002/(SICI)1521-3951(199912)216:23.3.CO;2-E
[19] R. Winkler, *Spin-Orbit Coupling Effects in Two-Dimensional Electron and Hole Systems*, vol. 191 (Springer, Berlin, 2003).
[20] V.R. Rasulov, R.Y. Rasulov, R.R. Sultonov, and B.B. Akhmedov, "Two- and Three-Photon Linear-Circular Dichroism in Cubic-Symmetry Semiconductors," Semiconductors, **54**(11), 1381–1387 (2020). https://doi.org/10.1134/S1063782620110226
[21] H. Haug and S. W. Koch, *Quantum Theory of the Optical and Electronic Properties of Semiconductors*, 5th ed. (World Scientific, Singapore, 2009).

ДО ТЕОРІЇ ВНУТРІШНЬОЗОННОГО МЕХАНІЗМУ ОДНОФОТОННОГО ПОГЛИНАННЯ В НАПІВПРОВІДНИКАХ З ВРАХУВАННЯМ ВПЛИВУ КОГЕРЕНТНОГО НАСИЧЕННЯ

Рустам Я. Расулов[a], Вохоб Р. Расулов[a], Форрух У. Касимов[b], Мардонбек Х. Насіров[a,c], Ісламм А. Мумінов[a]
[a]*Ферганський державний університет, Фергана, Узбекистан*
[b]*Андижанський державний університет, Андижан, Узбекистан*
[c]*Ферганський політехнічний інститут, Фергана, Узбекистан*

Проведено теоретичний аналіз частотно-температурної залежності коефіцієнта поглинання однофотонного поляризованого випромінювання у вузько- та широкозонних напівпровідниках з урахуванням внутрішньозонних оптичних переходів та ефекту когерентного насичення. Показано, що при фіксованій частоті випромінювання коефіцієнт поглинання однофотонного випромінювання спочатку зростає з температурою, досягає максимуму, а потім зменшується. Положення цього максимуму зміщується до нижчих частот як для вузько-, так і для широкозонних напівпровідників, якщо врахувати температурну залежність ширини забороненої зони та ефективних мас дірок. У напівпровідниках зі структурою ґратки цинкової суміші врахування температурної зміни параметрів зони призводить до зменшення амплітуди частотної та температурної реакції коефіцієнта поглинання однофотонного випромінювання. Зі зростанням температури поріг поглинання зменшується, що особливо помітно при використанні моделі забороненої зони Пасслера. Кожен тип внутрішньозонного оптичного переходу по-різному впливає на залежність коефіцієнта поглинання $K^{(1)}(\omega,T)$ від частоти, температури та поляризації для переходів, що включають зону відщеплення (SO) та зону легких дірок (LH).

Ключові слова: *ймовірність однофотонних переходів; коефіцієнти однофотонного поглинання та лінійно-кругового дихроїзму, ефект когерентного насичення; температурна залежність ширини забороненої зони*

East European Journal of Physics. 2. 452–460 (2025)
DOI: 10.26565/2312-4334-2025-2-56 ISSN 2312-4334

TWO-FLUID SCENARIO FOR DARK ENERGY COSMOLOGICAL MODEL IN FIVE DIMENSIONAL KALUZA-KLEIN SPACE TIME

Pranjal Kumar Ray[a*], **Rajshekhar Roy Baruah**[b]
[a] *Department of Mathematics, Gyanpeeth Degree College, Nikashi, Baksa-781372, Assam, India*
[b] *Department of Mathematical Sciences, Bodoland University, Kokrajhar, BTR-783370, Assam, India*
[*] *Corresponding Author e-mail: pkray3005@gmail.com*
Received March 3, 2025; revised April 24, 2025; in final form May 21, 2025; accepted May 23, 2025

In this work, we investigate the evolution of the dark energy equation of state parameter in a five-dimensional Kaluza-Klein homogeneous and isotropic cosmological model filled with a barotropic fluid and a dark fluid. We adopt a special form of the deceleration parameter, $q = -\frac{a\ddot{a}}{\dot{a}^2} = -1 + \frac{\alpha}{1+a^\alpha}$ as proposed by Singha and Debnath [28], which facilitates a smooth transition from early-time deceleration to late-time acceleration. Using this form, we solve the Einstein field equations and analyze the dynamics of the universe under both non-interacting and interacting two-fluid scenarios. The physical and geometrical implications of the model are examined in detail. Key cosmological quantities such as the dark energy density ρ_D, pressure p_D, and density parameter Ω_D are studied for various spatial curvatures—open, closed, and flat geometries. The solutions obtained are physically viable and in good agreement with current observational data, including those from Type Ia supernovae, the cosmic microwave background, and large-scale structure surveys. Additionally, we evaluate the jerk parameter to assess the model's deviation from the standard ΛCDM cosmology. The model demonstrates compatibility with the observed late-time accelerated expansion and provides a unified framework that accommodates a wide range of cosmic behaviors through appropriate parameter choices.

Keywords: *Kaluza-Klein space time; Two-fluid model; Dark energy; Special form of deceleration parameter; Jerk parameter*

PACS: 98.80.-k, 95.36.+x

1. INTRODUCTION

The recent advances in the cosmological observation decided that the universe not only expanding but also accelerating has been confirmed by high red shift type Ia Supernovae experiment (SNe.Ia) [1-3], cosmic background radiation (CMBR) [4], large scale structure observation [5], Sloan Digital Sky Survey (SDSS) [6, 7]. According to contemporary cosmology, this is created by a mystery type of energy known as dark energy, which has a positive energy density and a negative pressure. From the observational evidences First Year Wilkinson Microwave Anisotropy Probe (WMAP) [8], and Chandra X-ray observatory [9] combination found that the baryonic matter occupies 4.9%, the dark matter occupies 26.8% and the dark energy occupies 68.3%of the total energy of the universe [10].

It is still unknown exactly what the physical conditions at very early stages of the creation of our universe. The investigation of five dimensional space-time is important because it is thought that the universe may have once existed in a higher dimensional epoch during its early stages of the evolution of the universe. Kaluza [11] and Klein [12] introduced a five dimension that is a model that sought to unify the fundamental forces of gravity and electromagnetism. In a certain sense the Kaluza-Klein theory resembles ordinary gravity, except that it is inscribed in five dimensions instead of four. This theory has been regarded as a candidate of fundamental theory due to the possible work of unifying the fundamental principle. Five dimensional Kaluza Klein spatially homogeneous and isotropic cosmological models are generally considered as good approximation of the present and early stages of the universe. Numerous eminent authors have studied the five-dimensional Kaluza-Klein space-time within the context of general theory of relativity. Chodos et al. [13], Appelquist et al. [14] studied, the present universe is four-dimensional stage may have been preceded by a higher-dimensional phase, which turns into four-dimensional in the sense that any additional dimensions collapse to an undetected Planckian length scale as a result of dynamical contraction. Das et al. [15] studied interacting and non-interacting two-fluid scenario in the anisotropic five-dimensional Bianchi type-I universe within the framework of Lyra geometry. Ray et al. [16] investigated string cosmological model in five dimensional Kaluza-Klein space time. Many prominent authors has been investigated the evolution of the dark energy parameter under two-fluid scenario. Tiwari et al. [17] investigated the equation of state (EoS) parameter for dark energy (DE) in the spatially homogeneous and anisotropic Bianchi type-III spacetime filled with a barotropic fluid and dark energy by considering a variable deceleration parameter. Goswami et al. [18] have studied a Bianchi type-I cosmological model of universe filled with barotropic and dark energy (DE) type fluids. Mishra et al. [19] have studied the stability of the dark energy cosmological models with combination of matter fields and dark energy in an anisotropic space time. Ray et al. [20] discussed about an interacting and non-interacting two-fluid dark energy models in five dimensional Kaluza-Klein universe. Two-fluids cosmological models with matter and radiating source in $(2+1)$ dimensional Saez-Ballester scalar-tensor theory of gravitation has been

Cite as: P.K. Ray, R.R. Baruah, East Eur. J. Phys. 2, 452 (2025), https://doi.org/10.26565/2312-4334-2025-2-56

investigated by Kumar et al. [21]. Hatka et al. [22] have studied Bianchi type I cosmological model under two-fluids scenario in scale covariant theory of gravitation. Trivedi et al. [23] has explored the features of the five-dimensional Bianchi type-I cosmological universe filled with barotropic fluid and dark energy within the framework of Saez-Ballester theory of gravitation.

Motivated from the above literature. in this paper we have analyzed the evolution of dark energy parameter by considering five dimensional Kaluza-Klein homogeneous and isotropic cosmological filled with two-fluid model by considering a special form of deceleration parameter. In Sect 1, we discussed the introduction of Kaluza-Klein cosmology. The Kaluza-Klein models and its field equations are presented in Sect 2. In Sects 3 and 4 we discussed the interacting and non-interacting two fluid model. Sect 5 we discuss the jerk parameter in our derived models. In Sect 6 we discussed the physical interpretation of our model. Finally, conclusions and summarized are given in the last sect 7.

2. THE METRIC AND FIELD EQUATIONS

The FRW type homogeneous and isotropic 5D Kaluza-Klein space-time has been considered and it is as follows

$$ds^2 = dt^2 - a^2(t)\left[\frac{dr^2}{1-kr^2} + r^2(d\theta^2 + \sin^2\theta d\phi^2) + (1-kr^2)d\psi^2\right] \tag{1}$$

where $a(t)$ is a scale factor considered to be a function of cosmic time t and $k = -1, 0, +1$ is the curvature parameter for open, flat and closed universe respectively.

The Einstein's field eqn. (with $8\pi G = 1$ and $c = 1$) can be written as

$$R_{ij} - \frac{1}{2}g_{ij}R = -T_{ij} \tag{2}$$

where T_{ij} is the two fluid energy momentum tensor consisting of dark fluid and barotropic fluid.

The energy conservation law for two fluid is given by

$$\dot{\rho} + 4\frac{\dot{a}}{a}(\rho + p) = 0 \tag{3}$$

where $p = p_m + p_D$ and $\rho = \rho_m + \rho_D$. Here ρ_m and p_m are the energy density and pressure of the perfect fluid and ρ_D and p_D are the energy density and pressure of dark fluid respectively.

The Einstein field eqn (2) with (3) for the metric (1) we may write

$$6\left(\frac{\dot{a^2}}{a^2} + \frac{k}{a^2}\right) = (\rho_m + \rho_D) \tag{4}$$

and

$$3\frac{\ddot{a}}{a} + 3\left(\frac{\dot{a^2}}{a^2} + \frac{k}{a^2}\right) = -(p_m + p_D) \tag{5}$$

Here the over dot indicate a derivatives with respect to cosmic time t.

The EoS parameter (ω) which is considered as an important quantity in describing the dynamics of the universe, is given by

$$p_m = (\omega_m - 1)\rho_m \tag{6}$$

$$p_D = (\omega_D - 1)\rho_D \tag{7}$$

In the following sections we deal with two cases (I) non-interacting two fluid model and (II) interacting two fluid model

3. CASE-I: NON-INTERACTING TWO FLUID MODEL

In this section, the fluids do not interact with each other. The conservation equation for the dark and barotropic fluid separatly as

$$\dot{\rho_m} + 4\frac{\dot{a}}{a}(\rho_m + p_m) = 0 \tag{8}$$

$$\dot{\rho_D} + 4\frac{\dot{a}}{a}(\rho_D + p_D) = 0 \tag{9}$$

Integrating (8) we obtain

$$\rho_m = \rho_0 a^{-4\omega_m} \tag{10}$$

where ρ_0 is an integrating constant.

Now using (10) in (4) and (5) we obtain ρ_D and p_D in terms of scale factor $a(t)$.

$$\rho_D = 6\left(\frac{\dot{a}^2}{a^2} + \frac{k}{a^2}\right) - \rho_0 a^{-4\omega_m} \tag{11}$$

$$p_D = -3\left(\frac{\ddot{a}}{a} + \frac{\dot{a}^2}{a^2} + \frac{k}{a^2}\right) - \rho_0(\omega_m - 1)a^{-4\omega_m} \tag{12}$$

Now we assume the special form of deceleration parameter which is given by

$$q = -\frac{a\ddot{a}}{\dot{a}^2} = -1 + \frac{\alpha}{1 + a^\alpha} \tag{13}$$

where α is an arbitrary constant.

After integrating (13) we get

$$a(t) = (e^{m\alpha t} - 1)^{\frac{1}{\alpha}} \tag{14}$$

where m is an integration constant.

By using the scale factor $a(t)$ in (11) and (12) we obtain

$$\rho_D = 6[\frac{m^2 e^{2m\alpha t}}{(e^{m\alpha t} - 1)^2} + \frac{k}{(e^{m\alpha t} - 1)^{\frac{2}{\alpha}}}] - \rho_0(e^{m\alpha t} - 1)^{\frac{-4\omega_m}{\alpha}} \tag{15}$$

and

$$p_D = -3[\frac{m^2 e^{m\alpha t}(2e^{m\alpha t} - \alpha)}{(e^{m\alpha t} - 1)^2} + \frac{k}{(e^{m\alpha t} - 1)^{\frac{2}{\alpha}}}] - \rho_0(\omega_m - 1)(e^{m\alpha t} - 1)^{\frac{-4\omega_m}{\alpha}} \tag{16}$$

By using (15) and (16) in (7) we obtain

$$\omega_D = -\left[\frac{\frac{3m^2 e^{m\alpha t}(2e^{m\alpha t} - \alpha)}{(e^{m\alpha t} - 1)^2} + \frac{3k}{(e^{m\alpha t} - 1)^{\frac{2}{\alpha}}} + \rho_0(\omega_m - 1)(e^{m\alpha t} - 1)^{\frac{-4\omega_m}{\alpha}}}{\frac{6m^2 e^{2m\alpha t}}{(e^{m\alpha t} - 1)^2} + \frac{6k}{(e^{m\alpha t} - 1)^{\frac{2}{\alpha}}} - \rho_0(e^{m\alpha t} - 1)^{\frac{-4\omega_m}{\alpha}}}\right] + 1 \tag{17}$$

The expressions for the matter energy density Ω_m and DE density Ω_D are given by

$$\Omega_m = \frac{\rho_m}{6H^2} = \frac{\rho_0(e^{m\alpha t} - 1)^{\frac{-4\omega_m}{\alpha}+2}}{6m^2 e^{2m\alpha t}} \tag{18}$$

and

$$\Omega_D = \frac{\rho_D}{6H^2} = 1 + \frac{k(e^{m\alpha t} - 1)^2}{6m^2 e^{2m\alpha t}(e^{m\alpha t} - 1)^{\frac{2}{\alpha}}} - \frac{\rho_0(e^{m\alpha t} - 1)^{\frac{-4\omega_m}{\alpha}+2}}{6m^2 e^{2m\alpha t}} \tag{19}$$

From eqns. (18) and (19) we obtain

$$\Omega = \Omega_m + \Omega_D = 1 + \frac{k(e^{m\alpha t} - 1)^2}{6m^2 e^{2m\alpha t}(e^{m\alpha t} - 1)^{\frac{2}{\alpha}}} \tag{20}$$

From eqns. (13) and (14), the deceleration parameter q (Recently used Katore et al. [24]) as

$$q = \frac{-a\ddot{a}}{\dot{a}^2} = -1 + \frac{\alpha}{e^{m\alpha t}} \tag{21}$$

4. CASE-II: INTERACTING TWO FLUID MODEL

In this section we consider the interaction between dark fluid and barotropic fluid. The conservation equation for the dark and barotropic fluid are given by

$$\dot{\rho_m} + 4\frac{\dot{a}}{a}(\rho_m + p_m) = Q \tag{22}$$

$$\dot{\rho_D} + 4\frac{\dot{a}}{a}(\rho_D + p_D) = -Q \tag{23}$$

where the quantity Q represents the interaction between the matter and DE component. We consider $Q > 0$, as it shows that the energy transferred from DE to dark matter. Let us consider ((from ref. Gou et al. [25], Amendola et al. [26])

$$Q = 4H\sigma\rho_m \tag{24}$$

where σ is an coupling constant.

Using (24) in (22) and after integrating we obtain

$$\rho_m = \rho_0 a^{-4(\omega_m - \sigma)} \tag{25}$$

where ρ_0 is an integrating constant.

Now using (25) in (4) and (5) we obtain ρ_D and p_D in terms of scale factor $a(t)$.

$$\rho_D = 6\left(\frac{\dot{a}^2}{a^2} + \frac{k}{a^2}\right) - \rho_0 a^{-4(\omega_m - \sigma)} \tag{26}$$

$$p_D = -3\left(\frac{\dot{a}}{a} + \frac{\dot{a}^2}{a^2} + \frac{k}{a^2}\right) - \rho_0(\omega_m - 1)a^{-4(\omega_m - \sigma)} \tag{27}$$

Putting the value of $a(t)$ from (14) in eqns. (26) and (27) we obtain

$$\rho_D = 6[\frac{m^2 e^{2m\alpha t}}{(e^{m\alpha t} - 1)^2} + \frac{k}{(e^{m\alpha t} - 1)^{\frac{2}{\alpha}}}] - \rho_0(e^{m\alpha t} - 1)^{\frac{-4(\omega_m - \sigma)}{\alpha}} \tag{28}$$

and

$$p_D = -3[\frac{m^2 e^{m\alpha t}(2e^{m\alpha t} - \alpha)}{(e^{m\alpha t} - 1)^2} + \frac{k}{(e^{m\alpha t} - 1)^{\frac{2}{\alpha}}}] - \rho_0(\omega_m - 1)(e^{m\alpha t} - 1)^{\frac{-4(\omega_m - \sigma)}{\alpha}} \tag{29}$$

Using (28) and (29) in (7) we obtain

$$\omega_D = -\left[\frac{\frac{3m^2 e^{m\alpha t}(2e^{m\alpha t} - \alpha)}{(e^{m\alpha t} - 1)^2} + \frac{3k}{(e^{m\alpha t} - 1)^{\frac{2}{\alpha}}}] + \rho_0(\omega_m - 1)(e^{m\alpha t} - 1)^{\frac{-4(\omega_m - \sigma)}{\alpha}}}{\frac{6m^2 e^{2m\alpha t}}{(e^{m\alpha t} - 1)^2} + \frac{6k}{(e^{m\alpha t} - 1)^{\frac{2}{\alpha}}} - \rho_0(e^{m\alpha t} - 1)^{\frac{-4(\omega_m - \sigma)}{\alpha}}}\right] + 1 \tag{30}$$

The expressions for the matter energy density Ω_m and DE density Ω_D are given by

$$\Omega_m = \frac{\rho_m}{6H^2} = \frac{\rho_0(e^{m\alpha t} - 1)^{\frac{-4(\omega_m - \sigma)}{\alpha} + 2}}{6m^2 e^{2m\alpha t}} \tag{31}$$

and

$$\Omega_D = \frac{\rho_D}{6H^2} = 1 + \frac{k(e^{m\alpha t} - 1)^2}{6m^2 e^{2m\alpha t}(e^{m\alpha t} - 1)^{\frac{2}{\alpha}}} - \frac{\rho_0(e^{m\alpha t} - 1)^{\frac{-4(\omega_m - \sigma)}{\alpha} + 2}}{6m^2 e^{2m\alpha t}} \tag{32}$$

From eqns. (31) and (32) we obtain the total energy density parameter Ω as

$$\Omega = \Omega_m + \Omega_D = 1 + \frac{k(e^{m\alpha t} - 1)^2}{6m^2 e^{2m\alpha t}(e^{m\alpha t} - 1)^{\frac{2}{\alpha}}} \tag{33}$$

5. THE JERK PARAMETER (J)

In cosmology, the jerk parameter (j) is a dimensionless quantity that characterizes the rate of change of the universe's expansion acceleration, specifically the third derivative of the scale factor with respect to time, normalized by the hubble parameter cubed. The jerk parameter j is a suitable method to describe models close to ΛCDM model. A deceleration-to-acceleration transition occurs for models with a positive value of j and negative value of q. Flat ΛCDM models have a constant jerk $j = 1$. The jerk parameter in cosmology is defined as the dimensionless third derivative of the scale factor with respect to cosmic time t [27].

The Jerk Parameter in cosmology is defined as the dimensionless third derivative of the scale factor with respect to cosmic time t. It is defined as

$$j(t) = \frac{1}{H^3}\frac{\dddot{a}}{a} \tag{34}$$

where overhead dot denote derivatives with respect to cosmic time.

The jerk parameter (j) appears in the fourth term of a Taylor expansion of the scale factor around a_0.

$$\frac{a(t)}{a_0} = 1 + H_0(t-t_0) - \frac{1}{2}q_0H_0^2(t-t_0)^2 + \frac{1}{6}j_0H_0^3(t)^3 + 0\left[(t-t_0)^4\right] \tag{35}$$

In equation (34) can be written as

$$j(t) = q + 2q^2 - \frac{\dot{q}}{H} \tag{36}$$

where H is the Hubble parameter, q is the deceleration parameter and overhead dot denotes the derivatives with respect to cosmic time t.

For the derived model, the jerk parameter (j) can be written as

$$j(t) = 1 - \frac{3\alpha}{e^{m\alpha t}} + \frac{\alpha^2(e^{m\alpha t}+3)}{e^{2m\alpha t}} \tag{37}$$

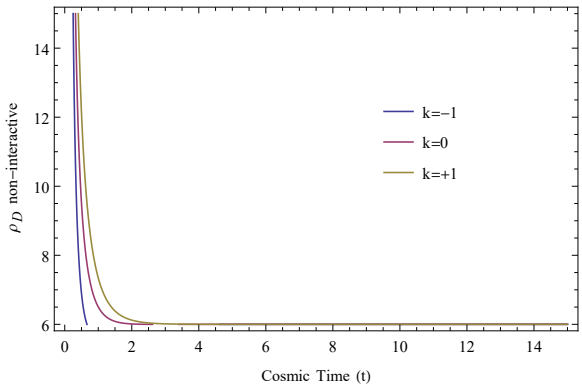

Figure 1. Plot of ρ_D vs. t (non-interactive) with $m = 1$, $\rho_0 = 1$, $\alpha = 3$, $\omega_m = 0.5$

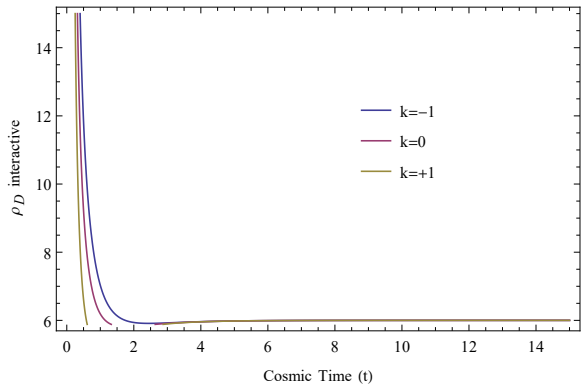

Figure 2. Plot of ρ_D vs. t (interactive) with $m = 1$, $\rho_0 = 1$, $\alpha = 3$, $\omega_m = 0.5$

6. RESULTS AND DISCUSSION:

We have plotted the various figures using these calculations for suitable values of the constants. We also used all the three values of $k = -1, 0, 1$ while plotting the figures.

In figures 1 and 2 we have shown the variation of dark energy density ρ_D versus cosmic time t for both non-interacting and interacting cases from equations (15) and (28). It is observed that for both cases the graphs of ρ_D is decreasing function of cosmic time t in all the three open, closed and flat universe. It indicates that the dark energy model start with infinite density and when cosmic time increases the energy density tends to a finite value.

Figs. 3 and 4 represent the variation of pressure for DE for both cases. We observed that at $t \to 0$ the pressure p_D is negative for open ($k = -1$) and flat ($k = 0$) universe and positive for closed ($k = 1$) universe. Finally, pressure p_D is zero all the three open, closed and flat universe for late time cosmic evolution.

The behavior of EoS for DE with respect to cosmic time t is shown in figs. 5 and 6 which correspond to the eqns. (17) and (30) for both non-interacting and interacting cases respectively. We observed that from both the figures the EoS parameter ω_D is a decreasing function of time t. At $t \to \infty$, the EoS parameter ω_D tends to zero. So, the model indicating matter dominated era of the universe .

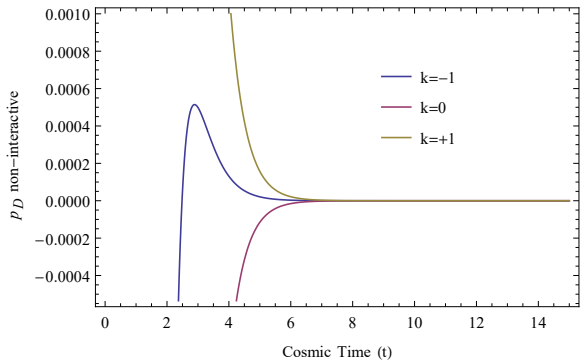

Figure 3. Plot of p_D vs. t (non-interactive) with $m = 1$,$\rho_0 = 1$,$\alpha = 3$,$\omega_m = 0.5$

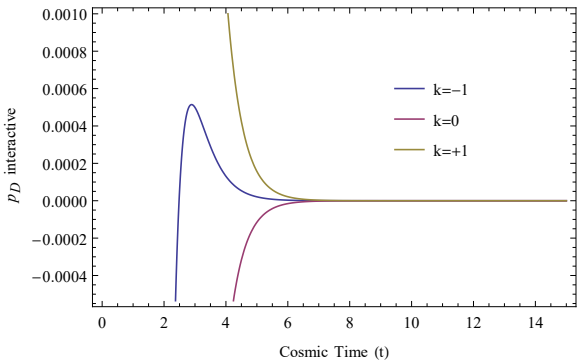

Figure 4. Plot of p_D vs. t (interactive) with $m = 1$,$\rho_0 = 1$,$\alpha = 3$,$\omega_m = 0.5$

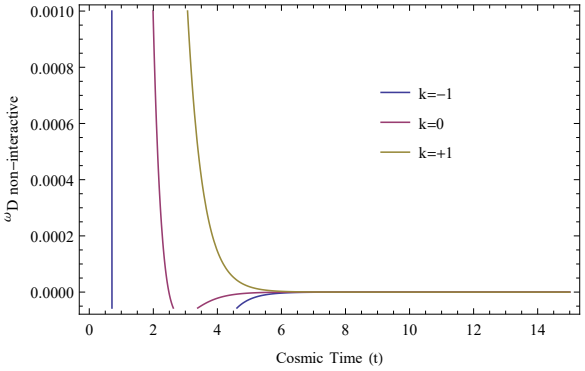

Figure 5. Plot of ω_D vs. t (non-interactive) with $m = 1$,$\rho_0 = 1$,$\alpha = 3$,$\omega_m = 0.5$

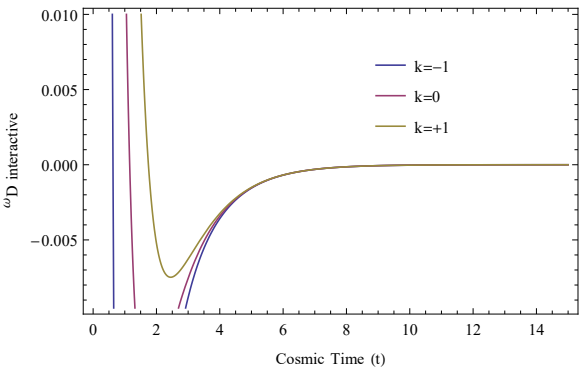

Figure 6. Plot of ω_D vs. t (interactive) with $m = 1$,$\rho_0 = 1$,$\alpha = 3$,$\omega_m = 0.5$

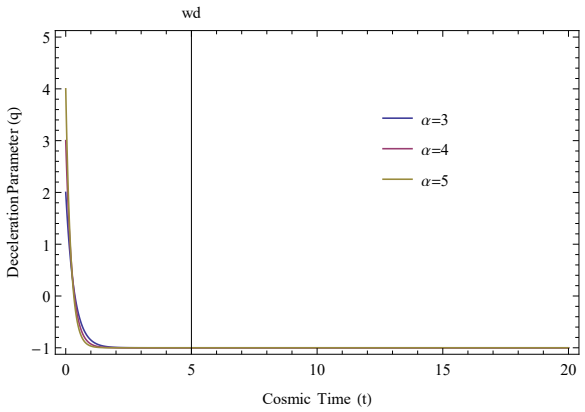

Figure 7. Plot of q vs. t for $m = 1$, $\alpha = 3, 4, 5$.

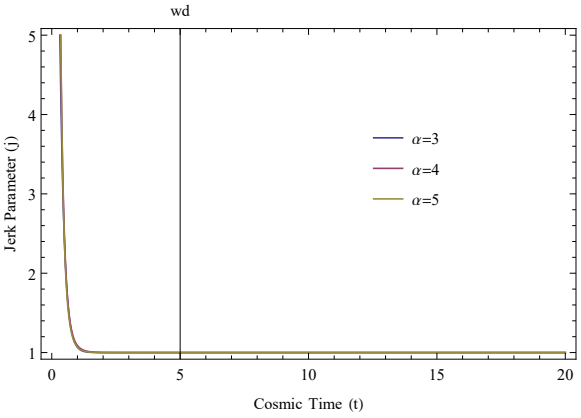

Figure 8. Plot of j vs. t for $m = 1$, $\alpha = 3, 4, 5$.

From eqns. (20) and (33) the total energy density parameter Ω for both non-interacting and interacting cases are same. From the right hand side of these two equations it is clear that for $k = 0$ (i.e for flat universe), $\Omega = 1$ and $k = 1$ (i.e for closed universe), $\Omega > 1$ and $k = -1$ (i.e for open universe), $\Omega < 1$. We also observed that, at late time, Ω approaches to 1 for all the three values of k, which is shows that the universe will acquire a flat structure. These results are fully consistent with the present day's observations.

From the equation (21), we observed that the deceleration parameter q is a decreasing function of cosmic time t . Initially at $t = 0$, the deceleration parameter q is positive which changes sign from positive to negative. As time approaches infinity, deceleration parameter q tend to -1 which indicates that the proposed model universe has a transition from decelerating to accelerating phase. It can be confirmed from the graph of figure 7, which plots the deceleration parameter q against cosmic time t. This graphical representation clearly illustrates the model's expanding behavior over time. Thus our model represents an interesting cosmological model of the universe.

A decelerate phase to accelerate phase transition of the universe occurs for models with a positive value of jerk and negative value of deceleration parameter. In figures 7 and 8 we can observed that deceleration parameter (q) is negative and jerk parameter (j) is positive so that we do have a transition of the model from decelerated to accelerated phase at late time cosmic evolution.

The cosmological model constructed here exhibits the following properties:

- The scale factor
$$a(t) = \left(e^{m\alpha t} - 1\right)^{1/\alpha}$$
evolves from zero at $t = 0$ and grows exponentially at late times, reflecting early decelerated and late-time accelerated expansion.

- The deceleration parameter q evolves from a positive value (decelerating phase) at early times to $q \to -1$ (de Sitter expansion) at late times, for all $\alpha > 0$.

- The total density parameter approaches unity, $\Omega \to 1$ as $t \to \infty$, consistent with observations of a spatially flat universe.

- For suitable choices of parameters, the equation of state parameter ω_D for the dark fluid can evolve through quintessence ($\omega_D > -1$), cosmological constant ($\omega_D = -1$), or phantom ($\omega_D < -1$) regimes.

- Interaction between the fluids alters the evolution of the matter density, allowing a more flexible fit to observational data through the coupling constant σ.

7. CONCLUSION

In this work, we have investigated a homogeneous and isotropic five-dimensional Kaluza-Klein cosmological model incorporating a two-fluid system—comprising a barotropic fluid and a dark fluid—within the framework of open, closed, and flat universes. The Einstein field equations were solved by adopting a hybrid scale factor that leads to a time-dependent deceleration parameter of the form $q = -\frac{a\ddot{a}}{\dot{a}^2} = -1 + \frac{\alpha}{1+a^\alpha}$ which smoothly describes a transition from early-time decelerated expansion to late-time accelerated expansion.

We analyzed both non-interacting and interacting scenarios for the two-fluid system and examined the dynamical behavior of key cosmological quantities including the energy density ρ_D, pressure p_D, and density parameter Ω_D of the dark fluid. In all cases, the solutions are physically realistic and consistent with current observational data from Type Ia Supernovae, cosmic microwave background (CMB), and large-scale structure surveys.

The total density parameter approaches unity at late times, indicating an asymptotically flat universe. Furthermore, the equation of state parameter for the dark fluid can exhibit quintessence, cosmological constant, or phantom-like behavior depending on the choice of parameters. The model remains valid for open, closed, and flat geometries, adding to its robustness. Additionally, the jerk parameter was derived and discussed to explore the model's deviation from the standard ΛCDM paradigm.

Overall, the proposed model successfully captures essential features of cosmic evolution and offers a flexible framework for understanding the late-time acceleration of the universe.

Acknowledgments

We would like to express sincere gratitude to the anonymous reviewer(s) for their valuable comments and constructive suggestions, which significantly improved the quality and clarity of this manuscript. Their careful reading and insightful feedback are greatly appreciated.

ORCID

Pranjal Kumar Ray, https://orcid.org/0000-0001-7313-7882; **Rajshekhar Roy Baruah**, https://orcid.org/0000-0002-5961-9540

REFERENCES

[1] A.G. Riess, A.V. Filippenko, P. Challis, A. Clocchiatti, A. Diercks, P.M. Garnavich, et al., "Observational Evidence from Supernova for an Accelerating Universe and a cosmological constant," The Astronomical Journal, **116**, 1009-1038 (1998). https://doi.org/10.1086/30049

[2] S. Perlmutter, G. Aldering, G. Goldhaber, R.A. Knop, P. Nugent, P.G. Castro, et al. "Measurements of Ω and *Lambda* From 42 High Red shift Supernovae," The Astronomical Journal, **517**, 565-586 (1999). https://doi.org/10.1086/307221

[3] A.G. Riess, "The Case for an Accelerating Universe from Supernovae," The Astronomical Society of the Pacific, 112, 1284-1299 (2000). https://doi.org/10.1086/316624

[4] C.H. Lineweaver, "The Cosmic Microwave Background and Observational Convergence in the $\Omega_m - \Omega_\Lambda$ Plane, The Astrophysical Journal," **505**, L69-L73 (1998). https://doi.org/10.1086/311613

[5] M. Tegmark, et al. "Cosmological parameters from SDSS and WMAP," Physical Review, **69**, 103501 (2004). https://doi.org/10.1103/PhysRevD.69.103501

[6] U. Seljak, et al. "Cosmological parameter analysis including SDSS Lyα forest and galaxy bias: Constraints on the primordial spectrum of fluctuations, neutrino mass, and dark energy," Physical Review D, **71**, 103515 (2005). https://doi.org/10.1103/PhysRevD.71.103515

[7] J.K. Adelman-McCarthy, et al. "The Fourth Data Release of the Sloan Digital Sky Survey," The Astrophysical Journal Supplement Series, **162**, 38-48 (2006). https://doi.org/10.1086/497917

[8] C.L. Bennett, et al. "First Year Wilkinson Microwave Anisotropy Probe (WMAP) observation Preliminary Maps and Results," The Astrophysical Journal Supplement Series, **148**, 1-27 (2003). https://doi.org/10.1086/377253

[9] S.W. Allen, et al. "Constraints on dark energy from Chandra observations of the largest relaxed galaxy clusters," Monthly Notices of the Royal Astronomical Society, **353**, 457-467 (2004). https://doi.org/10.1111/j.1365-2966.2004.08080.x

[10] H.R Ghate, "Kaluza-Klein Anisotropic Dark Energy Cosmological Model with hybrid Deceleration Parameter," The African Review of Physics, **11**, 0026 (2016). http://lamp.ictp.it/index.php/aphysrev/article/view/1307/501

[11] T. Kaluza, "On the Unification Problem in Physics," Preuss. Akad. Wiss. Berlin. Math. Phys. K1, 966-972 (1921). https://doi.org/10.1142/S0218271818700017

[12] O. Klein, "Quantentheorie and Fundamental Relativistic Theory," Zeitschrift Physik, **37**, 895-906 (1926). https://doi.org/10.1007/BF01397481

[13] A. Chodos and S. Detweiler, "Where has the Fifth Dimension Gone," The American Physical Society, **21**, 2167-2170 (1980). https://doi.org/10.1103/PhysRevD.21.2167

[14] T. Appelquist, et al. *Modern Kaluza-Klein Theories*, (Addison Wesley, Reading, 1987).

[15] K. Das and J. Bharali, "Higher-Dimensional Anisotropic Modified Holographic Ricci Dark Energy Cosmological Model In Lyra Manifold," Astrophysics, **64**(2), 295-311 (2021). https://doi.org/10.1007/s10511-021-09686-z

[16] P.K. Ray and R.R. Baruah, "Anisotropic cloud string cosmological model with five-dimensional kaluza-klein space-time," Frontiers in Astronomy and Space Sciences, **9**, 869020 (2022). https://doi.org/10.3389/fspas.2022.869020

[17] R.K. Tiwari, A. Beesham and B.K. Shukla, "Scenario of two fluid dark energy models in Bianchi type-III Universe," International Journal of Geometric Methods in Modern Physics, **15**, 1850189 (2018). https://doi.org/10.1142/S021988781850189X

[18] G. Goswami, M. Mishra, A.K. Yadav, and A. Pradhan, "Two-fluid scenario in bianchi type-i universe," Modern Physics Letters A, **35**(12), 2050086 (2020). https://doi.org/10.1142/S0217732320500868

[19] B. Mishra, F.M. Esmaeili, P.P. Ray and S. Tripathy, "Stability analysis of two-fluid dark energy models," Physica Scripta, **96**(4), 045006 (2021). https://doi.org/10.1088/1402-4896/abdf82

[20] P.K. Ray and R.R. Baruah, "An interacting and non-interacting two-fluid scenario for dark energy models in five dimensional Kaluza-Klein space-time," Journal of Mathematical and Computational Science, **11**(6), 7699-7716 (2021). https://doi.org/10.28919/jmcs/6382

[21] P. Kumar, G. Khadekar, and V. Dagwal, "Two fluids cosmological model in $(2 + 1)-$ dimensional saez-ballester scalar-tensor theory of gravitation," Journal of Dynamical Systems and Geometric Theories," **20**(1), 91–114 (2022). https://doi.org/10.1080/1726037X.2022.2079267

[22] S.P. Hatkar, P. Agre, and S. Katore, "Two fluids cosmological models in scale covariant theory of gravitation," Annals of Applied Sciences, **1**, 659 (2022). https://doi.org/10.55085/aas.2022.659

[23] D. Trivedi and A.K. Bhabor, "Higher-dimensional bianchi type-I dark energy models with barotropic fluid in saez-ballester scalar-tensor theory of gravitation," Indian Journal of Physics, **97**, 1317–1327 (2022). https://doi.org/10.1007/s12648-022-02448-3

[24] S.D. Katore and D.V. Kapse, "Accelerating universe with variable EoS parameter of dark energy in Brans–Dicke theory of gravitation," Journal of Astrophysics and Astronomy, **40**(3), 21 (2019). https://doi.org/10.1007/s12036-019-9589-y

[25] Z.K. Guo, N. Ohta and S. Tsujikawa, "Probing the coupling between dark components of the universe," Physical Review D, **76**(2), 023508 (2007). https://doi.org/10.1103/PhysRevD.76.023508

[26] L. Amendola, G.C. Campos, and R. Rosenfeld, "Consequences of dark matter-dark energy interaction on cosmological parameters derived from type Ia supernova data," Physical Review D, **75**(8), 083506 (2007). https://doi.org/10.1103/PhysRevD.75.083506

[27] M. Visser, "Jerk, snap and the cosmological equation of state," Classical and Quantum Gravity, **21**, 2603-2605 (2004). https://doi.org/10.1088/0264-9381/21/11/006

[28] A.K. Singha and U. Debnath, "Accelerating Universe with a Special Form of Decelerating Parameter," International Journal of Theoretical Physics, **48**, 351-356 (2009). https://doi.org/10.1007/s10773-008-9807-x

ДВОРІДИННИЙ СЦЕНАРІЙ ДЛЯ КОСМОЛОГІЧНОЇ МОДЕЛІ ТЕМНОЇ ЕНЕРГІЇ У П'ЯТИВИМІРНОМУ ПРОСТОРІ-ЧАСІ КАЛУЦИ-КЛЕЙНА

Пранджал Кумар Рей[a], **Раджшехар Рой Баруах**[b]

[a] *Кафедра математики, Колледж Гъянпит, Нікаші, Бакса-781372, Ассам, Індія*

[b] *Кафедра математичних наук, Університет Бодоланда, Кокрайхар, BTR, Ассам, PIN-783370, Індія*

У цій роботі ми досліджуємо еволюцію параметра рівняння стану темної енергії у п'ятивимірній однорідній та ізотропній космологічній моделі Калуци-Клейна, заповненій баротропною та темною рідинами. Ми використовуємо спеціальну форму параметра уповільнення, $q = -\frac{a\ddot{a}}{\dot{a}^2} = -1 + \frac{\alpha}{1+a^\alpha}$, як запропоновано Сінгхою та Дебнатхом [28], що сприяє плавному переходу від уповільнення на ранніх етапах до прискорення на пізніх етапах. Використовуючи цю форму, ми розв'язуємо рівняння поля Ейнштейна та аналізуємо динаміку Всесвіту як за невзаємодіючих, так і за взаємодіючих дворідинних сценаріїв. Детально розглядаються фізичні та геометричні наслідки моделі. Ключові космологічні величини, такі як густина темної енергії ρ_D, тиск p_D та параметр густини Ω_D, досліджуються для різних просторових кривин — відкритої, закритої та плоскої геометрій. Отримані рішення є фізично життєздатними та добре узгоджуються з сучасними даними спостережень, включаючи дані наднових типу Ia, космічного мікрохвильового фону та оглядів великомасштабних структур. Крім того, ми оцінюємо параметр ривка, щоб оцінити відхилення моделі від стандартної космології ΛCDM. Модель демонструє сумісність зі спостережуваним прискореним розширенням наприкінці часу та забезпечує єдину структуру, яка враховує широкий діапазон космічної поведінки завдяки відповідному вибору параметрів.

Ключові слова: *простір-час Калуци-Клейна; дворідинна модель; темна енергія; спеціальна форма параметра уповільнення; параметр ривка*